BEHAVIOR OF WALLS AND PILES IN COHESIVE SOILS UNDER CYCLIC LOADS

A Dissertation

by

AHMED QASIM OBAID AL-RAMTHAN

Submitted to the Office of Graduate and Professional Studies of
Texas A&M University
in partial fulfillment of the requirements for the degree of

DOCTOR OF PHILOSOPHY

Chair of Committee,	Charles P. Aubeny
Committee Members,	Gary T. Fry
	Marcelo Sanchez
	Jerome J. Schubert
Head of Department,	Robin Autenrieth

May 2019

Major Subject: Civil Engineering

ABSTRACT

The nonlinear cyclic behavior of a soil-structure system has a significant influence on the mechanical response of this system. The cyclic response of soil-structure system has been studied experimentally and analytically. However, the results of these studies are not yet reproducing the applicability of key aspects of soil-structure behavior concepts in practice. A key prerequisite is to model the cyclic response in a facilitative and realistic way. There are several constitutive models in the literature that are available for cumulative responses, but they need many soil tests for calibration and they can be used under specific numerical codes and can be only executed by specialists. To overcome these difficulties, this research develops a simplified constitutive model (a kinematic hardening constitutive model with Von Mises failure criterion) for analyzing nonlinear plastic response of a soil-structure system subjected to cyclic loading.

In addition, cumulative deformations are an essential aspect of the performance of walls and piles/caissons under cyclic loading. Therefore, reasonable estimates of the cumulative plastic displacements of structures in cohesive soils are necessary, particularly for soils which the cyclic influence may be significant. For example, the cumulative wall displacements that increase over time as the system is subjected to repeated live loading from trains passing near wall, in addition to the vertical settlements under the train track. Studying the effects of cyclic loading of railroads on the soil-wall system is necessary to improve train safety when a soil-wall system is near the tracks. As a second example, while pile and caisson anchors and foundations for offshore structures, such as wind turbines and the oil/gas exploration and production facilities have been the focus of considerable attention with respect to monotonic load capacity, much less attention has been given to cumulative displacements under cyclic loading. This issue is particularly crucial for inclined loading, since cumulative displacements can lead to loss of embedment of the caisson or pile.

Since stress-strain behavior of soils is inelastic even at small strains, analyses based on linear elasticity, or on elastoplastic models that assume purely elastic behavior beneath the ultimate yield surface, cannot predict the cumulative soil deformations. Hence, an analysis that takes inelastic soil behavior at low stress levels into account, such as a bounding surface plasticity model, is required to predict cumulative displacements under cyclic loading.

A cyclic nonlinear elastoplastic soil spring model has been applied to predict the monotonic and cyclic nonlinear *p-y* curve of piles in soft clay during the cyclic loading. Predictions of pile performance based on the kinematic hardening constitutive model used in this research are shown to match the centrifuge test results better than predictions based on the widely used API soil springs. This proposed spring model can overcome the limitations of the API clay model and can be implemented with either MATLAB or as UEL (User-defined elements) subroutine in ABAQUS/Standard. Predictions based on the spring model developed in this research shows good agreement with the measurements of cumulative displacement and soil stiffness from centrifuge tests involving cyclic loading of a single pile in soft clay.

DEDICATION

To my beloved wife ***Ruaa***,

to my children ***Noor*** and ***Ali***,

and to my parents.

Having you in my life truly a blessing.

Thank you!

ACKNOWLEDGEMENTS

It has been a true privilege for working under the supervision of Dr. Charles Aubeny. I would like to thank him for the guidance and mentoring that he kindly provided to me. Dr. Aubeny, thank you for all the motivation that kept me learning all of these years. I would like to thank you for helping me grow up as a professional and a researcher.

Also, I would like to express my deep appreciation and gratitude to Dr. Gary T. Fry, Dr. Marcelo Sanchez, and Dr. Jerome J. Schubert for contributing as members of my committee and for their guidance and support throughout the course of this research.

I would like to thank the staff at the Zachry Department of Civil Engineering at Texas A&M University, very specially to Mrs. Laura Byrd, and Mr. Chris Grunkemeyer, for all the help and support during my time as a graduate student.

Thank you to the Texas A&M High Performance Research Computing facility for providing resources needed to perform numerical simulations.

To my parents, thank you for bringing me to this world, supporting me, and encouraging me throughout my life. It is because of your love, care and life examples that I have had the motivation and inspiration to set and reach for every goal in my life.

Finally, I would like to thank my wife, Ruaa, and my kids, Noor and Ali. I am blessed by having you in my life. Thank you for your support and encouragement during my graduate study. You have been the sunshine and brightness of my life and without your inspiration and happiness during this journey, I wouldn't have been able to cross the finish line. I love you.

CONTRIBUTORS AND FUNDING SOURCES

This work was supervised by a dissertation committee consisting of the following:

- Dr. Charles P. Aubeny, P.E., Professor, Zachry Department of Civil Engineering, Texas A&M University, College Station, Texas, USA [Chair],
- Dr. Gary T. Fry, P.E., Adjunct Associate Professor, Zachry Department of Civil Engineering, Texas A&M University, College Station, Texas, USA [Member],
- Dr. Marcelo Sanchez, Professor, Zachry Department of Civil Engineering, Texas A&M University, College Station, Texas, USA [Member],
- Dr. Jerome J. Schubert, Associate Professor, Harold Vance Department of Petroleum Engineering, Texas A&M University, College Station, Texas, USA [Member].

All the work conducted for this dissertation was completed independently by the student. Graduate study was supported by a four-year Scholarship for Doctoral Studies sponsored by the Ministry of Higher Education and Scientific Research and University of Baghdad, Iraq.

NOMENCLATURE

A_p	Cross-sectional area of pile
B	Width
C_{bb}	Hardening constant for backbone curve
C_{un}	Unloading hardening constant
C_{re}	Reloading hardening constant
D	Diameter of caisson/pile
$Dist$	Distance
E	Elastic modulus
E_p	Elastic modulus of pile
F_a	Applied load
F_{ax}	Applied horizontal load
$F_{ax\text{-}rev}$	Applied horizontal load reversal
F_{peak}	Applied peak load
F_{ult}	Ultimate load capacity
G_p	Shear modulus of pile
FS	Factor of safety
H	Initial kinematic hardening modulus
I_p	Moment of inertia of plie
J_p	Polar moment of inertia of plie
L	Length of caisson
L/D	Aspect ratio

M	Moment
M_{peak}	Peak moment of the cycle
M_{res}	Residual moment of the cycle
N_p	Bearing factor
K^e	Soil modulus of the elastic region
K^p	Soil modulus of the plastic region
$\boldsymbol{S}$	Deviatoric stress tensor
p	Current force at displacement, y
p_a	Atmospheric pressure
p_{ult}	Size of the limit bounding surface
p_{yield}	Size of the yield surface
s_u	Undrained shear strength
t	Thickness of caisson wall
u_r	Cumulative resultant displacements
u_x	Cumulative horizontal displacements
u_y	Cumulative vertical displacements
y	Displacement
y_{yield}	Yield displacement at which the plastic deformation initiated
ΔM	Moment difference per cycle
Δx	Element size in x-direction
α	Adhesion factor
$\boldsymbol{\alpha_b}$	Backstress tensor
$\dot{\boldsymbol{\alpha}}_{\boldsymbol{b}}$	Backstress rate tensor

γ	Parameter
γ_{yield}	Shear strain of soil
δ_e	Ratchet strain
$\dot{\boldsymbol{\epsilon}}^{\boldsymbol{pl}}$	Plastic flow rate
$\dot{\bar{\epsilon}}^{pl}$	Equivalent plastic strain rate
ζ	Load reversal ratio
μ	Poisson’s ratio of soil
μ_p	Poisson’s ratio of pile
σ	Stress
σ_1	Major principal stress
σ_2	Intermediate principal stress
σ_3	Minor principal stress
σ_x	Horizontal stress
σ_0	Initial yield stress
σ_{max}	Ultimate stress
ψ	Load inclination angle

TABLE OF CONTENTS

LIST OF FIGURES

LIST OF TABLES

Page

1 INTRODUCTION

1.1 Retaining Walls

Permanent and temporary support systems for excavations near railways depend on retaining wall and temporary shoring systems (Smethurst and Powrie, 2007; Tatsuoka et al., 1996). There are two important manuals for retaining walls and shoring systems near railways in the US: the Manual for Railway Engineering (AREMA, 2010) and the Guidelines for Temporary Shoring (GTS, 2004). These guidelines recommend a minimum distance of 12 ft between the center-line of the train track and the track-side of the shoring system. Retaining systems utilize support structures near the excavation to provide lateral resistance for soil mass. The most common type of shoring system is the cantilever sheet pile walls, which rely on the passive resistance of soil below the base of the excavation. The required passive capacity is attained by the embedding wall to sufficient depth to prevent the uncontrolled rotation and translation of the wall. In addition, shoring systems can be classified into restrained and unrestrained types, where the restrained systems can be either braced or anchored walls while the unrestrained (non-gravity cantilevered) systems can either soldier pile or cantilever sheet pile walls. According to the manual of the California Department of Transportation (California Department of Transportation, 2011); to avoid large wall deflections, cantilever sheet pile retaining walls should not be used for excavation depths exceeding 18 ft.

1.2 Offshore Structures

Offshore energy structures have been utilized in the last 70 years. Early offshore structures were typically fixed structures to support oil/gas exploration and production. As exploitation of oil-gas resources progressed into deeper waters, floating structures secured to the seabed by anchors became more common. In recent years, interest in renewable energy as an alternative to fossil fuels has increased. Offshore wind farms offer great advantages regarding vigorous and sustained winds. In the U.S., the current high cost of offshore wind energy relative to land-based wind energy development can be offset to some extent by the proximity of potential offshore wind farm sites to the population centers using this energy; i.e., reduced transmission costs can offset the higher capital costs for offshore wind energy development. At present, most offshore wind turbines are supported caisson foundations. The design procedures for caisson foundations based usually on the monotonic loading analysis. While monotonic load capacity is undoubtedly important, and in many cases may be the dominant design consideration, cyclic loading can lead to excessive deformations and, possibly, reduction in embedment. Thus, the performance of caissons and piles under cyclic loading should be considered in their design. The loads that affect the offshore structures with suction caisson foundations can be classified into three types: static permanent loads, cyclic loads with low frequency, and cyclic loads with high frequency (Clukey and Morrison, 1993). Lifetime of offshore wind turbine has become a significant topic in industrial and academic fields, especially when two decades had passed for the early generation of the installed offshore wind farms in the world (Ziegler and Muskulus, 2016). For instance, the report of the European offshore wind industry (EWEA, 2016) indicated that 80% of the foundations of the offshore wind power are caissons. However, the suction caissons have a dominant advantage over other foundations types in lateral resistance performance (Aubeny, 2017). At present, the primary way in which cyclic effects on suction caissons are considered is to predict the degradation of strength under cyclic loading and then do a monotonic load capacity analysis. Thus, the functioning necessities of suction caissons under cyclic loading are not fully studied, especially, cyclic amplitude with high frequency and the reduction of the undrained shear strength of clay along the wall of caisson regarding a reliable estimate for their performance under cyclic loads with the growing usage of suction caisson foundations for offshore structures.

1.3 Problem Statement

The nonlinear, inelastic behavior of a soil-structure system has a significant influence on the mechanical response of a system subjected to cyclic loading. However, the analytical frameworks used in most previous studies (e.g. predictive models for deformations or ultimate load capacity under monotonic loading) do not consider cumulative deformations due to inelastic behavior at working stress levels. Thus, they do not consider all aspects of wall, pile, and anchor performances that need to be considered in practice. A major need at this time is a model that can be practically implemented that realistically models the cyclic response of piles and caissons.

Design methods for the behavior of soils to predict an accumulated, permanent deformation due to cyclic loading are typically based on elastic-plastic solutions for predicting the effects of repeated loads. While the elastic approach is a conservative approach that usually involves a significant simplification to compensate for the uncertainties in the existing design methodologies.

Current design methodology in this research for predicting soil movements with repeated loading utilizes plasticity analysis because linear elastic and elastic-perfectly plastic models of soil behavior are not capable of modeling the cumulative plastic deformations that are a key aspect of cyclic behavior. Thus, the predicting of soil behaviors employs bounding surface plasticity model (Dafalias, 1986). This approach is capable of simulating the permanent plastic deformations under sub-yield loading conditions, i.e. at stress levels well below the maximum yield stress.

Numerical modeling using the finite element method for the study of behaviors of some problems that involved (1) soil-sheet pile wall system near the railway track during the passage of trains, (2) soil-anchored caisson system under wind and wave actions, and (3) soil-single pile system under cyclic lateral loads are presented in this research.

1.4 Research Objectives

Considering the limitations of the elastic theory and the existing *p-y* curves to design retaining walls, large diameter caissons, and laterally loaded piles in cohesive soils regarding the long-term cyclic loading effects and the lack of research in evaluating the cyclic load effects of walls, caissons, and piles in clay. This research project aims to model numerically the behavior of cantilever sheet pile wall, suction anchor of offshore wind turbine farm, and laterally loaded pile subjected to cyclic loading. Thus, the objectives are:

1. To model the nonlinear stress-strain behavior of soil by implementing a cyclic hardening model.
2. To understand the long-term behavior of retaining wall when subjected to a large number of repeated live loads from the passage of trains.
3. To understand the long-term performance of suction caissons when subjected to a large number of loading cycles of different characteristics.
4. To better understand the lateral behavior of pile foundations under monotonic and cyclic loads.

5. To develop design suggestions and recommendations that addresses the shortcomings of the *p-y* curves for cyclic design.

Another significant contribution in this study is the nonlinear kinematic constitutive spring model for cohesive soils under cyclic loading that based on the bounding surface plasticity approach (Dafalias, 1986; Dafalias and Herrmann, 1986) for predicting the ratcheting behavior, soil stiffness degradation, and cumulative permanent deformations.

All modeling of FEA was conducted in cohesive soils under undrained conditions. Thus, the soil strength is independent of the vertical stress and the excess pore pressures are unable to dissipate.

2 LITERATURE REVIEW

2.1 Background for Walls

Sheet pile walls have usually consisted of continuously linked wall segments embedded in soils to resist the lateral earth pressures and used for various purposes; such as supporting excavations, cofferdams, cut-off walls under dams, stabilization of slope, and retaining wall structures. The sheet pile walls can be classified into two groups; cantilever and anchored. The design of sheet pile walls is usually based on the limit equilibrium approach (Bowles, 1988; Gopal Madabhushi and Chandrasekaran, 2005; King, 1995) notwithstanding of the changes of lateral earth pressure due to wall movements with time. In reality, sheet pile walls are considered as a flexible retaining wall system, can endure relatively large deformations. Thus, the limit equilibrium method as a rigid body concept is no longer suitable for sheet pile walls. Therefore, the design methods of sheet pile walls need to be further studied.

Lateral earth pressures acting on a retaining wall can be categorized into three types according to deformation states (Figure 2.1): active, passive, and at-rest. The at-rest state coincides with zero lateral stress, which would identify to a relatively rigid wall system. Active earth pressure evolves where the wall deforms away from the soil mass, while passive earth pressure can advance in regions where the wall thrusts into the soil. Thus, the lateral deformation of a wall in a soil-wall system has a major effect on the retaining wall systems, especially in developing the intensity of earth pressure. For instance, Bowles (1996) indicated the movement magnitudes of the wall depends on soil types that should be had to produce an active earth pressure when the sheet pile wall moves away from the soil, as shown in Table 2.1.

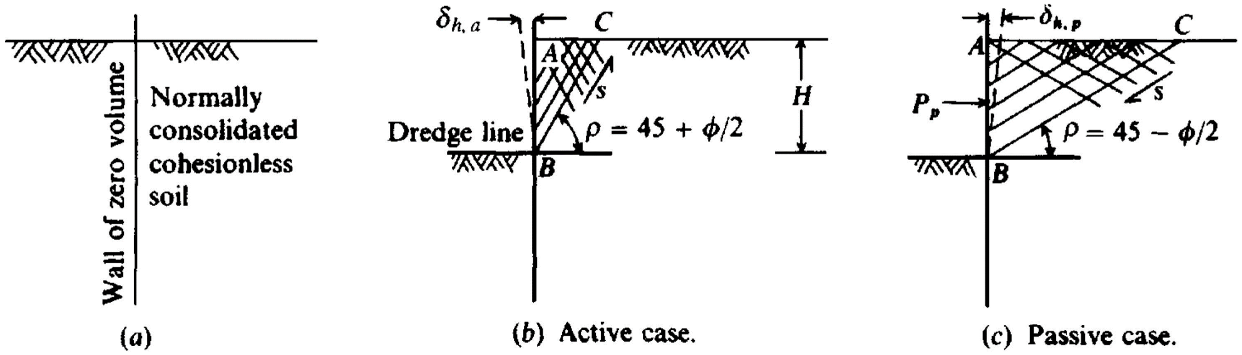

Figure 2.1. Types of lateral earth pressures (Bowles, 1996)

Table 2.1. Amount of active translation (Bowles, 1996)

Soil and condition	**Amount of translation, $\delta_{h,a}$**
Cohesionless, dense	$0.001\,H - 0.002\,H^*$
Cohesionless, loose	$0.002\,H - 0.004\,H$
Cohesive, firm	$0.01\,H - 0.02\,H$
Cohesive, soft	$0.02\,H - 0.05\,H$

H is the height of wall.

Generally, the active and passive earth pressures on walls are plastic state conditions that occurred when a sufficient level of deformation had been developed. Small deformations are typically required to generate active condition. However, higher deformations than the active case are usually needed to mobilize the passive condition. Typical values of mobilized deformations relative to the wall height are tabulated in Table 2.2.

Table 2.2. Mobilized wall deformations (Clough and Duncan, 1991)

Type of Backfill	**Value of Δ/H***	
	Active	**Passive**
Dense Sand	0.001	0.01
Medium Dense Sand	0.002	0.02
Loose Sand	0.004	0.04
Compacted Silt	0.002	0.02
Compacted Lean Clay	0.010	0.05
Compacted Fat Clay	0.010	0.05

Δ is the movement of the top of the wall required to achieve minimum active or maximum passive pressure, either by tilting or lateral translation; H is the height of wall.

Some researchers have studied earth pressure and deformation of sheet pile walls, via experimental tests, field measurements, and numerical computations (Bentler and Labuz, 2006; Bransby and Milligan, 1975; Georgiadis and Anagnostopoulos, 1998; Milligan, 1983). While, some others (Babu and Basha, 2008; Krabbenhoft and Damkilde, 2003; Krabbenhoft et al., 2005; Lyamin and Sloan, 2002) believed that the key prerequisites for designing the sheet pile wall are to obtain the yield moment and the depth of sheet pile wall. However, the lower bound limit analysis and nonlinear computations are too complex; the practical applications are still in the theoretical stage. Gopal Madabhushi and Chandrasekaran (2005) investigated a new method to estimate the location of the pivot point that is applicable to both cohesionless and cohesive soils. The pivot point's location that obtained by this approach matched satisfactorily with the centrifuge and laboratory test data. Unfortunately, this method is only valid for a rigid sheet pile wall.

In addition, the surcharge effects on the wall systems have been studied from multi-direction significances such as formations of the surcharge loads, i.e., concentrated, line, or uniformly distributed load and their distance from wall. Therefore, the consideration of additional lateral earth pressures generated from surcharge loads acting on the ground behind the wall is very essential. One of the methods that is currently utilized to estimate the earth pressure that produced by the surcharge loads is the elastic theory (Jarquio, 1981; Misra, 1980).

The elastic solutions based on Boussinesq's theory are widely used to evaluate the earth pressure of wall systems. Since this elastic theory does not consider the influence of soil strength along the wall system, Motta (1994) considered of using the Coulomb theory for his solution (Figure 2.2). He indicated that the surcharge applied on retaining wall systems has a significant impact on these systems. Therefore, he tried to derive a solution to estimate the active earth pressure by considering the effect of surcharge that applied at a distance from the wall head as well as the seismic influence by means of a pseudo-static method.

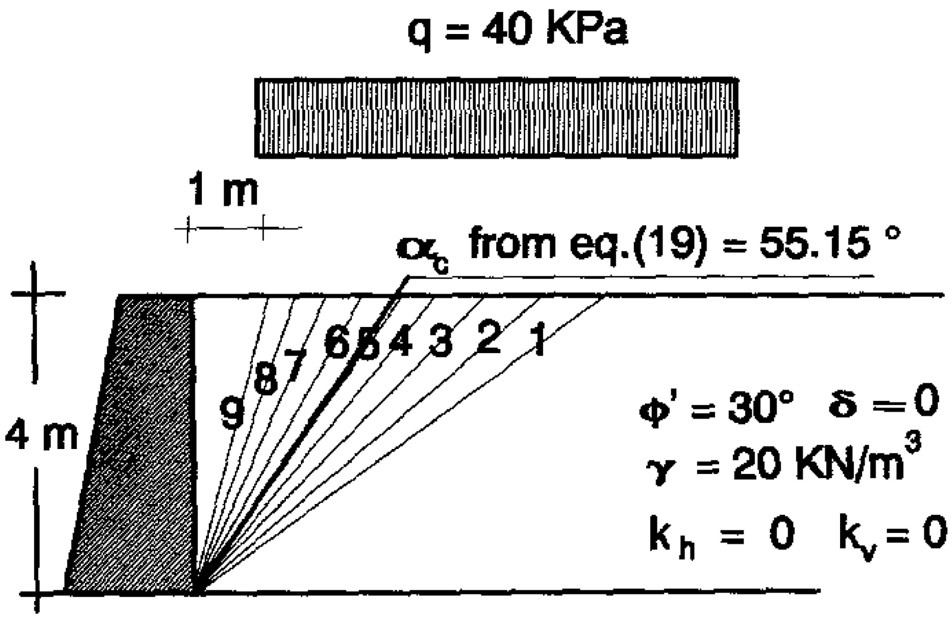

Figure 2.2. Graphical solution example (Motta, 1994)

Georgiadis and Anagnostopoulos (1998) did an experimental investigation that included several tests on a model of cantilever sheet pile wall to study the influence of surcharge loads. In addition, they compared their results to results of elastic finite element analyses. They indicated that the bending moment increases with increasing surcharge load intensity and reducing the distance between the wall and surcharge load (Figure 2.3), and the elastic analyses gave extremely large and unrealistic values of lateral pressures and bending moments for the soil-wall system.

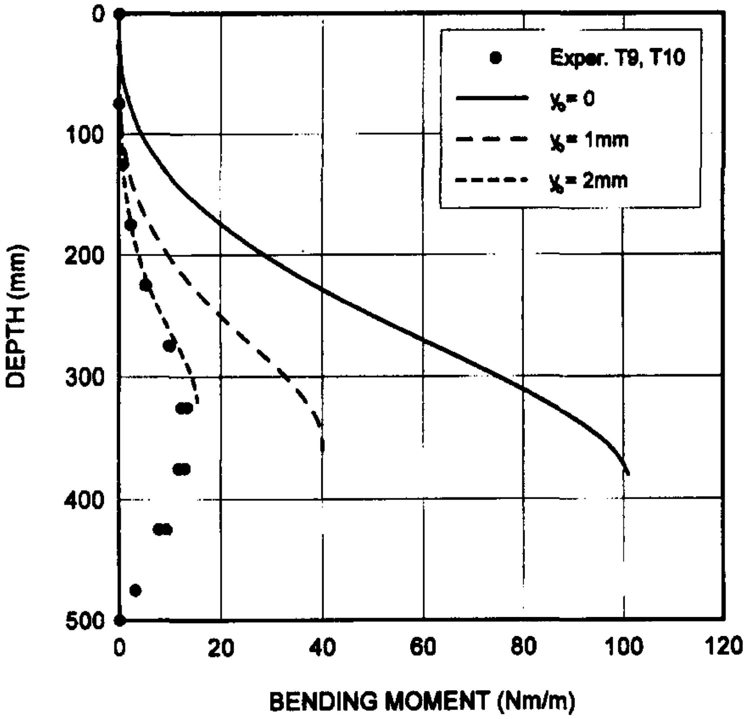

Figure 2.3. Effect of lateral wall movement on bending moments (Georgiadis and Anagnostopoulos, 1998)

Huang et al. (1999) performed experimental model wall tests, supported at the top and the bottom, to investigate the influence of different wall rigidities on deflections and lateral earth pressure distribution on walls. The backfill material was 120,000 pieces of 1.96 mm diameter stainless steel rods that were placed piece by piece behind the walls in a parallel and dense stack. Their study suggested that there was a remarkable relationship between the wall rigidity and wall response such as the lateral pressure distribution along the wall, as shown in Figure 2.4 and wall deflection, as shown in Figure 2.5. Thus, the experimental results showed that the highest flexible wall leads to the highest wall deflection, and consequently results the lowest lateral pressure distribution on wall.

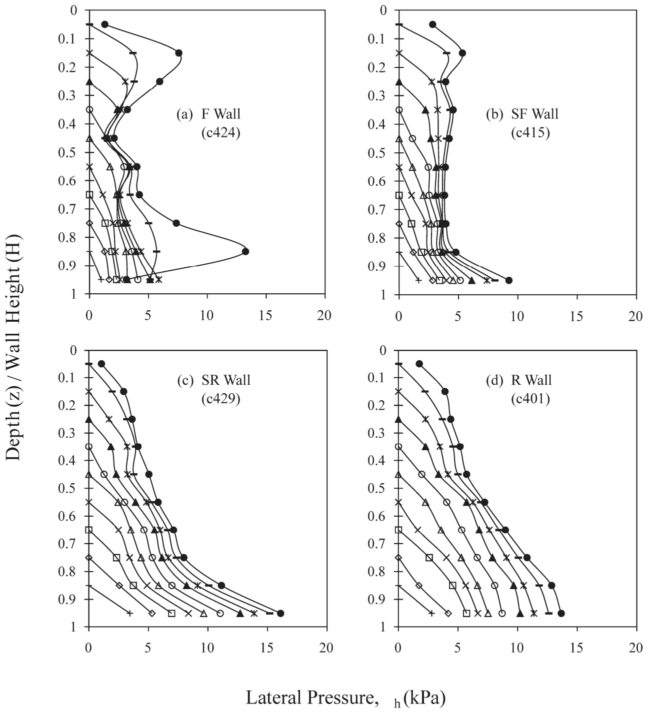

Figure 2.4. Lateral pressure distribution on walls with various wall rigidities (Huang et al., 1999)

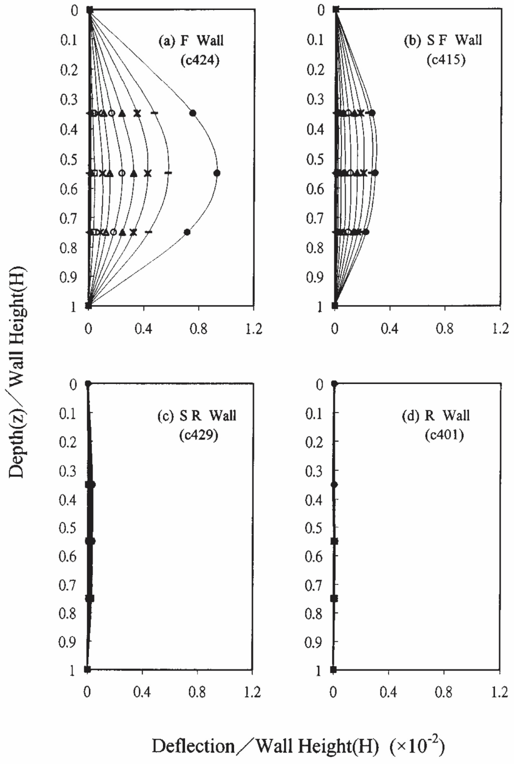

Figure 2.5. Deflections of walls with various wall rigidities (Huang et al., 1999)

Kim and Barker (2002) produced an analytical method to predict the earth pressure due to the effect of live load surcharges on retaining walls and abutments in highways. According to the conventional design of standard specifications for highway bridges (AASHTO, 1994; AASHTO, 1996), the lateral earth pressure from the live load surcharge of highway loads can be simulated by an equivalent height (h_{eq}) that is about 600 mm layer of backfill. They noticed that values of equivalent height for live load cases that designed depends on LRFD specifications (AASHTO, 1994) should not be constant for all wall height. Moreover, they tabulated some appropriate values for equivalent height (h_{eq}) for live load surcharge that were based on the wall height, the distance between the wall and surcharge load, and the direction of live load as a parallel or perpendicular to the wall. Figure 2.6 presents the results for an example of a specific case of live load surcharge where s is the distance between the wall and the load parallel to wall and k is the distance between the wall and the load perpendicular to wall. They modeled the truck and tandem loads as a point loads with the Boussinesq's theory to estimate the lateral earth pressure behind the wall.

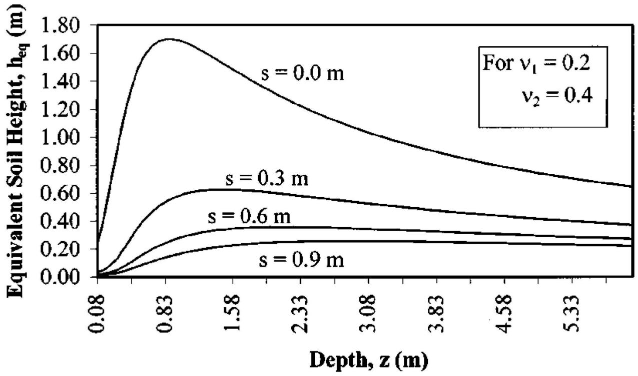

(a) Values of h_{eq} for various distances, s - Truck parallel to wall

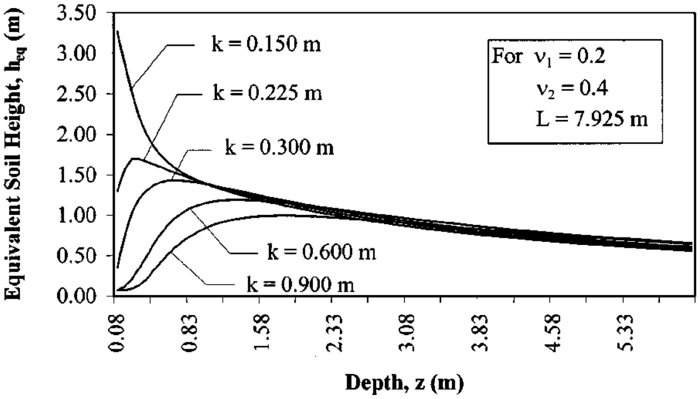

(b) Values of h_{eq} for various distances, k - Tandem perpendicular to wall

Figure 2.6. Values of h_{eq} for various distances, s and k (Kim and Barker, 2002)

Greco (2006) evaluated the active earth pressure for retaining wall when a strip load applied on the surface ground behind the wall. He mentioned that inconsistent magnitudes of lateral earth pressure that estimated from the research of Georgiadis and Anagnostopoulos (1998) from the elastic analyses and the experimental outcomes could result from considering the soil in an elastic condition and concurrently enforced the soil to sufficient movement to produce an active failure case. Thus, he utilized the numerical solutions of Coulomb's method only without using the elastic approach (Boussinesq's theory), as shown in Figure 2.7. He indicated that the active thrust depends on the position and intensity of the surcharge strip, the soil parameters, and the soil-wall system geometry.

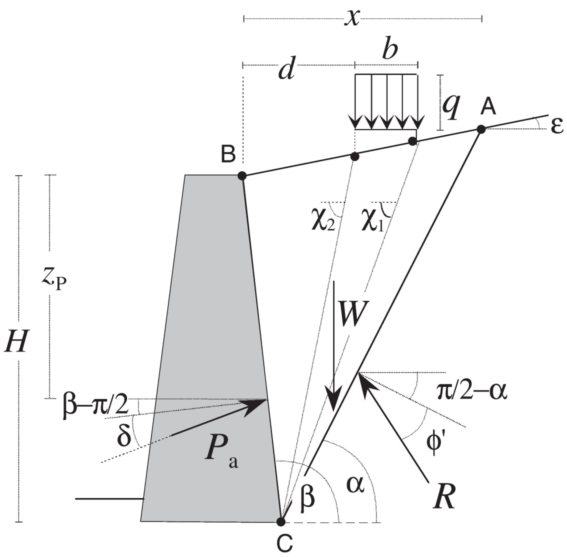

Figure 2.7. Wedge subject to a strip of vertical surcharge (Greco, 2006)

Wang's studies (2007a; 2007b) presented approximate analytical solutions for estimating the lateral force and its centroid location caused by surcharge surface loads acting on a cross-anisotropic backfill. He developed various formulas to determine the lateral earth pressure for three different types of surcharges like point, line, and rectangular loads that depended on the soil anisotropy, the distance between the wall and loads, and the direction of the load, either horizontal or vertical. Wang did not consider the strength and the variation of the stiffness of the soil and he assumed that the wall is perfectly smooth, which is limited to the applicability of the elasticity method.

Esmaeili and Fatollahzadeh (2012) studied the lateral pressure from train live load on the backfill embankment near railway bridge abutment. They utilized elasticity theory to determine the laterally induced pressure distribution on the abutment caused by rectangular area and strip loads regarding the railway live load. They applied the same approach of Kim and Barker (2002) in calculating the lateral pressure from the highway live load on the road bridge abutment by using an elastic numerical integration based on horizontal stresses. Also, they developed equations for Poisson’s ratio range (0.1-0.3) to determine the lateral earth pressure due to the surcharge. They compared between their equations’ results and the results of the UIC Code (UIC, 2006) with an infinitely long layer of earth fill with a constant height of 1.7m. They indicated that the calculated lateral forces and overturning moments on abutments from the UIC Code of surcharge live load for wall height of 7.5m were significantly underestimated and could lead to an unsafe structural design for this wall heights.

AASHTO (2014) stated that the simplified 2:1 distribution method can be utilized to compute the lateral earth pressure distribution that induced from strip load for flexible walls. In contrast, the Boussinesq’s solution method can be used for walls restrained from movement (rigid walls), as shown in Figure 2.8.

The Guidelines for Temporary Shoring (GTS, 2004) stated that the measured wall deflections of shoring system and deformations of railroad track must be less than the deformation criteria outlined in Table 2.3.

Table 2.3. Deformation criteria (GTS, 2004)

Horizontal distance (S) from shoring to track C/L measured at a right angle from track	Maximum horizontal movement of shoring system	Maximum acceptable horizontal or vertical movement of rail
12’ < S < 18’	3/8”	1/4”
18’ < S < 24’	1/2”	1/4”

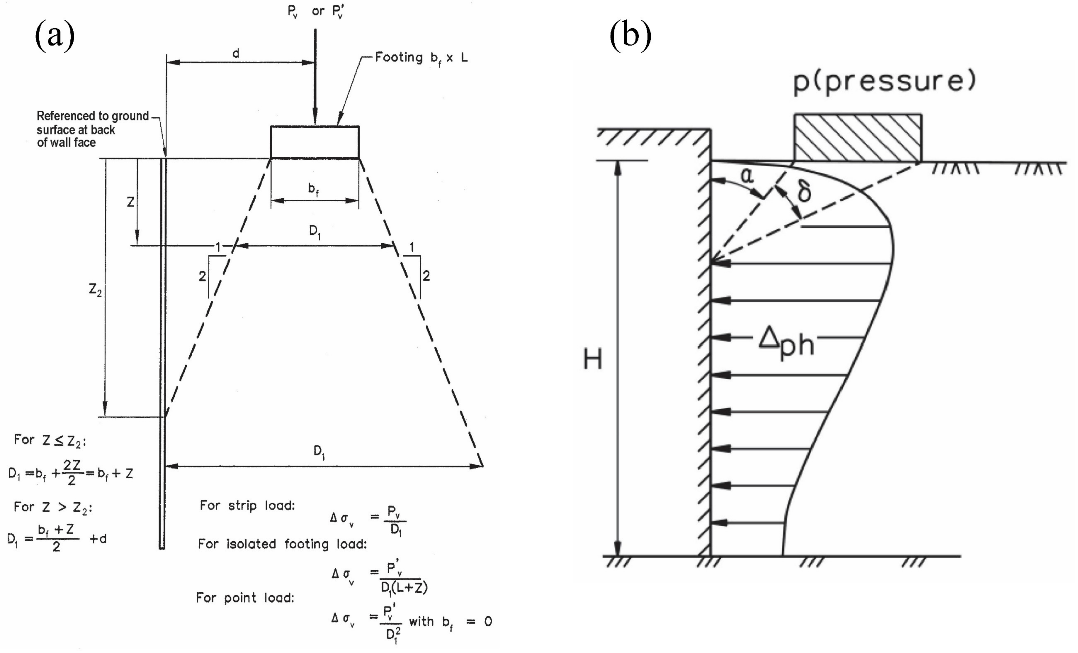

Figure 2.8. Lateral pressure computations for: (a) flexible walls, and (b) rigid walls (AASHTO, 2014)

Cantilever sheet pile walls are frequently used for retaining a moderate height of soils. In general, cantilever sheet pile walls resist the overturning moment due to lateral earth pressure from the retained soil by evolving a resisting moment due to passive lateral pressure along the embedment depth of the wall. Several studies stated experimental data and suggested design guidelines (Babu and Basha, 2008; Bowles, 1988; King, 1995; Viswanadham et al., 2009). The focus of the soil-wall system studies was on the design methods of sheet pile wall by estimating the penetration depth required to satisfy equilibrium of moments and lateral soil pressures. However, to the best knowledge of the authors, the cyclic behavior of a soil-wall system constructed in a cohesive soil adjacent to a train track using a sheet pile wall has not been investigated. Therefore, the aim of this study is to gain more understanding of the mechanical behavior and the failure mechanism of a soil-wall system adjacent to repeated live loading from train passing routines. The main objective is to determine and establish the relationship between the variable parameters that influence the lateral deflections and the lateral soil pressure of the sheet pile wall under cyclic loading.

The seismic forces and pressures for earth retaining structures are estimated by the Mononobe-Okabe analysis method (Finn et al., 1992). This seismic design method is based on Coulomb's theory of earth pressure for dry sands to get the forces. However, the Mononobe-Okabe analysis method was appeared to be conservative and to overestimate the peak moments at high levels of shaking, where the wall displacements of centrifuge shaking test do not meet the conditions of a Coulomb’s analysis.

Retaining structures near railroads would experience cumulative wall displacements as the system is subjected to repeated live loading. Studies of live load effects on retaining structures in cohesive soils showed that the stresses induced by typical railroad loads are well below the shear strength of the soils retained by the wall. Simple elastoplastic soil models assume elastic behavior for stresses below the maximum yield stress, with inelastic deformations only occurring when the maximum stress is reached. Thus, they are incapable of predicting cumulative plastic displacements when cyclic stress magnitudes are small relative to the maximum yield stress.

The limitations noted above can be overcome by using a kinematic hardening plasticity model contained in ABAQUS material library (Simulia, 2014). The key feature of this model is its capability for predicting inelastic deformations at relatively low levels of cyclic stress. It is also capable of predicting the ratcheting behavior that is the key to describing the cumulative plastic deformations that occur under repeated loading. This model was originally proposed for the analysis of cyclic loading of metals. However, Anastasopoulos and his coworkers (Anastasopoulos et al., 2011) demonstrated its utility for modeling the cyclic behavior of soils under shallow foundation. The kinematic hardening model, as implemented in this research, requires four input parameters for analysis in clays: uniaxial compressive strength σ_{max}, the elastic modulus at small strain E, Poisson's ratio μ, and the stress level at which inelastic strain initiates σ_0. It is noted that a simple elastoplastic model requires three input parameters: an elastic modulus, Poisson's ratio, and the soil strength. Thus, the kinematic hardening model proposed here requires only one additional model parameter above conventional elastoplastic models to produce much more realistic simulations of soil-wall behavior. The model parameters can be determined from conventional laboratory soil tests. It must be finally noted that soil properties typically vary with depth. Thus, the four parameters noted above must be determined at multiple locations.

2.2 Background for Caissons

Suction caissons are used widely in offshore wind turbine and the oil/gas industry as foundations for and fixed structures and anchors for mooring systems to maintain station for offshore floating structures. Suction caissons become a good alternative to piles in deep water for offshore structures due to their relatively low cost of installation. The initial penetration of the caisson into the seabed occurs due to the self-weight, and the remainder is accomplished by suction (actually differential water pressure) generated by pumping water from the interior of the caisson, as shown in Figure 2.9.

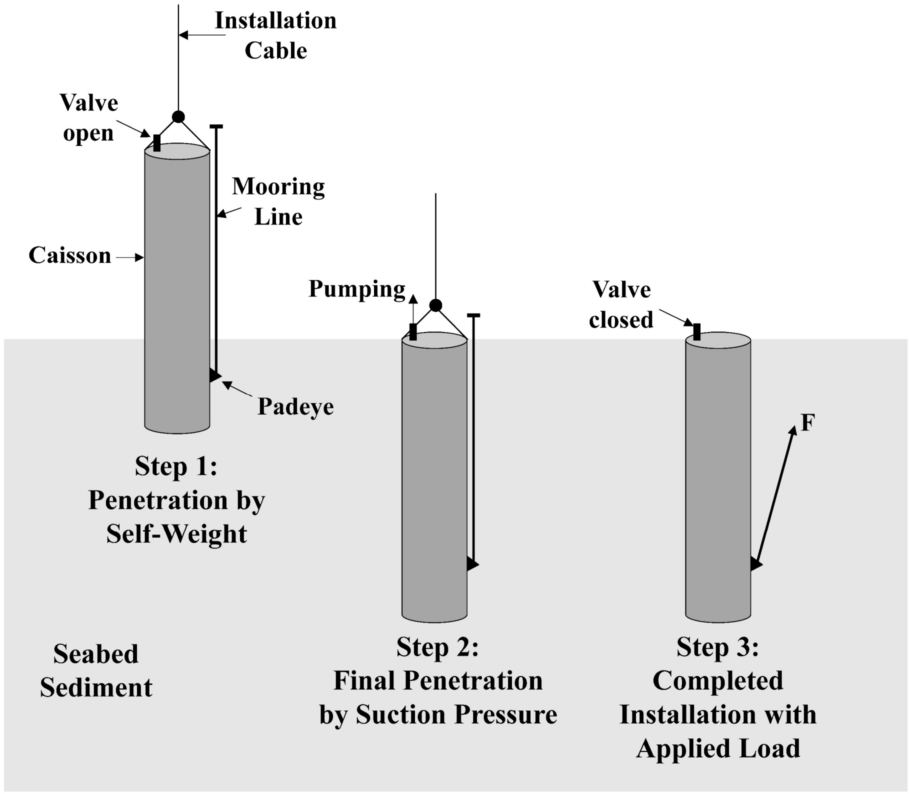

Figure 2.9. Installation steps of suction caissons

Suction caissons can afford a higher resistance to the horizontal and vertical loads compared to the driven piles for offshore structures (Colliat et al., 1995). The idea of the suction caisson was first stated by Goodman et al. (1961). They carried out experimental model tests on the pull-out resistance of suction caisson anchors. Suction caissons as mooring anchors were first presented by Senpere and Auvergne (1982) for a storage tanker at the Germ field offshore Denmark. Since then, the offshore industry has preferred the suction caissons because of the simplifying and shortening the installation procedure, in addition to the more control over the installation process. Therefore, suction caissons have been applied for diverse types of offshore structures and in various types of soils due to their efficiency and versatility. Generally, the holding capacity of suction caissons depends on the caisson geometry, soil type surrounding the caisson, load attachment point (padeye) of the caisson, and the suction pressure applied.

Suction caissons used for mooring systems are exposed mostly to cyclic loads arising from wind and wave loading. For instance, the report of the European offshore wind industry (EWEA, 2016) indicated that 80% of the foundations of the offshore wind power are caissons. The lifetime of an offshore wind turbine has become a significant topic in industrial and academic fields, especially when two decades had passed for the early generation of the installed offshore wind farms in the world (Ziegler and Muskulus, 2016). The use of suction caissons for anchoring in deep water as an effective solution has been significantly increasing (Randolph et al., 2005; Randolph et al., 2011). Ease of handling during field installations, accurate positioning, suitable pullout capacity all lead to widespread usage of suction caissons.

The design procedures for caisson foundations is based usually on the monotonic loading analysis, while actual loads are cyclic, which should be considered in the design of caissons. Actually, the loads that affect the offshore structures with suction caisson foundations can be classified into three types: static permanent loads, cyclic loads with low frequency, and cyclic loads with high frequency (Clukey and Morrison, 1993). However, the suction caissons have a dominant advantage over other foundations types in lateral resistance performance (Aubeny, 2017). Their performance under cyclic loading has not fully studied, especially, especially the effects of cyclic load amplitude and the reduction of the undrained shear strength of clay along the wall of caisson during the installation of caissons due to the remolding of soil.

Existing methods for predicting the deformation of caissons in clay were developed regarding linear elastic and elastoplastic soil models and, consequently, the estimates of cumulative displacements based on these models do not properly reflect the nonlinear cumulative permanent response of soil. Existing procedures in the literature often assume that the designers have to assume “typical” soil properties. Therefore, the linear elastic models cannot be counted on to determine the plastic cumulative response in cases where the assessment of caisson performance must consider permanent deformation of the soil. The influence of cyclic response for caissons in clay affect the assessment of lifetime operation of offshore floating structure, in other words, the estimations of lateral deformation and lateral soil resistance of caissons that result of cyclic loads.

One of the basic objectives of a caisson is to transfer the loads from a structure to the ground within the allowable deformations. One of the caisson design requirements is satisfactory performance at the serviceability limit state (SLS) and long-term deformation which would involve expecting the fatigue life of the caisson as well as the influences of cyclic loadings for a long time on the caisson foundation. Typically, suction caissons are exposed to inclined cyclic loading at the padeye. This padeye (load attachment) of a suction caisson is generally located at a depth about 2/3 of caisson’s embedment below mudline, while the load angle is inclined vertically from the horizontal direction.

Changes in the accumulated soil deformations resulting from continuous cyclic loadings that have been measured in small-scale experiments and centrifuge tests on monopiles supported by offshore wind turbines (Klinkvort and Hededal, 2013; Lombardi et al., 2013; Yu et al., 2015). Klinkvort and Hededal (2013) indicated from their centrifuge test results for monopiles under cyclic loading that the cumulative deformation and soil stiffness for soil-monopile system of offshore wind turbines depended intensively on the cycle number of the cyclic loading, and its amplitude. In addition, Lombardi et al. (2013) and Yu et al. (2015) studied the long-term cyclic/dynamic performance of the wind turbine structure regarding its natural frequency, which affected by the number of cycles and the cumulative strain of soil.

Gerolymos and Gazetas (2006) developed a finite difference code, NL-CAISSON, to simulate the the nonlinear soil response around the caisson by utilizing couple springs and dashpots for the caisson-soil system to study the effect of soil nonlinearity and especially the effect of gapping at the caisson-soil interface. They stated that the interaction between caisson and soil is strongly dependent on the lateral stress distribution along the embedment depth of caisson in soil (Figure 2.10).

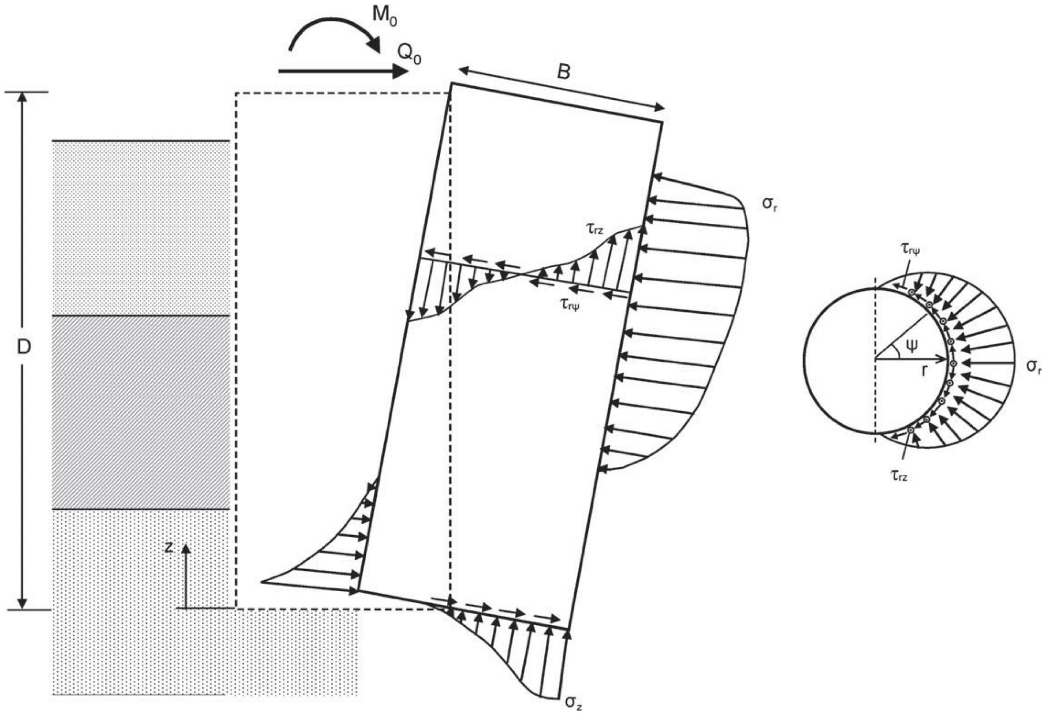

Figure 2.10. Stress distribution of caisson-soil system with circular shape (Gerolymos and Gazetas, 2006)

Lau (2015) studied laterally loaded monopiles in clay soils for offshore wind farms in the UK by carrying out nine centrifuge tests. He implemented displacement control for the monotonic test and load control for the cyclic test for two different dimeter monopiles. He mentioned that using the *p-y* method recommended by DNV (2014) is not suitable to the design of monopiles under cyclic response because this method underestimated the lateral stiffness of monopiles. Lau found from the experimental tests that the accumulated rotation of monopiles increased with the vertical load of applied load which could lead to the failure of the soil-monopile system.

Haiderali et al. (2015) studied the cyclic behavior of monopile by analyzing a monopile in London Clay with implicit 3D finite element simulation. They observed that the monopile would have an cumulative lateral displacement and rotation at the mudline, and a gradual increase in the bending moment and shear force along the monopile depth in the soil with increasing the cycle numbers. These results verified the cyclic plastic hardening response for the clay-caisson system.

Currently, the design of laterally cyclic loaded caisson foundations of offshore structures in clay is based on *p-y* curves (API, 2003; DNV, 2014). However, these curves were developed for slender piles (length to diameter ratio of 30 to 50), the length to diameter ratio of caissons is about 4 to 8 for offshore wind structures. Also, the *p-y* curves used in the API and DNV codes are related to flexible pile behavior. In contrast, the squat nature of suction caissons results in a condition of negligible flexural response and the caisson tends to rotate as a rigid body. In addition, the *p-y* curves are recommended for static loads. Although Matlock (1970) had established a cyclic *p-y* curve, it is not depending on amplitude or cycle frequency and also had developed only a lower bound of the lateral soil-pile response. Furthermore, several studies depicted that the *p-y* curves method is not appropriate for large-diameter and short-aspect ratio piles (Abdel-Rahman and Achmus, 2005; Pappusetty and Pando, 2013; Wiemann et al., 2004). Also, the estimation of displacements for cyclic loaded piles/caissons from the *p-y* method is a constant value and is independent of the cycle numbers and amplitudes. However, in the field observations, the cumulative deformations are strongly dependent on the cycle numbers and amplitudes (Li et al., 2015; Long and Vanneste, 1994).

In the present study, to overcome these shortcomings, a nonlinear elastoplastic kinematic hardening constitutive model was implemented in axisymmetric finite element analysis of a suction caisson in cohesive soils, where strength and stiffness properties linearly varied with depth. This study is focused on the behavior of caissons in clays under cyclic loading.

In addition, the forces at the mudline for suction caissons have different loading angles especially for the catenary mooring system (Aubeny, 2017). These loading angles depend on the mooring type as taut or semi-taut, the anchor type, and the surrounding soil type. Combing lateral and vertical loads that applied on suction caisson for offshore strutctures often reqiure to consider that the anchor in deep water can be affected with a sustain load with a mudline angle. For instance, a catenary system with pure horizontal loading at the mudline, the mooring line tension force will act at an uplift angle of approximately 14 degrees from the the horizontal due to the downward curvature of the chain in the soil.

2.3 Background for Piles

There are several modeling techniques for simulating the dynamic behavior of a single pile in elastic soils, such as the Winkler approach, the analytical elastic-continuum formulation, boundary element method, and finite element method (Kuo and Hunt, 2013). Piles can serve as foundations for fixed structures or anchors for floating structures. Loading on piles used as anchors can be purely vertical as for a tension leg platform, inclined as in a taut mooring line system, or nearly horizontal as in a catenary mooring system. The latter two cases require proper characterization of soil-pile interaction for lateral loading. In the most common methodology, the concept of *p-y* curves is widely used for describing the nonlinear response of individual soil springs connecting the laterally loaded piles to the soil medium. The analysis of laterally loaded piles by conducting the *p-y* approach such as the API methods (API, 2003) is very common because it is easier than the continuum mechanics method. The *p-y* models were developed in 1960s and 1970s for static and slow cyclic loading. The recommended cyclic *p-y* curves for cohesive soils (e.g. Matlock, 1970) have been used since 1970. Recent research has shown that the API p-y monotonic loading curves tend to underestimate soil stiffness. Jeanjean (2009) investigated the lateral response of a single pile in soft clay and concluded that the *p-y* curve computed by API model underestimate the soil resistance as measured in centrifuge tests. Also, Templeton (2009) found that *p-y* curves from API method underestimate the soil-pile interaction stiffness.

Long and Vanneste (1994) derived two empirical relations that could estimate *p-y* curve for cyclic lateral piles in sand regarding cycles number of lateral repetitive load, installation of pile, soil density, and cyclic load amplitudes. However, there are some limitations in these methods related to overpredict the effect of cyclic loading for piles in sand when the load ratio is less than zero and to be just valid for long piles with lateral loads of 50-100 cycles.

Gerolymos et al. (2005) proposed an explicit finite difference computer code, NL-DYAP, to study the lateral behavior of pile-soil interaction in stiff cohesive soil through using Winkler-type springs along the pile. They compared their proposed model results with results from 3-D finite element analysis using a plasticity model provided by ABAQUS. They proposed to apply initial yield stress for the ABAQUS plasticity model equal to zero (i.e. there is no elastic portion in the 3-D ABAQUS simulation). Comparing the finite element model results (grey line) and with the proposed model results (black line) is shown in Figure 2.11 for pile under 4 cycles of sinewaves of applying lateral displacement (1 cm) on pile head. Their proposed model had predicted higher maximum shear force and bending moment versus lateral displacement at the pile head compared to the results of finite element analysis using ABAQUS.

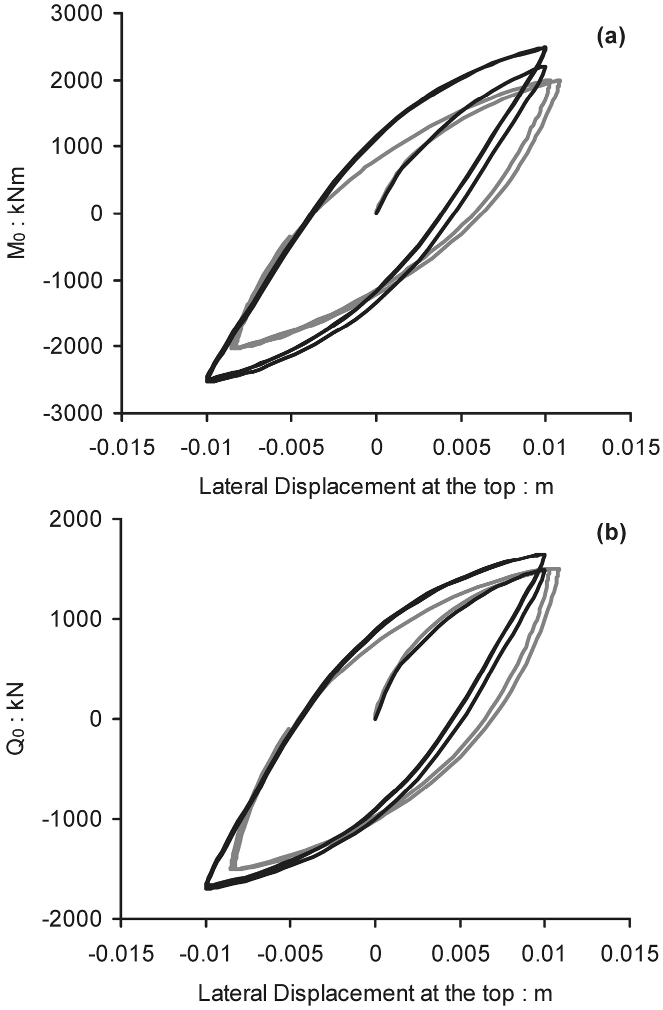

Figure 2.11. Comparison of results from the finite element model (grey line) and the proposed model (black line) of: (a) bending moment, and (b) shear force versus lateral displacement at the top of the pile (Gerolymos et al., 2005)

Hong et al. (2017) investigated the lateral cyclic behavior of a rigid pile and jet-grouting-reinforced pile in soft clay through centrifuge tests and finite element analyses. They stated that the API method underestimated the bending moment by 10% as shown in Figure 2.12 and the lateral pile displacement by 69% as shown in Figure 2.13 under the cyclic loadings.

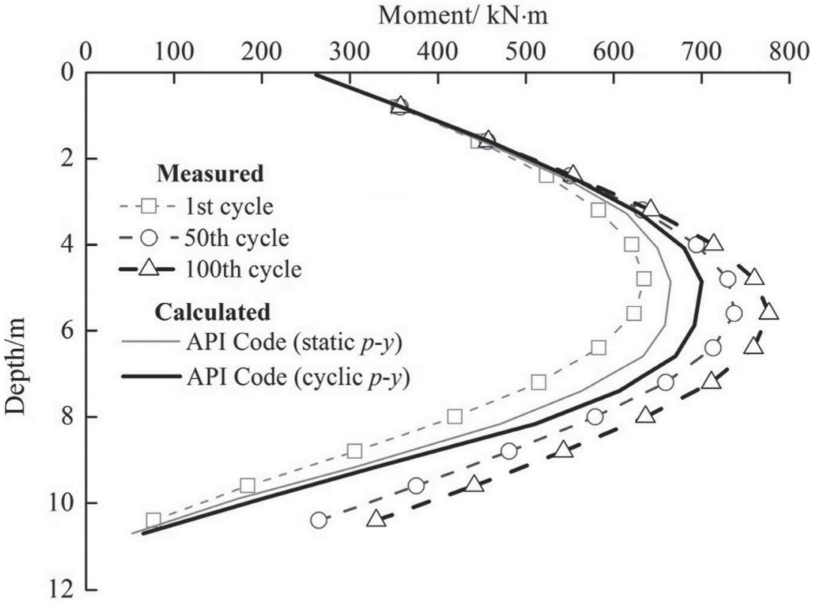

Figure 2.12. Comparison of cyclic measured and API calculated bending moment (Hong et al., 2017)

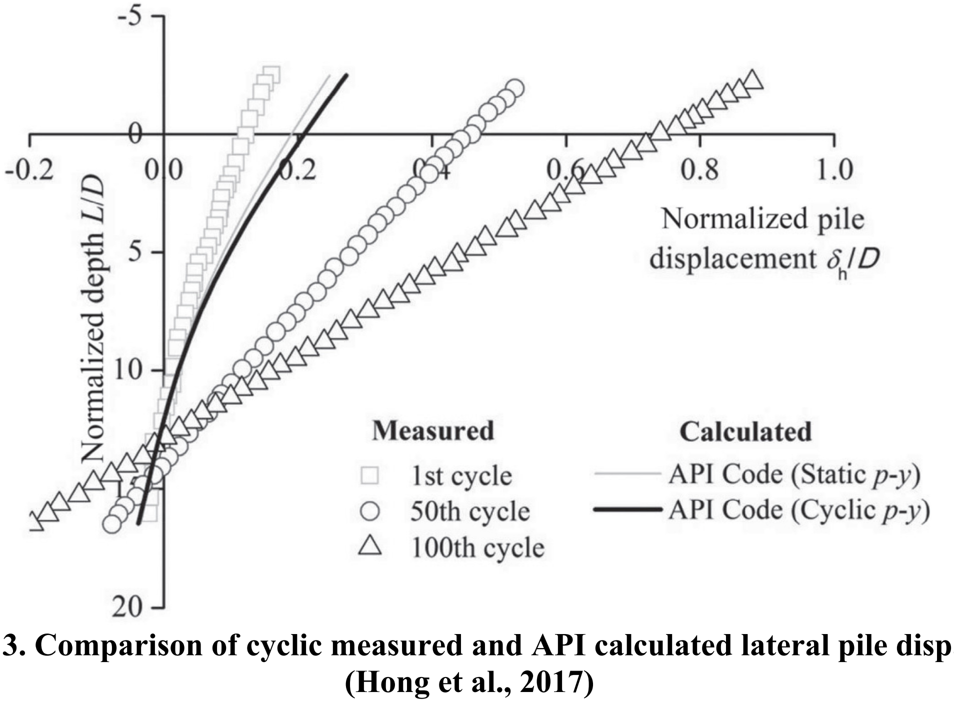

Figure 2.13. Comparison of cyclic measured and API calculated lateral pile dispalcement (Hong et al., 2017)

In addition, Hong et al. (2017) mentioned that increasing the cyclic amplitude value and the cycles number would increase the lateral pile displacement as shown in Figure 2.14 and Figure 2.15, and the bending moment as shown in Figure 2.16.

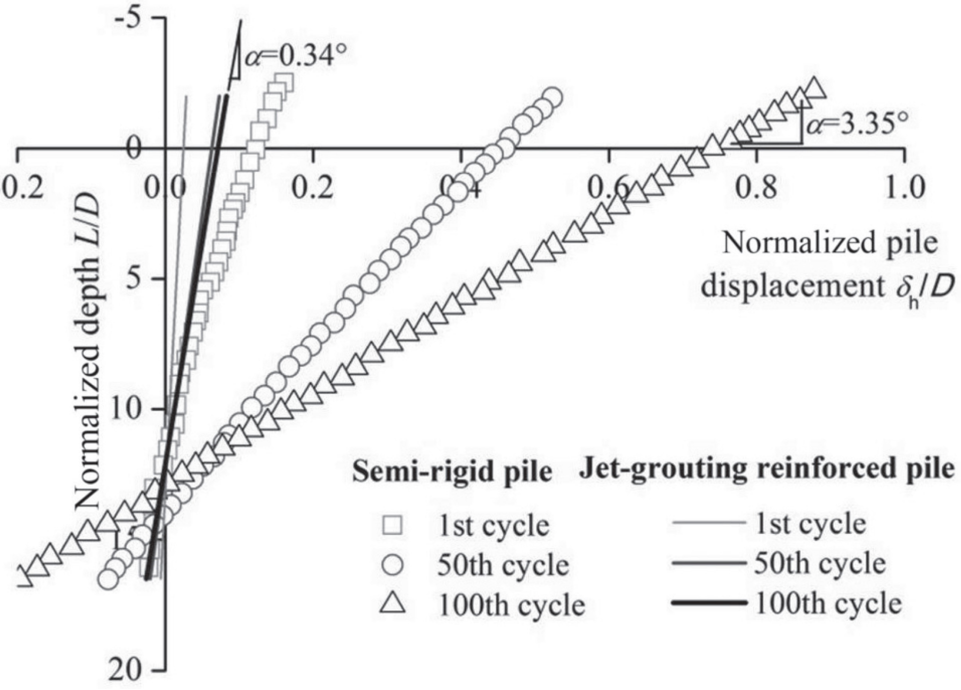

Figure 2.14. Measured lateral deformation of semi-rigid pile and jet-grouting-reinforced pile during third episode of cycling (Hong et al., 2017)

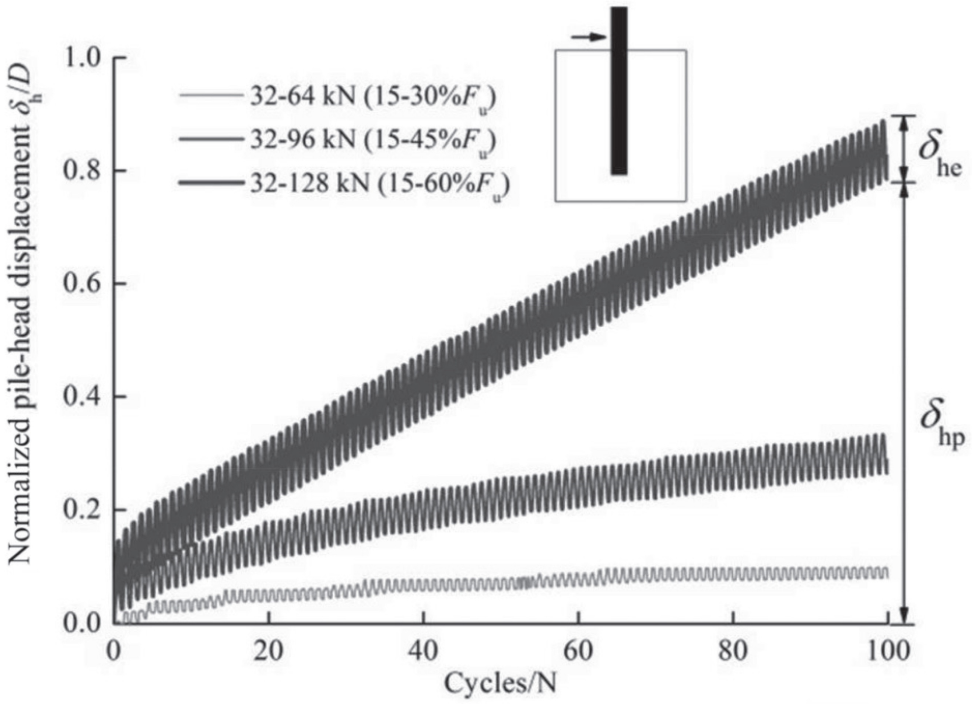

Figure 2.15. Measured lateral pile head displacement of semi-rigid pile (Hong et al., 2017)

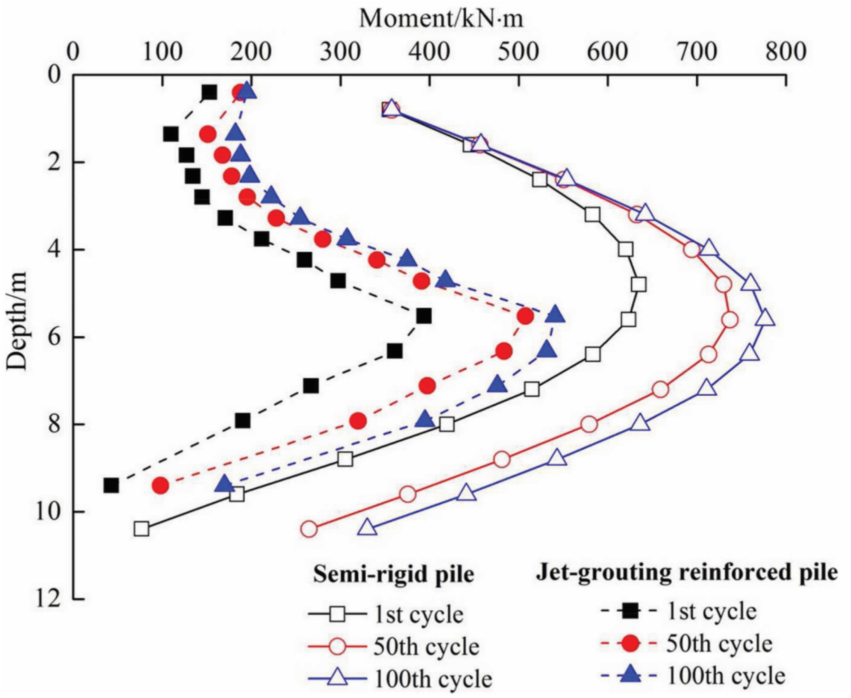

Figure 2.16. Measured bending moment of semi-rigid pile and jet-grouting-reinforced pile during third episode of cycling (Hong et al., 2017)

Developing a design method that is capable of predicting the nonlinear behavior of soils depending on the pressure-displacement approaches (*p-y* curves) with a cyclic nonlinear plastic model of soil deposits is very challenging. The current approach is evolved to relate the load-displacement characteristics of soil-pile systems by utilizing a bounding surface plasticity approach to introduce a nonlinear plasticity spring model that simulates the nonlinear behavior of the soil-pile system. The selection of *p-y* parameters plays a key role in the ability of the *p-y* approaches to simulate the realistic behavior of the lateral interaction between soil and pile. Thus, the proposed model comprised of parameters quantifying the real nonlinear behavior of soil-pile system relations. The goal of this spring model is to account for the accumulation of permanent deformation (ratcheting behavior) through determining the plastic response of cohesive soils under cyclic loading.

3 CONTINUUM METHODOLOGY

3.1 Soil Constitutive

This study employs the kinematic hardening model available in the ABAQUS (Simulia, 2014) finite element code. This model can predict the permanent plastic deformations at stress levels below the limit stress. Figure 3.1 shows a conceptual sketch of this hardening model in principal stress space. Following the symbol conventions, σ_1, σ_2, and σ_3 denote major, intermediate, and minor principal stresses respectively. The limit surface is defined by the strength of the soil in uniaxial compression σ_{max}, which remains constant under cyclic loading. Geotechnical site investigations often characterize fine-grained soil strength in terms of undrained shear strength, s_u. In this case, uniaxial strength is related to undrained shear strength by the following relationship:

$$\sigma_{max} = \sqrt{3}\, s_u \tag{1}$$

At small strains (within the dashed circle in Figure 3.1) the soil is linearly elastic. When a threshold stress σ_0 is reached, inelastic deformation begins to occur. In the general version of the model, inelastic deformation is accompanied by two types of hardening: isotropic and kinematic. Isotropic hardening involves an increase in σ_0; i.e., the interior yield surface (originally defined by the dashed lines) enlarges. Kinematic hardening involves migration of the center of the yield surface. Based on preliminary numerical studies, it was concluded that incorporating isotropic hardening effects into the model did not improve model performance with respect to predicting cumulative soil displacements. Thus, the yield stress σ_0 may be considered constant and only kinematic hardening need be considered.

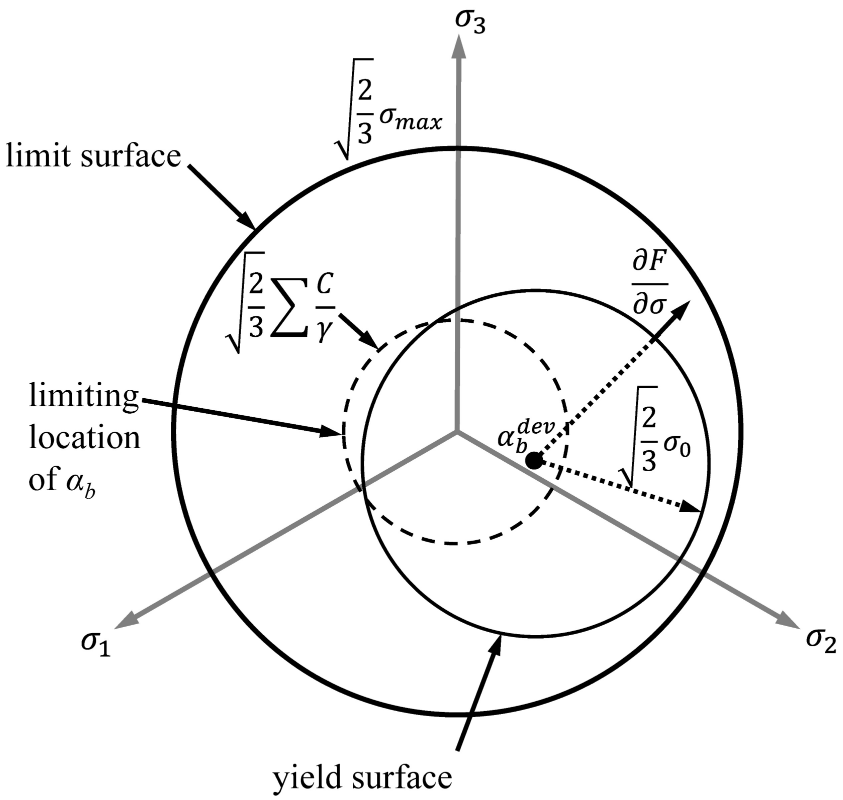

Figure 3.1. Hardening model (Simulia, 2014)

Figure 3.2 depicts kinematic hardening for the case of uniaxial loading, with stress plotted against plastic strain. For stress is less than σ_0, zero plastic strain occurs. Nonlinearity in the stress-strain response is governed by a kinematic hardening state variable α_b. The evolution of stresses in Figure 3.2 is defined as:

$$\boldsymbol{\sigma} = \sigma_0 + \boldsymbol{\alpha_b} \tag{2}$$

where:

σ_0 = the stress below which zero plastic strain occurs,

$\boldsymbol{\alpha_b}$ = the backstress determining the kinematic evolution of the yield surface in stress space.

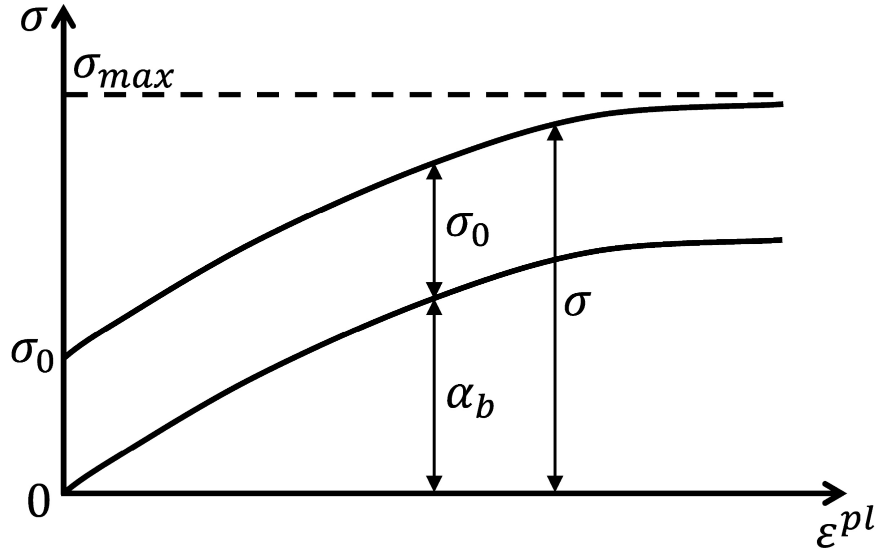

Figure 3.2. The constitutive model formulation (Simulia, 2014)

Application of cyclic loading to a soil element produces the response of stress-controlled loading shown in Figure 3.3a. Upon unloading from Point 1 in the figure, the stress-strain response is initially linear, the magnitude of the linear region being controlled by σ_0. As additional unloading occurs, nonlinearity and inelastic strains develop. Repeated unload-reload cycles produce the ratcheting pattern shown in the figure (ratcheting describes the cyclic accumulation of deformation). The magnitude of the ratchet strain δ_e gradually decreases as cyclic loading progresses.

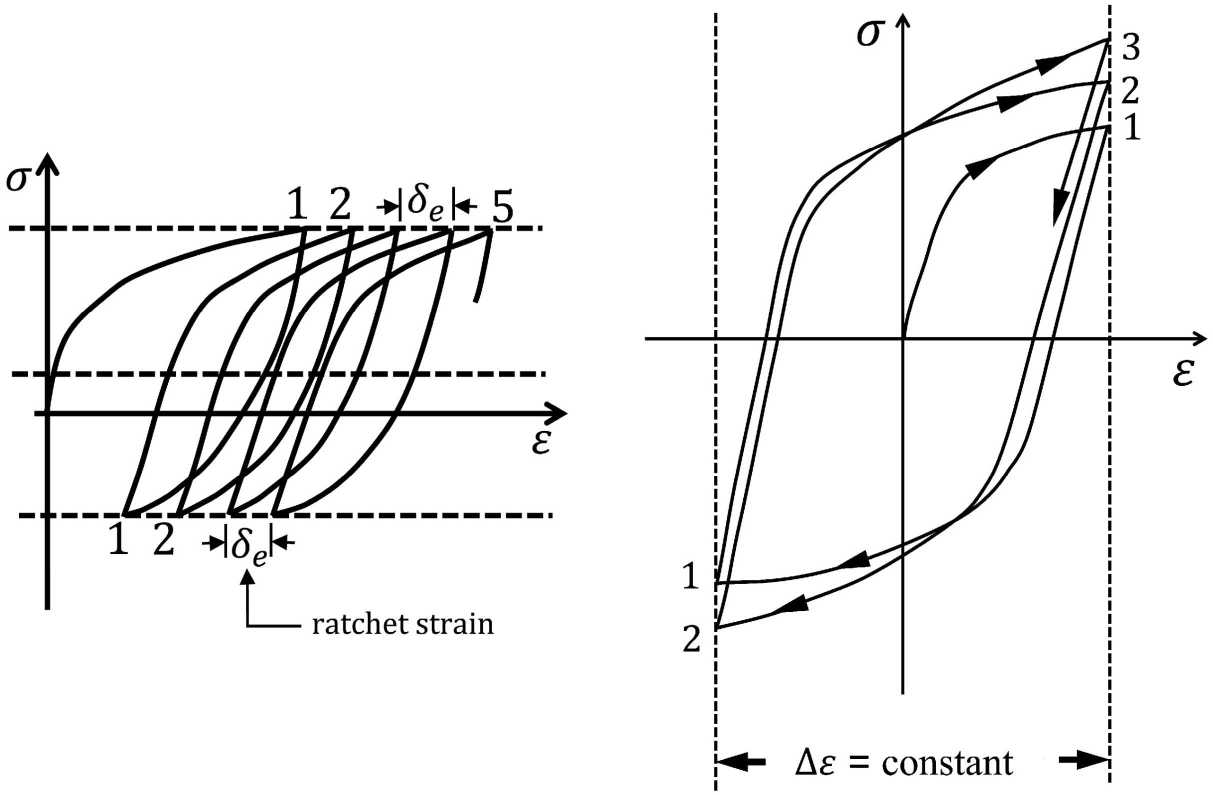

a) Stress-controlled loading **b) Strain-controlled loading**

Figure 3.3. Ratcheting behavior (Simulia, 2014)

All elastoplastic models require definition of (1) a yield surface, (2) a flow rule and (3) a hardening law. The yield surface (*F*) for the kinematic hardening model discussed herein is defined as:

$$F = f(\boldsymbol{\sigma} - \boldsymbol{\alpha_b}) - \sigma_0 = 0 \tag{3}$$

where $f(\boldsymbol{\sigma} - \boldsymbol{\alpha_b})$ is the equivalent Mises stress with respect to backstress, α_b, and σ_0 is the size of the yield surface.

As the function *F* is simply the definition of yield surface as described in the ABAQUS manual (Simulia, 2014), the equivalent Mises stress is defined as:

$$f(\boldsymbol{\sigma}-\boldsymbol{\alpha_b}) = \sqrt{\frac{3}{2}(\boldsymbol{S}-\boldsymbol{\alpha_b}):(\boldsymbol{S}-\boldsymbol{\alpha_b})} \tag{4}$$

where $\boldsymbol{S}$ is the deviatoric stress tensor and $\boldsymbol{\alpha_b}$ is the backstress tensor.

This model assumes an associated plastic flow, thus the flow rule that assumes an associated plastic flow is given by:

$$\dot{\boldsymbol{\epsilon}}^{\boldsymbol{pl}} = \frac{\partial f(\boldsymbol{\sigma}-\boldsymbol{\alpha_b})}{\partial \boldsymbol{\sigma}} \dot{\bar{\epsilon}}^{pl} \tag{5}$$

where:

$\dot{\boldsymbol{\epsilon}}^{\boldsymbol{pl}}$ = the plastic flow rate,

$\dot{\bar{\epsilon}}^{pl}$ = the equivalent plastic strain rate.

The equivalent plastic strain rate is defined by a scalar measure:

$$\dot{\bar{\varepsilon}}^{pl} = \sqrt{\frac{2}{3}\, \dot{\boldsymbol{\varepsilon}}^{\boldsymbol{pl}} : \dot{\boldsymbol{\varepsilon}}^{\boldsymbol{pl}}} \tag{6}$$

The hardening law defines the evolution of the backstress α_b as plastic straining occurs. This is described by the following expression:

$$\dot{\boldsymbol{\alpha}}_{\boldsymbol{b}} = H \frac{1}{\sigma_0} (\boldsymbol{\sigma} - \boldsymbol{\alpha_b})\, \dot{\bar{\epsilon}}^{pl} - \gamma \boldsymbol{\alpha_b} \dot{\bar{\epsilon}}^{pl} \tag{7}$$

where:

H = initial kinematic hardening modulus (the initial Young's modulus, E),

γ = a parameter determining the rate of decrease of the kinematic hardening with increasing plastic deformation.

Noting that $\sigma_{max} = {}^{H}/_{\gamma} + \sigma_0$ (Anastasopoulos et al., 2011), the parameter γ can be expressed as follows:

$$\gamma = \frac{H}{\sigma_{max} - \sigma_0} \tag{8}$$

Thus, γ is not an independent parameter, but can be determined in terms of H, σ_{max} and σ_0.

3.2 Soil Parameter Selection

Required model parameters are as follows:

1. The limit stress σ_{max} can be measured in an unconfined compression test. As noted earlier, since σ_{max} is simply the square root of three times the undrained shear strength, any accepted method for field or laboratory determination of undrained shear strength may be used to determine σ_{max}.
2. Poisson's ratio, μ can be measured in a triaxial test or simply estimated from correlations appearing in the published literature, e.g., Briaud (2013)
3. Small strain stiffness, E can be computed from measured shear wave velocity or estimated from empirical correlations to undrained shear strength. Based on a review of previously published correlations, Anastasopoulos et al. (2011) state that the small strain Young's modulus will likely lie in a range E/s_u = 300-1800.
4. The threshold stress level, σ_0 for the onset of nonlinear behavior and inelastic strains can be determined from the modulus degradation curves in dynamic analysis studies. In regard to the last item, Anastasopoulos et al. (2011) indicate that a likely range of yield stress σ_0 is in a range 0.1-0.3 of the maximum stress σ_{max}. In the small strain range, the degradation curves are defined from torsional shear tests. Examples of these curves are given by Ishibashi and Zhang (1993).

Alternatively, σ_0 can be estimated by back-analyzing measured cumulative displacements in cyclically loaded model pile tests.

3.3 Numerical Simulations

3.3.1 Wall Numerical Simulation

The soil-wall system was modeled using 2D geometry of the real system. The system consists of soil and a sheet pile wall embedded in the middle, as shows in Figure 3.4. The mesh generation of this system was carried out by using a MATLAB code in order to develop different models in an efficient and straight forward way. The typical length of train is very long regarding the length of a typical retaining wall; therefore, the soil-wall system may reasonably be analyzed as plane strain condition with a strip load of width B and intensity q.

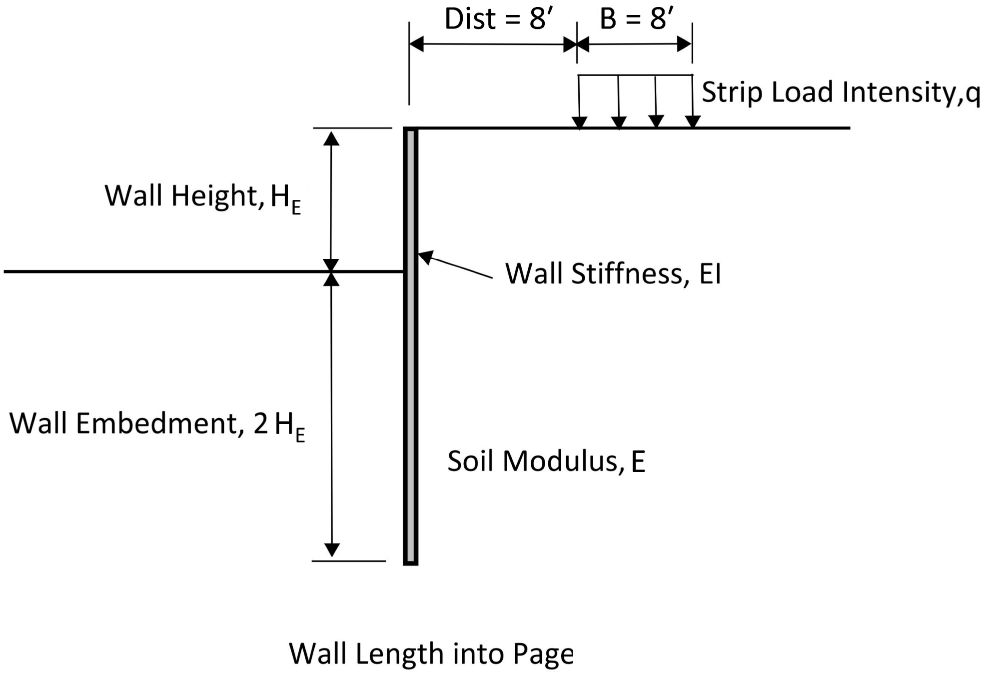

Figure 3.4. 2D geometry of the soil-wall system

The computing of live load intensity q for railroads are based on the Cooper E80 loading, which is acknowledged in the design specifications for live railroads for retaining walls and temporary shoring (AREMA, 2010; GTS, 2004). Cooper E80 was designed to approximate 2 locomotives with 80 kips per axle pulling an infinite train of 8 kips per foot (Figure 3.5).

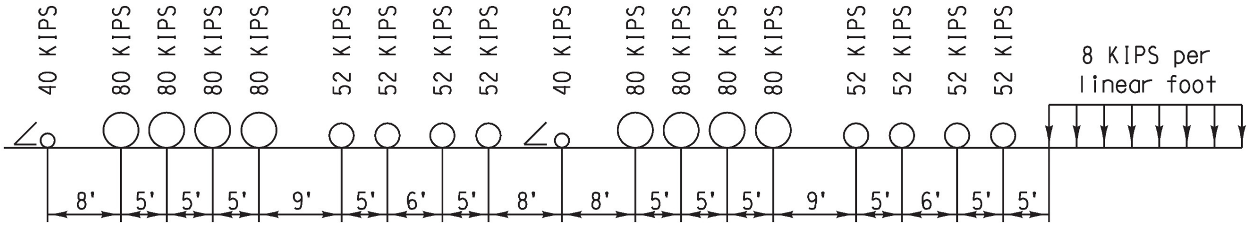

Figure 3.5. Cooper E80 loading (GTS, 2004)

Since the track width, B of the train was equal to 8 ft, the full train load intensity, q was computed as an infinite strip load intensity of 2000 psf. This is based on an infinite load of 80,000 lb/ft distributed across an 8 ft width and the spacing between axle wheels of 5 ft.

Selection of specific soil parameters for this study is based on the site characterization data presented in a PhD dissertation (Mohammadrajabi, 2016). Figure 3.6 shows the undrained shear strength profiles. The initial Young's modulus of soil was computed from the ratio E/s_u = (300-1800) that cited by Anastasopoulos et al. (2011). The quality of the data (Mohammadrajabi, 2016) from the unconfined compression test at 4 feet was such that a reasonable estimate of undrained shear strength was not possible. Therefore, only values from depths of 6 and 8 feet were used in developing the undrained shear strength (s_u) profiles shown in Figure 3.6. As noted earlier, small strain stiffness values are most reliably obtained from shear wave velocity data, which are not available for this site. A Poisson's ratio μ = 0.45 was used in the finite element simulations. This value was selected based on review of published values (Briaud, 2013) for clay soils. This value corresponds to undrained conditions for saturated or nearly saturated clay.

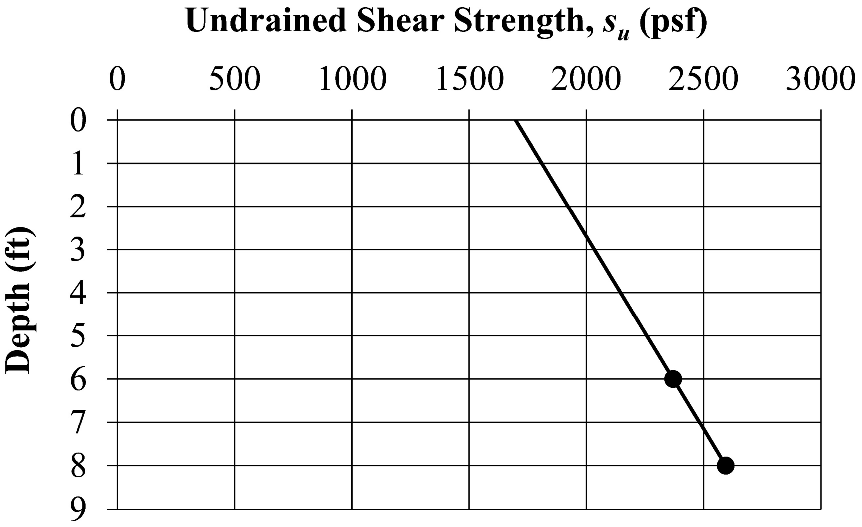

Figure 3.6. Soil strength profile at the monitoring site

As described before, selection of σ_0 (or, practically speaking σ_0/σ_{max}) requires test data capable of producing reliable stiffness degradation curves, as would be measured in a resonant column test and bender element test. Since such data were not available, a value of σ_0/σ_{max}= 0.1 was selected for the finite element simulations, based on the recommendation of Anastasopoulos et al. (2011).

The sheet pile wall type was PZ27 with 30 ft. deep and it was a cantilevered with 10 ft. above ground and 20 ft. below ground. The properties of the sheets are presented in Table 3.1. Where the sheet pile wall stiffness was controlled by specifying the Young's modulus of wall equals to 4.176 $\times 10^9$ psf and the moment of inertial of the PZ27-type wall from Table 3.1 to estimate a specific target value of flexural stiffness (EI). In addition, the Poisson's ratio for this steel sheet pile wall was considered to be 0.1.

Table 3.1. Sheet pile section properties

Section index	Width (in)	Height (in)	Area Per Foot of Wall (in^2/ft)	Moment of Inertia Per Foot of Wall (in^4/ft)	Section Modulus Per Foot of Wall (in^3/ft)
PZ22	22.0	9.0	6.47	84.38	18.1
PZ27	18.0	12.0	7.94	184.2	30.2
PZ35	22.64	16.1	10.29	361.22	48.5
PZ40	19.69	14.9	11.77	490.85	60.7

Figure 3.7 illustrates a typical 2D mesh of the finite element models. The boundaries of the finite element models were fixed at the bottom of the model in both the horizontal and vertical directions. While the boundaries at the far sides of the model were represented with infinite elements reducing time-consuming and ensuring proper modeling of radiation damping. Perfect bonding is assumed at the soil-wall interface. It was employed a finer mesh under and around the wall to provide a higher precision in the results and coarser mesh further from the wall to reduce time-consuming of the parametric studies. Thus, the different soil element sizes of the model were tied to eliminate the contact difficulties in the finite element simulations. The mesh size was extended to a horizontal distance of five times the total depth of the sheet pile wall (H_w) from the center of wall for each side. Also, the bottom boundaries of the finite element model were considered as five times the whole depth of wall (H_w). These boundaries were opted after performing a number of initial trial analyses with several boundary distances until the displacements and stresses of the wall-soil system did not vary significantly with further increase in the distance.

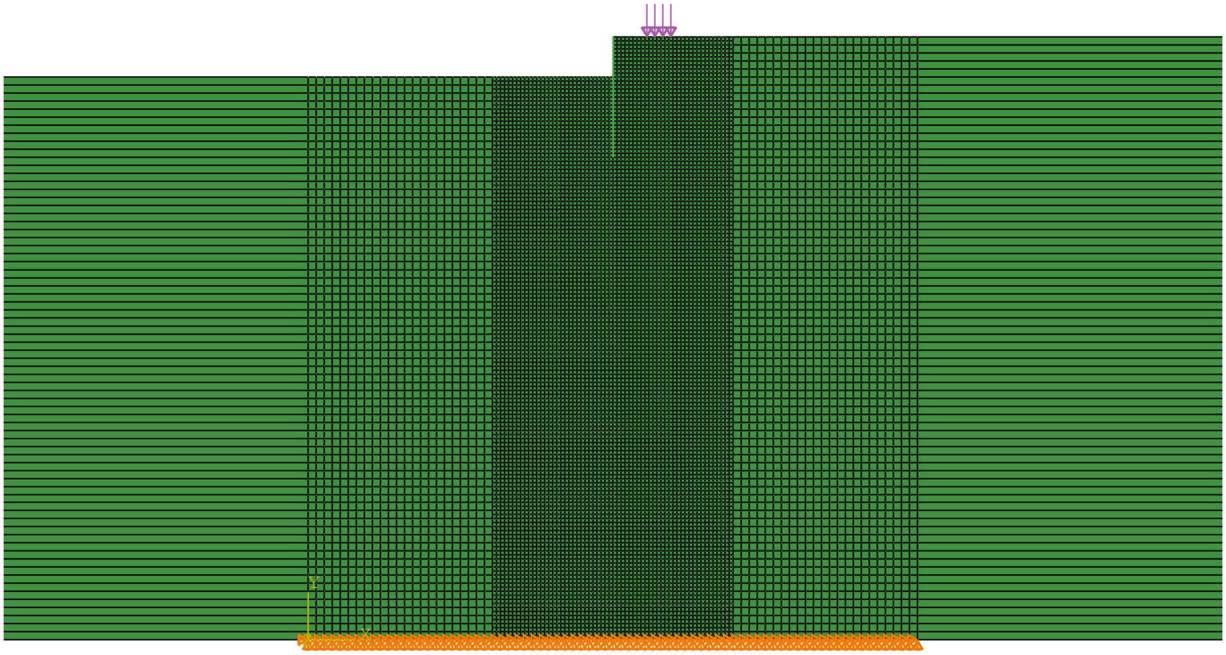

Figure 3.7. Typical 2D mesh

The analysis employed continuum plane strain (CPE4) elements with four nodes for the soil mass, and shear flexible beam (B21) elements with two nodes for the retaining wall. The material model for soil mass was assumed to be cyclic elastic-plastic response depends on the kinematic hardening model. The wall material was assumed to have an elastic behavior. For the far side boundaries, it had been used the plane strain continuum infinite (CINPE4) elements with four nodes type.

As already mentioned, model parameters can be easily calibrated, even with limited experimental or field data. In summary, the calibration requires the following data: (1) soil strength for clay; (2) small-strain stiffness, where the soil properties have been assumed to be varies with depth to simulate the realistic soil behavior. In the absence of shear wave velocity or initial shear modulus data measurements, parameter H (i.e., the initial or small-strain stiffness) of our constitutive model was calibrated to exploit the field results of mid-height deflection of wall, thus the small-strain stiffness of soil was parametrically varied from 500 s_u to 800 s_u.

3.3.2 Caisson Numerical Simulations

In this study, a finite element model of a caisson foundation system was simulated in a software program ABAQUS (Simulia, 2014). To reduce computational time when dealing with many load cycles, axisymmetric elements with nonlinear, asymmetric deformation (Fourier elements) were employed. The analysis employed bilinear, axisymmetric continuum (CAXA) elements with four Fourier modes in the soil mass, and axisymmetric shell (SAXA) element with four Fourier modes for the caisson. The FE simulation has been selected with an anchored applied force (F_a) that can be applied to the caisson at the optimum attachment point (padeye) that is about two-third the length of caisson with an inclination angle (ψ) of the caisson load, as shown in Figure 3.8. The far-field boundary condition (distance from the caisson wall to the far end of the mesh) was set to be 10 times the caisson radius, while the mesh depth has set to be twice the length of the caisson embedment.

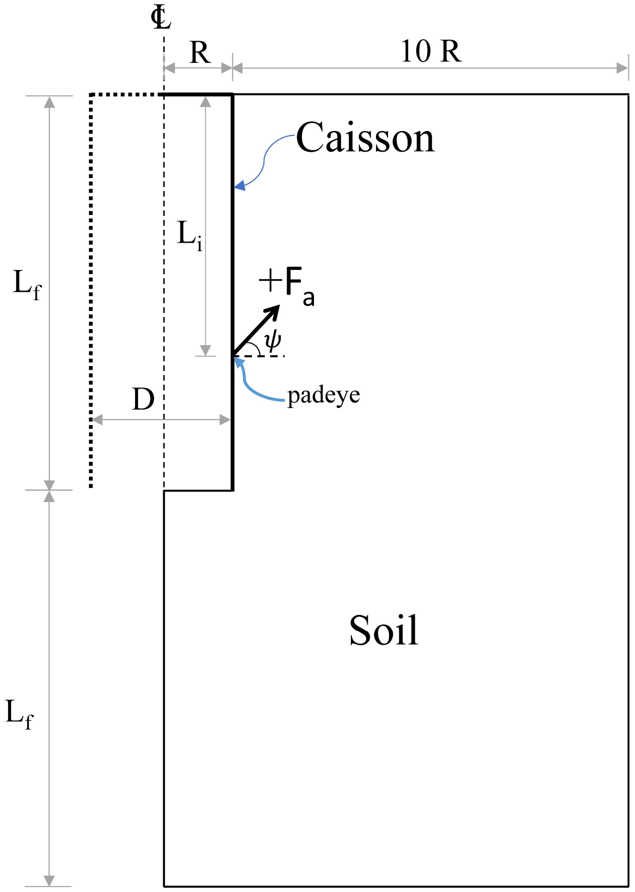

Figure 3.8. Soil-Caisson system diagram

To confirm the accuracy of the Fourier analysis, a full 3-dimensional simulation was compared to the quasi-3D Fourier axisymmetric for monotonic loading to ultimate capacity for a 5 m diameter by 25 m long caisson embedded in a normally consolidated clay. The case considered here is identical to the base case analysis for the parametric study, which is discussed later in this dissertation. Figure 3.9, comparing predicted padeye load-displacement curves, shows excellent agreement between the two methods.

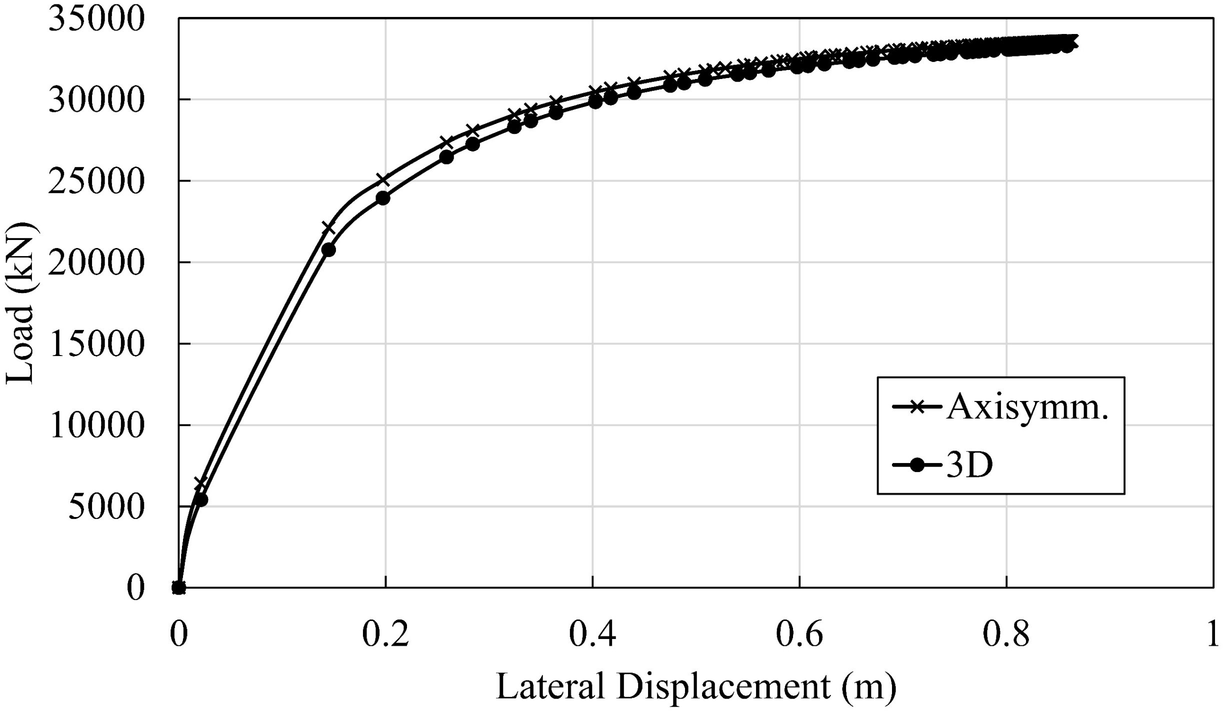

Figure 3.9. Load vs. Displacement from full 3D and fourier analyses

The form of the material model as utilized in this study considers only kinematic hardening. In this case four material model parameters are required: initial elastic modulus E, Poisson's ratio μ, ultimate resistance σ_{max}, and stress at initial yield σ_0. As noted earlier, the incompressibility constraint establishes the value of Poisson's ratio μ. Similarly, the strength profile adopted for the analysis (to be discussed subsequently), together with Equation (1), establishes the profile of ultimate shearing resistance σ_{max}. In this study, the remaining two parameters E and σ_0 are inferred by matching finite element predictions of pile response under cyclic loading to laboratory model tests. Both parameters are conveniently expressed in normalized form as E/s_u and σ_0/σ_{max} throughout the remainder of this work. It is noted that while the laboratory tests provide reasonable best estimates for these parameters, the parametric study presented later in this study nevertheless investigates the sensitivity of pile response to both parameters. Selection of specific material properties for this study is based on the site characterization data presented in previously published studies regarding the soil site of the Gulf of Mexico, where the soil is a normally consolidated clay.

As a base case for investigating cyclic loading effects, 5-m in diameter caisson with aspect ratio L/D = 5 (Figure 3.10) was selected. A “typical” normally consolidated clay profile was used in all analyses, with undrained shear strength at the mudline taken as 2 kPa, and the shear strength increasing with depth at a rate of 1.6 kPa/m. All analyses were considered to be undrained, implying a Poisson’s ratio μ = 0.5. The caisson in this base case analysis had a thickness t = 6.25 cm, corresponding to a diameter-wall thickness ratio D/t = 80. A very large modulus of elasticity (E = 1×10^{12} kPa) was used in the analyses to model the caisson as a rigid body. As is typical for anchor applications, the padeye was set at the two-thirds point along the depth of the pile, approximately at the optimal load attachment depth for maximizing the load capacity. The initial Young’s modulus of soil was computed from the ratio E/s_u = (200-900). Also, as described previously, selection of σ_0 (or, practically σ_0/σ_{max} ratio) requires test data capable of producing reliable stiffness degradation curves.

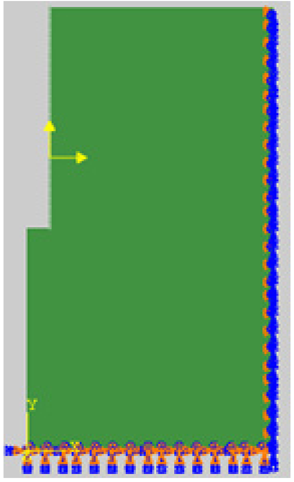

(a) Bottom and far-field boundaries

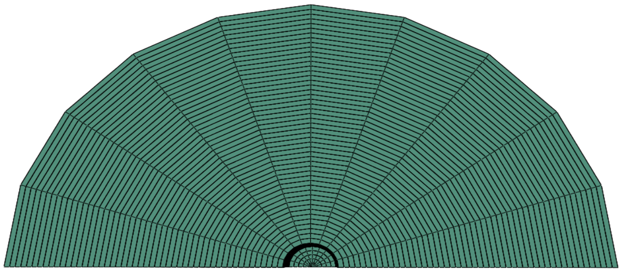

(b) Top view (with Fourier expansion)

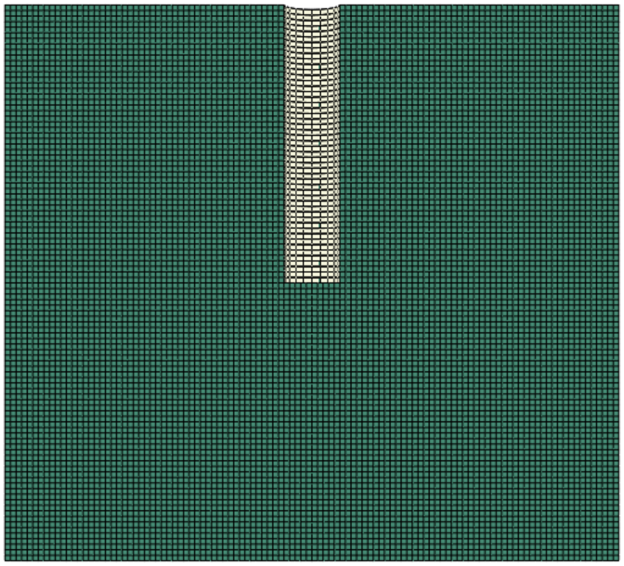

(c) Elevation view (with Fourier expansion)

Figure 3.10. Finite element mesh

Evaluation of cumulative deformations under cyclic loading first requires a realistic estimate of the working loads to be applied to the pile. The approach adopted here is to first estimate the ultimate load capacity of the pile, and then apply a typical safety factor reduction to compute an applied operational load. A simplified upper bound analysis (Aubeny et al., 2003; Aubeny et al., 2001), validated through comparisons to finite element solutions, was used to compute ultimate load capacity (F_{ult}).

Table 3.2 lists the ultimate and applied loads, F_{ult} and F_a respectively, used in the parametric study for various load inclination angles (ψ). It is recognized that a large number of repetitions of F_a seldom occurs; i.e. F_a is usually a peak load in a random load sequence. Thus, analyses involving repeated loading at F_a generally represent an upper estimate of cumulative displacements. The parametric study presented below also considers the more common case of a single peak load (F_a) in conjunction with cyclic loading at various fractions of the peak load.

In order to get a full idea about the cyclic behavior for the analyzed soil-caisson system, it has been selected a range of load angle (ψ) with various adhesion factors (α) to get the minimum applied force (F_a), according to American Bureau of Shipping (ABS, 2013), that can be applied to the caisson at the optimum attachment point (padeye) on the caisson wall that is about two-third the length of caisson (L_w = 17 m), as listed in Table 3.2.

Table 3.2. Force control for soil-caisson system

ψ (°)	α	F_{ult} (kN)	FS	$F_a \approx \frac{F_{ult}}{\mathrm{FS}}$ (kN)	min F_a (kN)
0	1	32434.64	1.5	21623	20186
	0.9	31716.18	1.5	21144	
	0.8	30997.63	1.5	20665	
	0.7	30279.08	1.5	20186	
15	1	29912.14	2	14956	13888
	0.9	29200.40	2	14600	
	0.8	28488.57	2	14244	
	0.7	27776.52	2	13888	
30	1	29370.80	2	14685	13425
	0.9	28565.99	2	14283	
	0.8	27730.60	2	13865	
	0.7	26850.50	2	13425	
45	1	23885.08	2	11943	10130
	0.9	22679.92	2	11340	
	0.8	21470.72	2	10735	
	0.7	20259.04	2	10130	

3.4 Continuum Mesh Verification

Several mesh configurations have been assessed in order to maximize efficiency of the model and to fulfill the acceptable accuracy with reasonable consuming time for cyclic computations. For both the wall and caisson simulations, diverse models with different mesh sizes were conducted.

Thus, the results of several wall models with different element dimensions of 2, 1, and 0.5 ft were compared to each other and the effects of change in mesh size were studied. Based on the results of the permanent top-height wall deflection at the end of 100th cycle that tabulated in Table 3.3 , a mesh size of 1 ft was selected for the soil-wall system.

Table 3.3. Element size verification for soil-wall system

Element Size (a)	Permanent Top-Height Wall Deflection (ft) at cycle# 100	Difference in Subsequent Results (ft)	Difference In Subsequent Results (%)
2	-0.092563866	-	-
1	-0.090873207	-0.001690659	1.83%
0.5	-0.090332642	-0.000540566	0.59%

To establish an acceptable level of mesh refinement for caisson problem, ultimate load capacity calculations from finite element calculations were compared to those obtained from plastic limit analysis (PLA) calculations (Aubeny et al., 2003; Aubeny et al., 2001). These studies demonstrated that a FE simulation using the mesh shown in Figure 3.10, having a typical element dimension of 0.5 m for caisson simulations, was able to match the PLA prediction of ultimate load capacity to within 2%. A summary of these results can be seen in Table 3.4.

Table 3.4. Element size verification for soil-caisson system

Element Size (a)	D (m)	L_f/D	α	H_{max} (PLA) (kN)	H_{max} (FEA) (kN)	Difference in H_{max} (%)
0.5	5	5	1	32924.44	33593.53	1.99%
1	=	=	=	=	36547.10	9.91%

3.5 Continuum Model Validation

3.5.1 Wall Model

Some researchers stated that the cumulative vertical plastic strains under the train track from different train load levels are assumed to be power law curves (Figure 3.11) but are not assumed to be continue with the same behavior for the entire life of soil behavior under the track (Li et al., 2016) but it will be increasing in the strain, as shown in Figure 3.12. The bounding surface model simulated the same behaviors of soil under the train track of power curves as well as the behavior of increased the displacement rates in accordance with increasing the repeated load for many cycles of train passing, as illustrated in Figure 3.13.

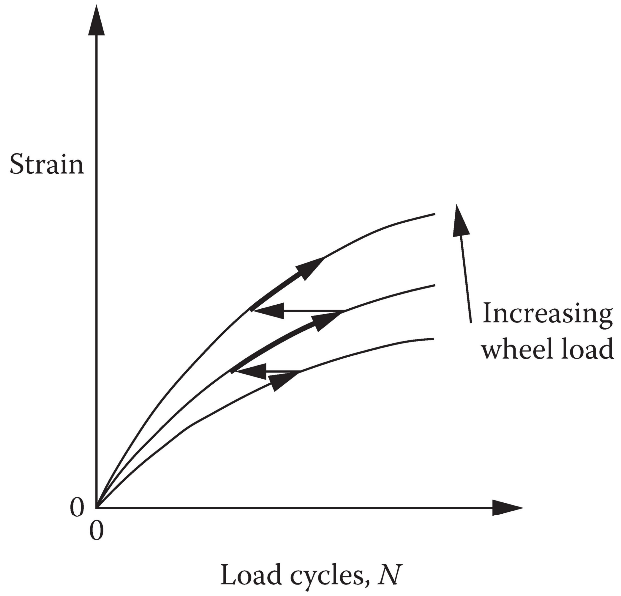

Figure 3.11. Ballast strain accumulation with load cycles for increasing wheel loads (Li et al., 2016)

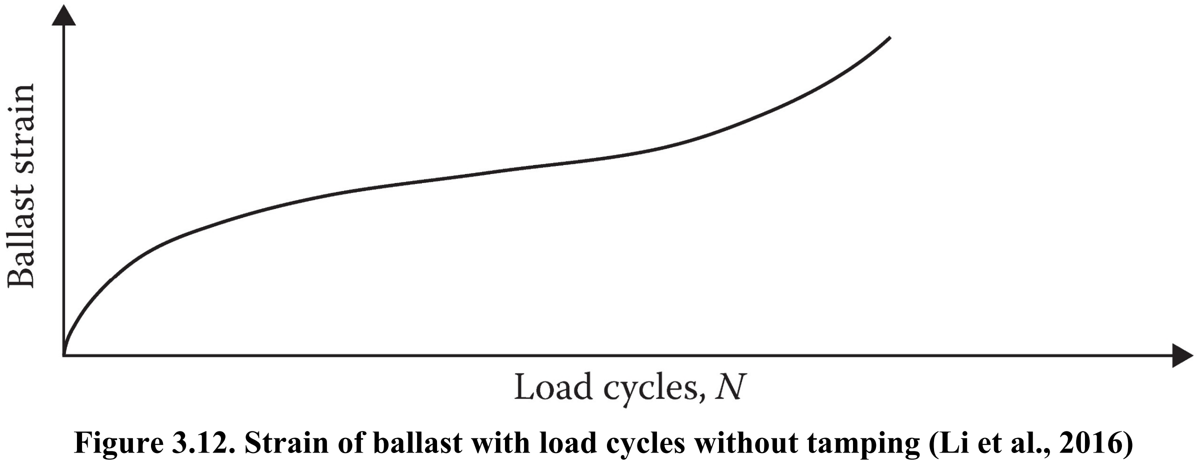

Figure 3.12. Strain of ballast with load cycles without tamping (Li et al., 2016)

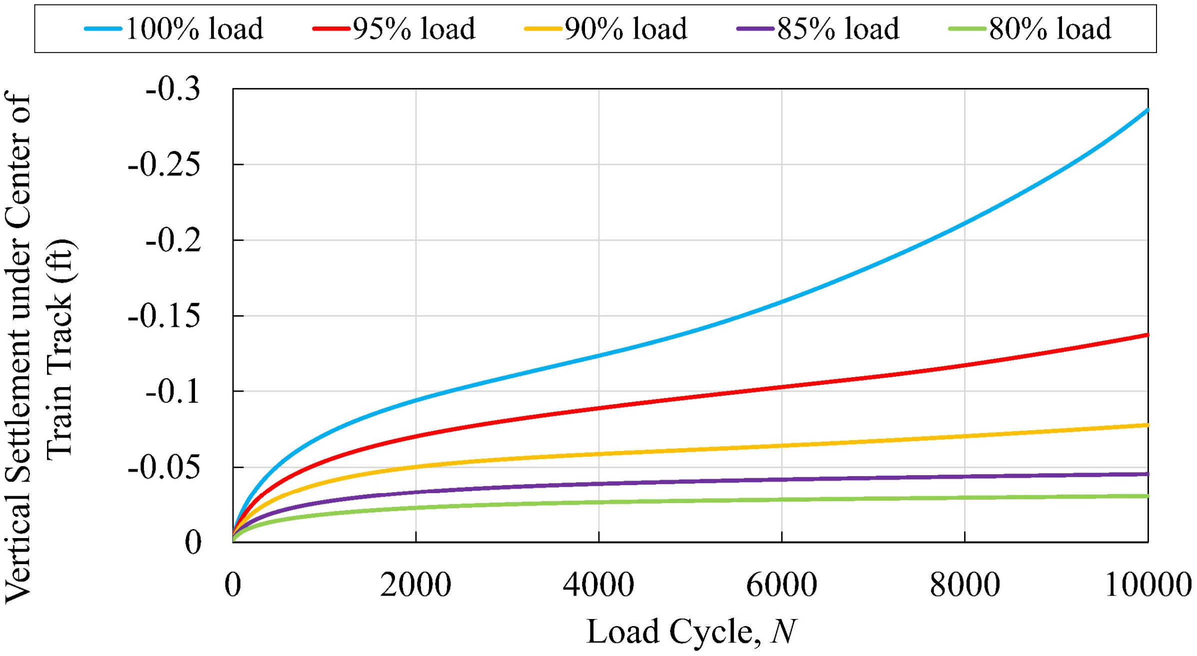

a) E/s_u = 800

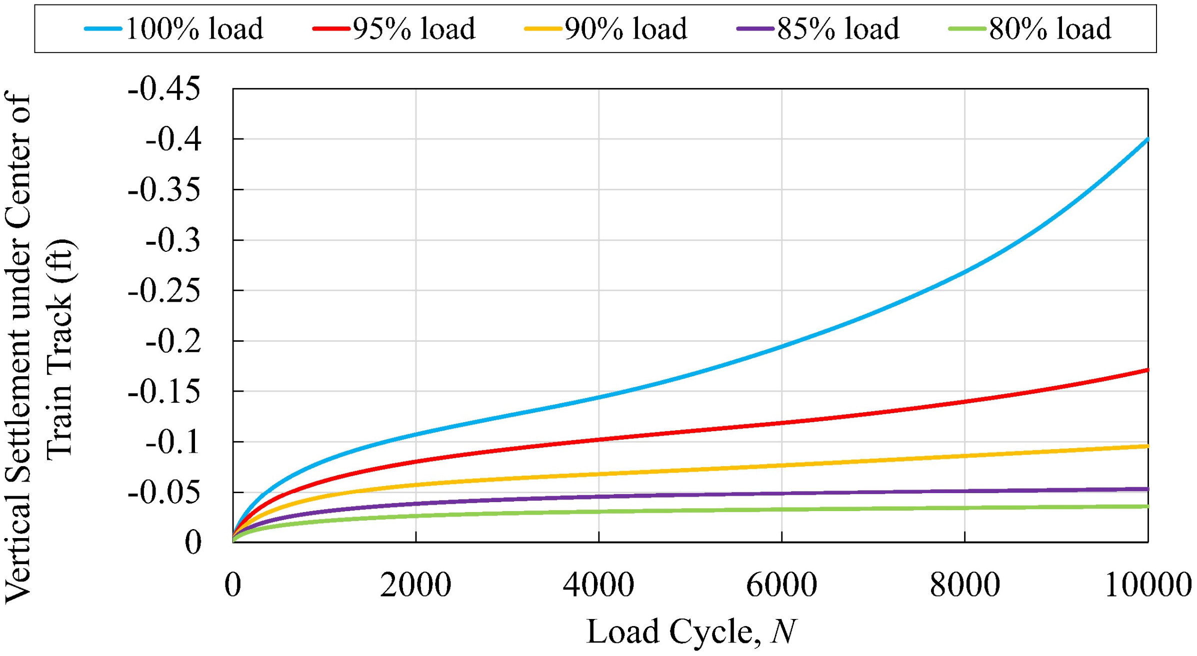

b) E/s_u = 700

Figure 3.13. Vertical settlements with cycles under different train load intensity of various E/s_u ratio

In the second stage of verification, the proposed bounding surface model was applied for retaining walls subjected to live loads from railroad operations for the Union Pacific Railroad (UPRR) project at College Station, Texas. A brief description of the project was given by Mohammadrajabi (2016). From comparing the filed measurements of mid-height wall lateral deflection during the cycles of train passing with the results that computed by the FEA showed that the best fit was achieved for E/s_u = 700 (Figure 3.14). While the comparison showed that in the early cycles there are some differences in the lateral displacements because the load of train was not the same in every passing of train operation.

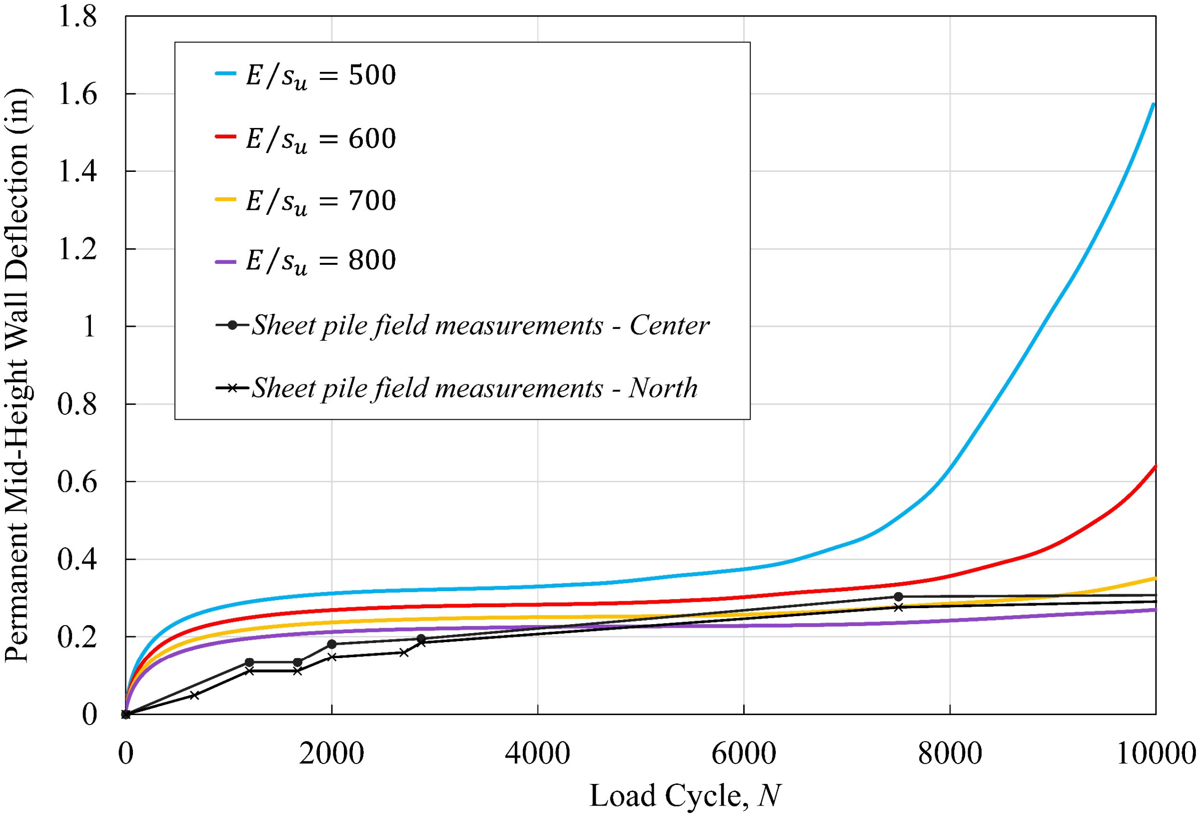

Figure 3.14. Comparison between field measurements and analysis computations of various E/s_u ratio

3.5.2 Caisson Model

The calibration presented herein makes use of experimental single-gravity test results conducted by Gilbert et al. (2015) and Senanayake (2016) on laterally loaded monopiles in clay subjected to cyclic loading. Tests were displacement-controlled with load applied at a specified distance (eccentricity) from the pile head. Imposed displacements were selected to achieve target pile tilt angles ranging from 0.5 to 2 degrees. The laboratory model tests were conducted in testbeds comprised of both kaolinite and Gulf of Mexico marine clays. The piles were embedded to a depth to achieve an aspect ratio L/D = 8, and the load was applied at a distance L/D = 5 above the mudline. Model test pile diameters of 2, 3 and 4 inches (5.05, and 7.62 and 10.2 cm) were used in the test program. In this study, finite element predictions are calibrated to cumulative displacements from a model test on a 4-inch diameter aluminum pile having a wall thickness of 0.125 inch (0.317 cm), and a Young's modulus of 1×10^7 psi (69 GPa), with a 2-degree target tilt in a kaolinite testbed. The soil-pile interface had an interface adhesion factor α = 1.0.

The axisymmetric FE model with asymmetric Fourier elements described earlier was utilized to simulate the soil-caisson system in the model tests. The undrained shear strength profile shown in Figure 3.15 was used in the simulations. Based on the discussion of the laboratory model tests presented by Gilbert et al. (2015) and Senanayake (2016), the small-strain Young's modulus of clay was taken as E/s_u = 90. Poisson's ratio (μ = 0.45) was selected to approximate undrained conditions. The ratio σ_0/σ_{max} was varied from 0.01 to 0.15 to identify the value that achieves the best fit to experimental data. Figure 3.16a, showing measurements versus FE calculations of degradation in the peak load at the pile head, indicates that σ_0/σ_{max} = 0.1 provides the best fit to the experimental data. Interestingly, this value is consistent with the recommended a range σ_0/σ_{max} = 0.1-0.3 given by Anastasopoulos et al. (2011). This figure plots load versus time, where the period of each load cycle is about 10 seconds. Figure 3.16b shows the full history of predicted versus measured load for the case of σ_0/σ_{max} = 0.1. While the predictions of maximum load closely match measurements, the predicted minimum load intensity (i.e. the load at the trough of an unloading cycle) deviates significantly from the experimental measurements during the early load cycles, say, the first 5 cycles. At larger number of load cycles, the agreement between predicted and measured minimum load is very good.

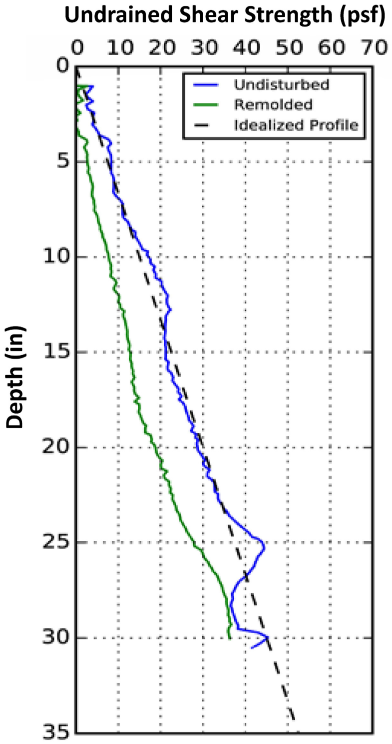

Figure 3.15. Undrained shear strength profile in model tests from Gilbert et al. (2015)

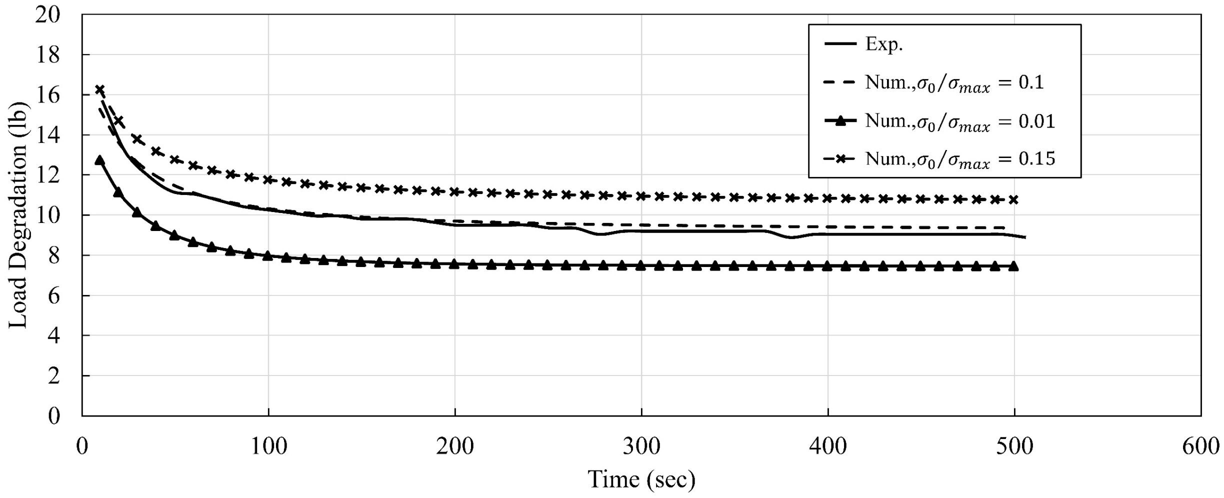

a) Peak resistance during cycling

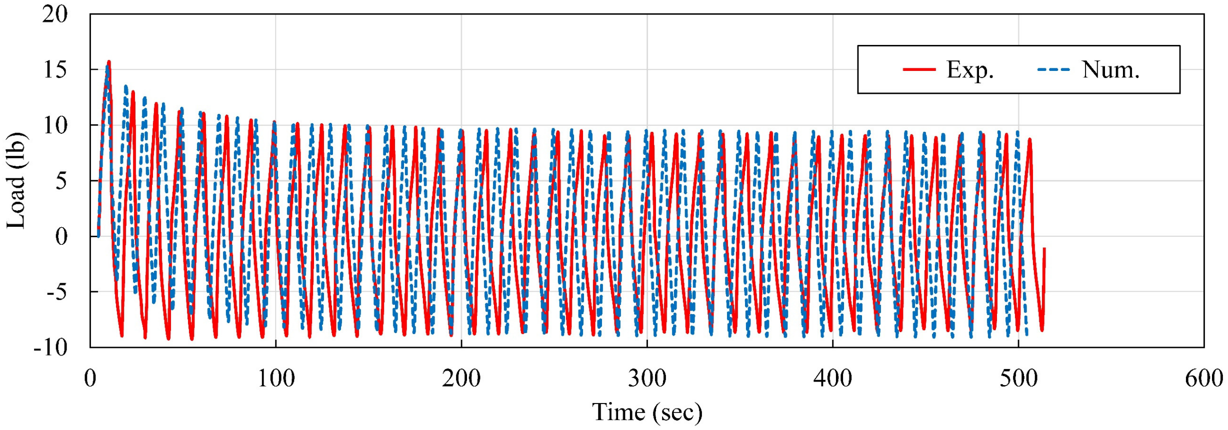

b) Full load history for σ_0/σ_{max} = 0.1

Figure 3.16. Matching of finite element simulations to model test data

4 RESULTS AND DISCUSSION OF CONTINUUM APPROACH

4.1 Wall Problem

At the instant of full application of the train load with E/s_u ratio = 700 for the soil around the wall system, a peak moment M_{peak} occurs. Complete removal of the load leaves a residual moment M_{res} as shown in Figure 4.1, while for each recurring load cycle an incremental trough-to-peak moment ΔM occurs.

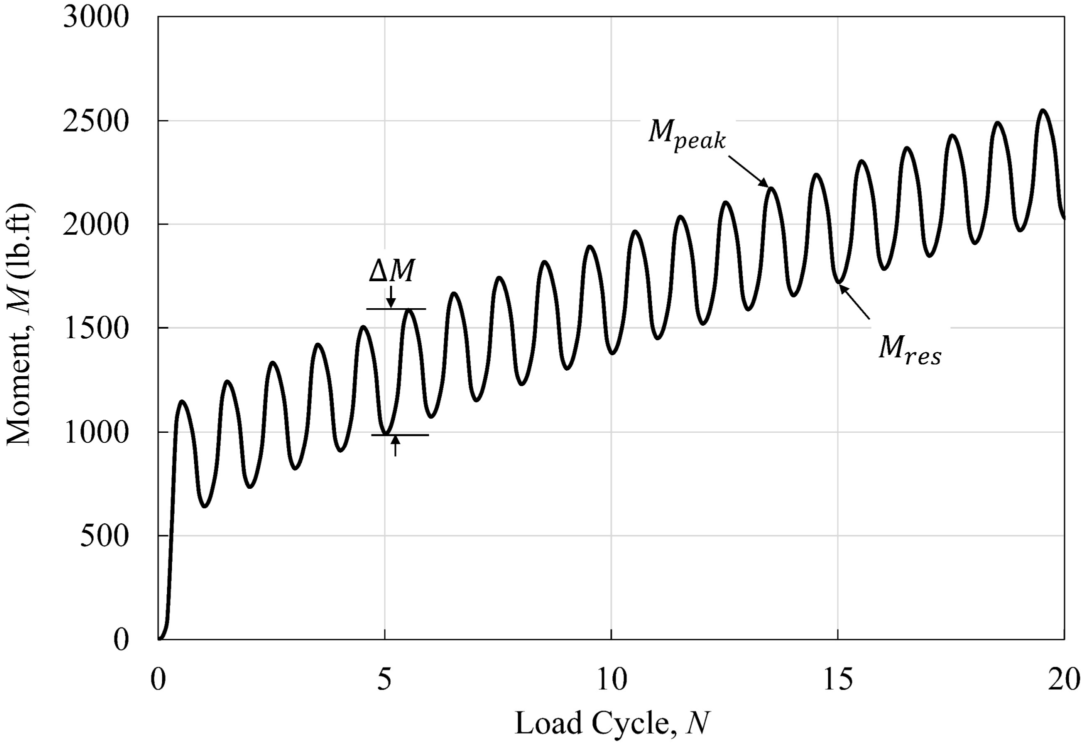

Figure 4.1. Typical moment history

Figure 3.14 shows measured versus predicted (for the case of full Cooper E80 loading) residual lateral deflections at the wall mid-height. The deflections were measured at the sheet pile wall center and the north edge. The predicted displacement versus load cycle curves actually show three stages of deformation: (1) a steep initial portion in roughly the first 1,000 load cycles,

(2) a plateau extending to about 4,000 to 8,000 load cycles, and (3) a region of rapidly increasing deformations at large numbers of cycles that ultimately leads to instability. The FE predictions tend to over-estimate measurements in the first stage; however, the FE predictions of the plateau (the second stage) in displacements are in reasonable agreement with measurements. While the measurements do not show evidence of the third stage of the mid-wall deflection vs. the load cycles curve, it can be noticed that the track and ballast maintenance process would prevent such excessive displacements from occurring.

Given that wall performance is often evaluated within the framework of a Boussinesq strip load solution, comparing the finite element solutions to Boussinesq solutions can be instructive. If the train load is idealized as a strip load and the wall is considered to undergo zero lateral displacement at all points, then the horizontal stress distribution acting along the wall becomes twice that of the basic strip load solution, producing the following Boussinesq strip load to compute the horizontal pressure distribution (σ_x) due to the Cooper E80 loading equation when the train track is parallel to the wall system (GTS, 2004):

$$\sigma_x = \frac{2q}{\pi}\,[\beta - sin\beta\,\cos(2\alpha)] \tag{9}$$

For the case of a cantilevered wall bending moments M are evaluated through double integration of lateral stresses, imposing zero shear and moment boundary constraints at the top of the wall. Similarly, lateral wall deflections are computed through double integration of the wall curvature (M/EI) based on an estimated Point of Fixity (PoF); i.e. the point below the base of the excavation at which the wall deflection and slope may be taken as zero.

Since the Boussinesq-based analysis applies only to monotonic loading, the comparisons to finite element solutions presented here are made for ten instants during the loading history, the end of loading at cycles N = 1,000-10,000. It is noted that the FE simulations generally show (e.g. Figure 3.14) a pattern of steeply rising displacement during the early stages of cycling, followed a gently sloping displacement-load cycle curve at intermediate N, followed finally by a region of upward curvature. The latter stage of loading is considered here to represent a condition of unstable system response that would eventually lead to a failure state. It is noted that in practical situations repairing the ballast would avert this unstable condition. In the comparisons that follow, system response during the unstable stage of loading is flagged to emphasize that the variable under consideration corresponds to a condition that would normally be avoided through a proper maintenance program.

Figure 4.2 shows comparisons of residual displacements and residual bending moments for the base case analysis; i.e. E/s_u = 700, full Cooper E80 loading, σ_0/σ_{max} = 0.1, $Dist$ = 8 ft, and B = 8 ft. It is emphasized that the moments and displacements shown are purely associated with the live component of loading, in excess of the respective values due to soil self-weight. To provide a full picture of the wall response the plots extend to the tip of the sheet piles, recognizing that comparisons to the Boussinesq have no meaning below a depth of 10 ft, i.e. the base of the excavation. The simulations indicate that during early stages of loading (say N = 1,000) the FE bending moment falls well below that predicted from the Boussinesq analysis. With increased cycling (up to about 6,000 cycles) the maximum stresses and moments predicted from the FE analysis reach a rough level of parity with the Boussinesq predictions. As cycling further increases beyond N = 6,000 cycles to drive the soil-wall system into an unstable mode, FE predictions of maximum lateral stresses and moments substantially exceed the Boussinesq values. In regard to lateral displacements, the choice of point of fixity (PoF) in predicted displacements at the top of the wall clearly has an enormous influence. In this case, assuming the higher value of the depth to the PoF, 0.75 H_E, is needed to achieve some level of parity between the FE and Boussinesq-based solutions. Noting that the soil profile for the case under consideration comprised a stiff clay, this somewhat contradicts common practice (California Department of Transportation, 2011), which usually recommends an assumed depth to PoF equal to 0.25 H_E for stiff clays. For a PoF equal to 0.75 H_E, the displacements at the top of the wall for load cycles in the range N = 1,000 to 6,000, the Boussinesq values agree remarkably well with the FE predictions. As was the case for bending moments, when the system becomes unstable, the FE predicted displacements substantially exceed the Boussinesq-based values. While the FE and Boussinesq predictions of moment and displacement at the approximate limit of stable behavior (N = 6,000 cycles) are roughly comparable, the distributions with depth are not in particularly good agreement. This is not necessarily a matter of great significance, since selection of the wall section is usually based on maximum bending moment values.

For the case analyzed, the most important takeaway is the Boussinesq-based solution using Equation (9) provides an estimated maximum bending moment in the wall that is roughly comparable to that obtained from the much more rigorous FE analysis, provided that the number of load cycles is less than the critical value marking the onset of unstable behavior. In the case of displacements, Boussinesq-based predictions can be reconciled to FE predictions only when a PoF depth greater than normally assumed is used in the analysis, even when the comparison is restricted to stable conditions.

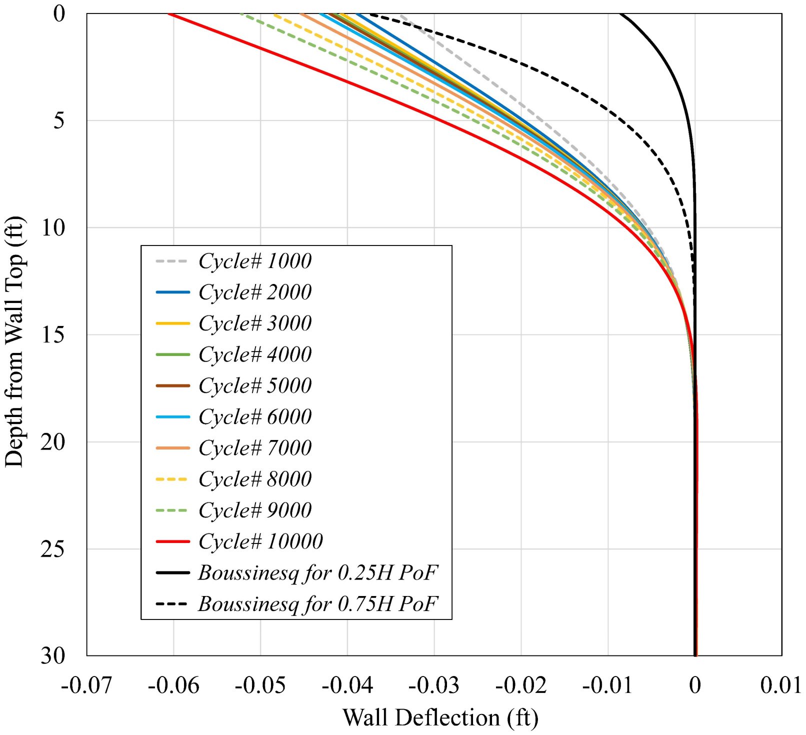

(a)

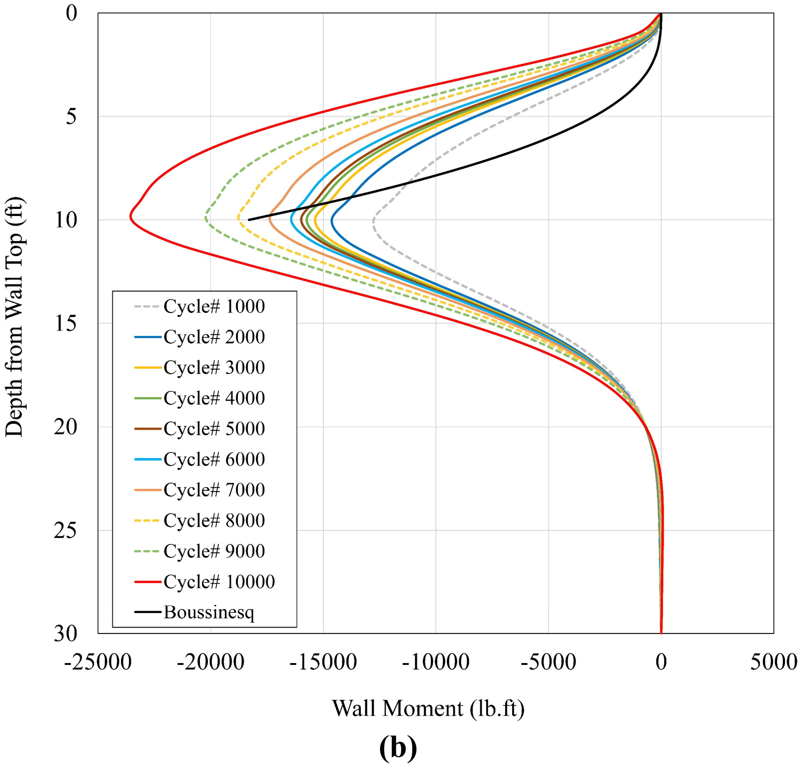

(b)

Figure 4.2. Comparison of Boussinesq-based solutions to FE results at the end of cycles along the wall depth in soil with E/s_u =700 and 100% of full train load

A parametric study was undertaken to study the influences of soil properties, load intensity, wall type, wall embedment, wall height, and wall stiffness on the soil-wall system. Thus, the following parameters were considered in this parametric study:

- The soil stiffness was implemented by the E/s_u ratio with a range of (500-800).
- The load intensity (q) was carried from 100% to 80% of train full load.
- The value of σ_0/σ_{max} ratio was ranged between 0.09 to 0.15.
- The sheet pile wall types of PZ22, PZ27, PZ35, and PZ40 were considered in order to study the effect of wall stiffness (EI).
- The Wall height (depth of excavation), H_E with a depth of wall embedment $2H_E$ was used for all cases because it is typically the wall embedment equal to twice the wall height for sheet pile retaining walls.
- The distance ($Dist$) from the edge of the train load to the wall top.

After the analysis of the soil-wall system with 10000 cycles of full train load for various ratio of E/s_u = (500-800), it can be computed that the lateral displacements along the wall depth decreased with increasing the initial elastic modulus of the soil (Figure 4.3). In addition, the shear, bending moment and soil pressure diagrams along the wall depth in soil have the same trends of decreasing as the soil modulus increasing (Figure 4.4, Figure 4.5, and Figure 4.6 respectively).

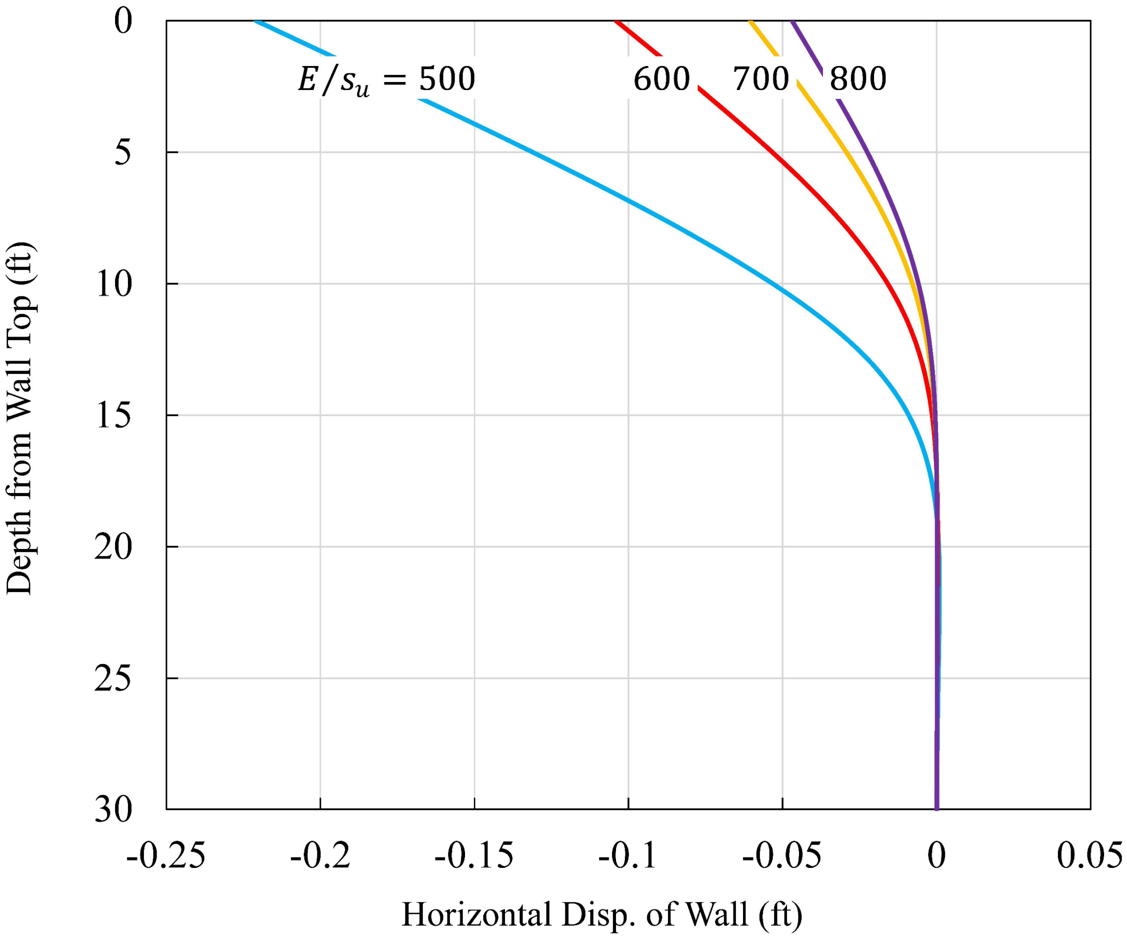

Figure 4.3. Horizontal displacement along the wall depth in soil for various E/s_u ratios at the end of 10000 cycles

Furthermore, from Figure 4.5, it can be noticed that the maximum bending moment for soils with E/s_u ratio = 800-600 is less than the allowable bending moment of wall, which equals 6.292×10^4 lb.ft, while for the soil with E/s_u ratio = 500 is larger than the allowable moment of wall, which is calculated by the multiplication of allowable stress design of steel sheet pile wall, 25000 psi with section modulus of wall, 30.2 in^3/ft from Table 3.1.

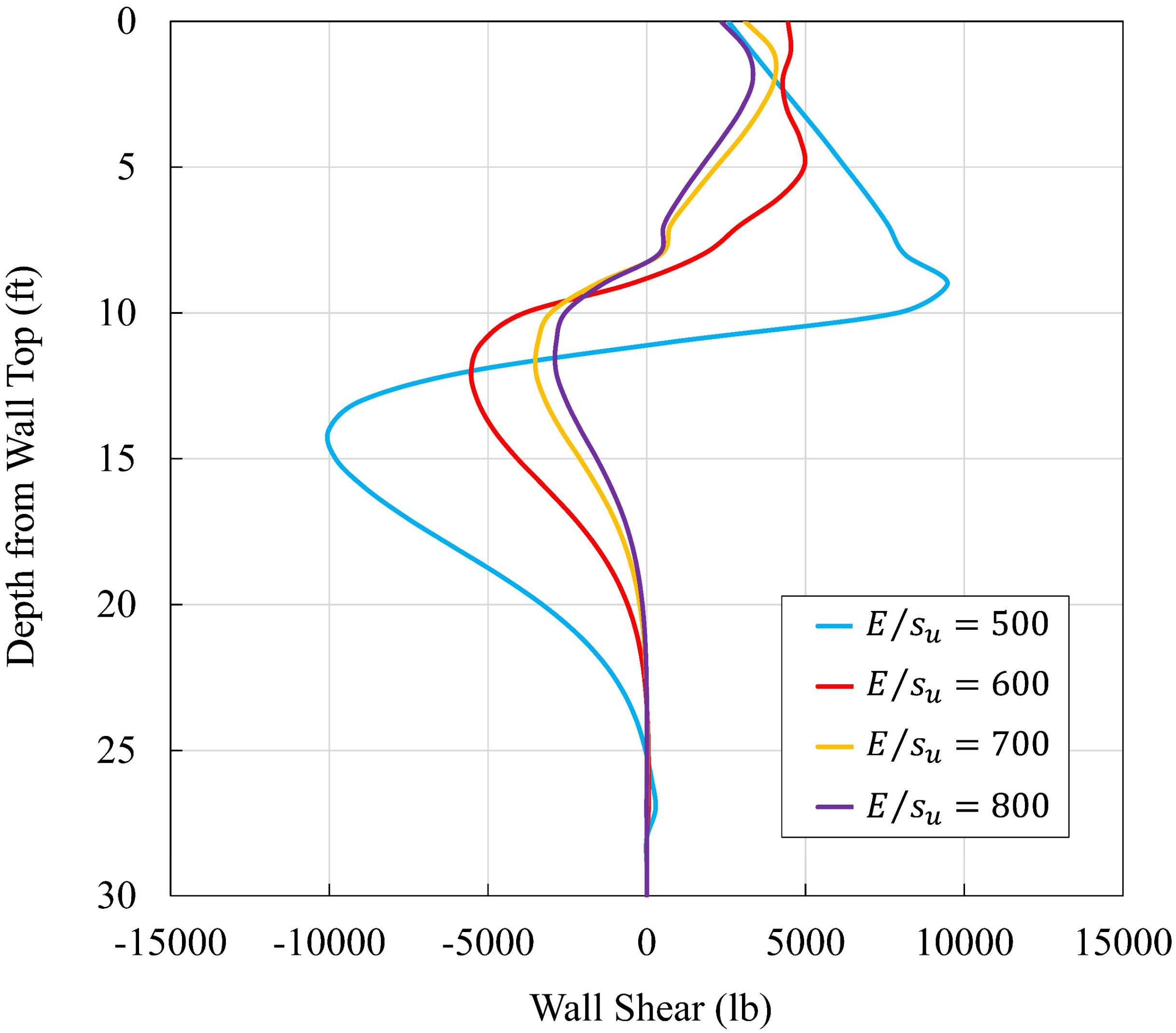

Figure 4.4. Shear diagram along the wall depth in soil for various *E/s_u* ratios at the end of 10000 cycles

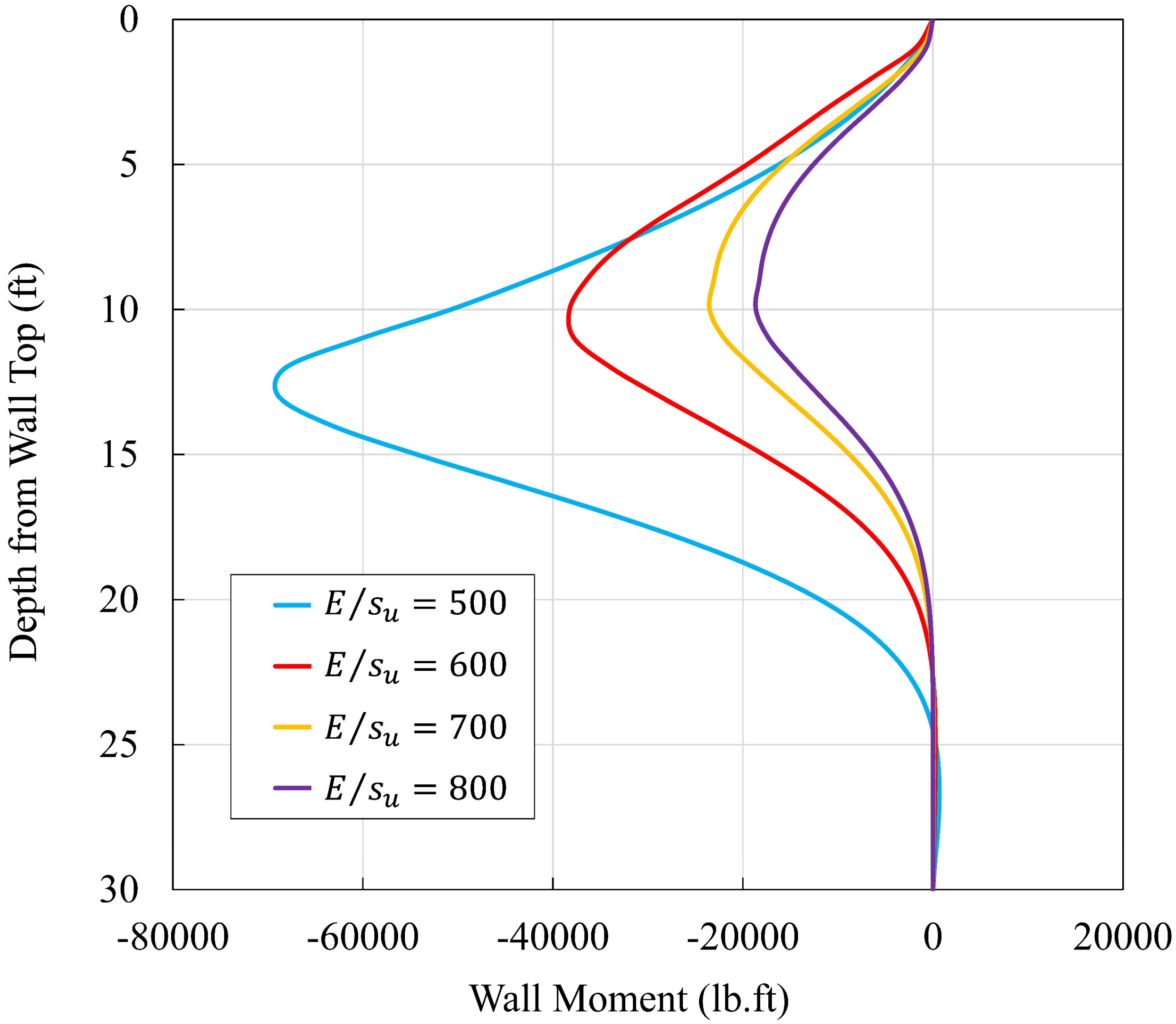

Figure 4.5. Bending moment diagram along the wall depth in soil for various *E/s_u* ratios at the end of 10000 cycles

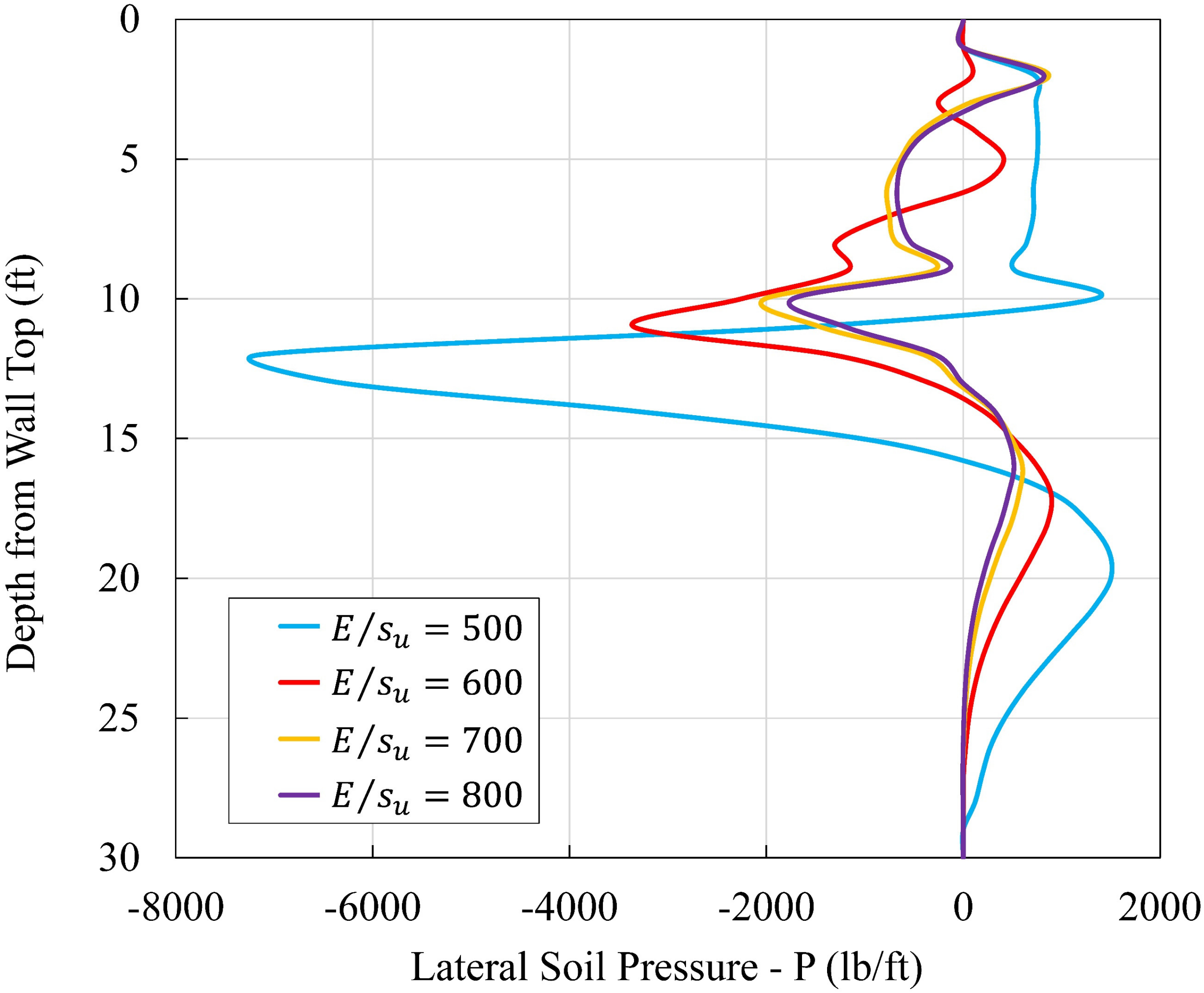

Figure 4.6. Lateral soil pressure distribution along the wall depth in soil for various *E/s_u* ratios at the end of 10000 cycles

From the case of simulation with E/s_u =700 and 80% of full train load, it is noted that the horizontal displacements, the bending moments, and the lateral soil pressure distributions along the wall increase with the cycles (Figure 4.7, Figure 4.8, and Figure 4.9 respectively). However, the displacement, the moment and the pressure gradually decrease for the succeeding cycles.

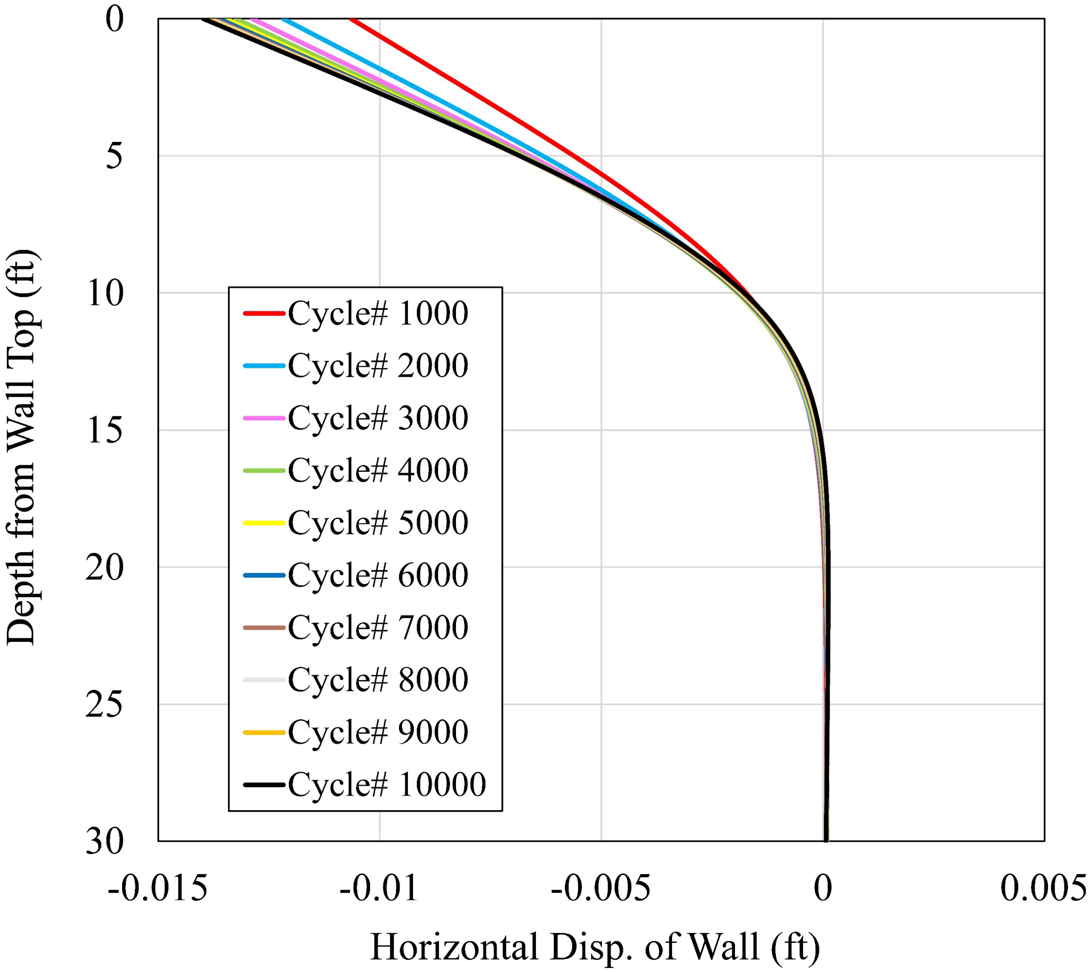

Figure 4.7. Horizontal displacement along the wall depth in soil with E/s_u =700 and 80% of full train load

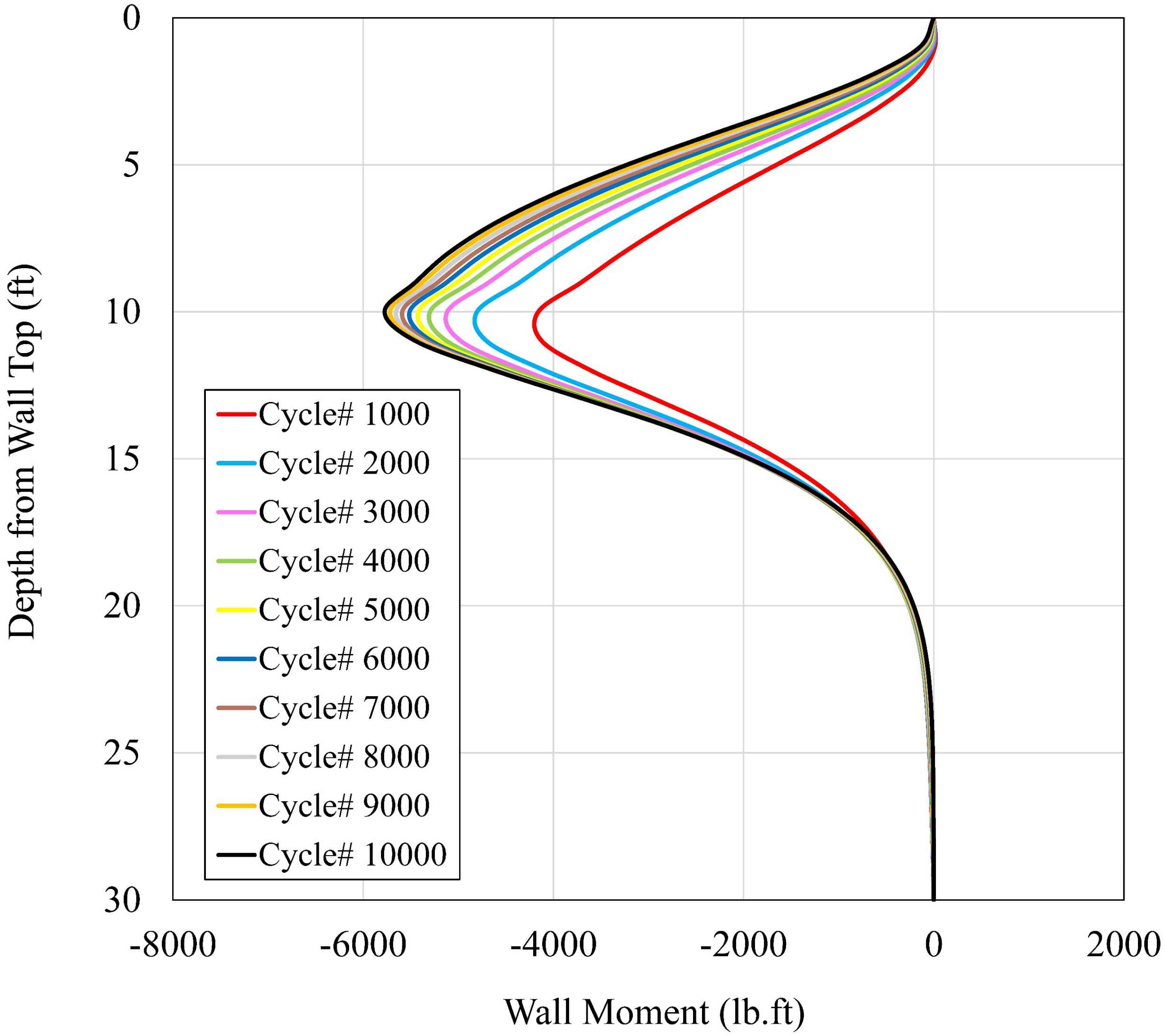

Figure 4.8. Bending moment diagram along the wall depth in soil with E/s_u =700 and 80% of full train load

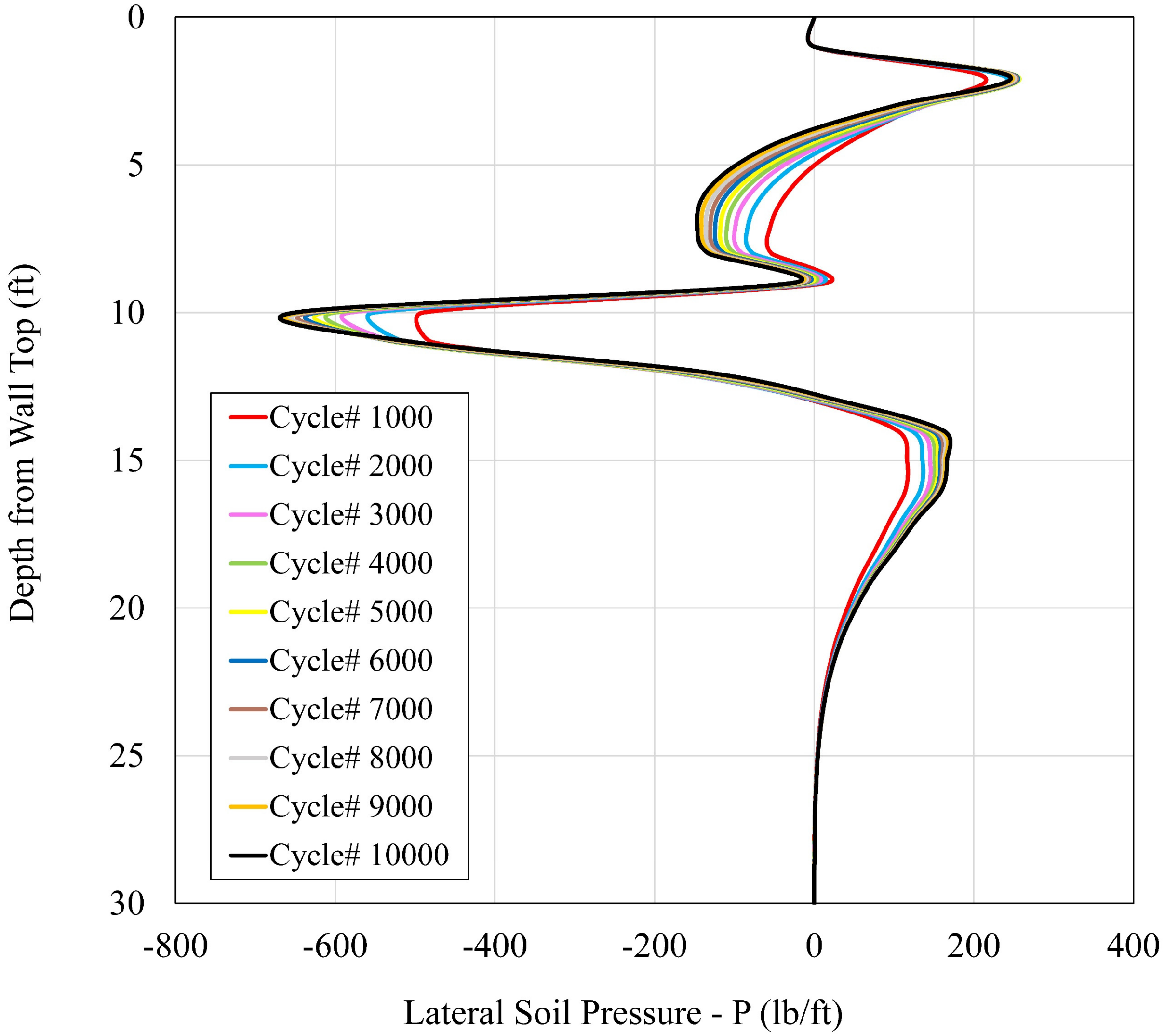

Figure 4.9. Lateral soil pressure distribution along the wall depth in soil with E/s_u =700 and 80% of full train load

Also, this proposed model illustrated the ratcheting behavior of the soil of the sheet pile wall-soil system, as shown in Figure 4.10, Figure 4.11, and Figure 4.12. Moreover, the ratchet strain gradually decreased between the subsequent cycles with increasing the number of cycles. Notice the similarity of the cyclic behaviors that captured with this model analysis and essentially observed in any cyclic soil experiment.

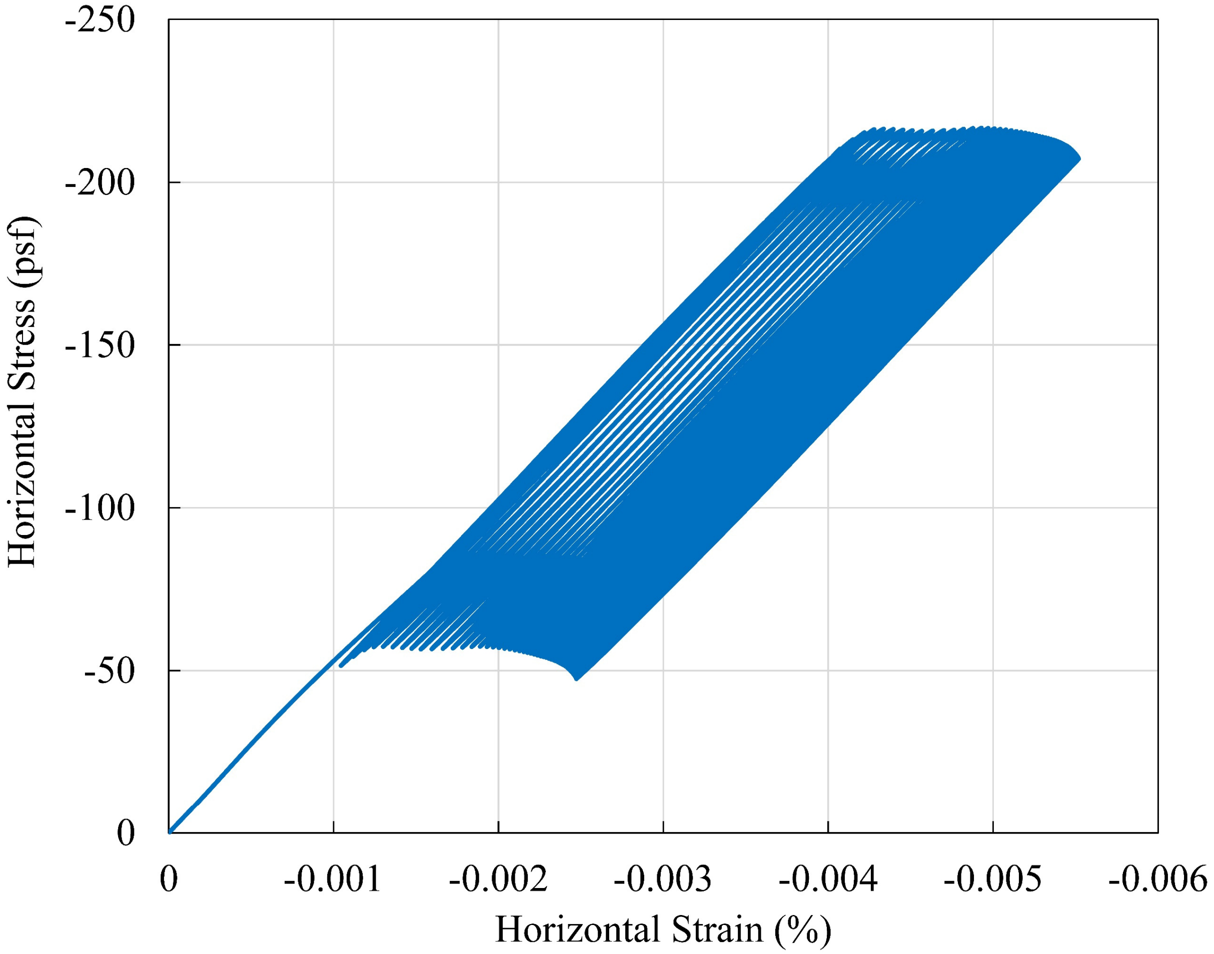

Figure 4.10. Horizontal stress and strain in soil for 50 cycles at depth 5.5 ft behind the wall directly with E/s_u =800 and 100% of full train load

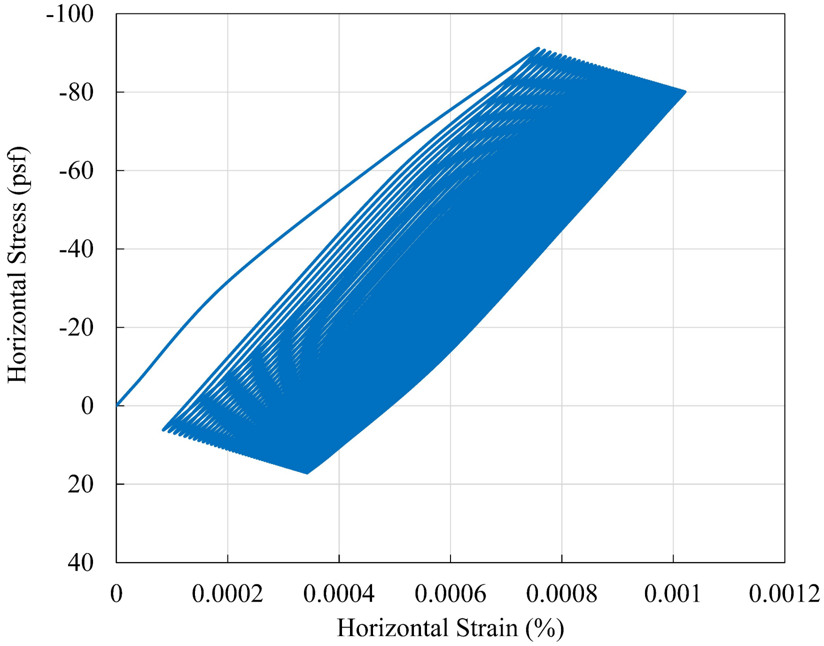

Figure 4.11. Horizontal stress and strain in soil for 50 cycles at depth 20.5 ft behind the wall directly with E/s_u =800 and 100% of full train load

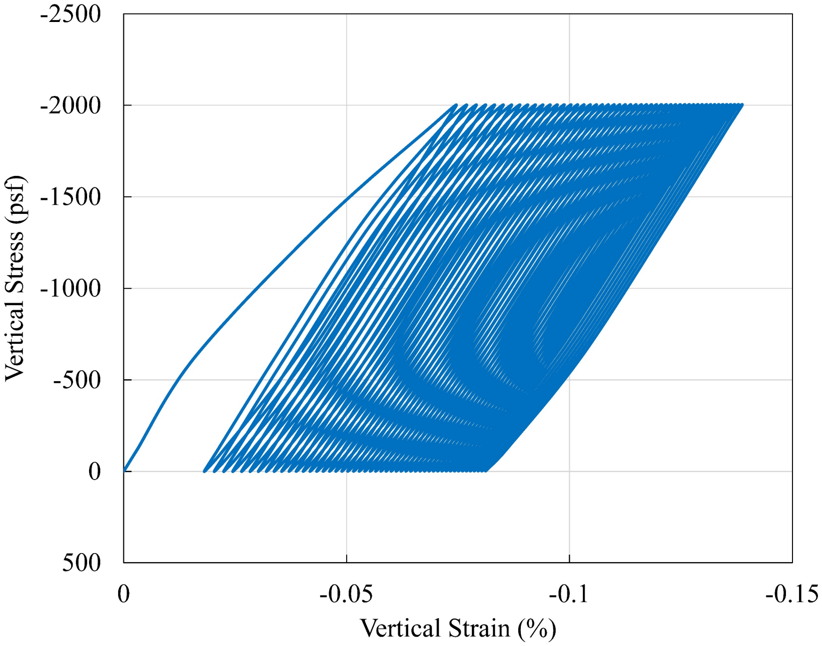

Figure 4.12. Vertical stress and strain in soil under train track for 50 cycles at distance 11.5 ft from the wall top with E/s_u =800 and 100% of full train load

After changing a value of σ_0/σ_{max} ratio, it can be observed that the lateral displacement of wall would be changed significantly (Figure 4.13). The displacements with cycles tend to decrease with increasing the σ_0/σ_{max} ratio, and even decreasing this ratio less than 0.1 with a magnitude of 0.09 can make an enormous displacement at the end of 10000 cycles. As well as, decreasing this ratio can increase impressively the lateral displacements, bending moment, and soil pressure along the wall, as shown in Figure 4.14, Figure 4.15, and Figure 4.16 respectively.

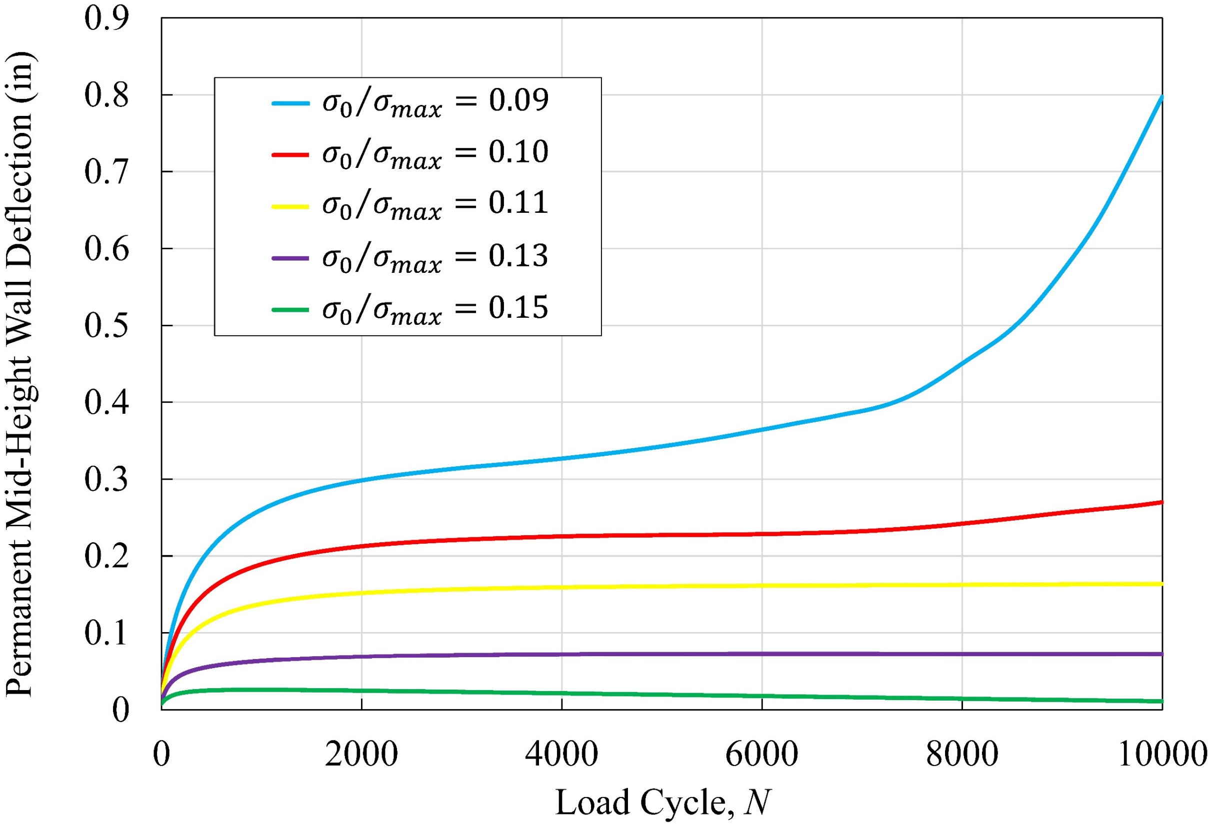

Figure 4.13. Permanent mid-height lateral displacement of wall using various σ_0/σ_{max} ratio with E/s_u =800 and 100% of full train load

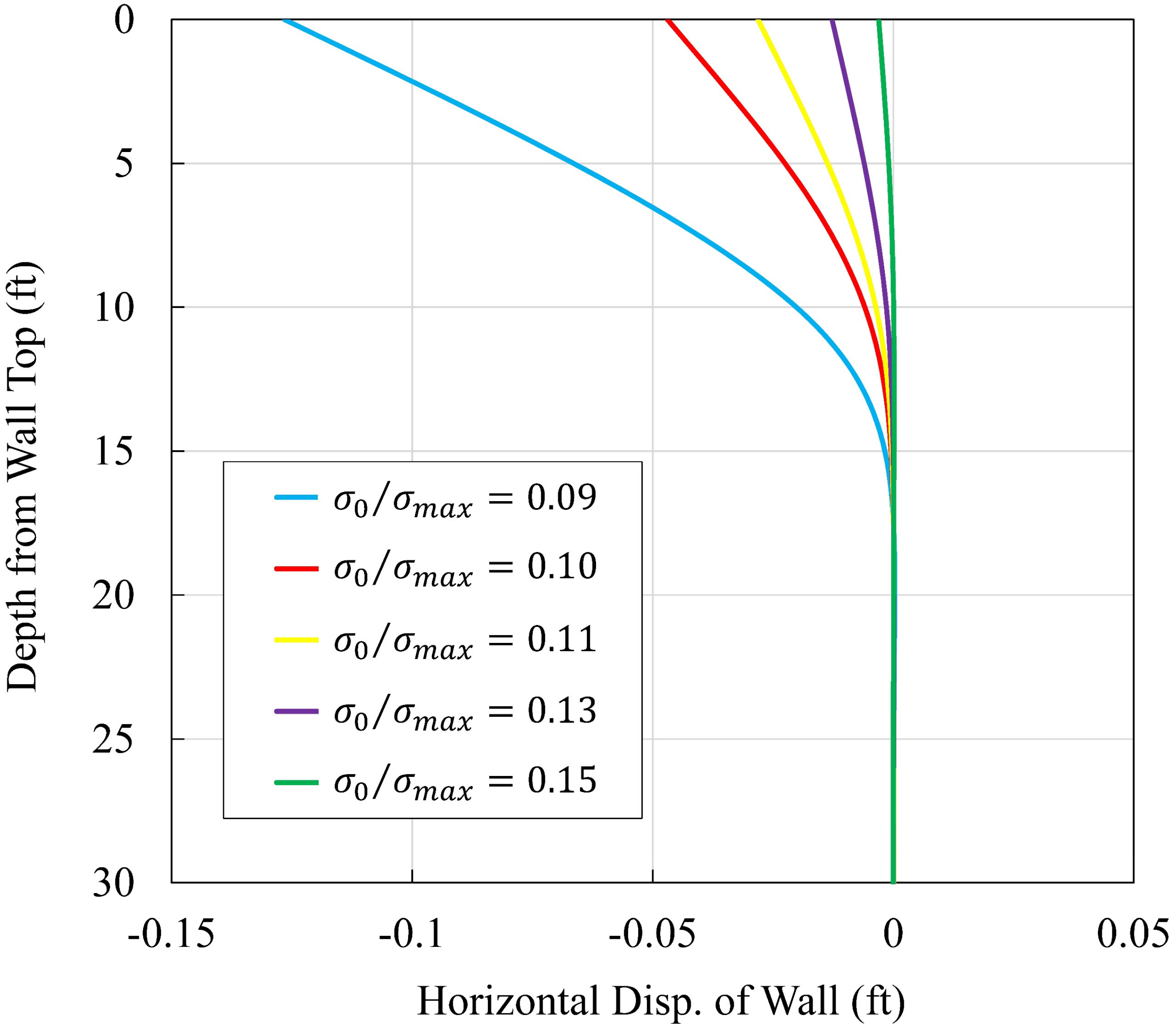

Figure 4.14. Horizontal displacement along the wall depth in soil at the end of 10000 cycles using various σ_0/σ_{max} ratio with E/s_u =800 and 100% of full train load

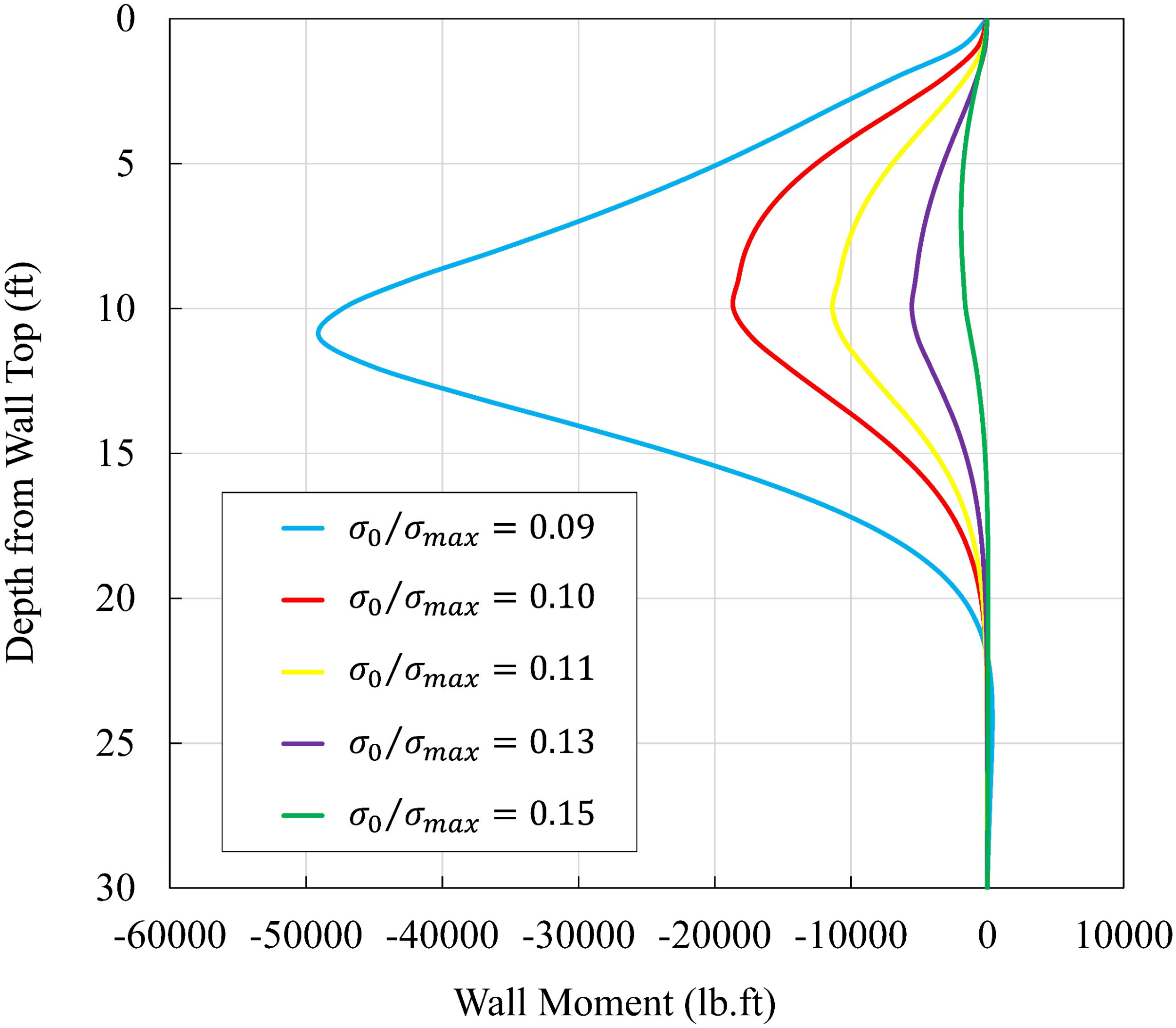

Figure 4.15. Bending moment along the wall depth in soil at the end of 10000 cycles using various σ_0/σ_{max} ratio with E/s_u =800 and 100% of full train load

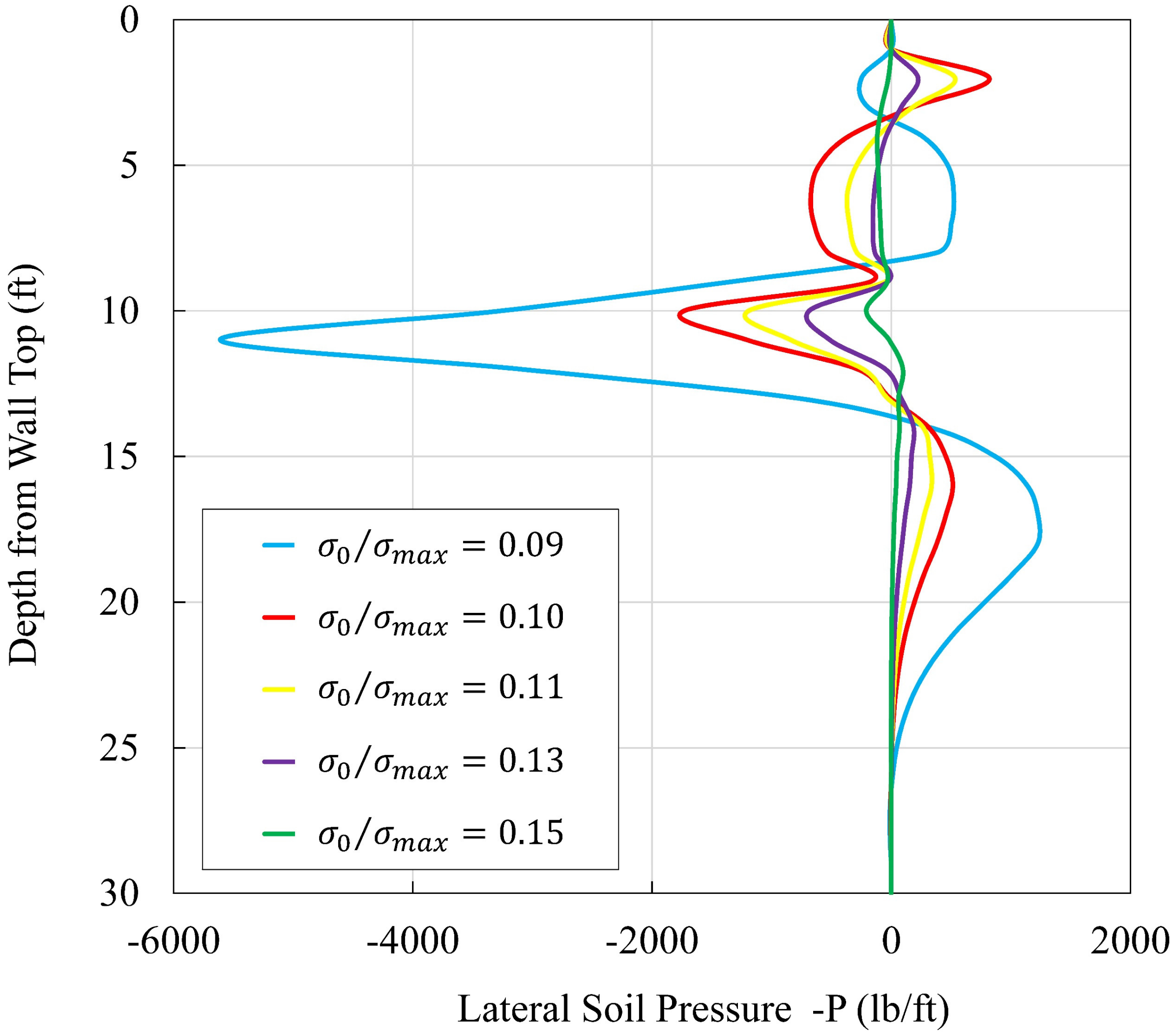

Figure 4.16. Lateral soil pressure along the wall depth in soil at the end of 10000 cycles using various σ_0/σ_{max} ratio with E/s_u =800 and 100% of full train load

After using different types of sheet pile sections (PZ22, PZ27, PZ35, and PZ40), the lateral displacement of wall with cycles would decrease as the EI increased for the sheet pile sections, as depicted in Figure 4.17. However, the increasing of EI of wall leads to decrease the lateral displacement along the wall (Figure 4.18), the bending moment will increase with increasing the EI of wall (Figure 4.19) due to the direct proportion of EI with moment. Accordingly, the lateral soil pressure distribution under the base of excavation will increase as the EI of the wall increases (Figure 4.20).

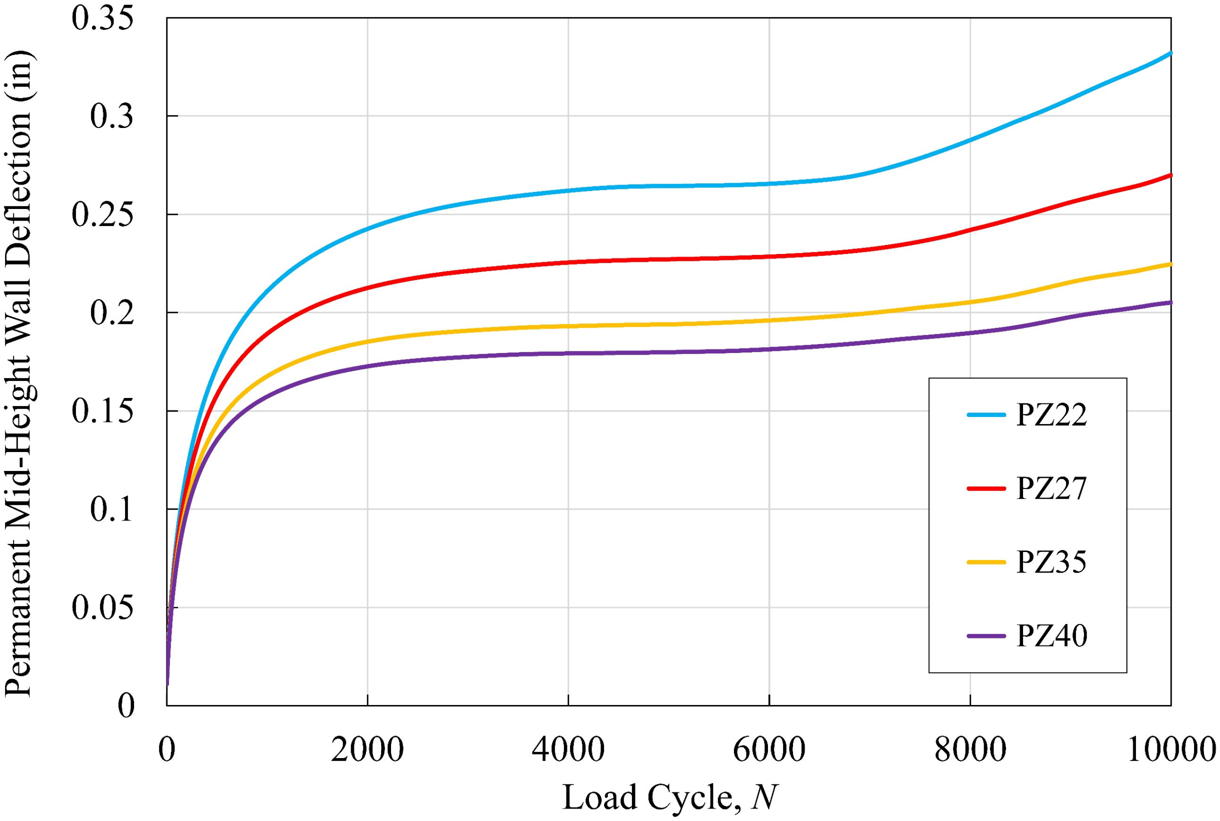

Figure 4.17. Permanent mid-height lateral displacement of wall using various PZ sections with *E/s_u* =800 and 100% of full train load

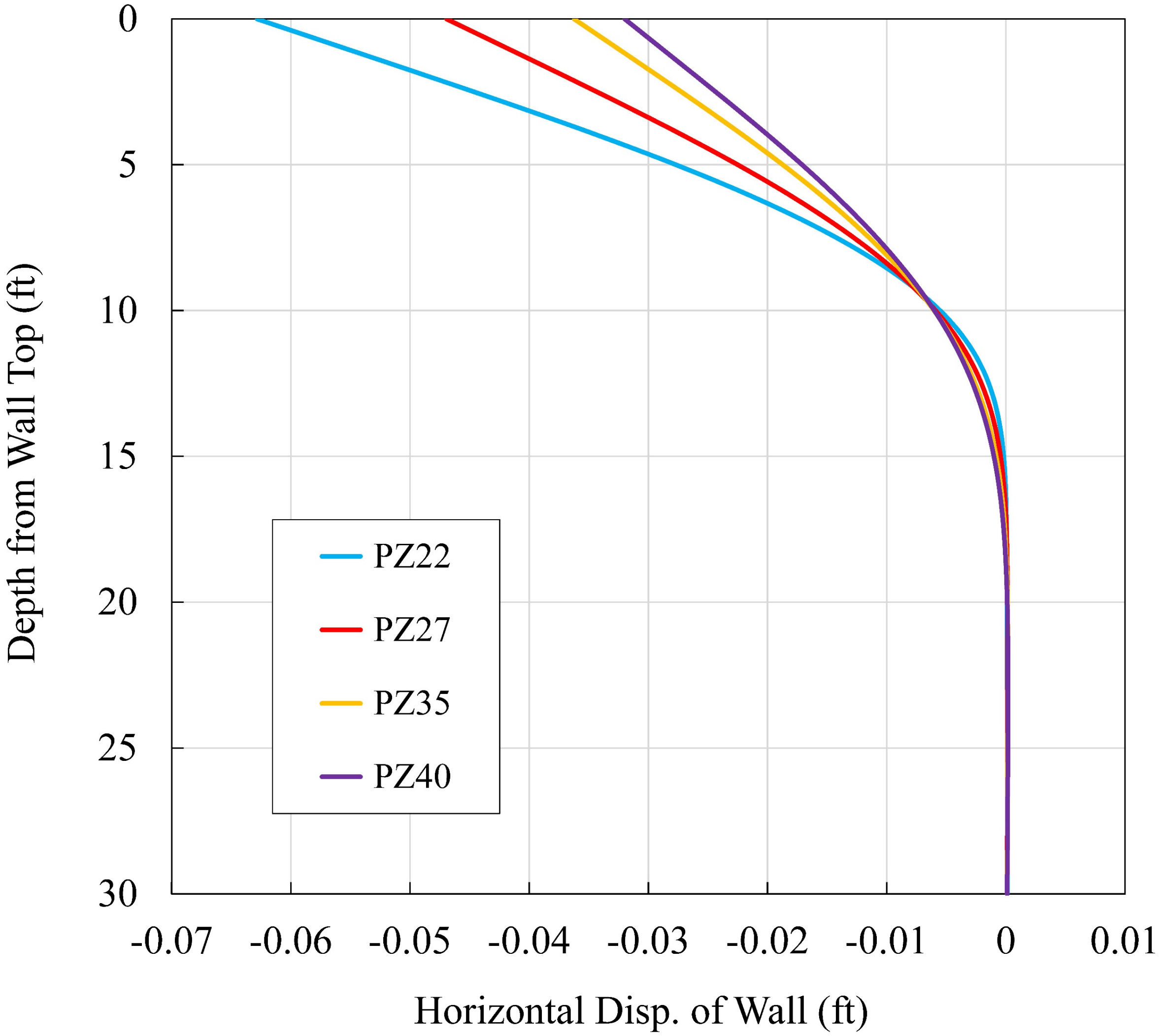

Figure 4.18. Horizontal displacement along the wall depth in soil at the end of 10000 cycles using various PZ sections with E/s_u =800 and 100% of full train load

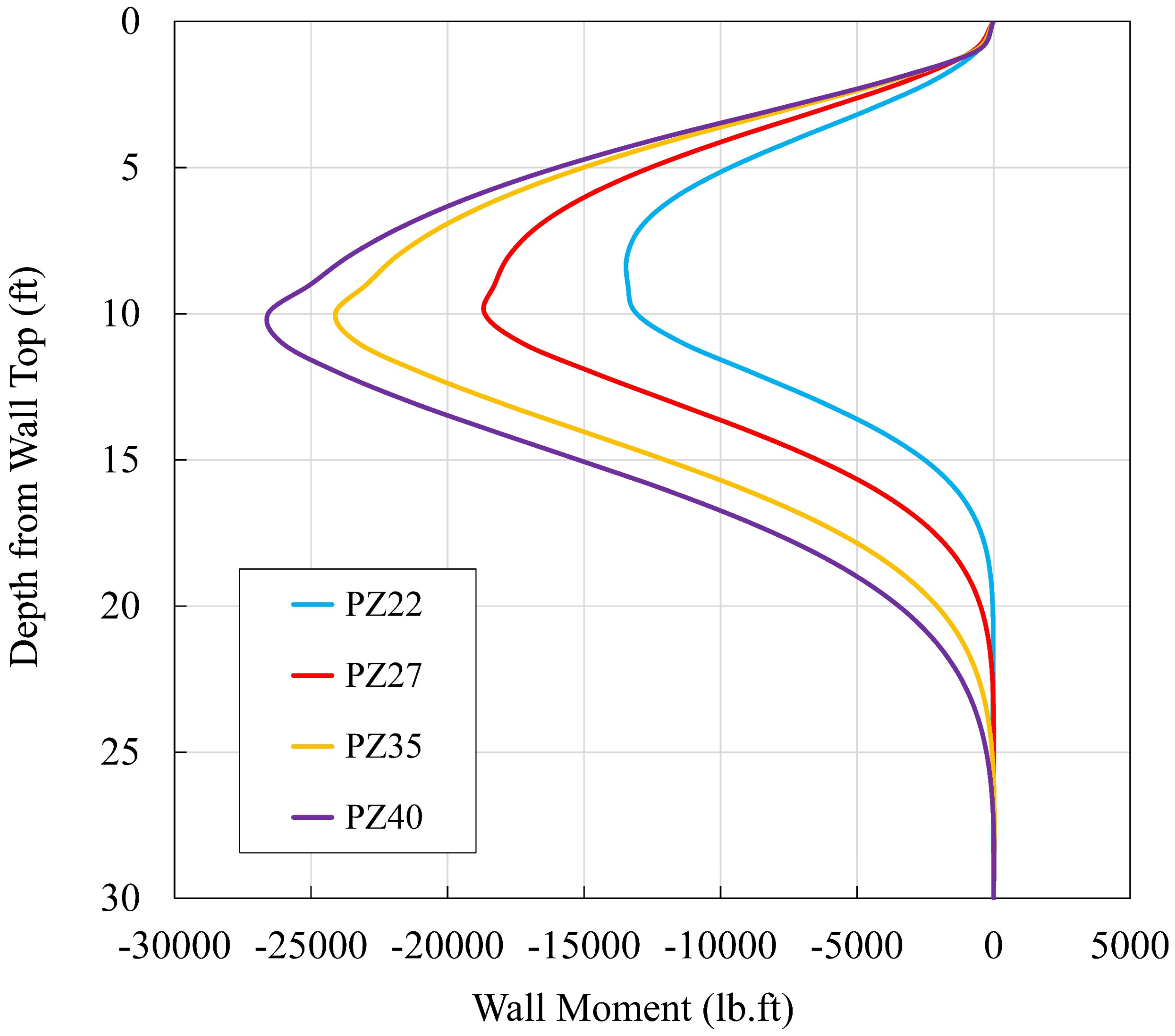

Figure 4.19. Bending moment along the wall depth in soil at the end of 10000 cycles using various PZ sections with E/s_u =800 and 100% of full train load

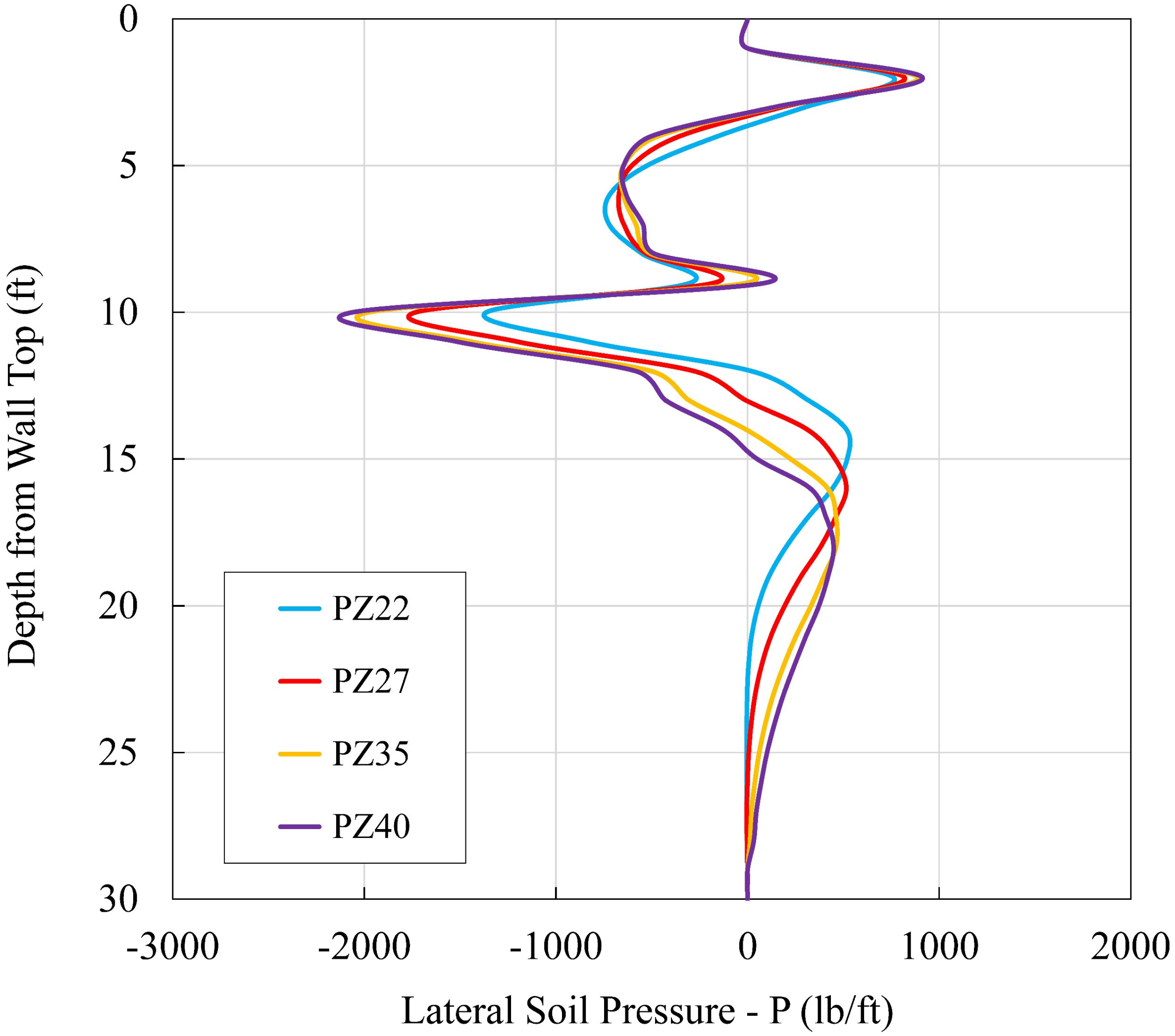

Figure 4.20. Lateral soil pressure along the wall depth in soil at the end of 10000 cycles using various PZ sections with E/s_u =800 and 100% of full train load

The wall height (H_E) above the base of excavation can affect dramatically on the results of the wall-soil system. Further, increasing the wall height, even when the wall embedment under the base of excavation is twice the wall height each case, can tend to increase generally the displacement of the system. Note the lateral deflection at wall top increases with increasing the wall height (Figure 4.21). In addition, the maximum wall moment and the lateral wall displacement along the wall depth in soil increase with increasing the wall height, as depicted in Figure 4.22 and Figure 4.23 respectively. While the maximum lateral soil pressure under the base of excavation for each case can decrease with increasing the wall height (H_E) of the system, as depicted in Figure 4.24.

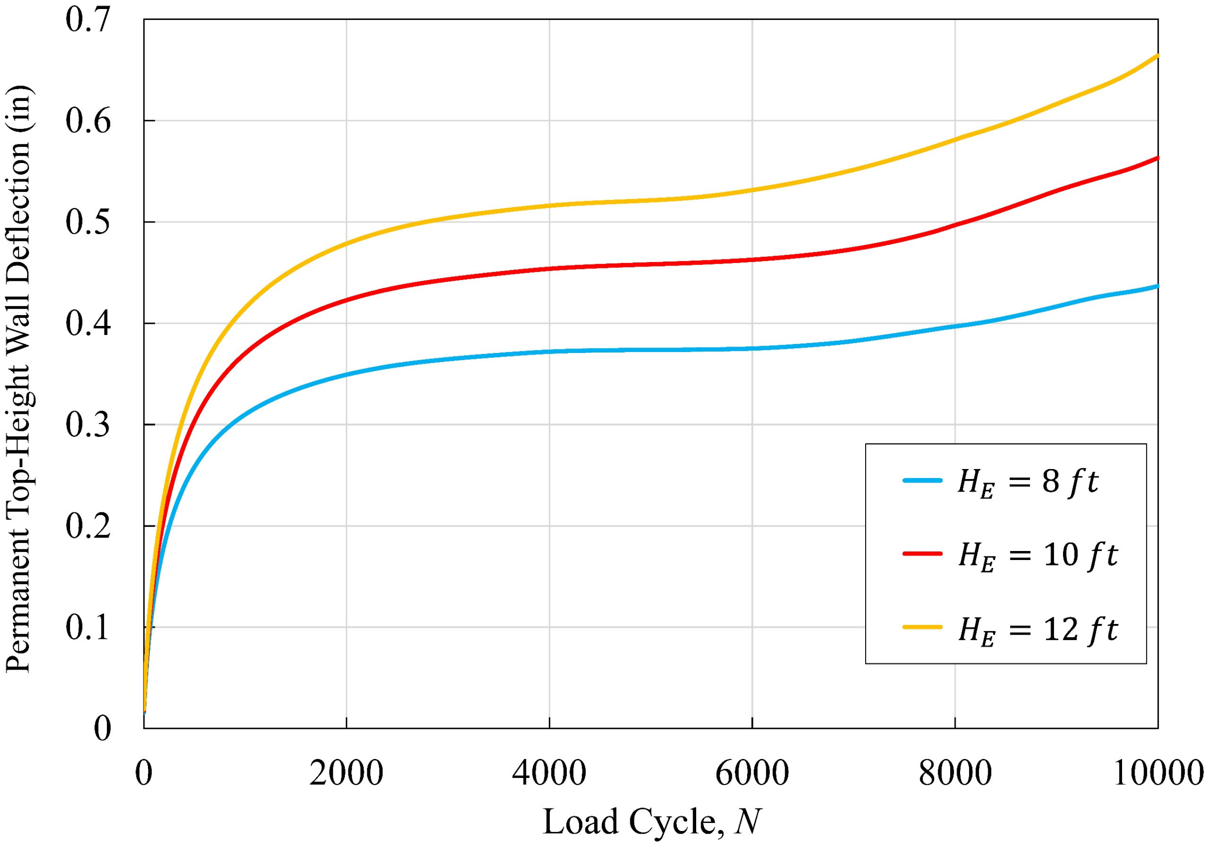

Figure 4.21. Permanent top-height lateral displacement of wall using various H_E with E/s_u =800 and 100% of full train load

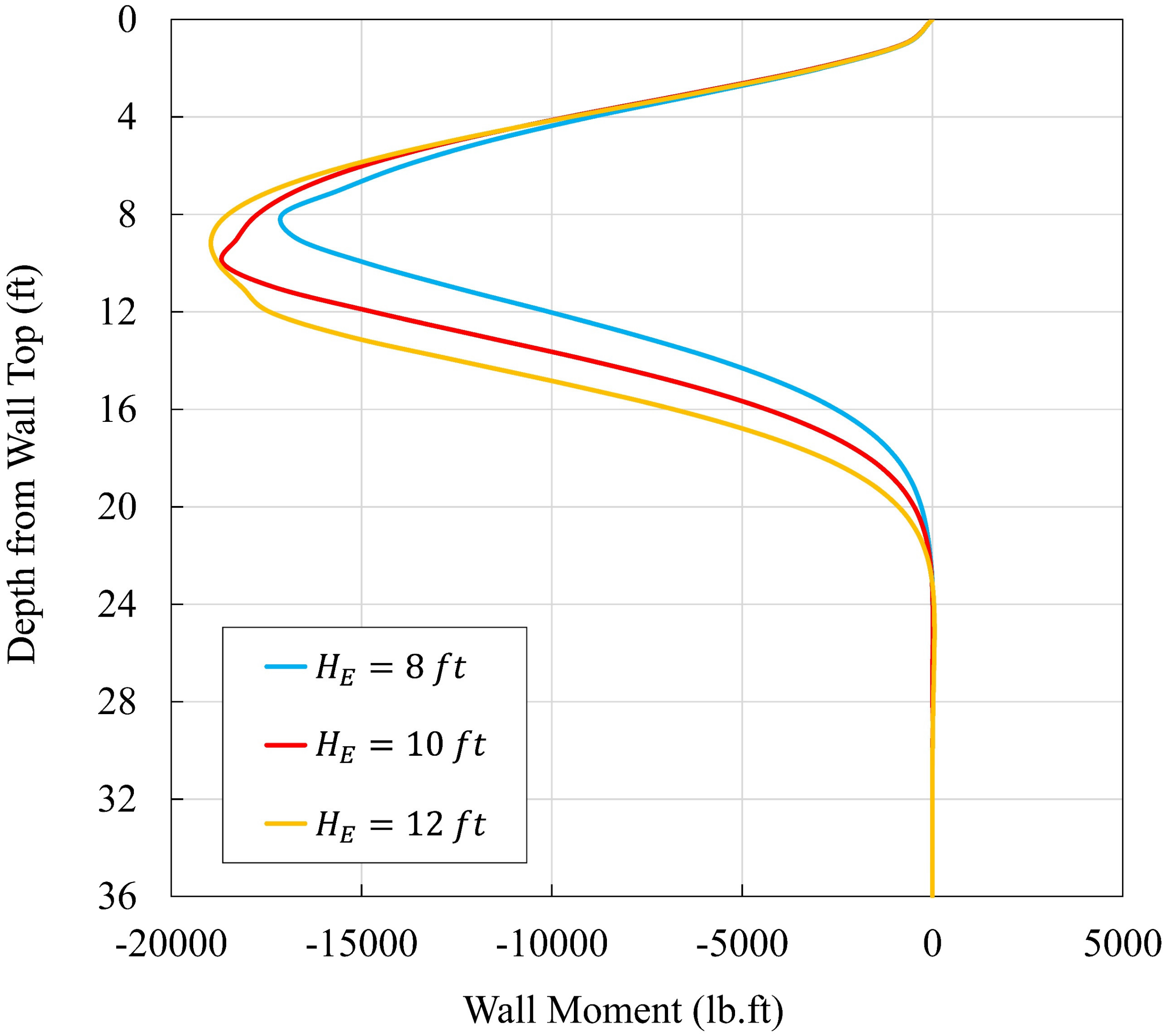

Figure 4.22. Bending moment along the wall depth in soil at the end of 10000 cycles using various H_E with E/s_u =800 and 100% of full train load

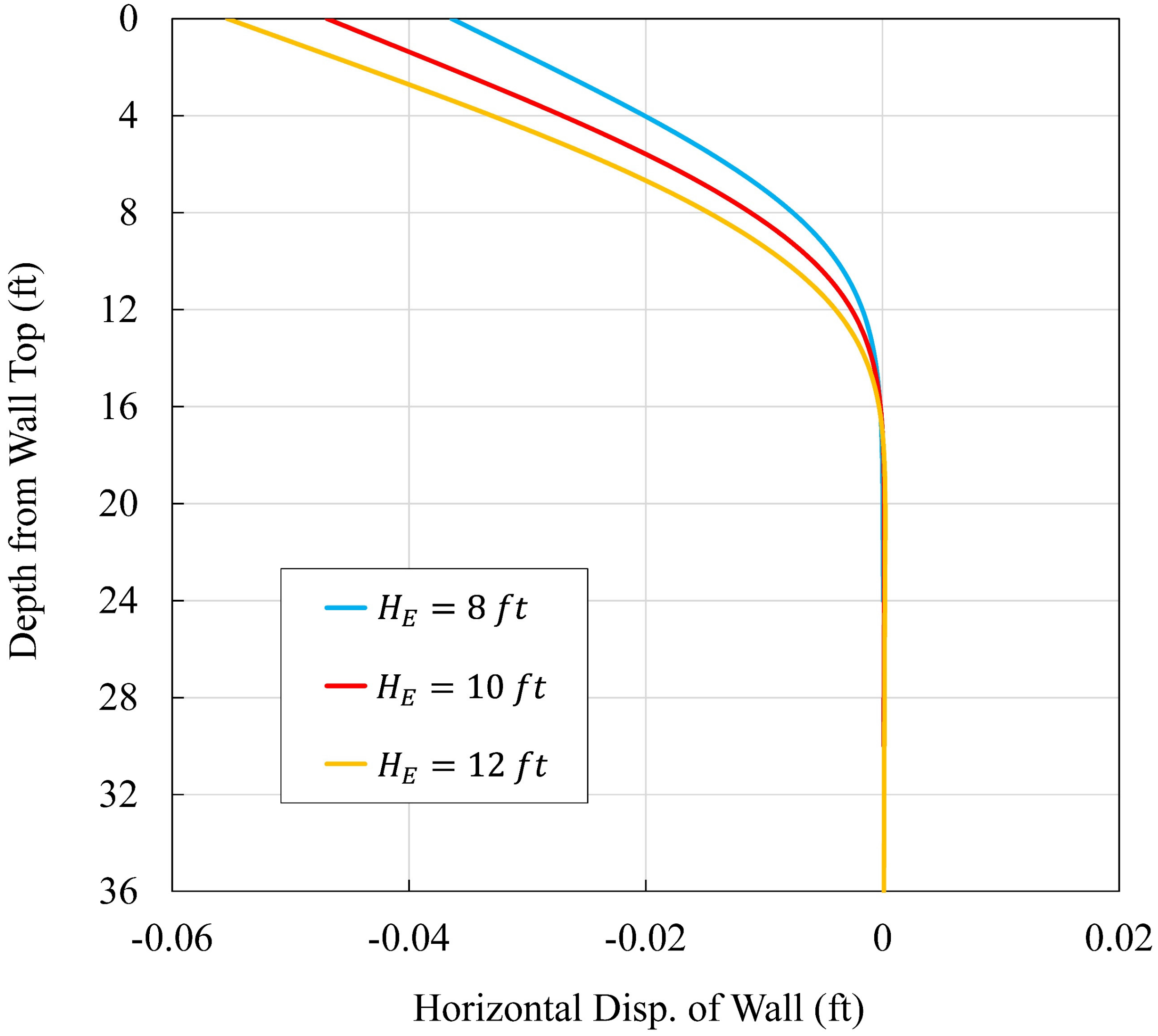

Figure 4.23. Horizontal displacement along the wall depth in soil at the end of 10000 cycles using various H_E with E/s_u =800 and 100% of full train load

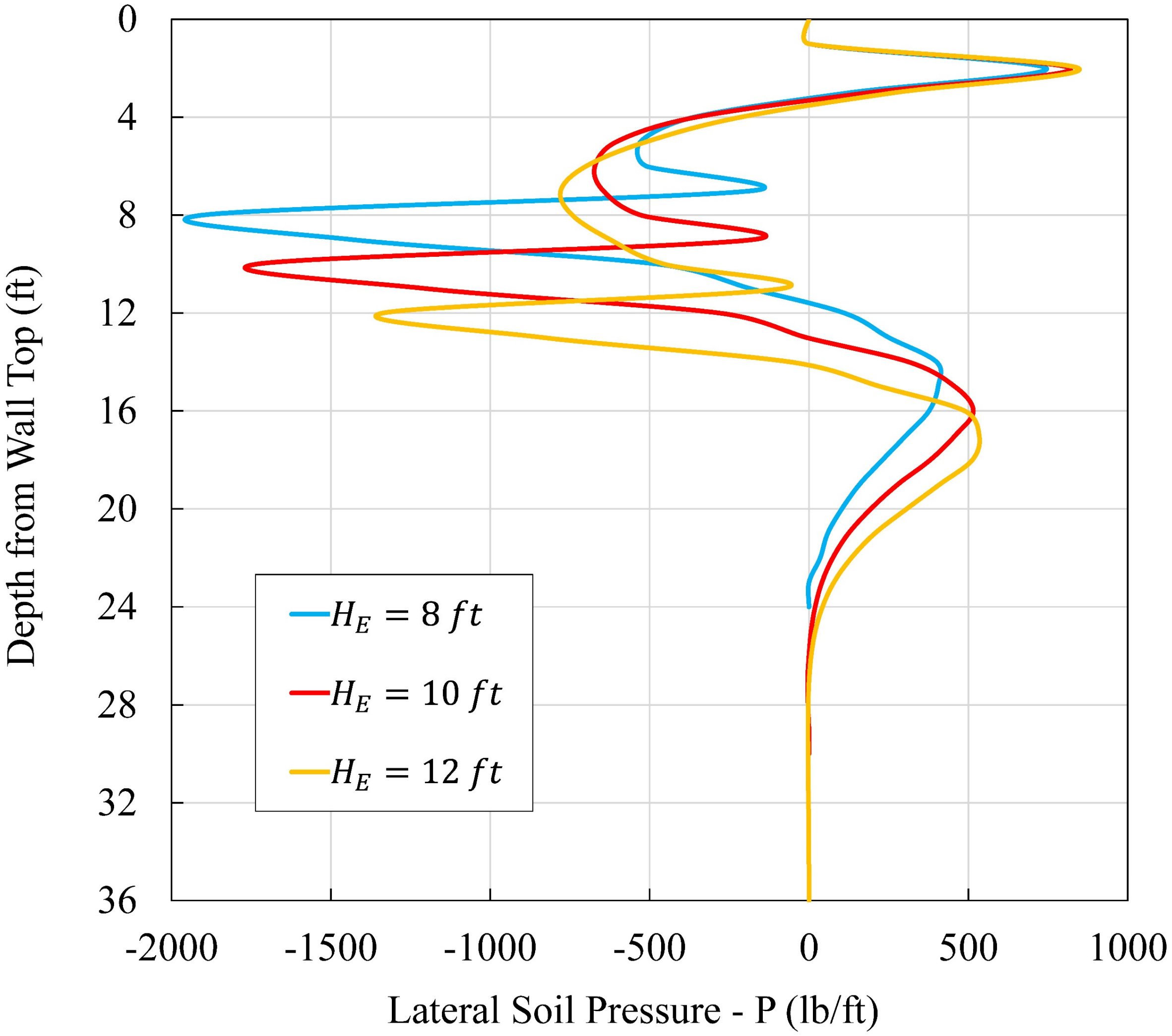

Figure 4.24. Lateral soil pressure along the wall depth in soil at the end of 10000 cycles using various H_E with E/s_u =800 and 100% of full train load

Increasing the distance ($Dist$) between the edge of train track and the top of wall can cause to decrease the lateral displacement and the bending moment along the wall depth in soil, as illustrated in Figure 4.25 and Figure 4.26 respectively. As well, from Figure 4.27, the lateral mid-height wall deflection decreased significantly as the distance ($Dist$) increased.

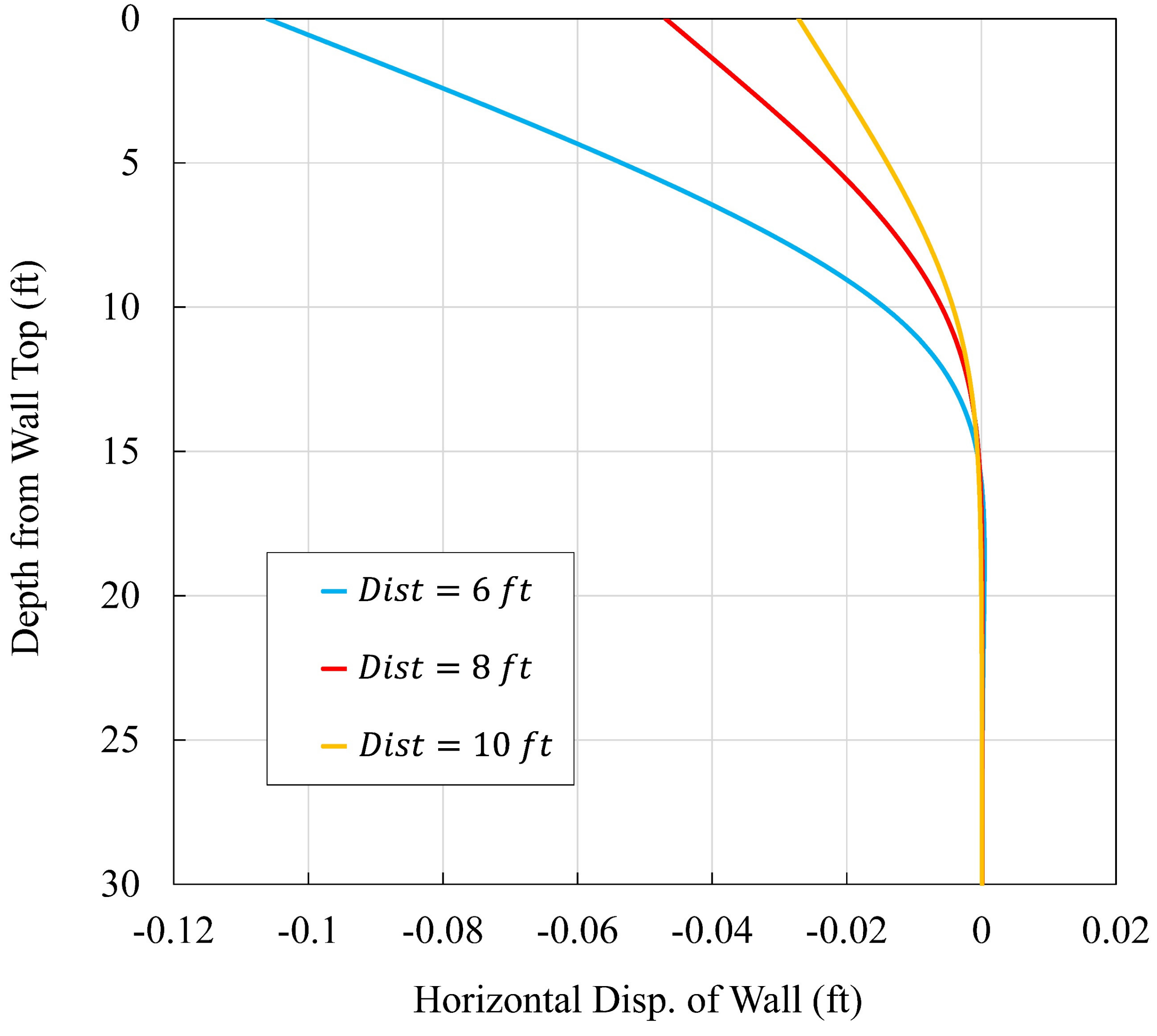

Figure 4.25. Horizontal displacement along the wall depth in soil at the end of 10000 cycles using various *Dist* with E/s_u =800 and 100% of full train load

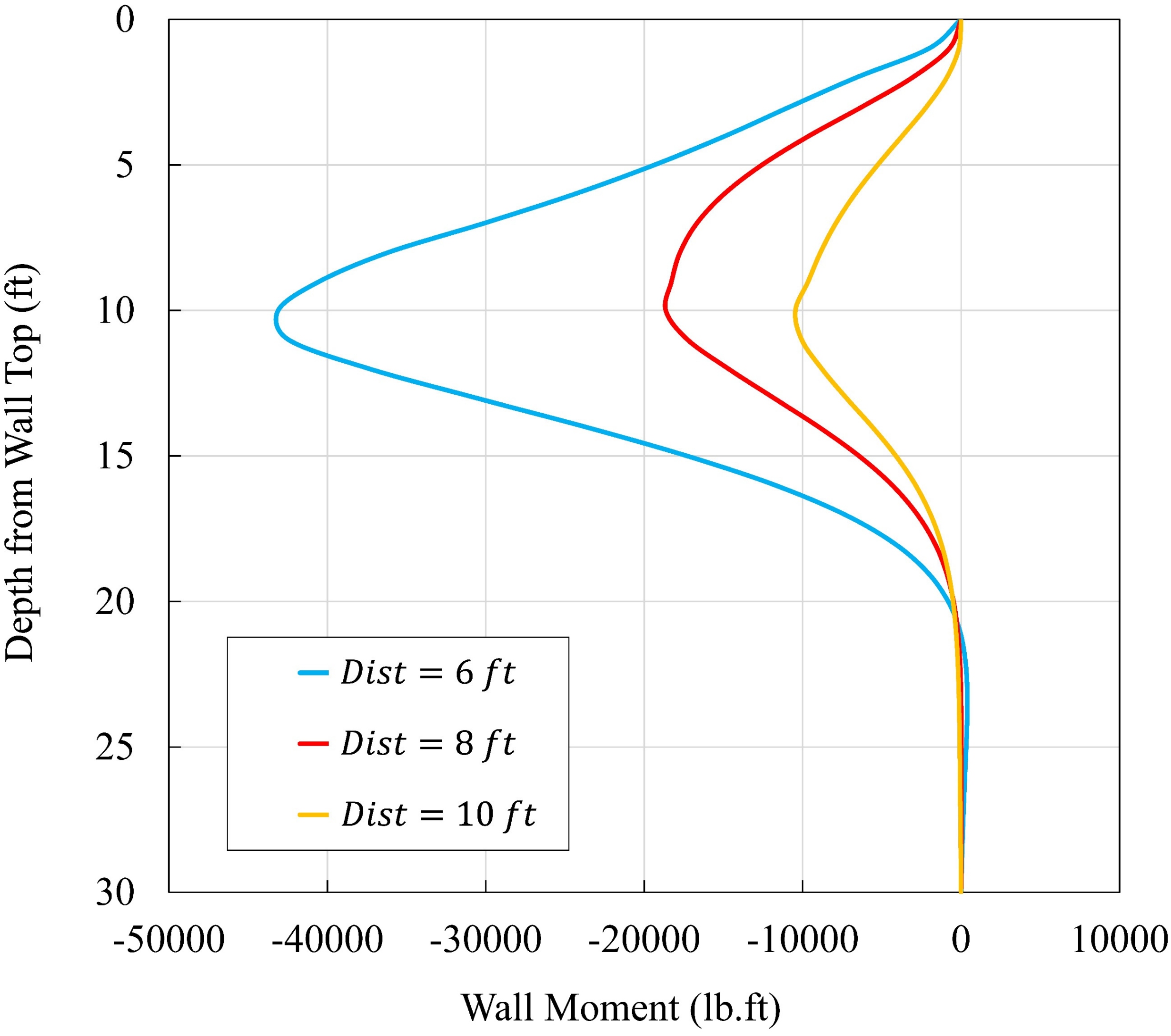

Figure 4.26. Bending moment along the wall depth in soil at the end of 10000 cycles using various *Dist* with E/s_u =800 and 100% of full train load

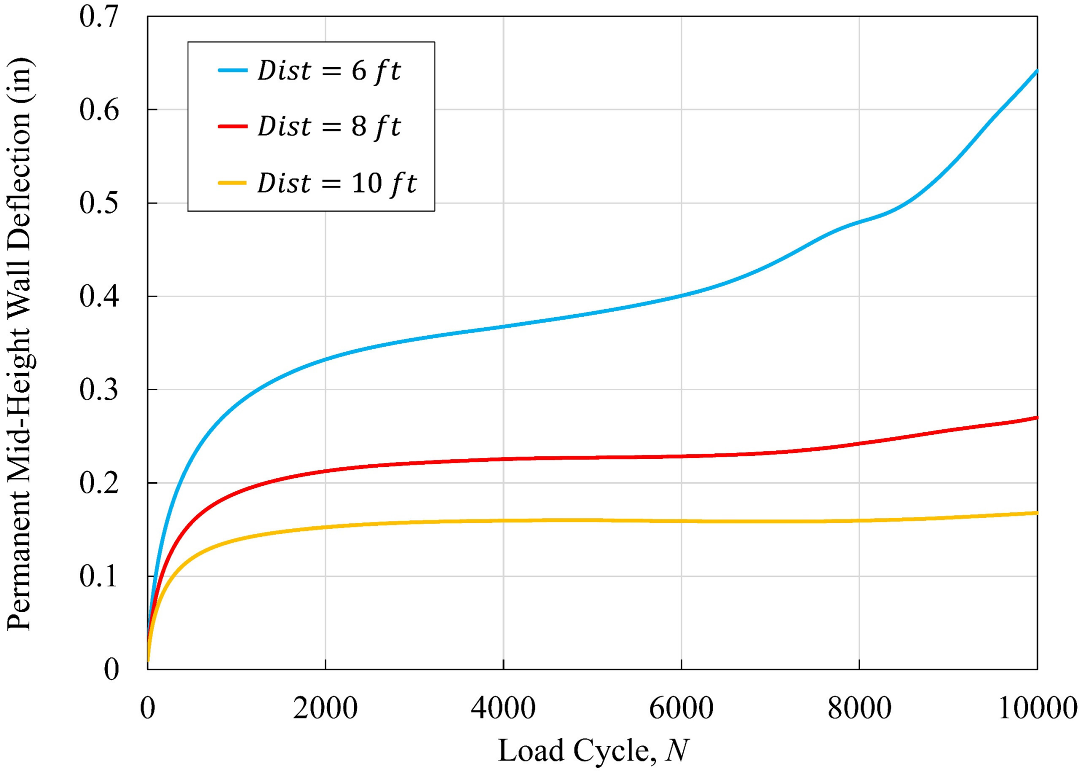

Figure 4.27. Permanent mid-height lateral displacement of wall using various *Dist* with *E/s$_u$* =800 and 100% of full train load

From Figure 4.28, Figure 4.29 and Figure 4.30 of plotting the permanent top-height lateral displacement of wall vs. the vertical settlement under center of train track using various E/s$_u$ ratio and different percentages of full train load, it can be observed that the relation between the lateral displacement at the top-height of wall and the vertical settlement under the center of the train track can be describes as a power law curve. While Figure 4.31 shows that the relation of displacements for load intensity = 95% of full train load does not converge with the power law curve. Thus, the following table (Table 4.1) gives the coefficients of the power equation (Eq. 10) that can satisfy the power curve with the data of displacements.

$$y = (a\,x^{b} + c) \qquad (10)$$

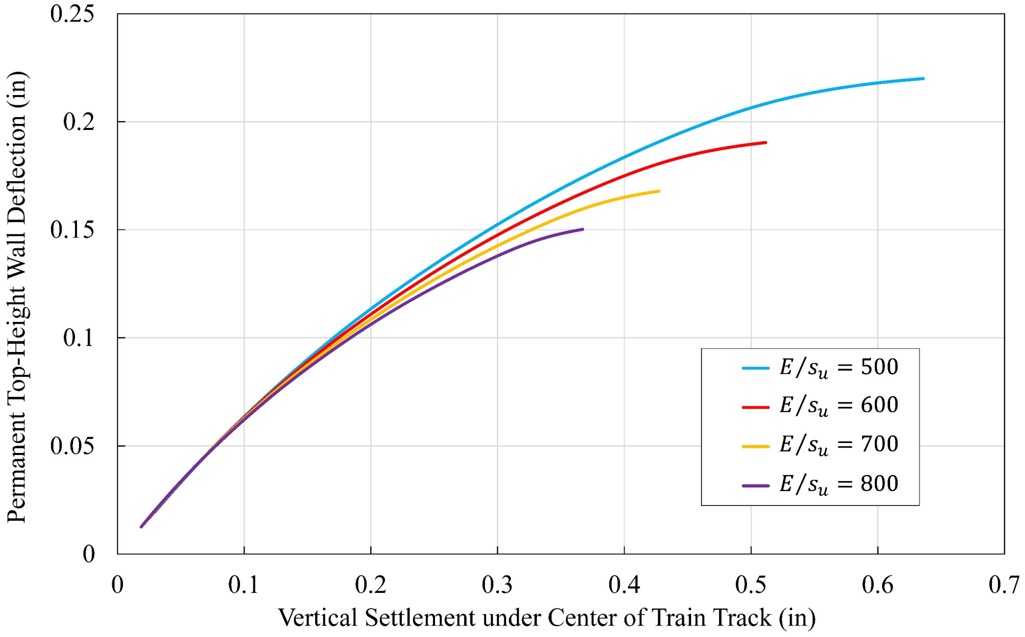

Figure 4.28. Permanent top-height lateral displacement of wall vs. vertical settlement under train track with various *E/s_u* ratio and 80% of full train load

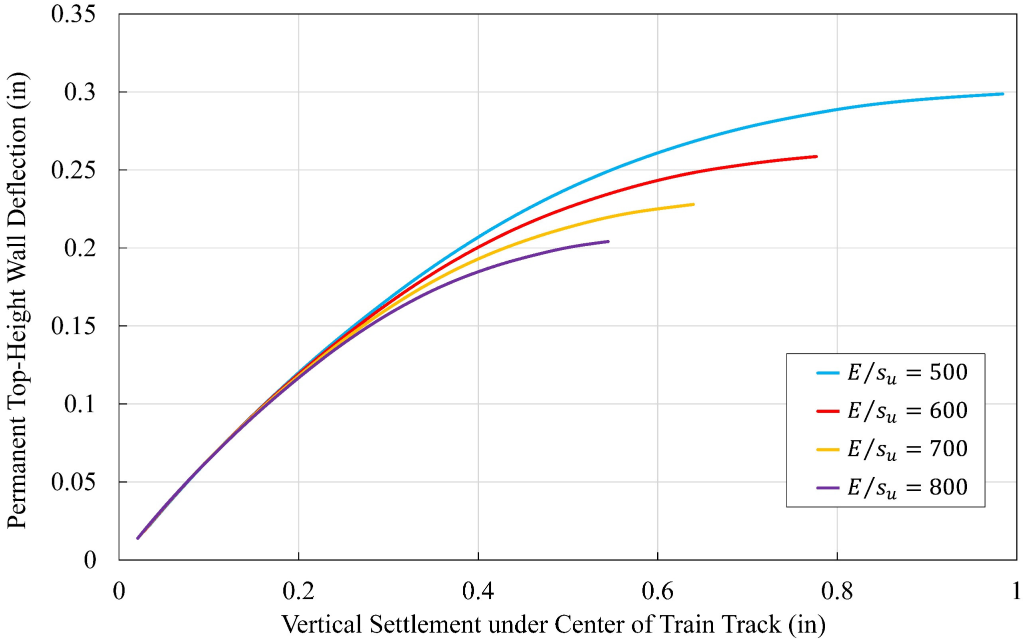

Figure 4.29. Permanent top-height lateral displacement of wall vs. vertical settlement under train track with various *E/s_u* ratio and 85% of full train load

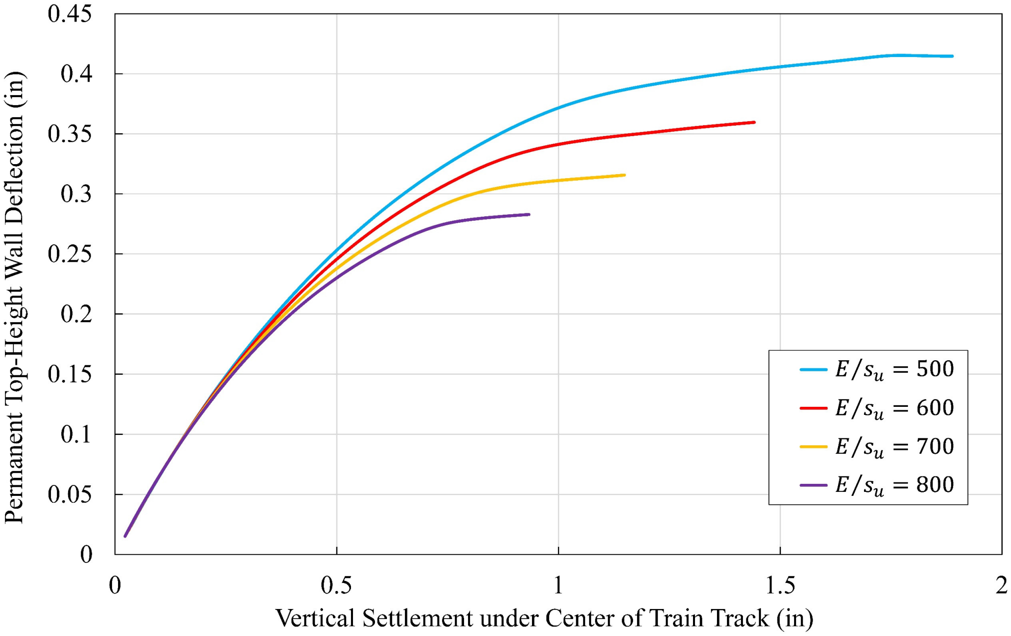

Figure 4.30. Permanent top-height lateral displacement of wall vs. vertical settlement under train track with various E/s_u ratio and 90% of full train load

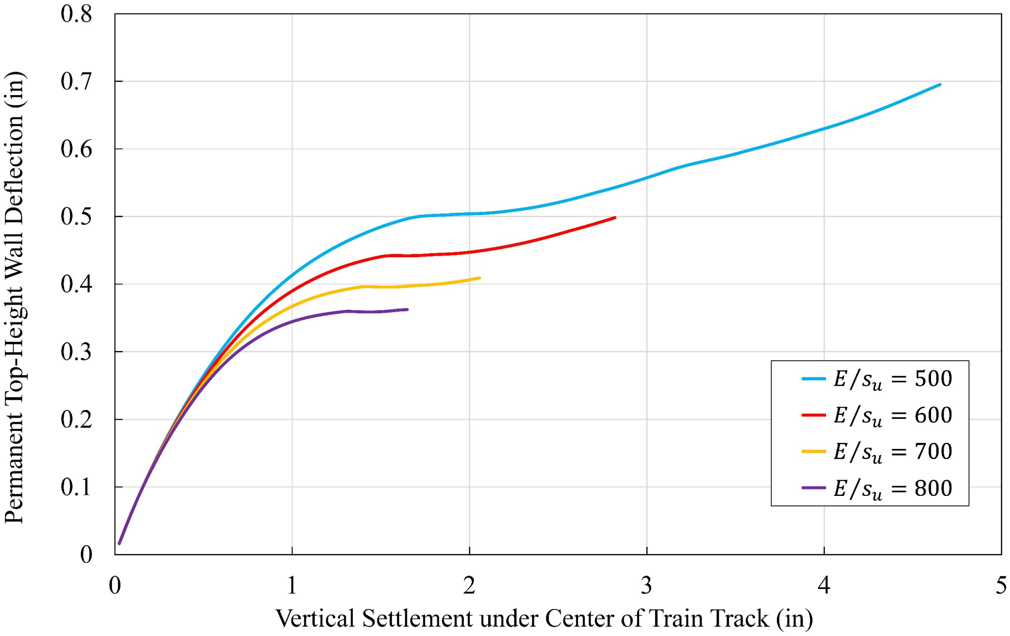

Figure 4.31. Permanent top-height lateral displacement of wall vs. vertical settlement under train track with various E/s_u ratio and 95% of full train load

Table 4.1. Coefficients of power law fitted curve for various *E/s*$_u$ ratio and

a) 80% of full train load

Case	a	b	c
$E/s_u = 500$	0.8718	0.1162	-0.6016
$E/s_u = 600$	0.5112	0.2074	-0.2503
$E/s_u = 700$	0.4004	0.2765	-0.1456
$E/s_u = 800$	0.3494	0.3282	-0.0989

b) 85% of full train load

Case	a	b	c
$E/s_u = 500$	-2.2826	-0.0444	2.5905
$E/s_u = 600$	0.3174	0.5856	0.0
$E/s_u = 700$	1.2915	0.0741	-1.0173
$E/s_u = 800$	0.8119	0.1164	-0.5487

c) 90% of full train load

Case	a	b	c
$E/s_u = 500$	-0.7405	-0.1568	1.1011
$E/s_u = 600$	-0.9222	-0.1141	1.2557
$E/s_u = 700$	-1.7638	-0.0573	2.0776
$E/s_u = 800$	2.9660	0.0354	-2.6644

4.2 Caisson Problem

After choosing the allowable applied force control (Table 3.2) that should be applied at the padeye of the suction caisson of the soil-caisson system for each case depends on its load angle. Parametric studies were undertaken to study the influences of soil strength parameters, cycle load amplitude, and inclination angle of load. In addition to the series of parametric studies, two types of cyclic loading amplitudes were conducted. Firstly, the peak amplitude for each cycle was consistent (Figure 4.32) and the second type was a random peak amplitude for each cycle (Figure 4.33).

The following parameters were considered in this parametric study:

- The soil stiffness was implemented by the E/s_u ratio with a range of (200-900).
- The value of (σ_0/σ_{max}) ratio was ranged between 0.05 and 0.15.
- The adhesion factor (α) was carried from 0.7 to 1.0 for the soil-caisson interface along the wall of caisson.
- The inclined angle of load (ψ) was opted between 0° and 45°.
- Cycle load amplitude.

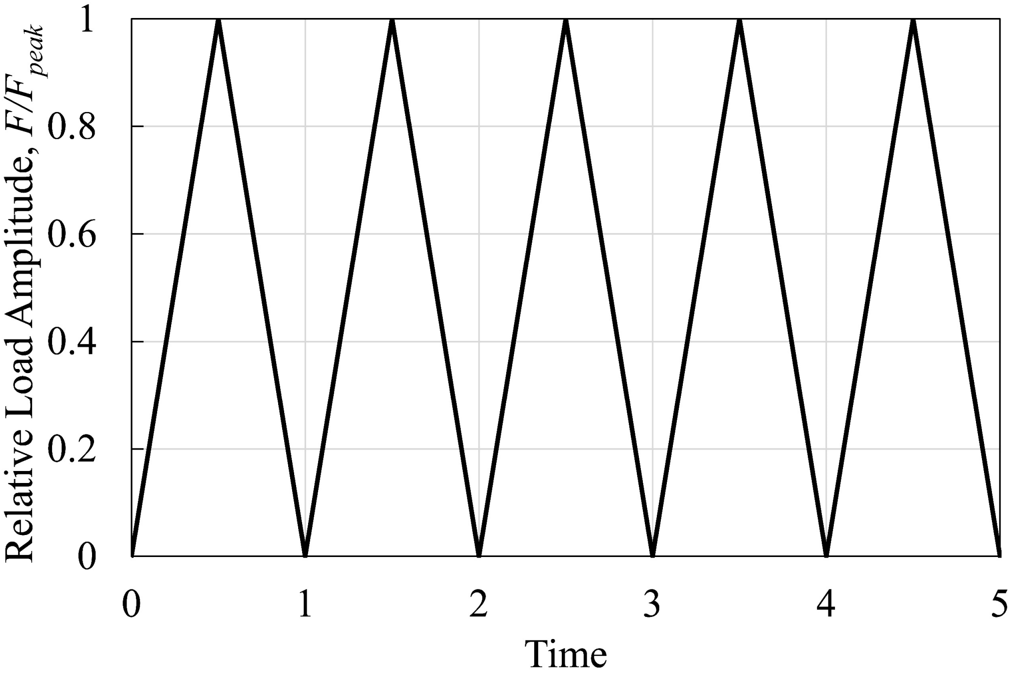

Figure 4.32. Consistent cyclic loading (e.g. 5 cycles)

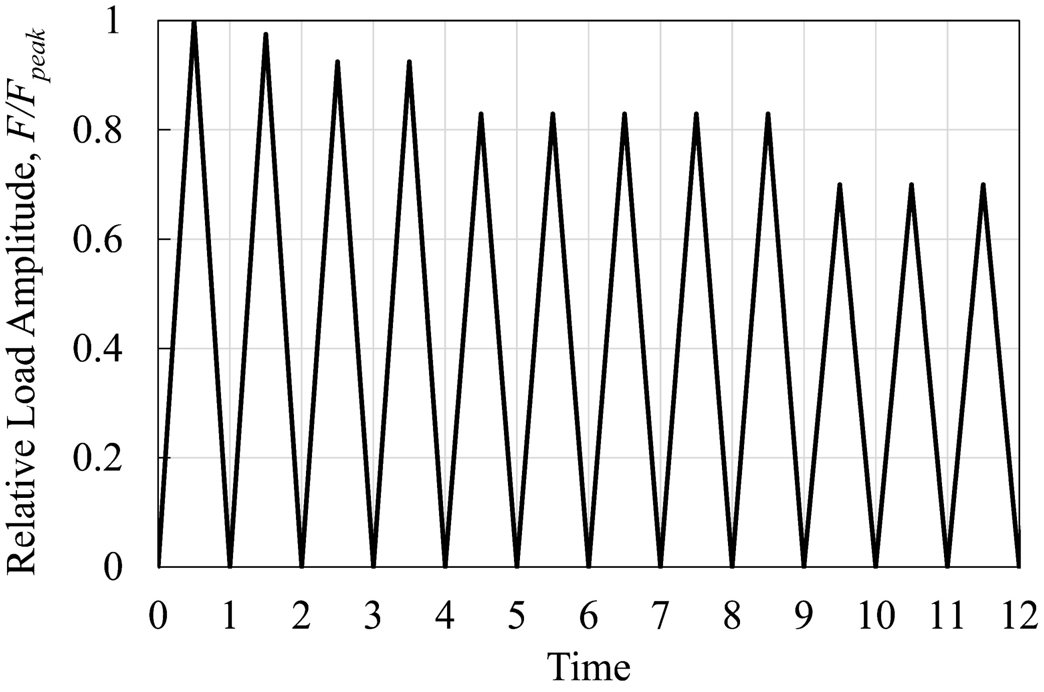

Figure 4.33. Random cyclic loading (e.g. 12 cycles)

Analyzing the soil-caisson system with 100 cycles of uniform cyclic amplitudes for various ratio of E/s_u equals to a range of 200 to 900 and essentially with an inclined angle (ψ) equals to 15° and adhesion factor (α) of soil near the wall of caisson equals to 1.0, it can be observed that the resultant displacements at the padeye of the caisson would tend to decrease with increasing the E/s_u ratio of the soil (Figure 4.34). In addition, the trajectory of caisson wall movement would decrease with increasing the initial soil modulus (Figure 4.35).

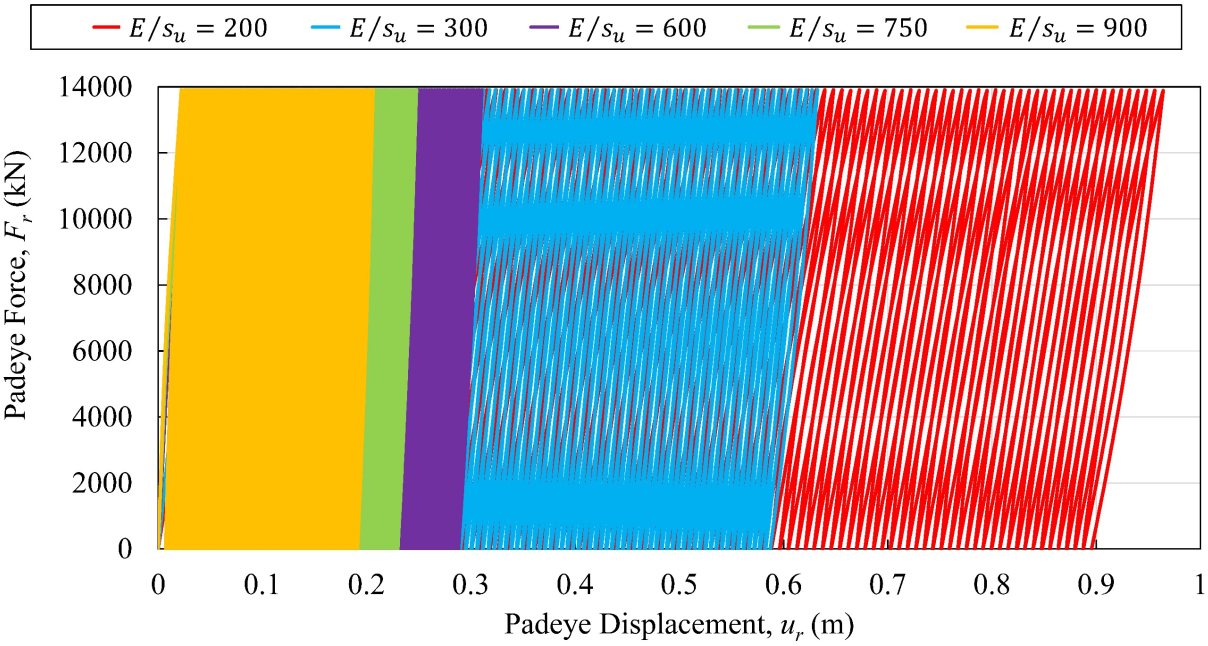

Figure 4.34. Ratcheting behavior in load direction at the padeye for 100 cycles with various E/s_u ratio, $\psi = 15^{o}$, and $\alpha = 1.0$

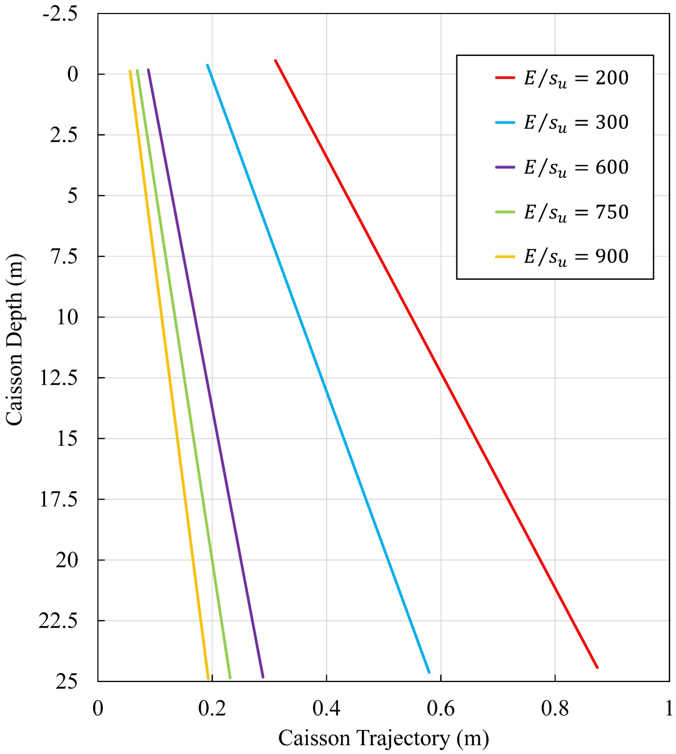

Figure 4.35. Trajectory of caisson movement at the end of 100 cycles for various E/s_u ratio, $\psi = 15^{o}$, and $\alpha = 1.0$

From plotting the soil pressure distributions at the end of 10, 50, and 100 cycles along the depth of the caisson for a range of E/s_u from 200 to 900 with the system case of an inclined angle (ψ) equals to 15° and adhesion factor (α) of soil near the wall of caisson equals to 1.0 as shown in Figure 4.36, Figure 4.37, and Figure 4.38 respectively. It can be noticed that there is a little difference in the lateral soil pressure along the embedment depth of caisson at the early cycles where the soil pressure distribution in the lower portion of caisson depth decreases with increasing the soil stiffness, and then this difference will decrease significantly after the 50th cycle and the 100th cycle.

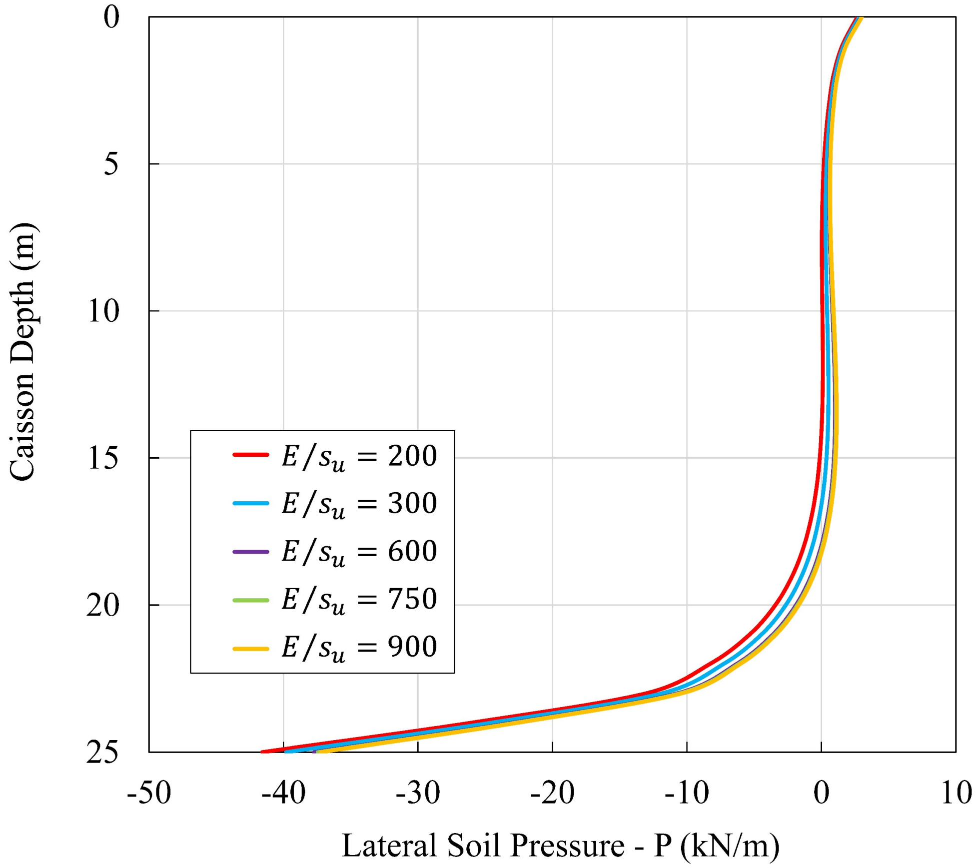

Figure 4.36. Lateral soil pressure along the embedment depth of caisson at the end of 10 cycles for various E/s_u ratio, ψ = 15°, and α = 1.0

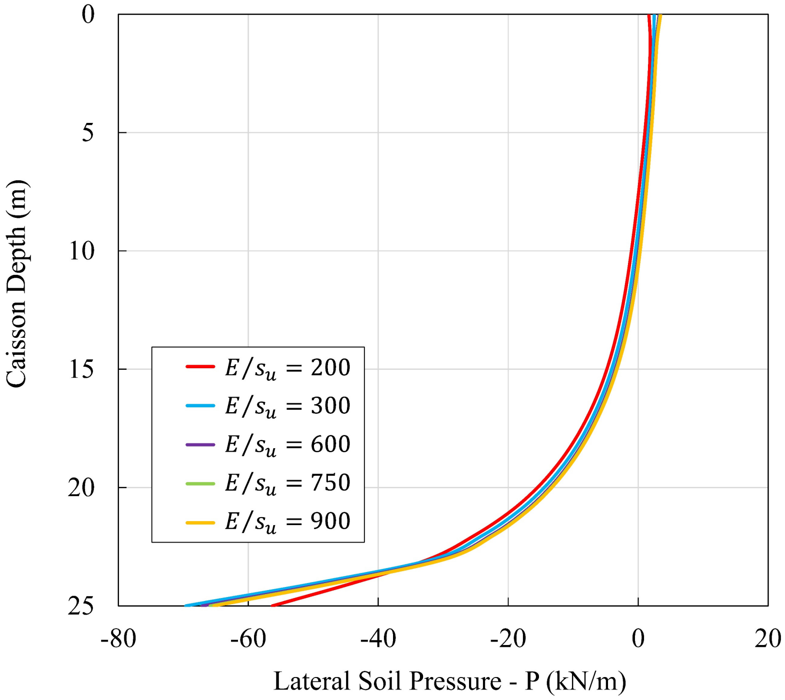

Figure 4.37. Lateral soil pressure along the embedment depth of caisson at the end of 50 cycles for various E/s_u ratio, $\psi = 15^o$, and $\alpha = 1.0$

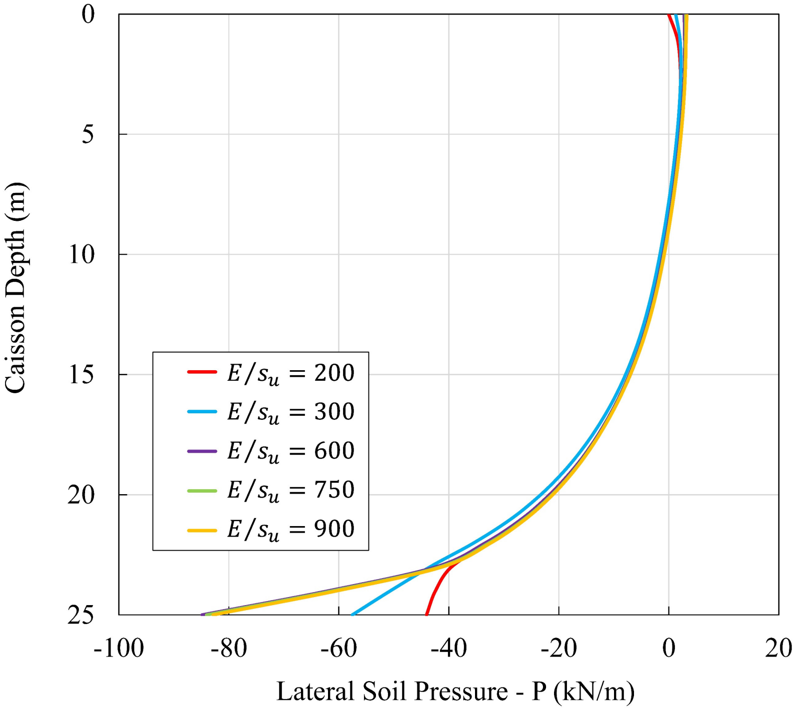

Figure 4.38. Lateral soil pressure along the embedment depth of caisson at the end of 100 cycles for various E/s_u ratio, $\psi = 15^o$, and $\alpha = 1.0$

Additionally, the circumferential bending moment in the caisson shell for the same case, which mentioned before, show similar behavior of differences in the moment values at the end of the 10th cycle and gradually decrease with increasing the number of cycles, as shown in Figure 4.39 and Figure 4.40.

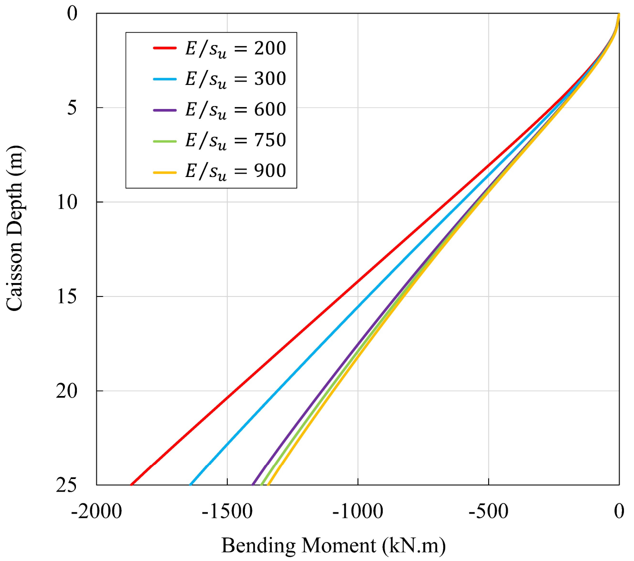

Figure 4.39. Bending moment along the embedment depth of caisson at the end of 10 cycles for various E/s_u ratio, $\psi = 15^o$, and $\alpha = 1.0$

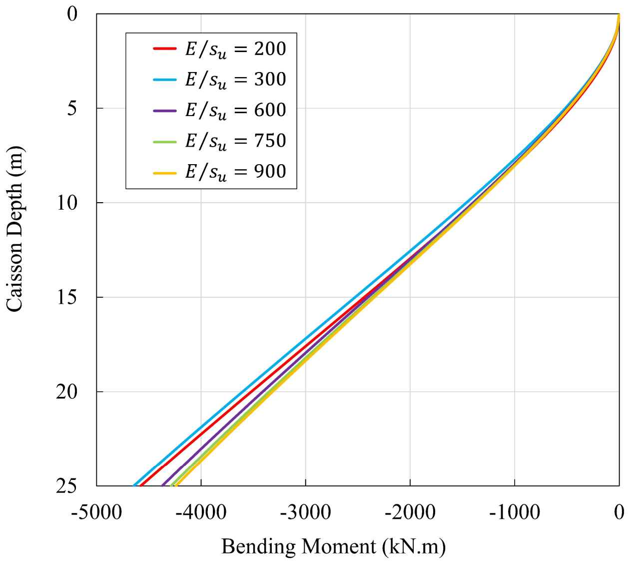

Figure 4.40. Bending moment along the embedment depth of caisson at the end of 50 cycles for various E/s_u ratio, $\psi = 15^o$, and $\alpha = 1.0$

Furthermore, Figure 4.41, Figure 4.42, and Figure 4.43 show the plotting of the lateral soil pressure distribution along the embedment depth of caisson of the end of subsequent cycles as 10, 25, 50, and 100 for the same E/s_u ratio of 300, 600, and 900 with an inclined angle (ψ) equals to 15° and adhesion factor (α) equals to 1.0. It can be observed that the soil pressure will increase with increasing the number of cycles. Although, the difference in the soil pressure distributions gradually decreases for the succeeding cycles.

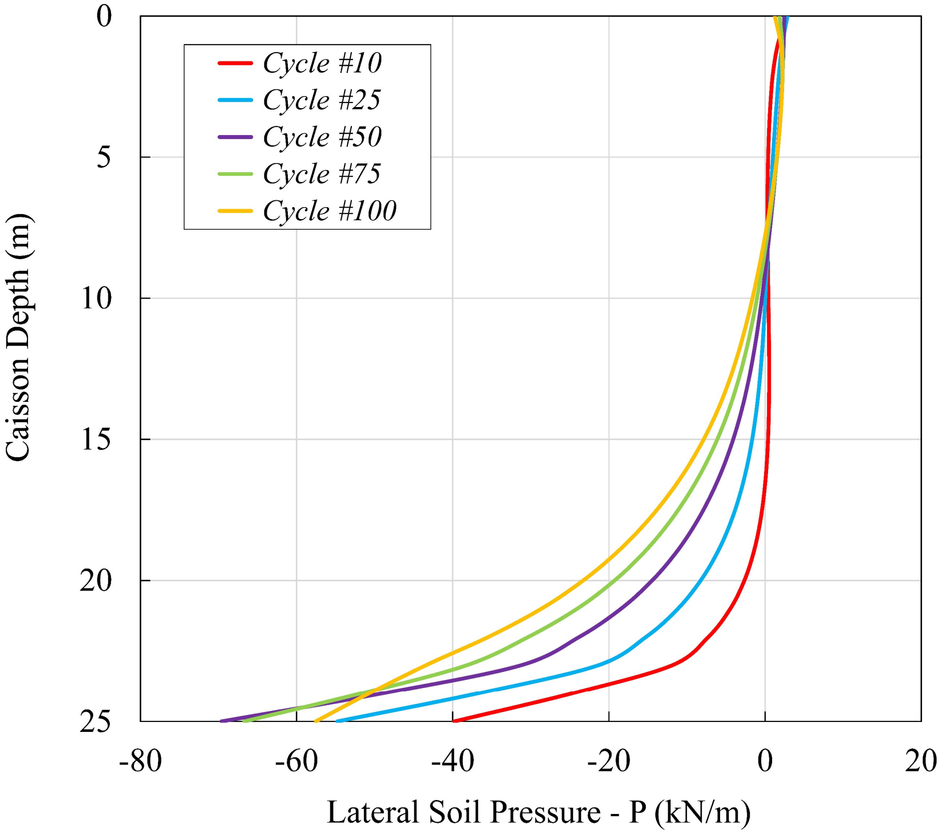

Figure 4.41. Lateral soil pressure along the embedment depth of caisson at the end of subsequent cycles for $E/s_u = 300$, $\psi = 15^{o}$, and $\alpha = 1.0$

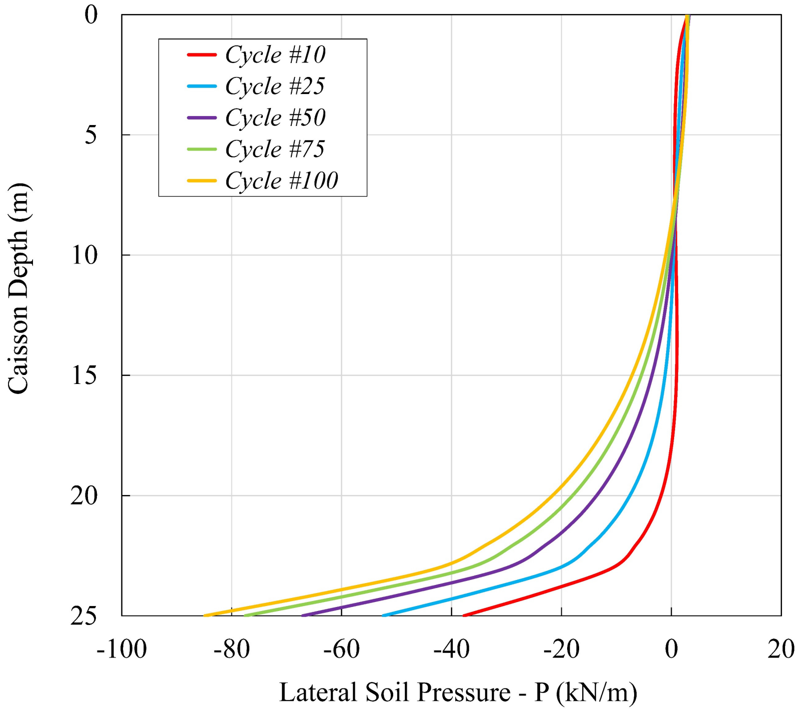

Figure 4.42. Lateral soil pressure along the embedment depth of caisson at the end of subsequent cycles for E/s_u = 600, ψ = 15°, and α = 1.0

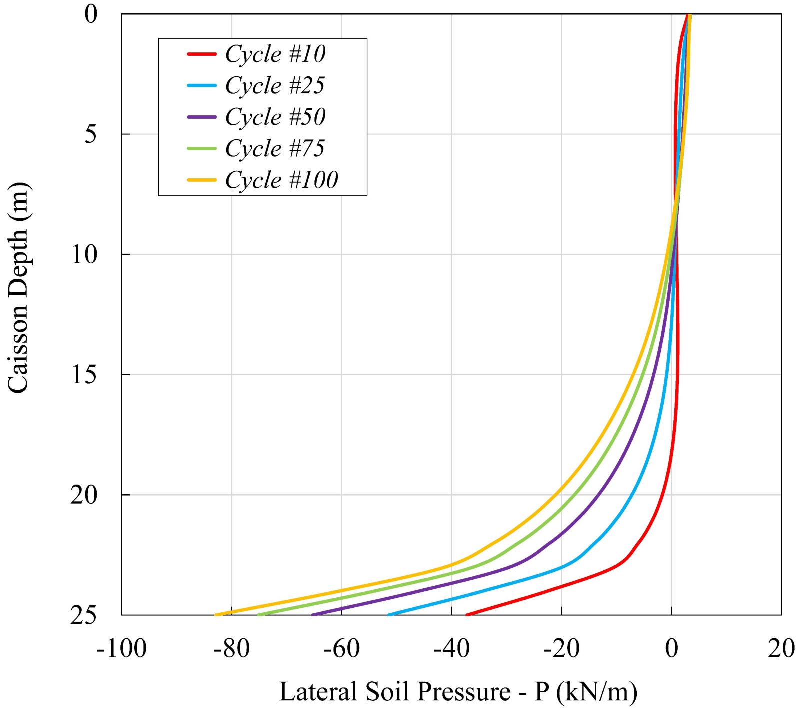

Figure 4.43. Lateral soil pressure along the embedment depth of caisson at the end of subsequent cycles for E/s_u = 900, ψ = 15°, and α = 1.0

Clearly, Figure 4.44 and Figure 4.45 show the predicted effects of soil stiffness on cumulative displacements, considering a range of E/s_u from 200 to 900. All predictions are for an initial yield stress ratio σ_0/σ_{max} = 0.1, a load angle ψ = 15° and an adhesion factor α = 1.0. The u_r-N curve is slightly nonlinear for $N < 20$ and nearly linear at greater numbers of cycles. The predictions show the selected stiffness to have a strong influence on both displacement and tilt, with an order of magnitude reduction in stiffness, reducing E/s_u from 900 to 200, leading to roughly an order of magnitude increase in displacement and rotation.

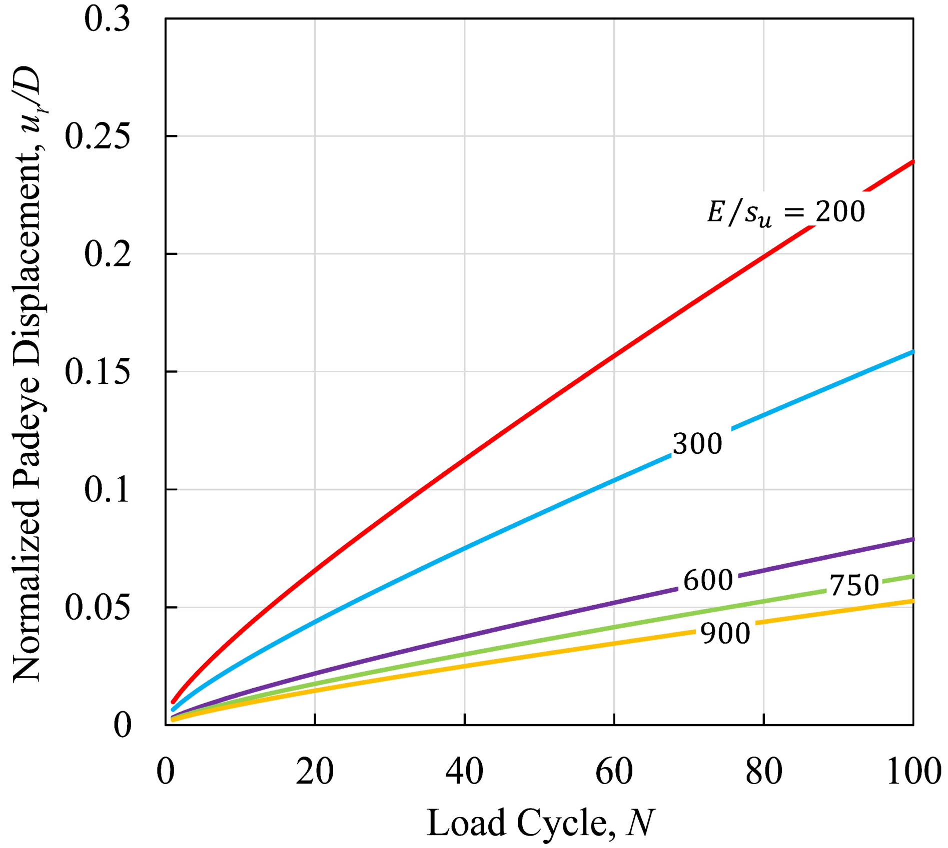

Figure 4.44. Effect of small strain stiffness E/s_u on caisson displacement for 100 cycles

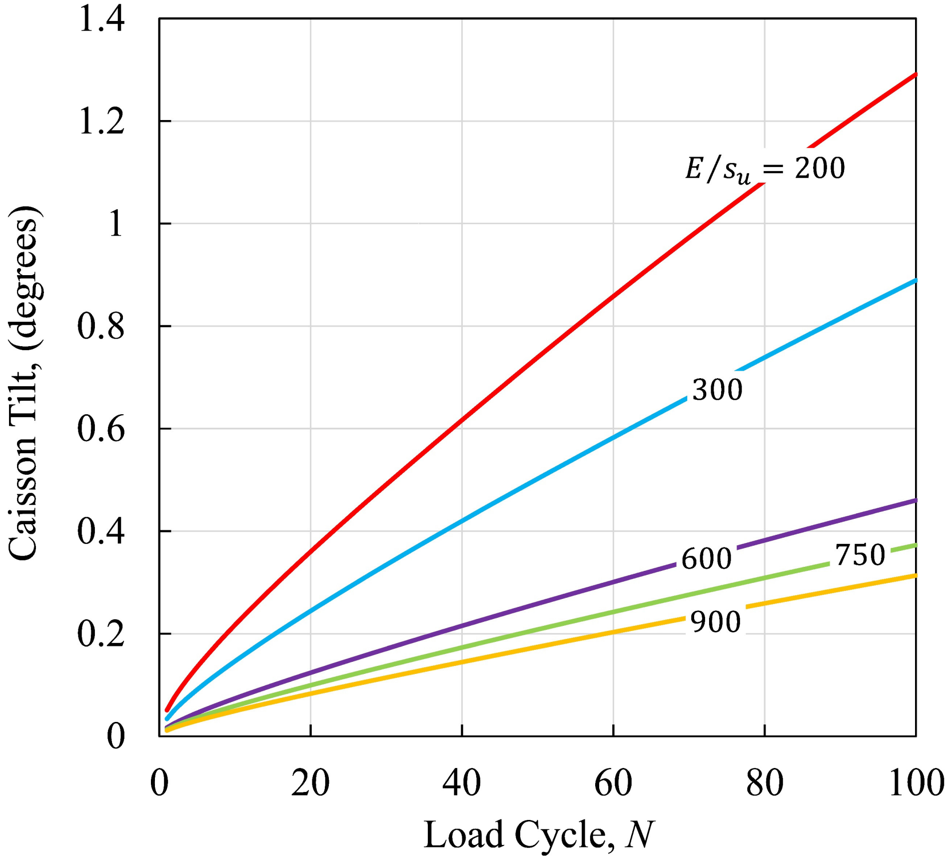

Figure 4.45. Effect of small strain stiffness *E/s_u* on caisson tilt for 100 cycles

The significant parameter that can affect seriously to the behavior of caisson under cyclic loads is the yield stress (σ_0/σ_{max}) ratio. Decreasing this ratio can increase dramatically the deformations of soil-caisson system. For instance, analyzing the system with 100 cycles of consistent cyclic amplitudes for various (σ_0/σ_{max}) ratio with E/s_u ratio equals to 600, an inclined angle (ψ) equals to 15°, and an adhesion factor (α) of soil equals to 0.7. The horizontal displacement at the padeye of the caisson clearly increases with decreasing yield stress ratio (Figure 4.46). The same trend exists for the vertical displacement at the padeye (Figure 4.47). The trajectory of caisson (Figure 4.48) depicts clearly that the movements and tilt of caisson increase with decreasing yield stress (σ_0/σ_{max}) ratio.

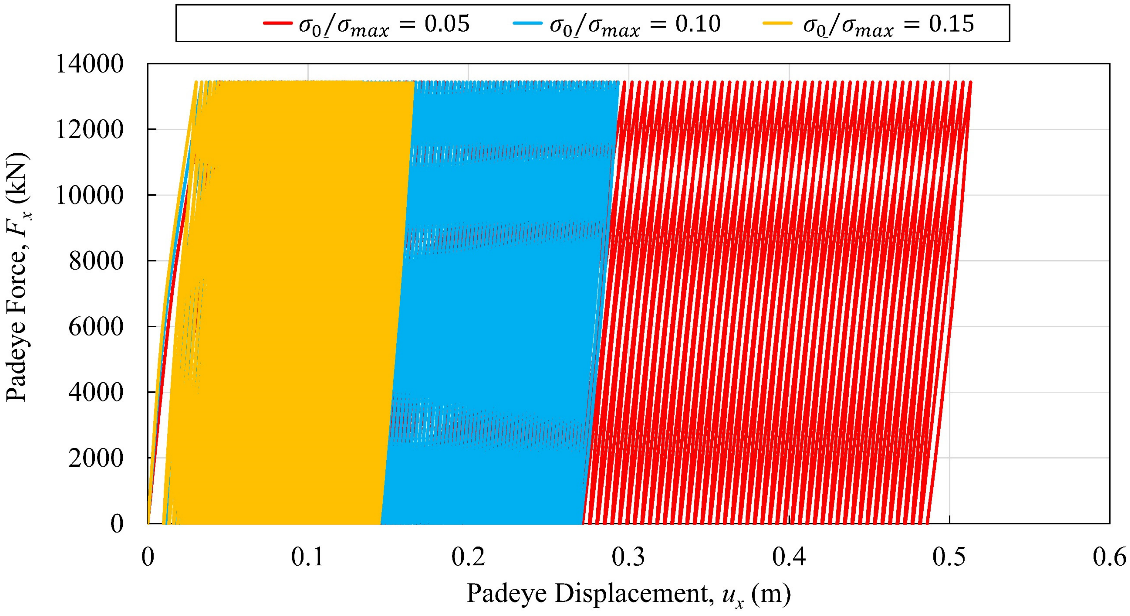

Figure 4.46. Ratcheting behavior in horizontal direction at the padeye for 100 cycles with various σ_0/σ_{max} ratio

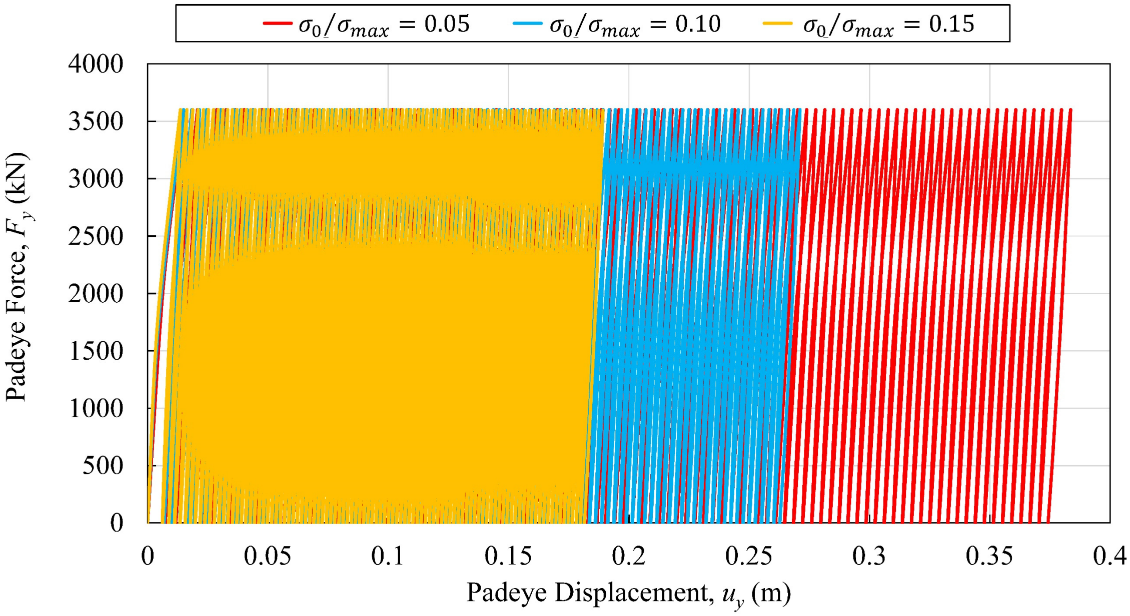

Figure 4.47. Ratcheting behavior in vertical direction at the padeye for 100 cycles with various σ_0/σ_{max} ratio

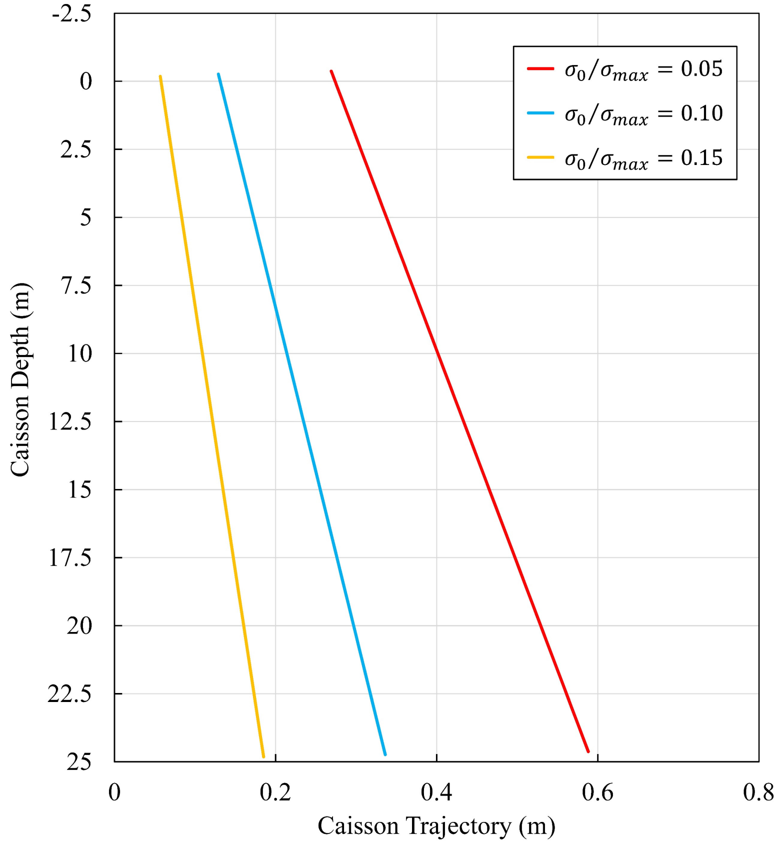

Figure 4.48. Trajectory of caisson movement at the end of 100 cycles for various σ_0/σ_{max} ratio

Furthermore, Figure 4.49 and Figure 4.50 show the predicted effects of initial yield on cumulative horizontal and vertical displacements respectively, considering a range of σ_0/σ_{max} = 0.05 to 0.15. All predictions are for a stiffness E/s_u = 600, a load angle ψ = 15° and an adhesion factor α = 0.7.

Figure 4.51 shows the pile tilts for associated with the predicted padeye displacements. Again, displacements and rotations are highly sensitive to the initial yield stress, with a threefold decrease in σ_0/σ_{max} increasing displacements and rotations by a factor of 2-3.

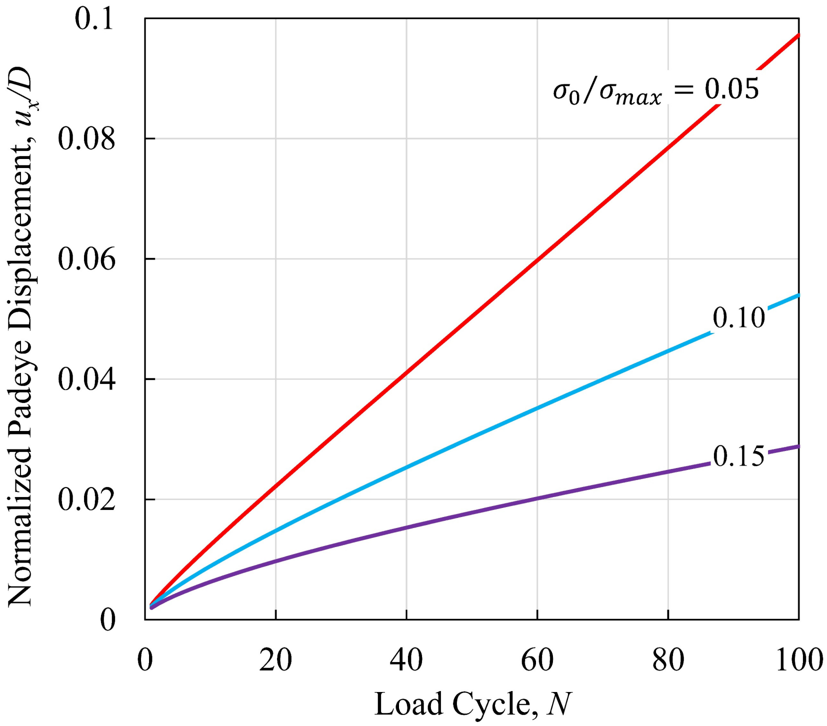

Figure 4.49. Effect of yield stress σ_0/σ_{max} ratio on horizontal permanent padeye displacement

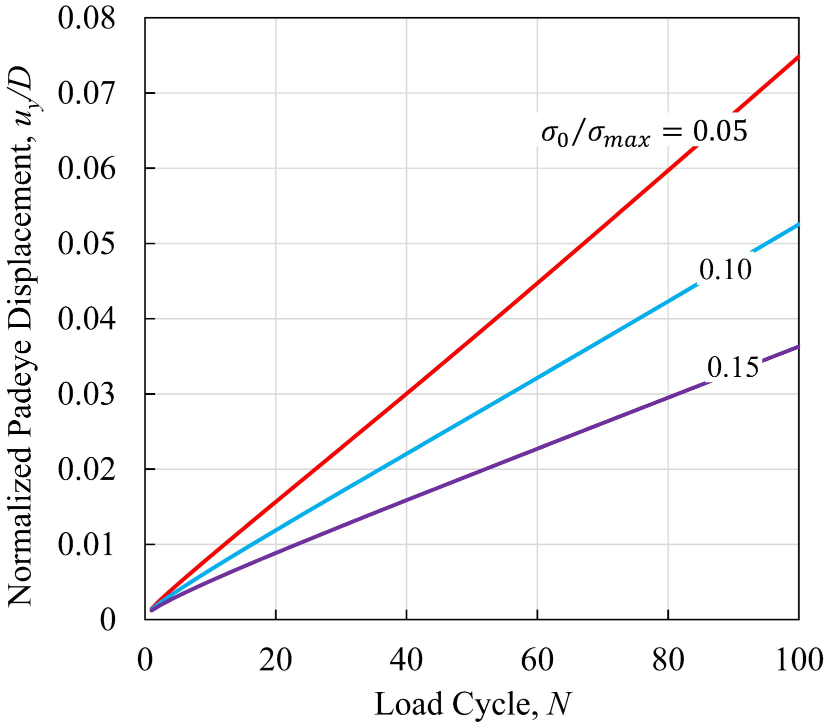

Figure 4.50. Effect of yield stress σ_0/σ_{max} ratio on vertical permanent padeye displacement

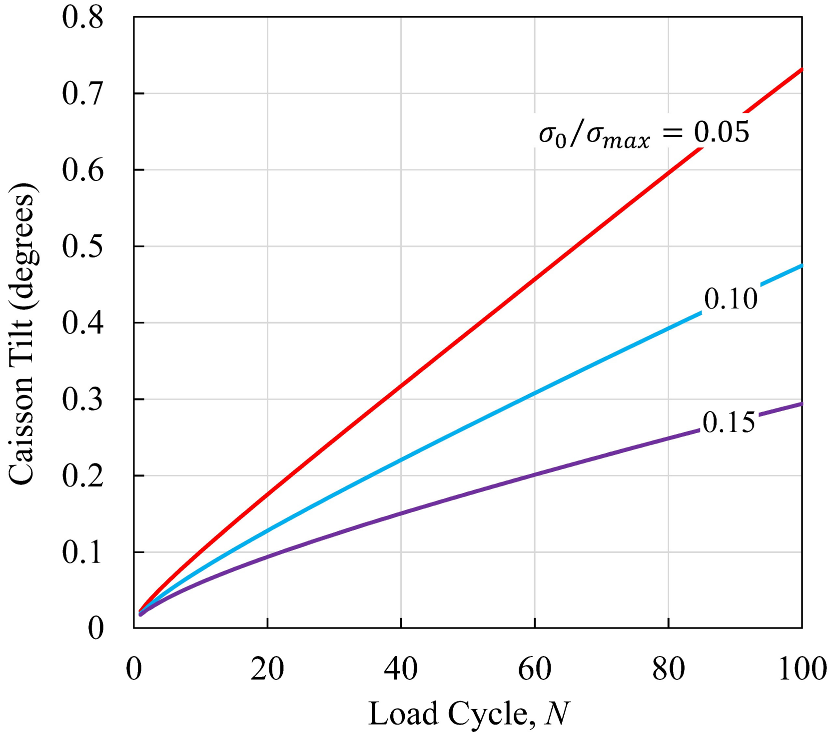

Figure 4.51. Effect of yield stress σ_0/σ_{max} ratio on permanent caisson tilt

Another important parameter for the caisson design is the adhesion factor (α) of soil along the wall of caisson. Analyzing the soil-caisson system with 100 cycles of consistent cyclic amplitudes for various adhesion factor (α) of soil with E/s_u ratio equals to 600, and inclined angles (ψ) equal to 15º and 30º. For the case with ψ=15º (Figure 4.52) and the case with ψ=30º (Figure 4.53), it can be illustrated that the deformations at padeye increase with decreasing the adhesion factor along the wall of caisson.

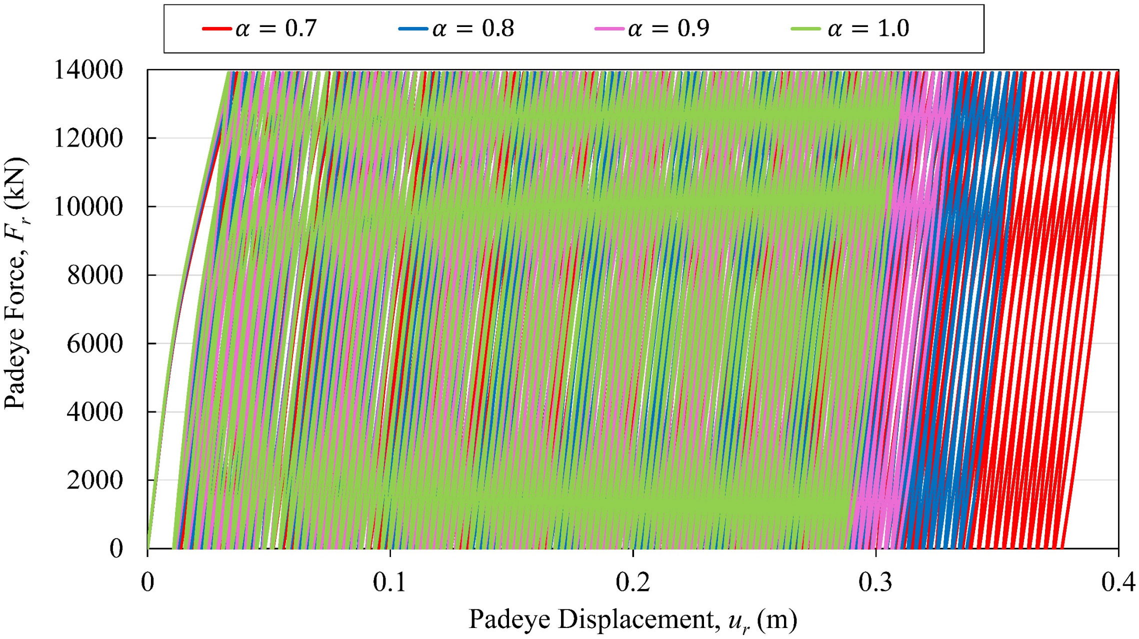

Figure 4.52. Ratcheting behavior in load direction at the padeye for 100 cycles with ψ=15^o and various adhesion factors

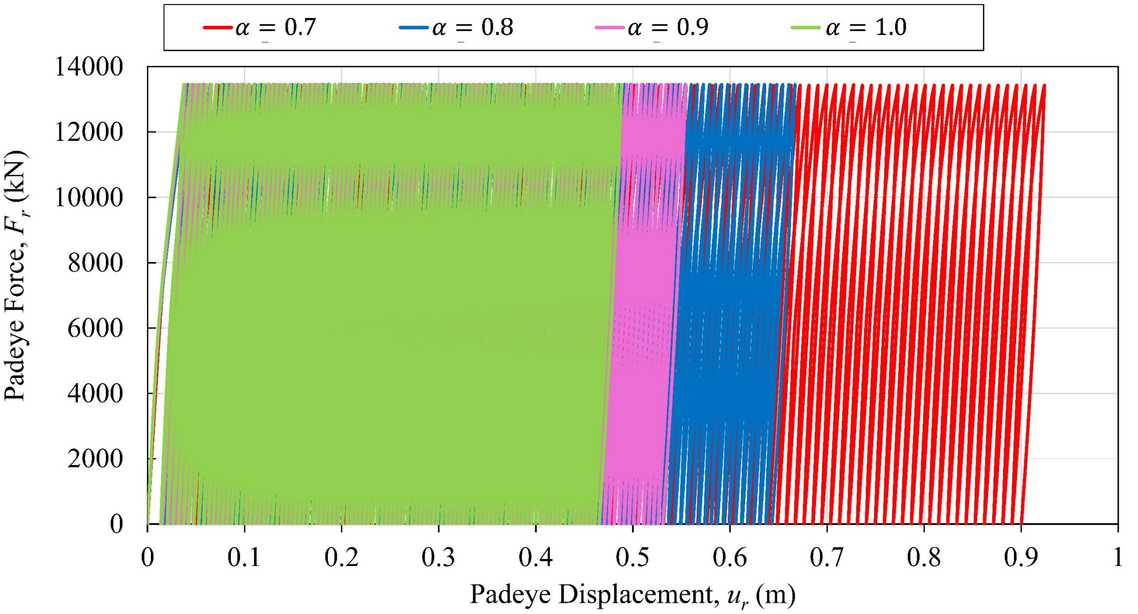

Figure 4.53. Ratcheting behavior in load direction at the padeye for 100 cycles with ψ=30^o and various adhesion factors

However, the applied forces for the case with ψ=15° (Figure 4.52) and the case with ψ=30° (Figure 4.53) had a little difference of about 3% in value between them. The resultant total deformation with α=0.7 at the end of 100 cycles for the case with ψ=30° is about more than the double of the case with ψ=15° (Figure 4.54), even when the allowable force for the case with ψ=15° is larger than that for the case with ψ=30° in about 3%. Thus, it can be noticed obviously from the estimations of total deformations of padeye at the end of 100 cycles for various adhesion factors and inclined load angles, as shows in Figure 4.55.

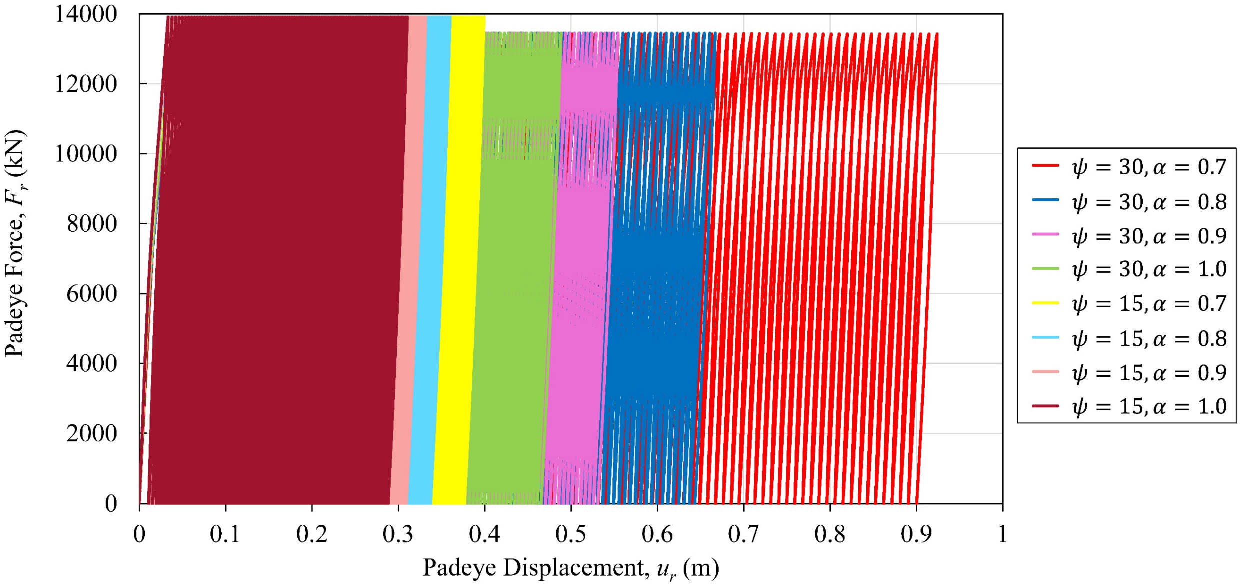

Figure 4.54. Ratcheting behavior in load direction at the padeye for 100 cycles with ψ=15°, 30° and various adhesion factors

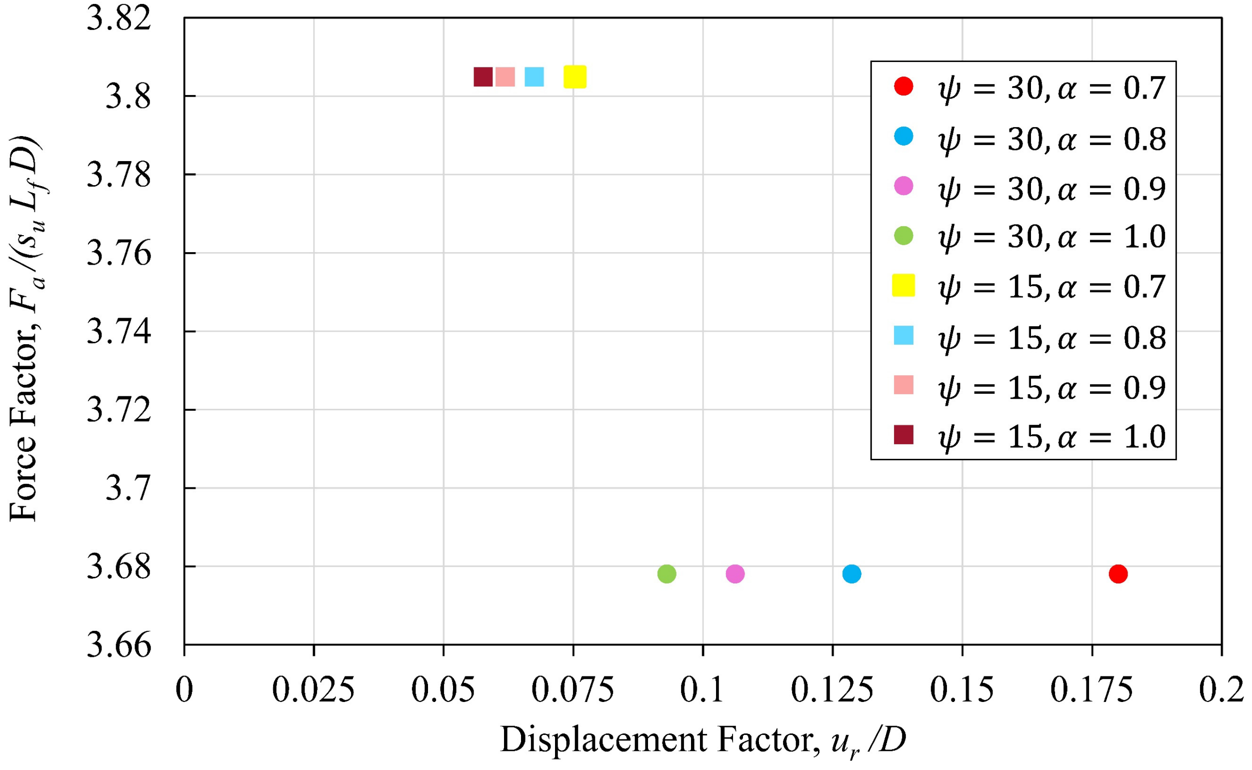

Figure 4.55. Total deformations of padeye at the end of 100 cycles for various adhesion factors and inclined load angles

Figure 4.56 and Figure 4.57 show the predicted effects of adhesion factor along the 100 cycles for load angles $\psi = 15^{\circ}$ and 30° respectively, considering a range of α from 0.7 to 1.0. All predictions are for stiffness $E/s_u = 600$, and an initial yield stress ratio $\sigma_0/\sigma_{max} = 0.1$. Adhesion is predicted to have a modest effect on displacements at shallow (ψ =15 degrees) load inclination angles, with a reduction in adhesion from α = 1.0 to 0.7 increasing displacements u_r by about 30%. By contrast, at a somewhat greater load inclination angle (ψ =30 degrees) the same decrease in α nearly doubles the displacement.

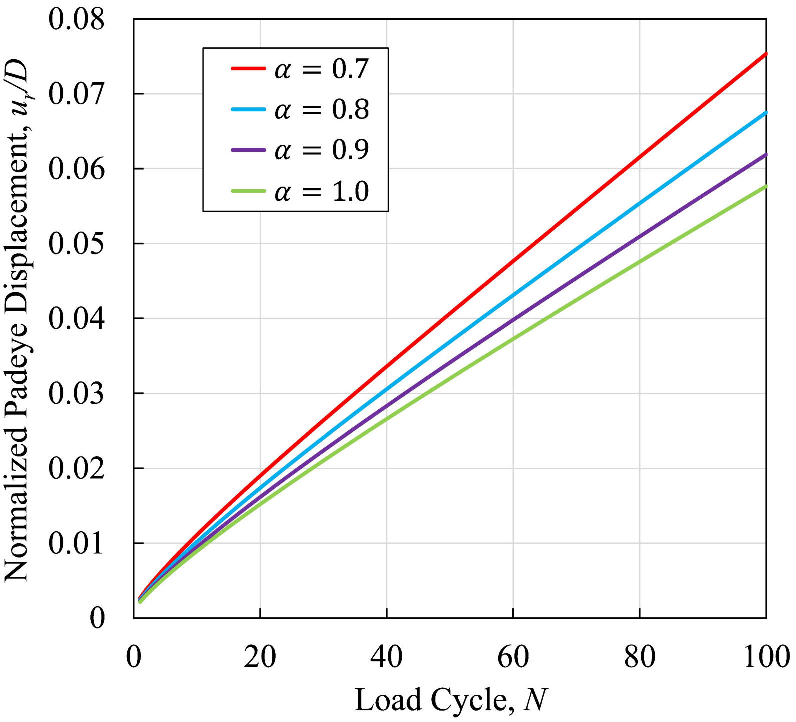

Figure 4.56. Effect of adhesion factor on caisson behavior for load inclination ψ=15^o

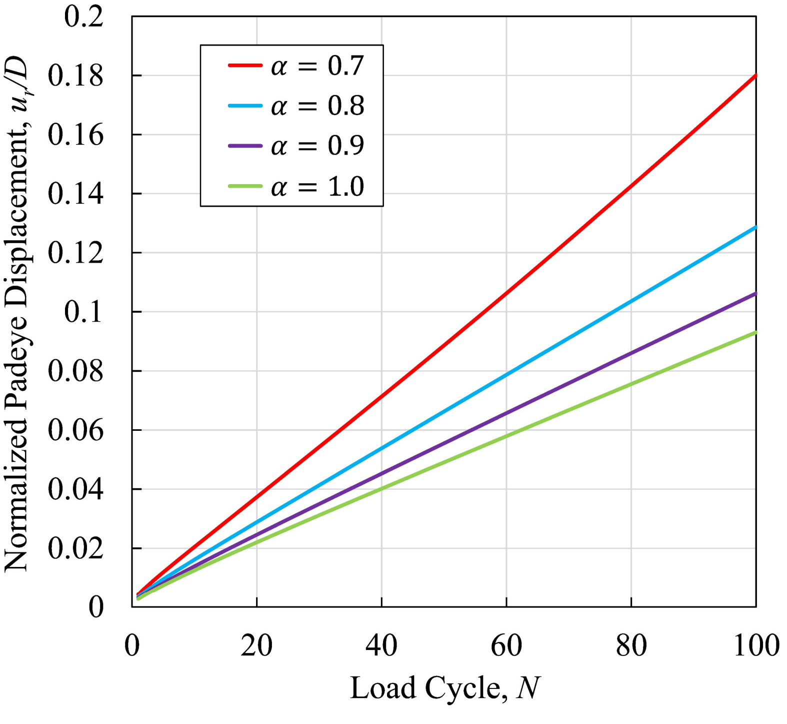

Figure 4.57. Effect of adhesion factor on caisson behavior for load inclination ψ=30^o

Studying the effect of inclined load angle can lead to interesting parametric study when using the same allowable force for each case of load angle criteria. For example, analyzing a soil-caisson system with the same force of 10130 kN, E/s_u ratio of 600, attachment point depth of 17 m, and adhesion factor (α) of 0.7 with various inclined load angle (0^o, 15^o, 30^o, 45^o). It can be determined that the inclination of caisson movement will tend to increase with increasing the load angle, as shown in Figure 4.58. Also, after plotting the ratcheting behavior in load direction at the padeye for 100 cycles with various inclined load angles (Figure 4.59), it can be noticed that the increase in displacement at the padeye has a direct proportion with increasing the inclined load angle. In addition, the total deformations of padeye at the end of 100 cycles (Figure 4.60) showed clearly the trend of increasing the deformations with increasing load angles. Figure 4.61 and Figure 4.62 show the predicted effects of load inclination angle along the 100 cycles, considering a range of $\psi = 0^o$ to 45^o. All predictions are for stiffness $E/s_u = 600$, an initial yield stress ratio $\sigma_0/\sigma_{max} = 0.1$, and adhesion factor $\alpha = 0.7$. The predictions indicate a high sensitivity of cumulative displacement to variations in load inclination angle, with an increase in ψ from 0^o to 45^o leading to nearly an order of magnitude increase in permanent displacements.

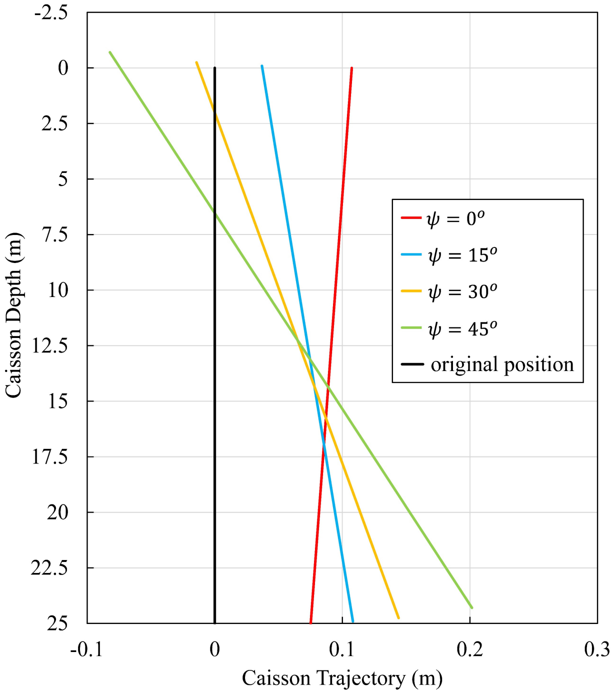

Figure 4.58. Trajectory of caisson movement at the end of 100 cycles for various load angles

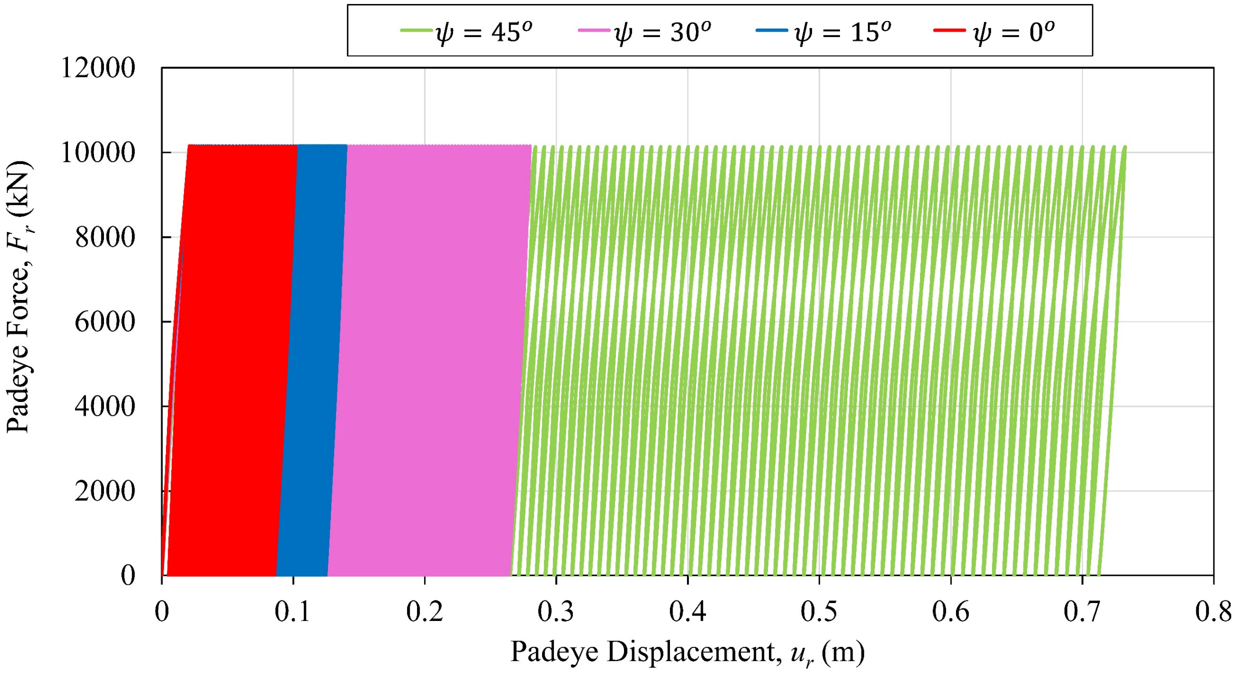

Figure 4.59. Ratcheting behavior in load direction at the padeye for 100 cycles with various inclined load angles

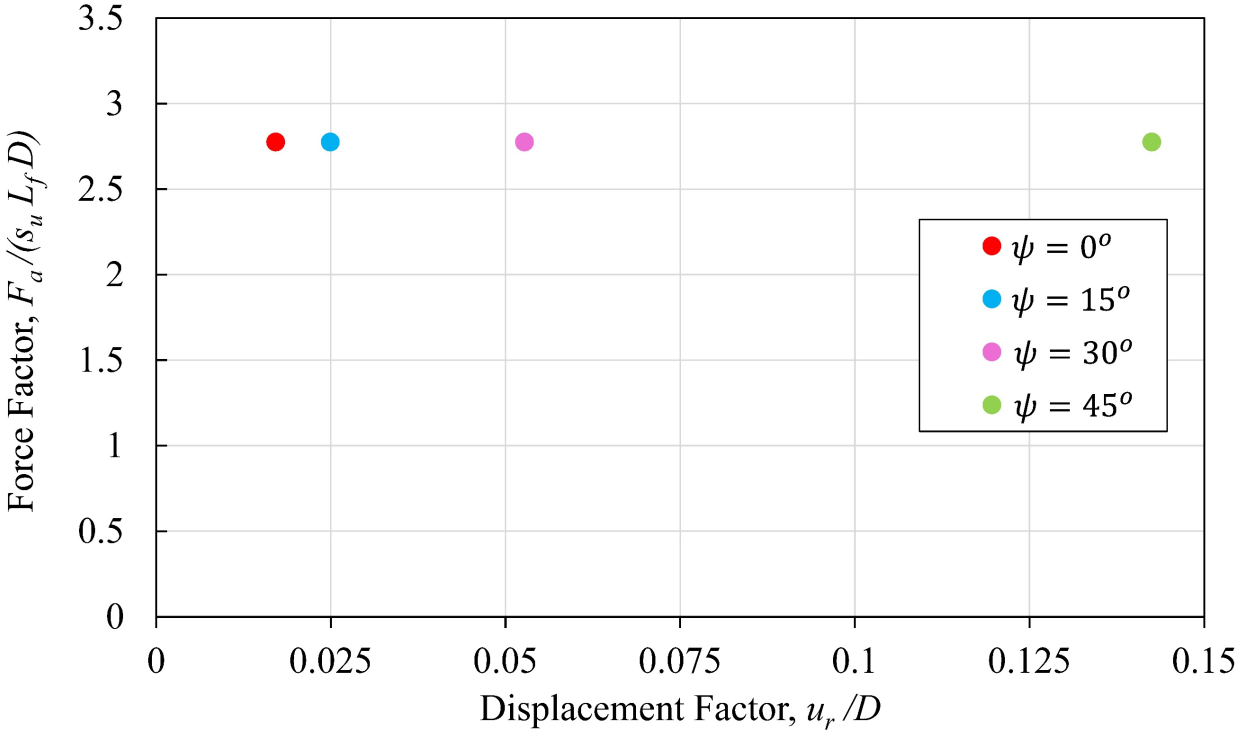

Figure 4.60. Total deformations of padeye at the end of 100 cycles for various inclined load angles

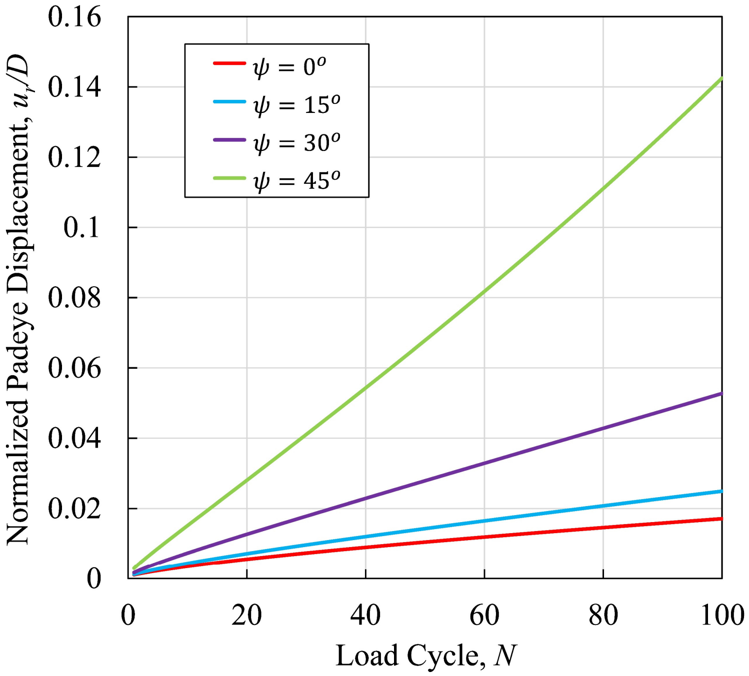

Figure 4.61. Effect of load angle on padeye resultant displacement

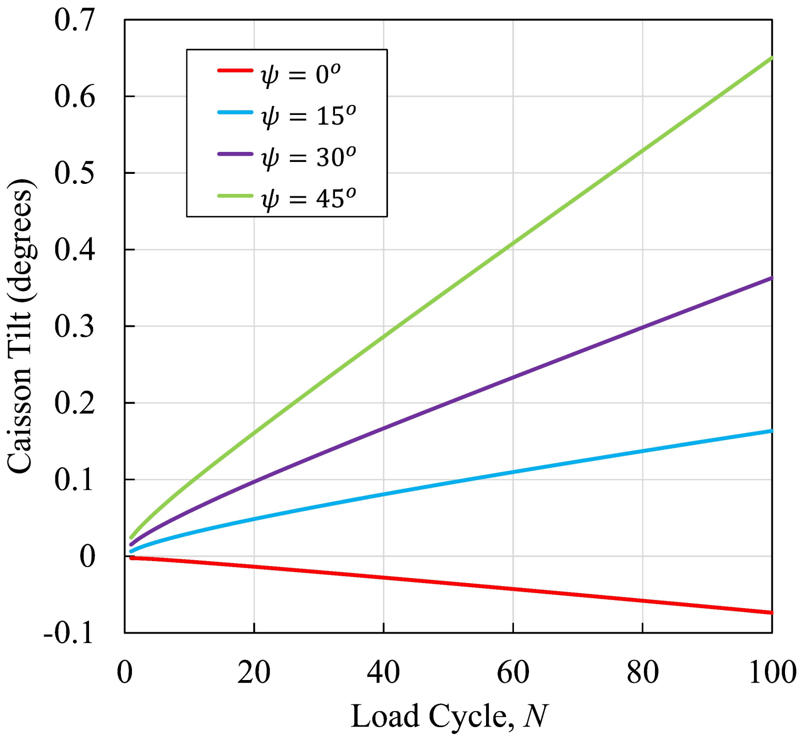

Figure 4.62. Effect of load angle on caisson tilt

For the cyclic amplitude, it has been studied in two different ways: the consistent amplitude and the random amplitude. For the consistent amplitude in order to investigate the effects of reversals in loading, a series of simulations were performed using the loading sequences shown in Figure 4.63. As shown in Figure 4.64, reversals are applied only to the horizontal component of loading. The direction of vertical applied load is always positive (upward) irrespective of the direction of horizontal load. The parametric study considers a range of load reversal from $\zeta = 0$ to -1, where $\zeta = F_{ax\text{-}rev} / F_{ax}$, with $F_{ax\text{-}rev}$ defined as the horizontal component of the minimum (reverse) load and F_{ax} defined as the horizontal component of the peak (forward) load. Where, the maximum amplitude of each cycle will be the same, in addition, it has been added a negative amplitude to each cycle to study the effect of these negative amplitudes on the ratcheting behavior of a soil-caisson system, as shown in Figure 4.63. While, the negative amplitudes were applied to the other side of the caisson wall, as shown in Figure 4.64.

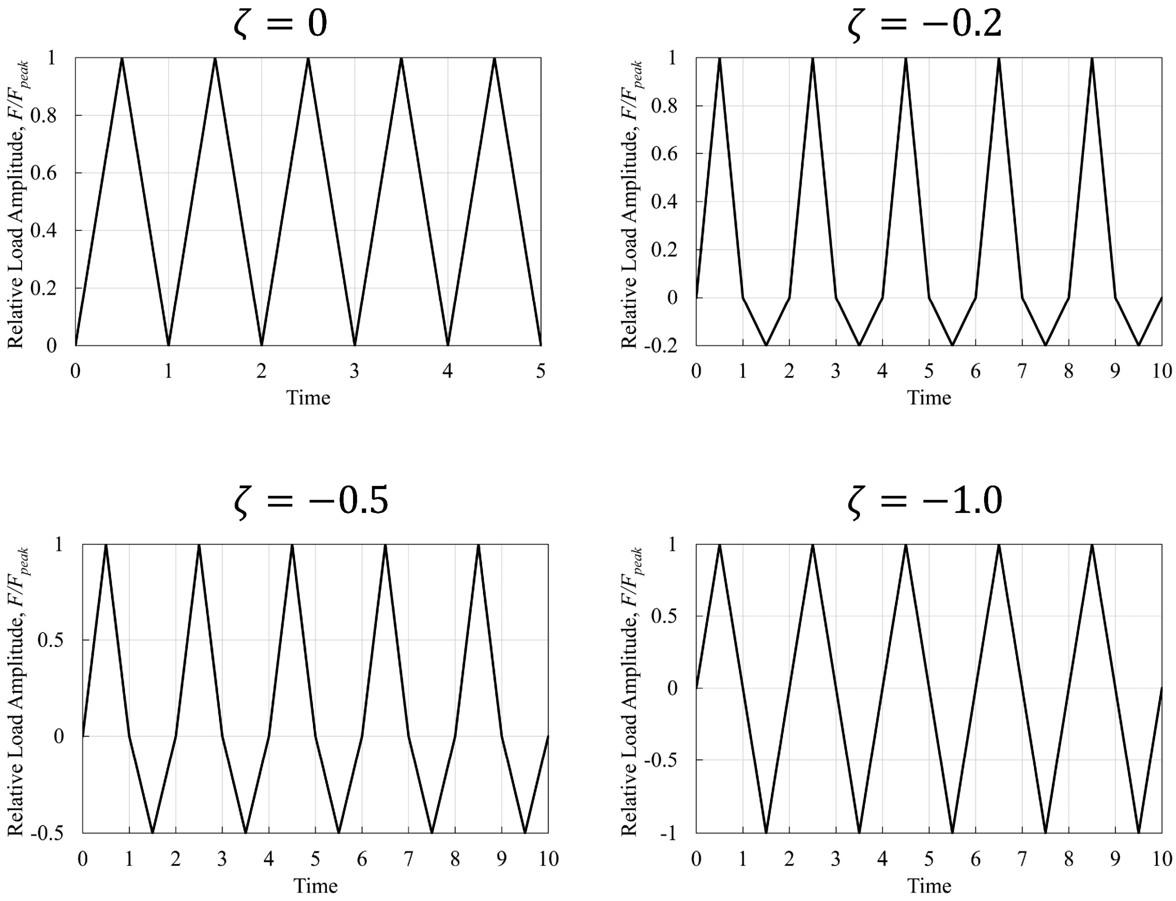
$\zeta = 0$

$\zeta = -0.2$

$\zeta = -0.5$

$\zeta = -1.0$

Figure 4.63. Load reversal types of consistent cyclic amplitudes (e.g. 5 cycles)

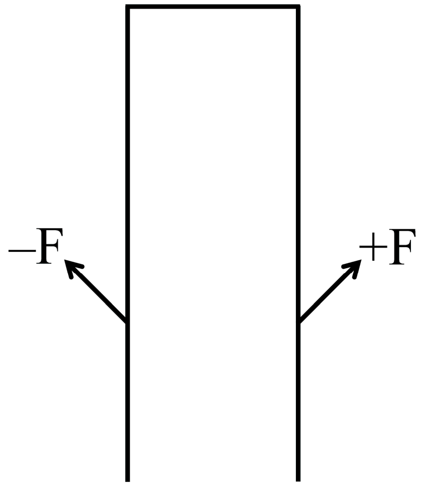

Figure 4.64. Loading applications of load reversal

From the analyses of the same parameters of a soil-caisson system, such as E/s_u = 600, F_a = 13888 kN, L_w = 17 m, ψ = 15°, and α = 1.0, it can be depicted that the caisson movement increase a little bit with increasing the negative amplitude of cycles (ζ = -0.2 and -0.5) but for the case with a negative amplitude cycle (ζ = -1.0), the negative action tries to rebound the positive action of cycle, as shown in Figure 4.65.

Also, from the ratcheting behavior in the horizontal direction (Figure 4.66), it can be illustrated that how the negative amplitude with -1.0 would act as a steady case on the padeye deformations, while the other cases with negative amplitudes (ζ = -0.2 and -0.5) their deformations increase with increasing the negative amplitudes. But the ratcheting behavior in vertical direction increases dramatically with increasing the negative amplitudes in general, as depicted in Figure 4.67, and especially from Figure 4.68 that showed the increase in vertical displacements at the top of caisson with increasing the reversal amplitudes.

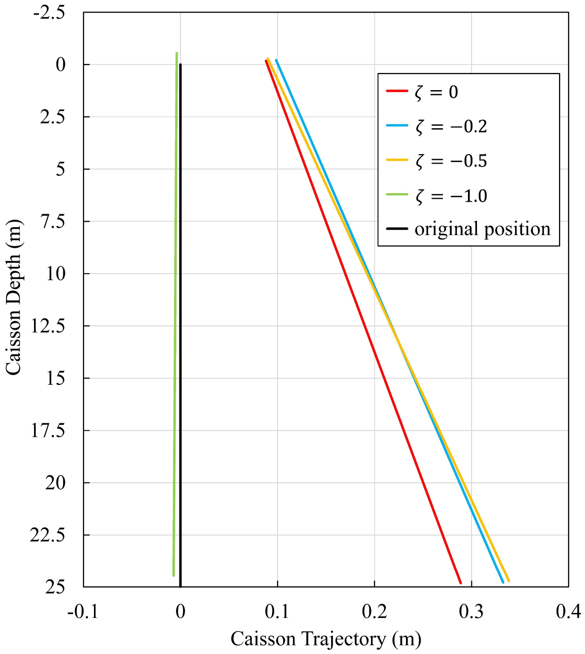

Figure 4.65. Trajectory of caisson movement at the end of 100 cycles for various consistent cyclic amplitudes

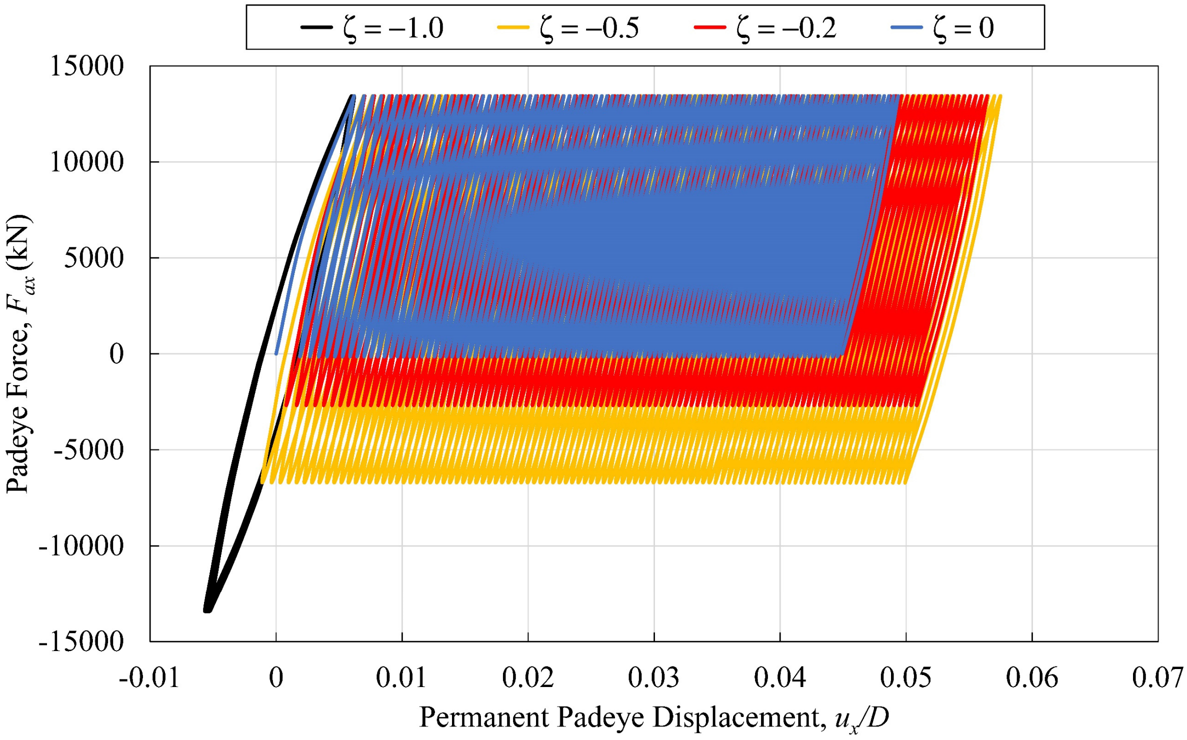

Figure 4.66. Ratcheting behavior in horizontal direction at the padeye for 100 cycles with various consistent cyclic amplitudes

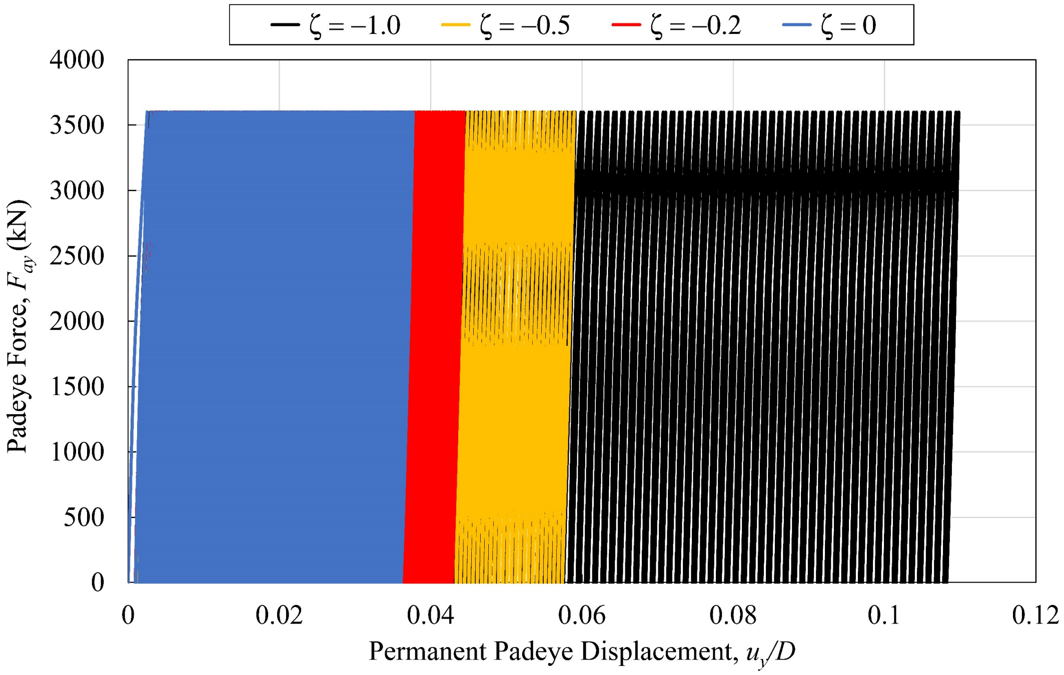

Figure 4.67. Ratcheting behavior in vertical direction at the padeye for 100 cycles with various consistent cyclic amplitudes

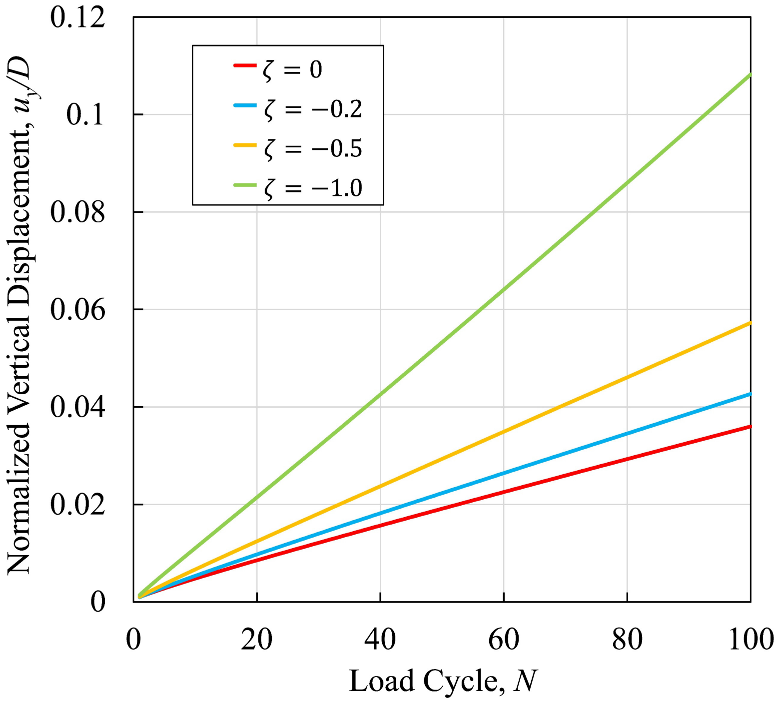

Figure 4.68. Effect of load reversals on cumulative vertical displacement at the top of caisson

Specifically, the cumulative horizontal displacement u_x/D at padeye versus load cycle N in Figure 4.69 shows that full load reversal, $\boldsymbol{\zeta}$ = -1, produces the lowest cumulative permanent displacement. This is not entirely unexpected, since full load reversals tend to push the pile back into its original position. However, the predictions do not indicate a simple trend of permanent displacement increasing with lower levels of load reversal. For example, permanent displacements associated with zero load reversal, $\boldsymbol{\zeta}$ = 0, are about 10% less than those associated with partial load reversal, $\boldsymbol{\zeta}$ = -0.5. Noting that the vertical component of loading is always upward, the predictions in Figure 4.70 not unexpectedly indicates progressively increasing cumulative vertical displacement u_y/D at padeye as ζ varies from 0 to -1. Overall, the predictions show the effects of load reversal to be relatively benign in regard to horizontal displacements. Taking the case of no reversal, ζ = 0, as a reference point, as ζ progresses from 0 to -1, cumulative horizontal displacement can increase by as much as 20% or, for the case of full load reversal, ζ = -1, decrease to essentially zero. By contrast, load reversal can seriously increase cumulative vertical displacements, with u_y quadrupling as ζ progresses from 0 to -1.0.

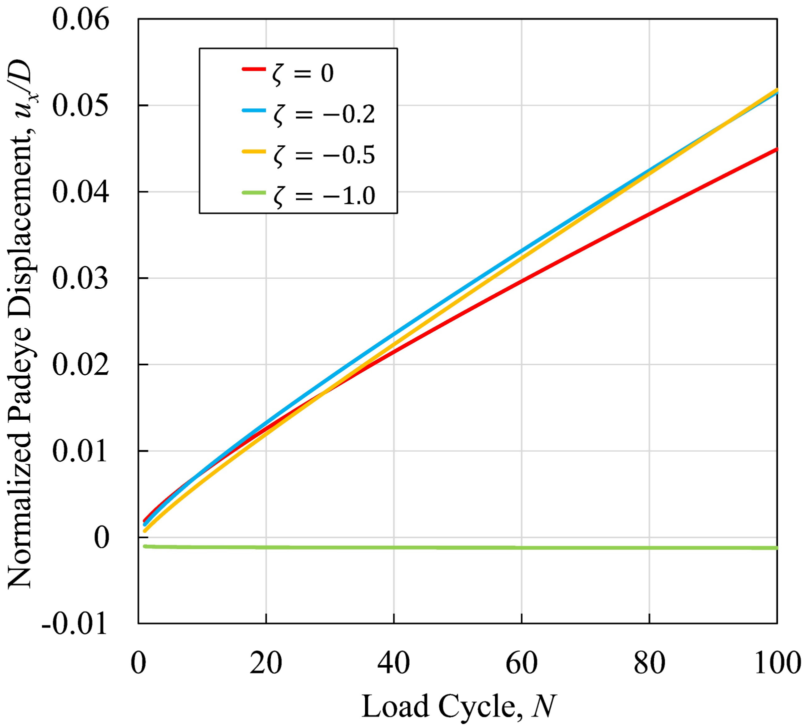

Figure 4.69. Effect of load reversals on cumulative padeye horizontal displacement

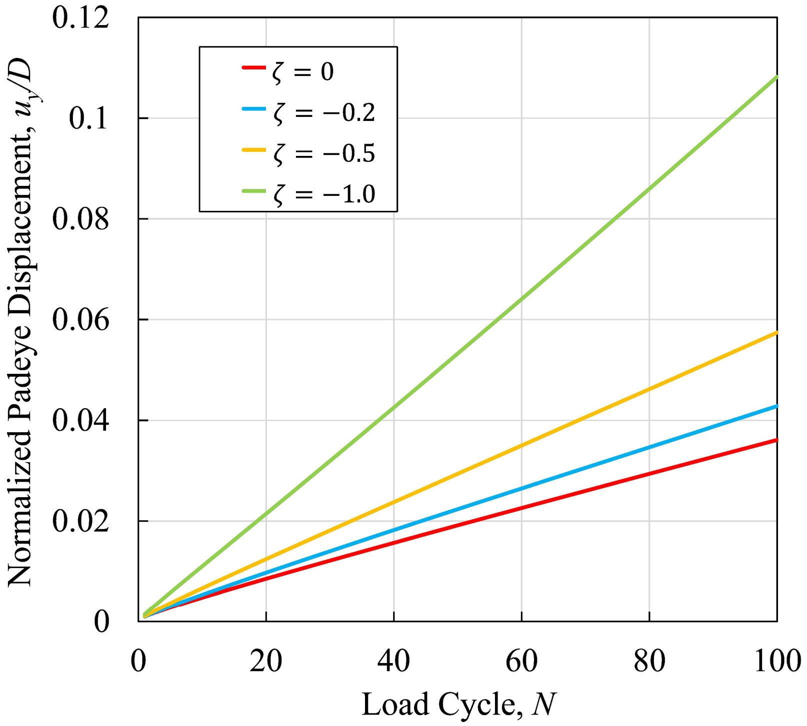

Figure 4.70. Effect of load reversals on cumulative padeye vertical displacement

The simulations to this point cover uniform load amplitudes at relatively large load magnitudes; i.e. the applied load intensity F_a was taken as the ultimate load capacity F_{ult} of the pile under consideration divided by a typical factor of safety FS. In offshore foundation and anchor applications, a more common storm load history comprises a single occurrence at load intensity F_{ult}/FS, in conjunction with a large number of smaller loads. Figure 4.71 shows typical load distribution given by Andersen (2015). Noting that actual storm loading is a random sequence, the figure illustrates the common practice of grouping the loads into packets of uniform load intensity, where the random load amplitudes (variable load amplitudes) were about 1228 cycles.

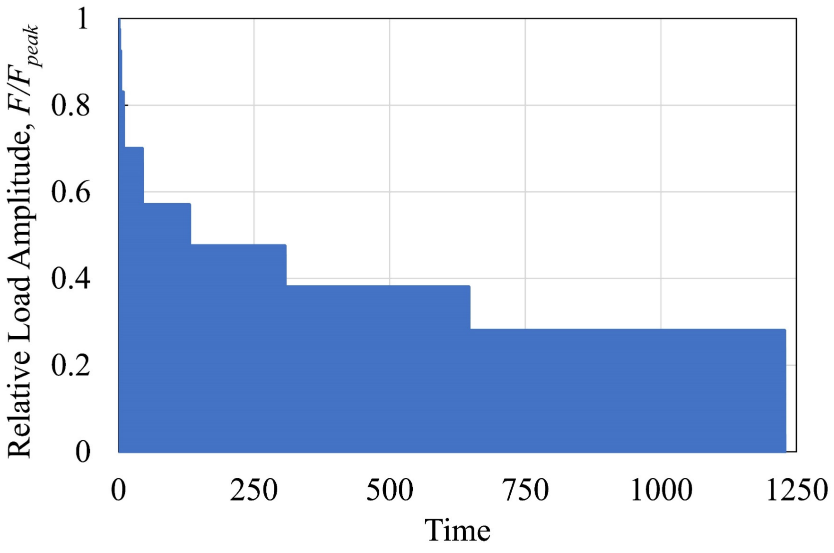

No. of cycles	cyclic load amplitude
1	1
1	0.975
2	0.925
5	0.83
35	0.7
87	0.57
176	0.475
339	0.38
582	0.28

Figure 4.71. Variable amplitude load history (Andersen, 2015)

Figure 4.72 and Figure 4.73 show the results of applying the random cyclic load history in Figure 4.71 to the base case condition, with an applied peak load $F_{peak} = F_a$ = 13900 kN (Table 3.2). Soil stiffness was set at E/s_u = 300, initial yield stress σ_0/σ_{max} = 0.1, applied load angle ψ =

15°, and α = 0.7. Two variants of loading history were considered in the simulations: Case 1 follows the load sequence shown in Figure 4.71, with the peak load occurring first (at $N = 1$) followed by progressive packets of decreasing load amplitudes, and Case 2 for which the loading is in the reverse order of the sequence in Figure 4.71, with progressively decreasing load amplitudes occurring. It can be noticed that the padeye deformations in horizontal and vertical directions will be different, as shown in Figure 4.72, and Figure 4.73 respectively and also showed that the higher amplitudes in the end of the reverse random load history can increase the deformations in general.

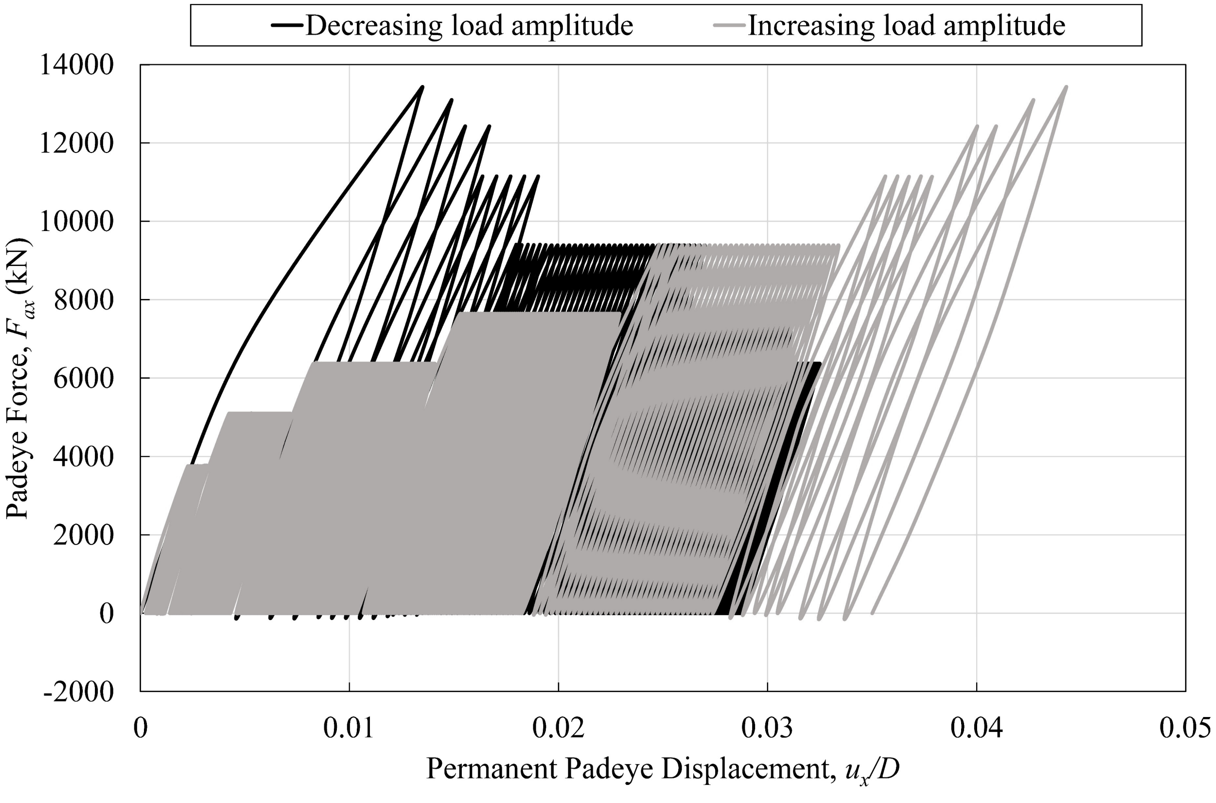

Figure 4.72. Ratcheting behavior in horizontal direction at the padeye for random cycles and reverse random cycles

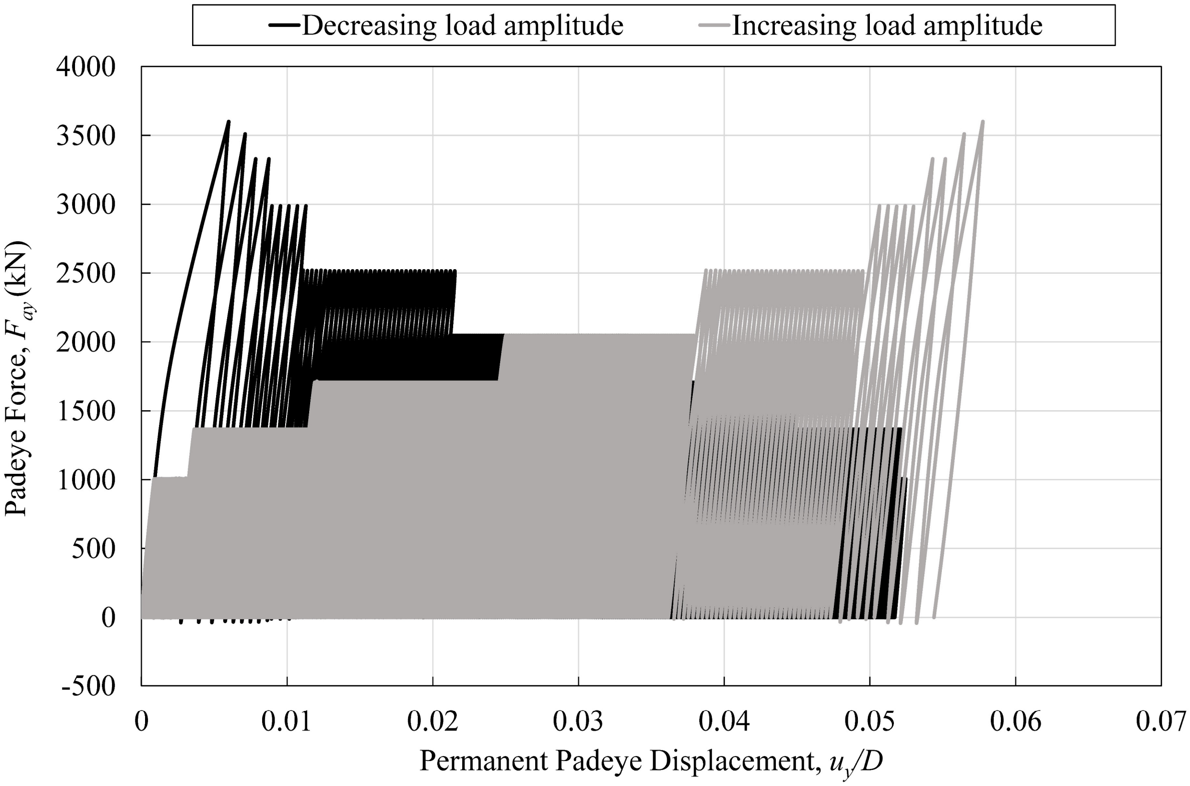

Figure 4.73. Ratcheting behavior in vertical direction at the padeye for random cycles and reverse random cycles

Furthermore, the caisson movements increase a little at the top of the caisson while the inclination of caisson increases a lot when the caisson is exposed to the reverse random history (increasing load amplitude), as illustrated in Figure 4.74.

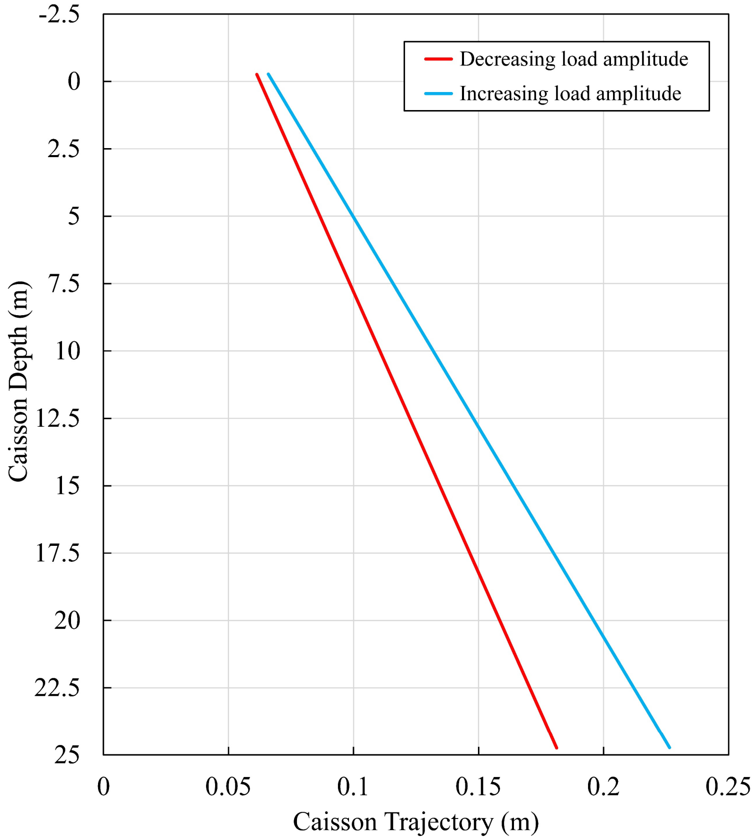

Figure 4.74. Trajectory of caisson movement at the end of random cycles and reverse random cycles

Figure 4.75 and Figure 4.76 show the predicted nonlinear accumulated displacements at the padeye of caisson for horizontal and vertical directions respectively versus load cycles. For Case 1, a condition of progressively increasing load amplitude, a large number of small amplitude loads (582 cycles at $F = 0.28\ F_{peak}$) applied at the end of the loading sequence produces negligible displacements. This is in contrast to Case 2, where small loads are applied at the beginning of the sequence produce noticeable permanent displacements. Similar trends are observed for other packets of loads at the small end of the sequence; they generate larger cumulative displacements when they are applied early in the sequence. The net result of this effect is that applying increasingly greater load amplitudes (Case 2) generates larger cumulative displacements; in this case, about 25% greater for horizontal displacements and about 4% greater for vertical displacements. It is also noted that, except for the variable load amplitude, the soil and loading conditions for the predictions in Figure 4.75 and Figure 4.76 are identical to the uniform loading case shown in Figure 4.44. Application of a more realistic loading history is seen to generate much lower cumulative displacements.

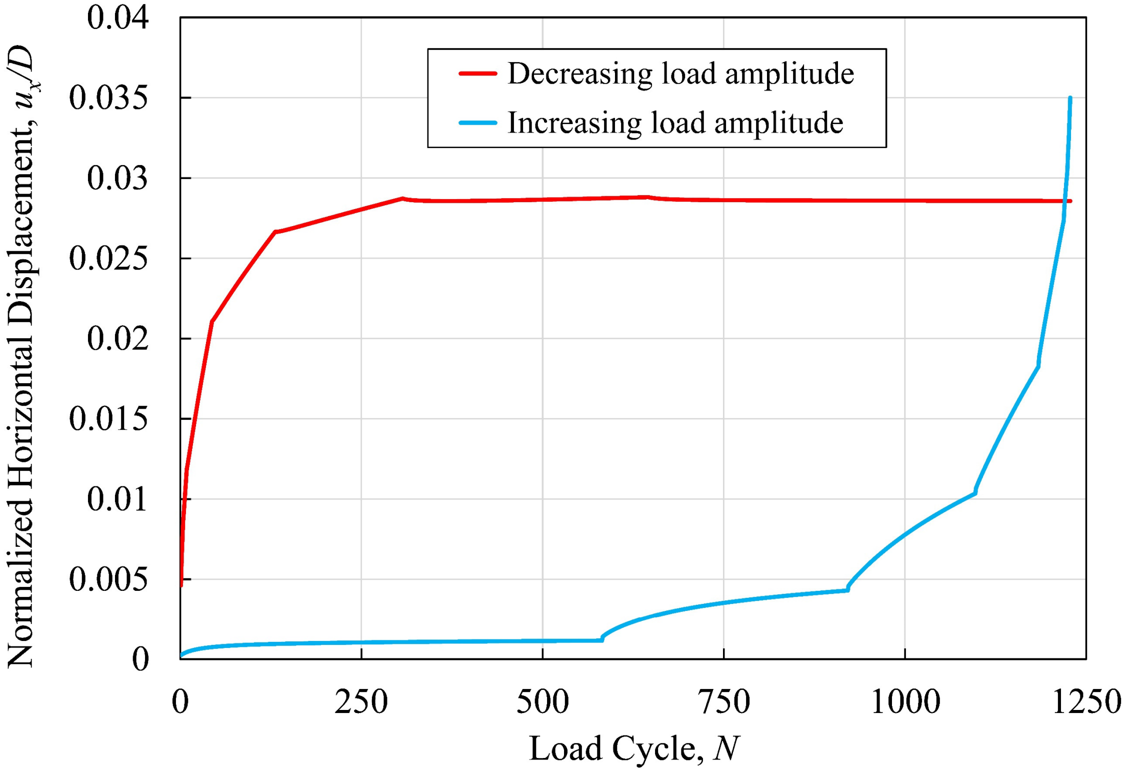

Figure 4.75. Horizontal displacement at the padeye of caisson for random cycles and reverse random cycles

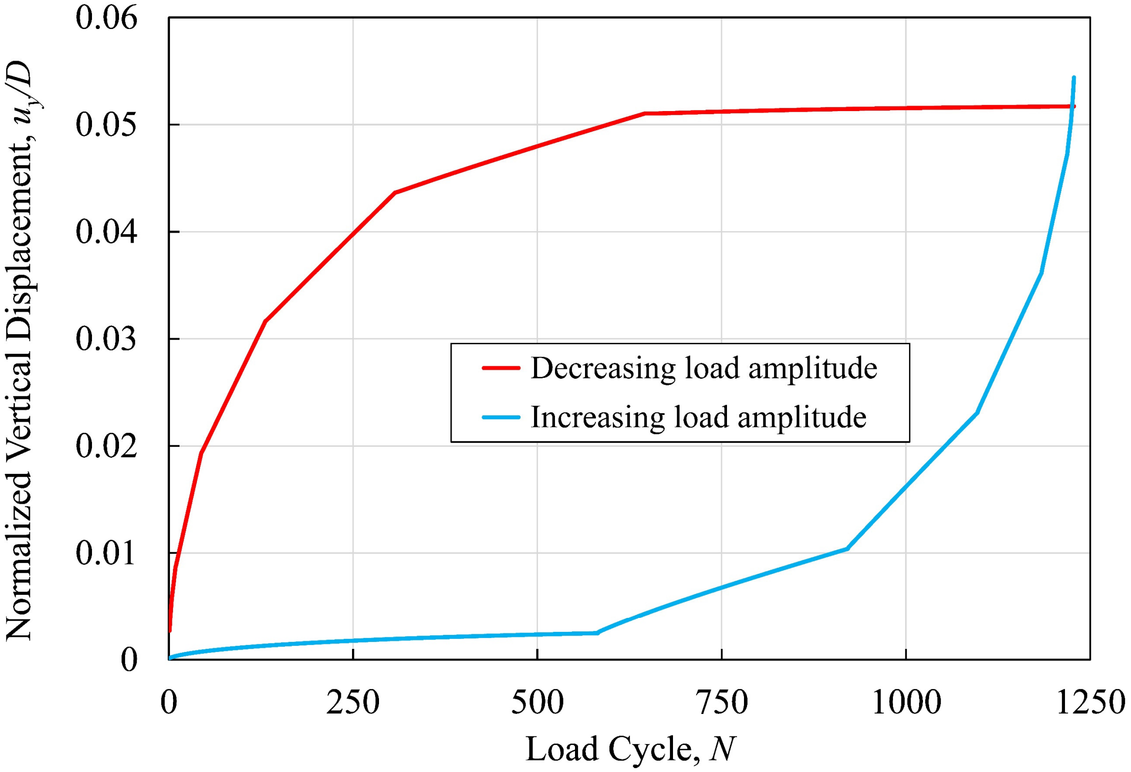

Figure 4.76. Vertical displacement at the padeye of caisson for random cycles and reverse random cycles

5 MULTILINE AND SINGLE-LINE CONCEPTS FOR CAISSONS

5.1 Overview

Anchoring offshore floating structures can be achieved by using the suction caisson anchors. The purpose of suction caissons is to anchor the floating structures to the seabed by utilizing the mooring line system. Therefore, using moorings system would expose the caissons to cyclic loads that initiated by wave and wind effects. Nowadays, most floating offshore wind turbines (FOWT) are anchored by 3 single-line suction caisson anchors. However, for the multiline concept as shown in Figure 5.1, the caisson anchors can attached to more than one FOWT, that leads to the notion of sharing suction caissons anchors among the FOWTs (Fontana et al., 2018).

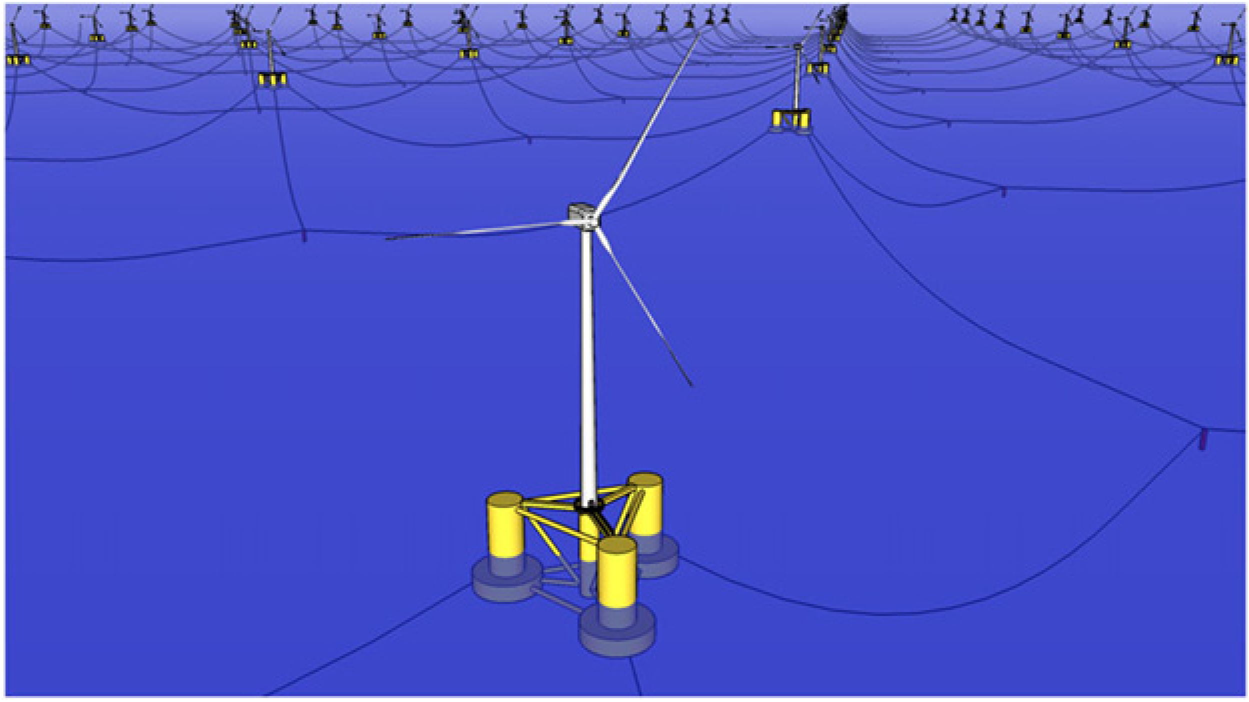

Figure 5.1. Multiline system for FOWT (Fontana et al., 2018)

However, the current design methods of laterally loaded piles had been applied for caisson design of offshore structures to predict the lateral deflection of caissons. There are still some limitations for these methods. The developing of the *p-y* method (API, 2003; DNV, 2014) is for flexible slender piles while the suction caissons are stiffer than piles and the length to diameter ratio of caisson for wind turbine is about 4 to 8. Moreover, these methods are applied for static loads even though Matlock (1970) found a cyclic *p-y* curve but his curve did not consider the influences of amplitude or cycle frequency. Where in real life, the long-term deformations are strongly dependent on cyclic loading features regarding the amplitudes and cycle numbers and the accumulated deformations may produce from the repetitive loadings (Klinkvort and Hededal, 2013; Li et al., 2015; Lombardi et al., 2013; Long and Vanneste, 1994; Yu et al., 2015).

Using different types of anchor concepts, as single-line and multiline systems, are explored in this study in terms of the influences of soil types and features of multidirectional values of anchor forces that conduct on the soil-caisson system.

5.2 Anchor Force Determination

This section describes the FOWT model, simulation software, and environmental loading conditions used to generate time histories of the single-line and multiline anchor forces. The turbine chosen for this analysis is the National Renewable Energy Laboratory's (NREL) 5-MW reference turbine (Jonkman et al., 2009) and the support structure chosen is the OC4-DeepCwind semisubmersible floating system (Coulling et al., 2013). Spatial layout of the OC4-DeepCwind floating system for 3-line multiline anchor geometry is shown in Figure 5.2, and relevant properties of the OC4-DeepCwind mooring system are provided in Table 5.1 (Robertson et al., 2014).

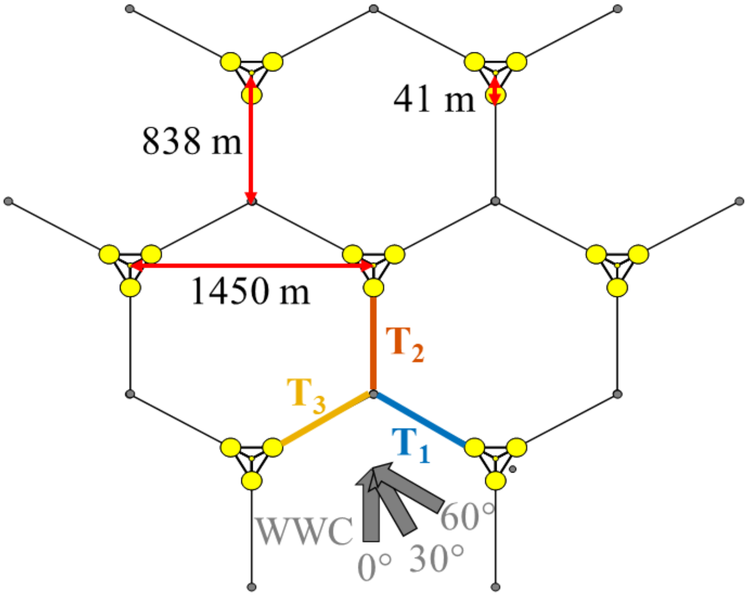

Figure 5.2. Spatial layout of the multiline anchor connection and OC4-DeepCwind floating system for a 3-line anchor (Fontana et al., 2018)

Table 5.1. Properties of the OC4-DeepCwind semisubmersible floating system (Robertson et al., 2014)

Mooring System	Catenary
Mooring Line Type	Studless Chain
Extensional Stiffness	753.6 MN/m
Water Depth	200 m
Line Length	835.35 m
Chain Nominal Diameter	0.0766 m
Mass per Unit Length Chain	113.35 g/m

The dynamics of the floating system are modeled with NREL's FAST (Fatigue, Aerodynamics, Structures, and Turbulence) Code (Jonkman and Jonkman, 2016; Jonkman and Buhl Jr, 2005). Mooring line and anchor force dynamics were simulated via MoorDyn, a lumped-mass mooring model within FAST. The model accounts for mooring line axial stiffness and damping, weight and buoyancy forces, and hydrodynamic forces from Morison's equation assuming still water (Hall, 2017). Line properties for the OC4-DeepCwind mooring system in the MoorDyn input file are taken from Hall and Goupee (2015). Seabed friction forces were incorporated via the procedures outlined in Fontana et al. (2018).

The Survival Load Case (SLC) utilized in this study is a wave-dominated load case, as detailed in Table 5.2. The WWC parameters for this critical environmental condition are taken from the full scale VolturnUS project (Viselli et al., 2016), harvested from over ten years of buoy data at a site off Monhegan Island, Maine (Pettigrew et al., 2008; UMaine, 2013).

Table 5.2. Details of Survival Load Case, SLC (Viselli et al., 2015)

Condition	Extreme Non-Operating (Strength)
Wind Speed at Hub Height	45 m/s (500-yr)
Turbulence Intensity	10%
Significant Wave Height	12 m (500-yr)
Peak Spectral Wave Period	15.3 sec
JONSWAP Gamma Factor	2.5
Current Speed	0.55 m/s

The turbulent wind field is generated with a Kaimal spectrum via Turbsim (Jonkman and Kilcher, 2012). Waves are generated with a JONSWAP spectrum, and wave heights are Rayleigh distributed (Jonkman et al., 2015). Current is steady and equal at each FOWT. Co-directional WWC directions of 0°, 30° and 60° are evaluated, and the range of 0° - 60° is suitable for capturing the range of important dynamics due to the 120° rotational symmetry. Six 1-hour simulations using different random seeds were completed for each combination of load case and WWC direction. Additional details on the modeling of the anchor forces can be found in Fontana et al. (2018).

5.3 Geotechnical Model

The same proposed model was used in this work that predicted the long-term plastic deformations under sub-yield loading conditions, i.e. at stress levels well below the maximum yield stress. As mentioned before, this model deals with four parameters; the limit stress, σ_{max}, yield stress, σ_0, small strain soil stiffness, E, and Poisson's ratio, μ.

Before analyzing the soil-caisson system with the cyclic anchor forces that applied at the padeye of the caisson, it would be required to determine the ultimate capacity of caisson regarding the soil type, caisson dimension, the inclination angle of load, and the adhesion factor for adjacent soil along the wall of caisson. Therefore, the simplified upper bound solutions (Aubeny et al., 2003; Aubeny et al., 2001) can offer a convenient computational method for obtaining the inclusive design that can be implemented for each case in a simplified way.

5.4 Simulation Parameters

5.4.1 Soil Strength

Three different types of soils applied in the simulation of soil-caisson system. The first soil was soft clay with undrained shear strength that increased with depth (Table 5.3). The second soil was stiff clay with constant shear strength along the soil layer (Table 5.4). The third one was a combination between soft clay and stiff clay with the properties as shown in Table 5.5.

Table 5.3. Undrained shear strength of soil 1

Depth, z (m)	Sediment	$s_{u\text{-}(DSS)}$ (kPa)
0 - 5	Holocene, MH	$1.4 + 0.92\,z$
> 5	Pleistocene, CH/CL	$6.0 + 1.61\,(z - 5)$

Table 5.4. Undrained shear strength of soil 2

Depth, z (m)	Sediment	$s_{u\text{-}(DSS)}$ (kPa)
> 0	Very Stiff Clay	165

Table 5.5. Undrained shear strength of soil 3

Depth, z (m)	Sediment	$s_{u\text{-}(DSS)}$ (kPa)
0 - 5	Holocene, MH	$1.4 + 0.92\,z$
> 5	Very Stiff Clay	165

5.4.2 Upper Bound Design for Caissons

In order to study the cyclic influences on the permanent deformations of the soil-caisson system, it is required to determine the design of caisson regarding the soil types. It had been used the simplified upper bound theory to get the optimum caisson design to resist the applied anchor forces with safety factor equals to 1.5 that satisfy the offshore wind turbine requirements (ABS, 2013) to get the allowable force for each design. Thus, three designs for caisson had been determine for each soil type that studied in this research. The three design parameters are shown for soils 1, 2, and 3 in Table 5.6, Table 5.7, and Table 5.8 respectively.

Table 5.6. Caisson design for soil 1

D (m)	L/D	L (m)	Adhesion factor	Padeye depth (m)	Padeye angle (°)	F_{ult} (kN)	F.S.	F_{all} (kN)
3.2	5	16	0.75	11	15	6040	1.5	4027

Table 5.7. Caisson design for soil 2

D (m)	L/D	L (m)	Adhesion factor	Padeye depth (m)	Padeye angle (°)	F_{ult} (kN)	F.S.	F_{all} (kN)
1.9	1.5	2.85	0.75	1.9	23	5860	1.5	3907

Table 5.8. Caisson design for soil 3

D (m)	L/D	L (m)	Adhesion factor	Padeye depth (m)	Padeye angle (°)	F_{ult} (kN)	F.S.	F_{all} (kN)
2	3.25	6.5	0.75	5	23	5965	1.5	3977

5.4.3 Anchor Forces

In designs implemented for this study, a tension force of mooring line systems is included to account for vertical and horizontal forces that act exactly at the padeye point of caisson. In catenary mooring systems, the mudline angle of anchor line (θ_0) as well as the soil type of seabed can affect the tension force and angle of anchor line at padeye (T_a, θ_a). It has been calculated the anchor line at padeye for each seabed angle of mooring lines, as depicted in Table 5.9. It has been optimized a load attachment angle (θ_a) depends on soil types and the maximum seabed anchor force (T_0) in order to get the anchored force (T_a) that can be applied to the caisson at the optimum attachment point (padeye), which is located at about two-third the length of caisson with an inclination angle (θ_a) of the caisson load.

Table 5.9. Anchor forces for each soil type

Soil Type	WWC Direction (°)	Line Type	Seabed Angle, θ_0 (°)	Maximum Seabed Force, T_0 (kN)	Padeye Angle, θ_a (°)	Maximum Padeye Force, T_a (kN)
1	0	Single	0	4200	15	3889
		Multi	0	3748	15	3470
	30	Single	0	3583	15	3318
		Multi	0	2863	15	2651
	60	Single	0	2223	15	2058
		Multi	0	1512	15	1400
2	0	Single	0	4200	23	3724
		Multi	0	3748	23	3323
	30	Single	0	3583	23	3177
		Multi	0	2863	23	2538
	60	Single	0	2223	23	1971
		Multi	0	1512	23	1341
3	0	Single	0	4200	23	3724
		Multi	0	3748	23	3323
	30	Single	0	3583	23	3177
		Multi	0	2863	23	2538
	60	Single	0	2223	23	1971
		Multi	0	1512	23	1341

5.5 Numerical Simulation

The finite element model of a soil-caisson system was simulated in a software program ABAQUS (Simulia, 2014). In order to reduce the computational time when dealing with many cycles of applying loads, an axisymmetric model with asymmetric Fourier elements was utilized to mesh both the caisson foundation with SAXA-type and the soil with CAXA-type. The faraway boundary condition (distance from the caisson wall to the far end of the mesh) has set to be equal 10 times the caisson radius, while the mesh depth has set to be 2 times the length of the caisson embedment. Also, in order to scope the effect of boundary conditions with a suitable accuracy of the results, initial analyses were carried out for the purpose of mesh fineness. The FE simulation has been selected with an anchored force (T_a) that can be applied to the caisson at the center-padeye point which is a prolongation of the optimum attachment point (padeye) that is about two-third the length of caisson with an inclination angle (θ_a) of the caisson load, as shown in Figure 5.3.

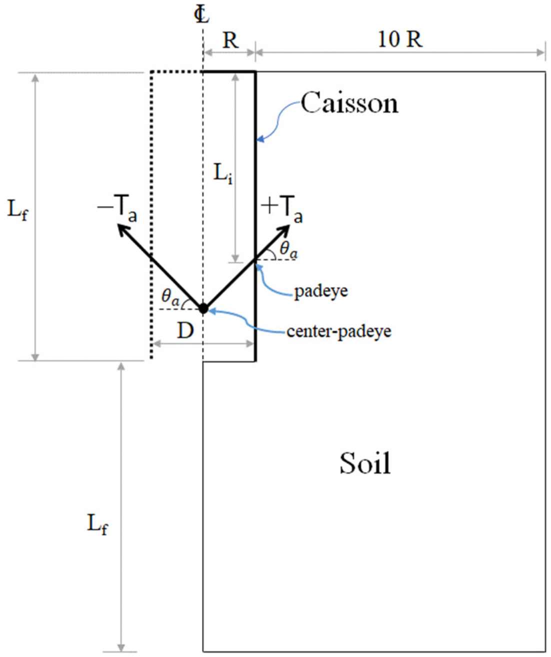

Figure 5.3. Soil-Caisson system diagram

The initial Young's modulus of soil was computed from the ratio E/s_u that is increase nonlinearly with depth and depends on the ratio of the ultimate capacity of caisson (F_{ult}) with the applied anchor force (T_a) at the padeye for each design, as examples are shown for soft clay (soil 1) case of single-line and multiline anchor forces for WWC direction=0° in Figure 5.4. A Poisson's ratio ($\mu = 0.5$) was used in the finite element simulations. This value corresponds to undrained conditions for saturated or nearly saturated clay. Also, as described previously, a value of $\sigma_0/\sigma_{max} = 0.1$ was selected for the finite element simulations. For the caisson's material parameters, a thickness of $t = D/80$ and a very large modulus of elasticity ($E = 1\times10^{12}$ kPa) were applied in order to achieve a rigid behavior for caisson.

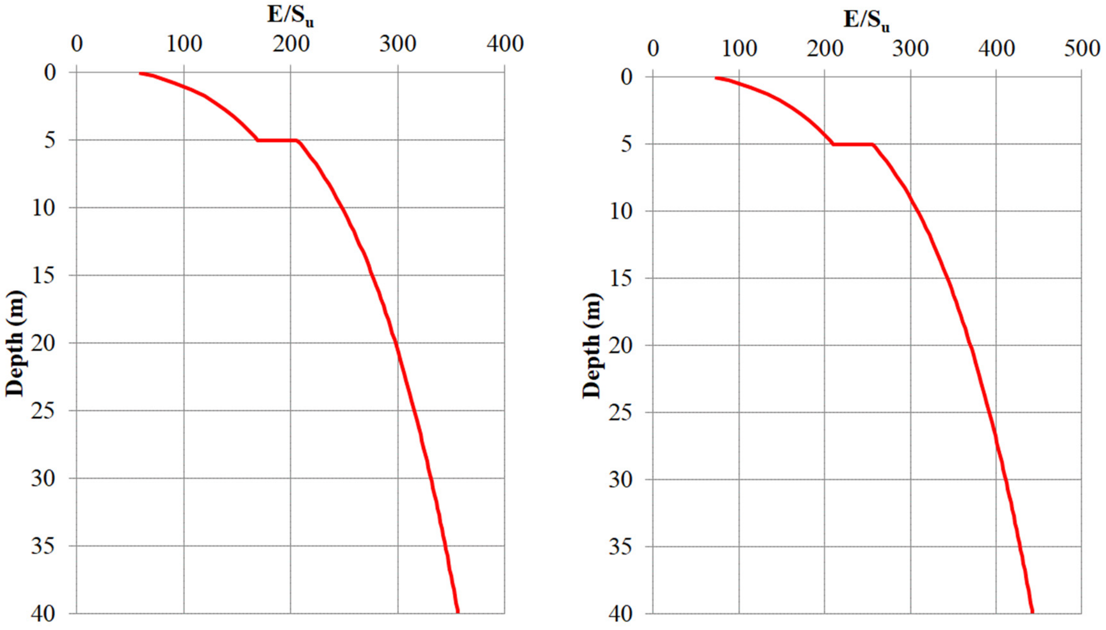

a) Single-line case

b) Multiline case

Figure 5.4. Profile of *E/s$_u$* ratio for soft clay (soil 1) case of single-line and multiline anchor forces for WWC direction=0°

5.6 Results of Multiline and Single-Line Concepts

Applying the cyclic anchor forces (T_a) at the padeye of the suction caisson of the soil-caisson systems depends on each case of soil types and depends on the design of the mooring line as a single-line or multiline system. For instance, the soft clay case shows that the multiline approach reduced the cumulative displacements of the caisson dramatically in contrast to the results of implementing the single-line concept, as illustrated in Figure 5.5. Thus, comparing the displacements at the end of simulation the survival load case (SLC) for each mooring line types can observe that the multiline anchor system decreased the horizontal and vertical displacements at top of caisson in about 49% and 47% respectively in regards to the conventional single-line system. In addition, changing the WWC direction for the multiline system affects significantly on the results of displacements that predicted for a range of WWC from 0^o to 60^o. Thus, increasing the WWC will lead to decrease the cumulative displacements (Figure 5.6).

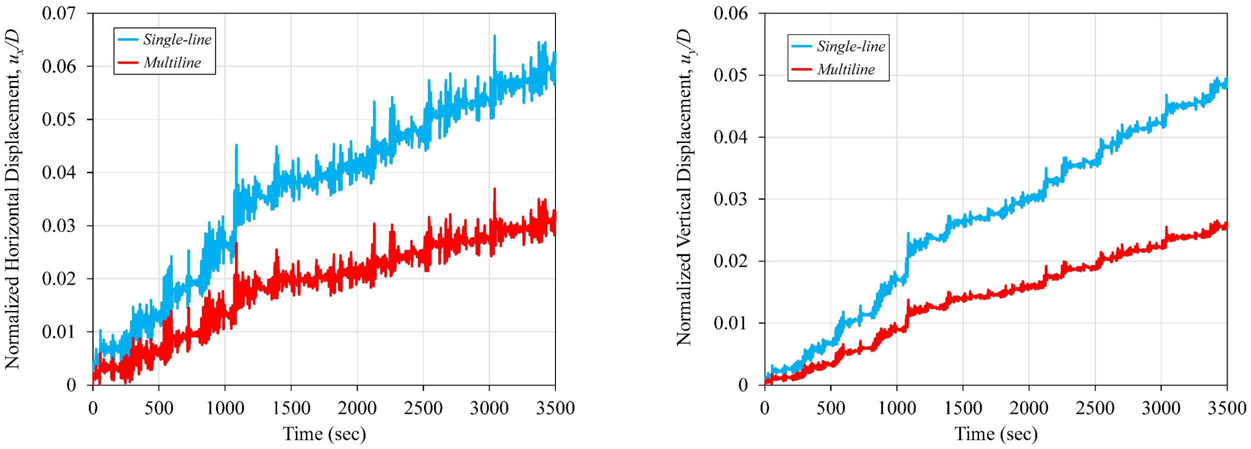

a) padeye of caisson

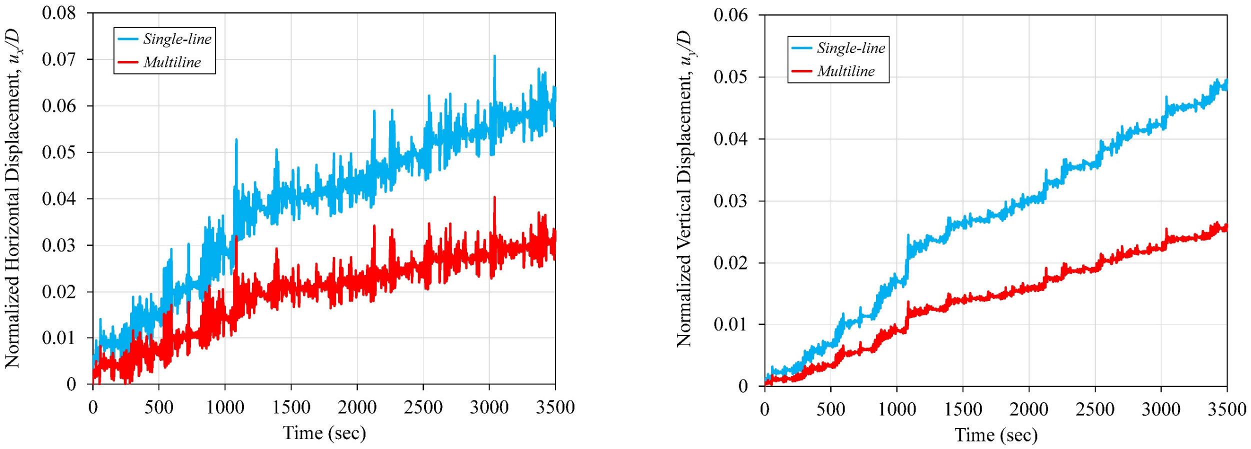

b) top of caisson

Figure 5.5. Displacements at (a) padeye and (b) top of caisson for soft clay (soil 1) case of single-line and multiline anchor forces for WWC direction=0°

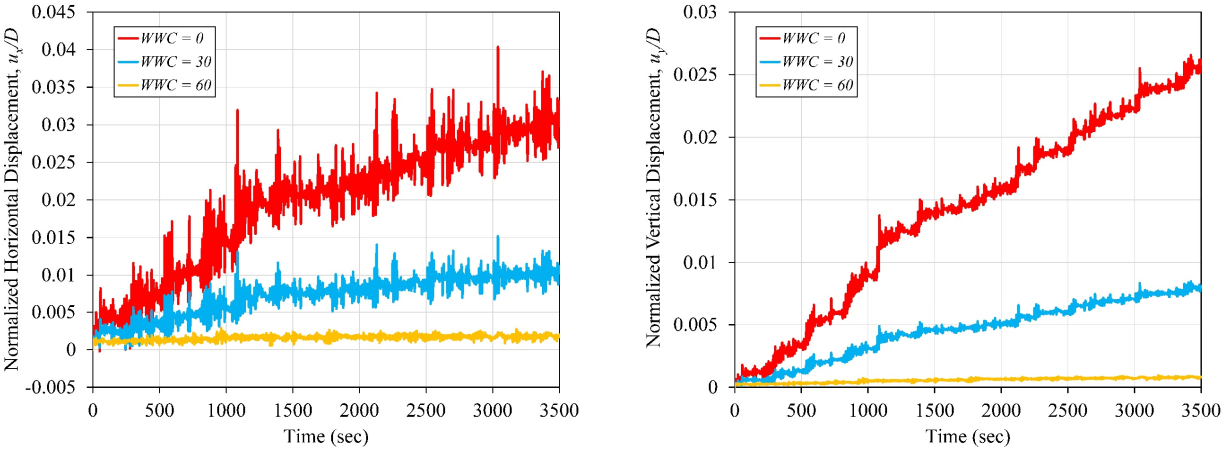

Figure 5.6. Displacements at top of caisson for soft clay (soil 1) case of multiline anchor forces for WWC direction=0°, 30°, and 60°

The second case of stiff clay depicts the same behavior of the soft clay case regarding the decreasing of deformations for the multiline system in contrast to the single-line system of the direction of WWC=0° (Figure 5.7) at both the padeye and top of caisson locations. In the same way of soft clay case, the results of stiff clay case indicate that the displacements of the highest WWC direction of 60° with multiline systems have the lowest magnitudes (Figure 5.8). Obviously, the use of multiline system decreases the horizontal and vertical permanent displacements at top of caisson in about 61% and 49% respectively for the WWC=0°. Moreover, from plotting the trajectory movements of the caisson in

Figure 5.9, the angular rotation of caisson for single-line system is about 1.01 degree from the vertical axis in contrast the one for multiline system is about 0.52 degree from the vertical axis. Thus, it can be observed that the tilt of caisson decreases with using the multiline concept in about 49%.

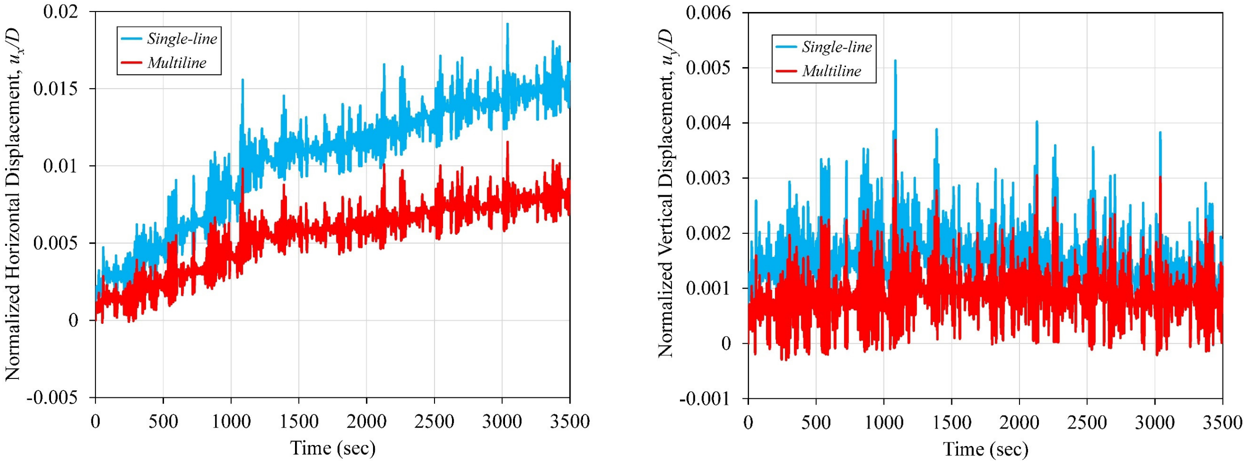

a) padeye of caisson

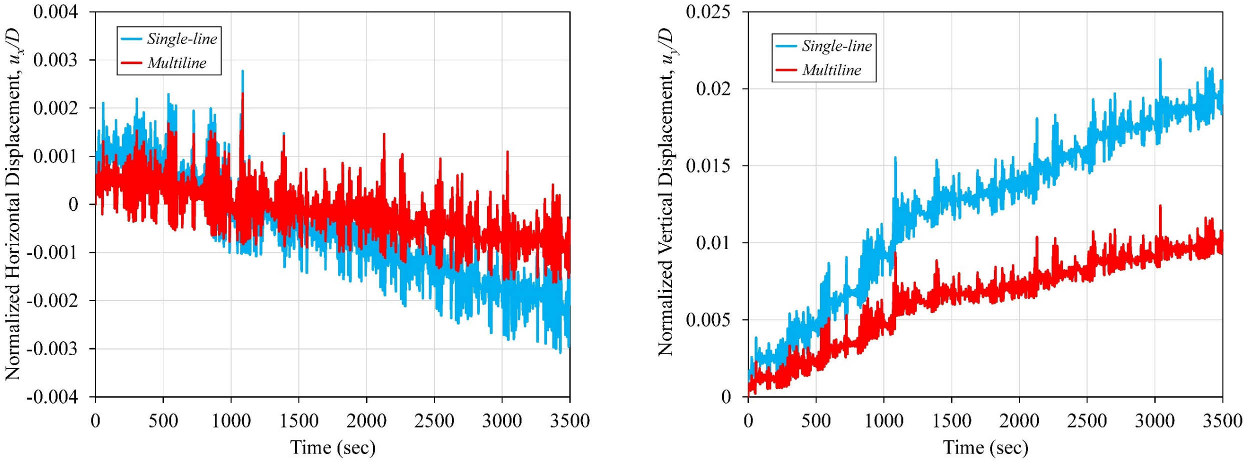

b) top of caisson

Figure 5.7. Displacements at (a) padeye and (b) top of caisson for stiff clay (soil 2) case of single-line and multiline anchor forces for WWC direction=0°

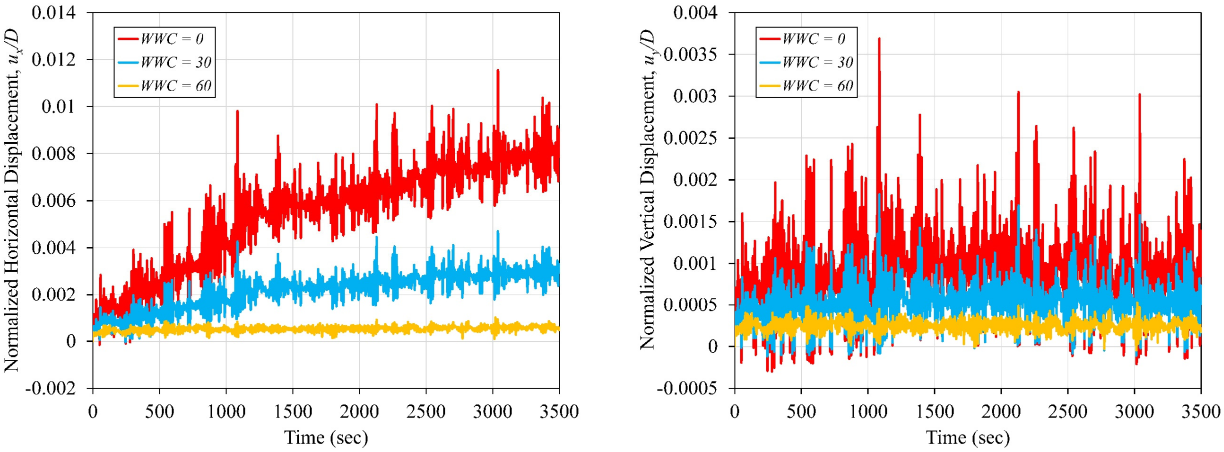

Figure 5.8. Displacements at padeye of caisson for stiff clay (soil 2) case of multiline anchor forces for WWC direction=0°, 30°, and 60°

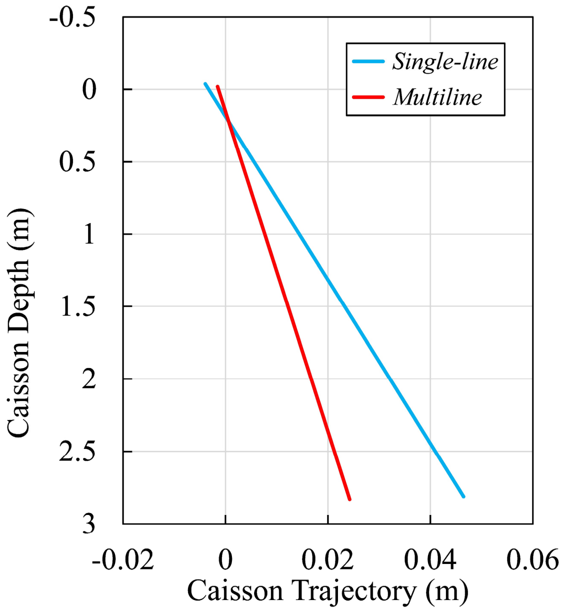

Figure 5.9. Trajectory of caisson movement for stiff clay (soil 2) case of single-line and multiline anchor forces for WWC direction=0°

The results of multiline anchor system for the case (3) of soft clay over stiff clay shows the similar trend of reduction in the magnitudes of long-term displacements at WWC=0°, as illustrated in Figure 5.10, where the percentages of reduction in deformations are about 49% and 52% for horizontal and vertical displacements respectively. Where plotting the tilt of caisson can indicate that the caisson rotation decreases with about 50% by using the multiline anchor system, as shown in Figure 5.11. Consequently, the rotation of caisson for single-line system is about 2.14 degree from the vertical axis and the caisson tilt for multiline system is about 1.06 degree from the vertical axis.

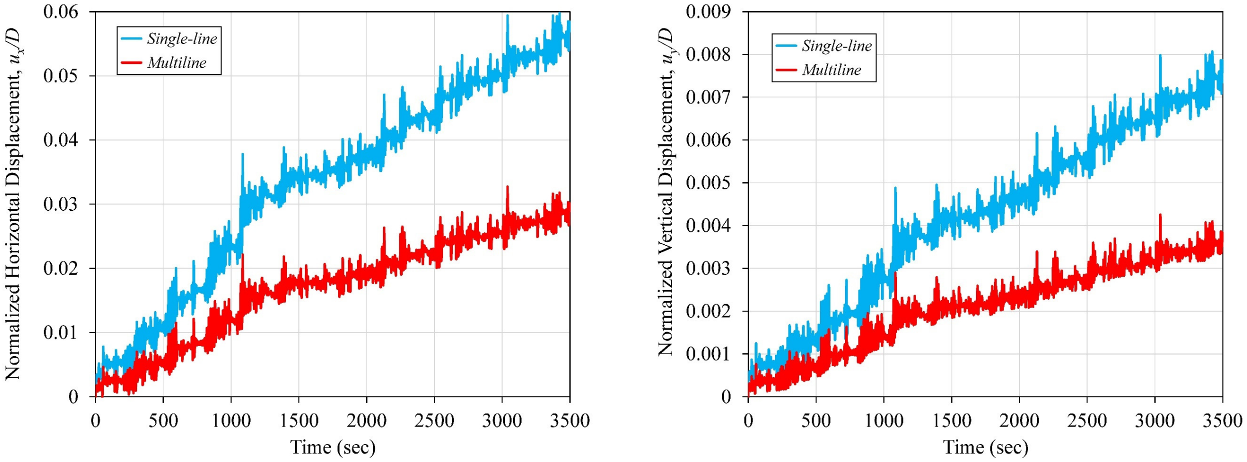

a) padeye of caisson

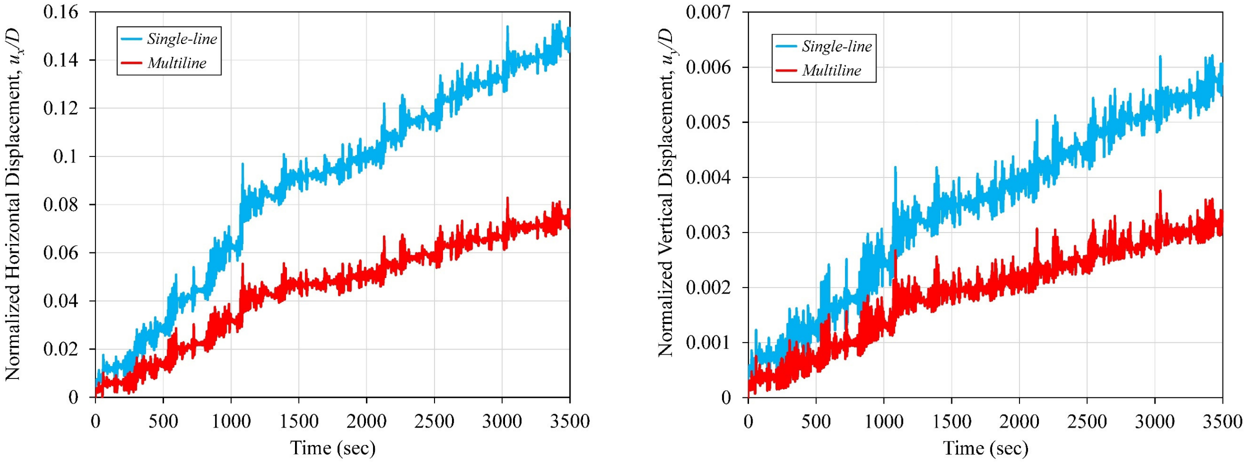

b) top of caisson

Figure 5.10. Displacements at (a) padeye and (b) top of caisson for soft over stiff clay (soil 3) case of single-line and multiline anchor forces for WWC direction=0°

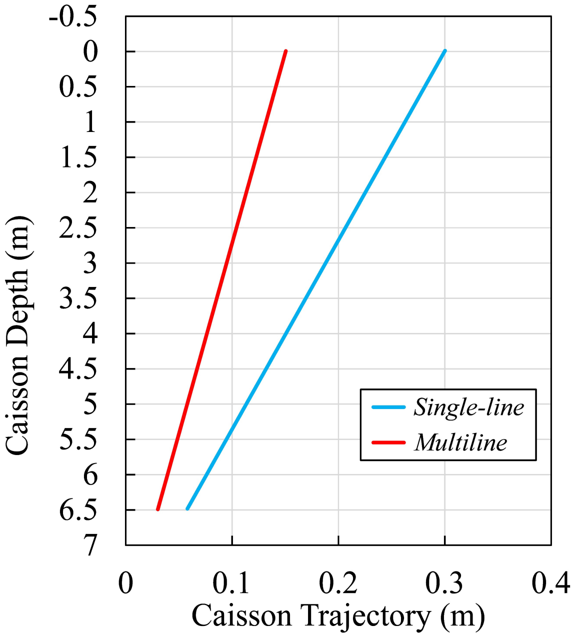

Figure 5.11. Trajectory of caisson movement for soft over stiff clay (soil 3) case of single-line and multiline anchor forces for WWC direction=0°

Further, the WWC direction for the multiline system had affected the permanent displacements that predicted for a range of WWC from 0° to 60°. Thus, increasing the WWC would result in reducing the cumulative displacements (Figure 5.12).

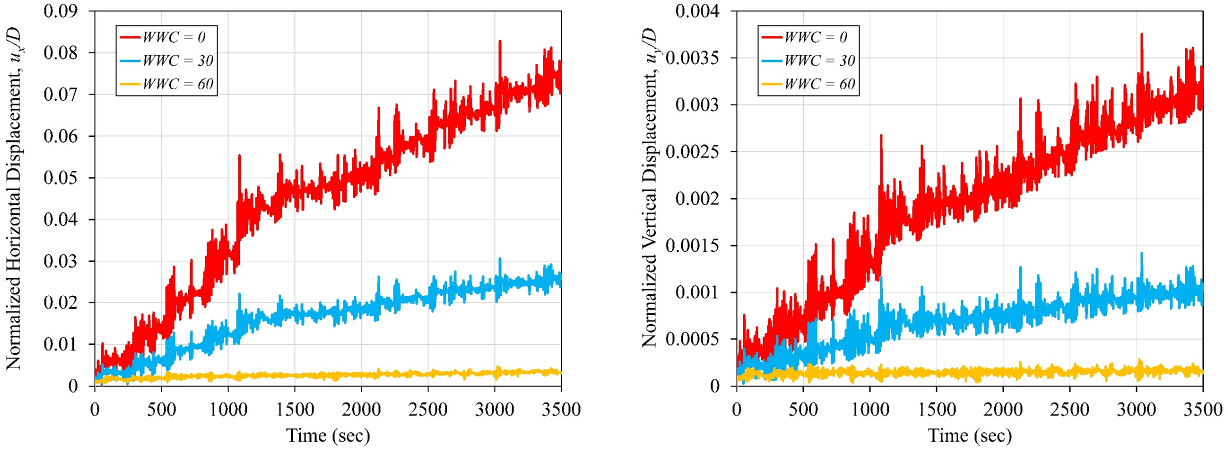

Figure 5.12. Displacements at top of caisson for soft over stiff clay (soil 3) case of multiline anchor forces for WWC direction=0°, 30°, and 60°

Furthermore, it had been used the common practice of grouping the cyclic loads into packets of uniform load intensity for the single-line system of soft clay case, where the random load amplitudes were about 350 cycles and each cycle was about 10 sec. Two modifications of loading history were considered in the simulations: Case 1 follows the load sequence shown in Figure 5.13, with the peak load occurring first at the first cycle followed by progressive packets of decreasing load amplitudes, and Case 2 for which the loading is in the reverse order of the sequence in Case 1, as shown in Figure 5.14. Comparing these both sequences with the irregular load history of the SLC time history that mentioned before for suction caisson showed some differences that depend on the sequence of implementing these cyclic loads.

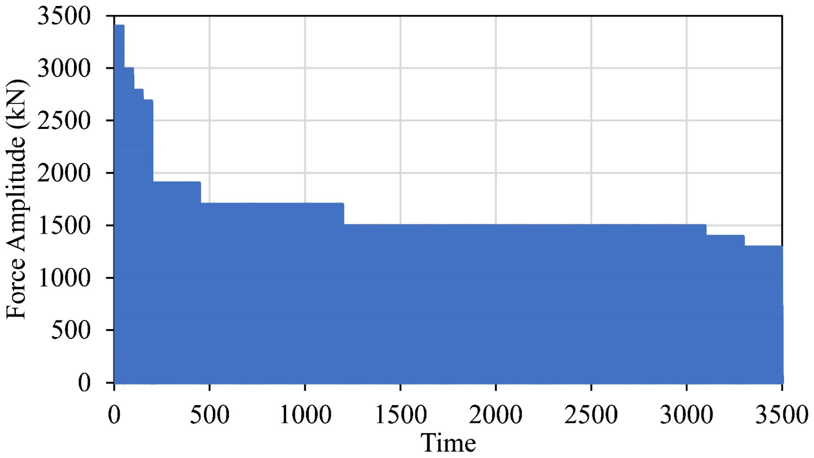

No. of cycles	Peak Force Amplitude (kN)
5	3400
5	2992
5	2788
5	2686
25	1904
75	1700
190	1496
20	1394
20	1292

Figure 5.13. Random uniform load history (decreasing sequence)

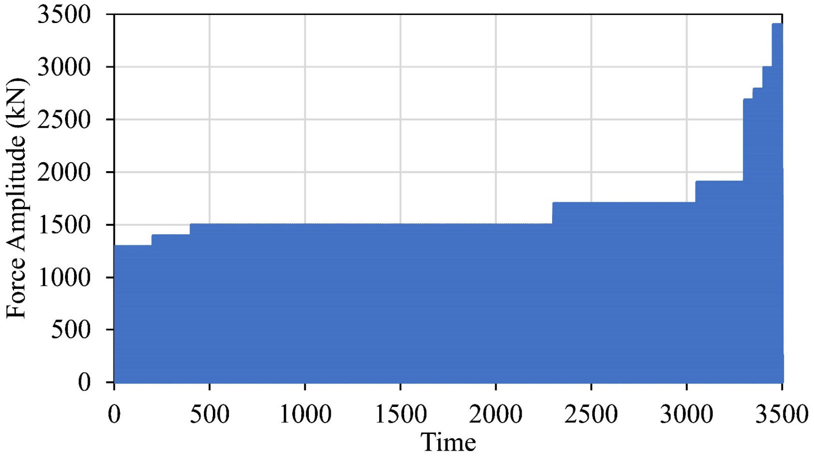

No. of cycles	Peak Force Amplitude (kN)
20	1292
20	1394
190	1496
75	1700
25	1904
5	2686
5	2788
5	2992
5	3400

Figure 5.14. Random uniform load history (increasing sequence)

Figure 5.15 and Figure 5.16 show the predicted nonlinear accumulated displacements at the padeye of caisson for horizontal and vertical directions respectively versus different load histories.

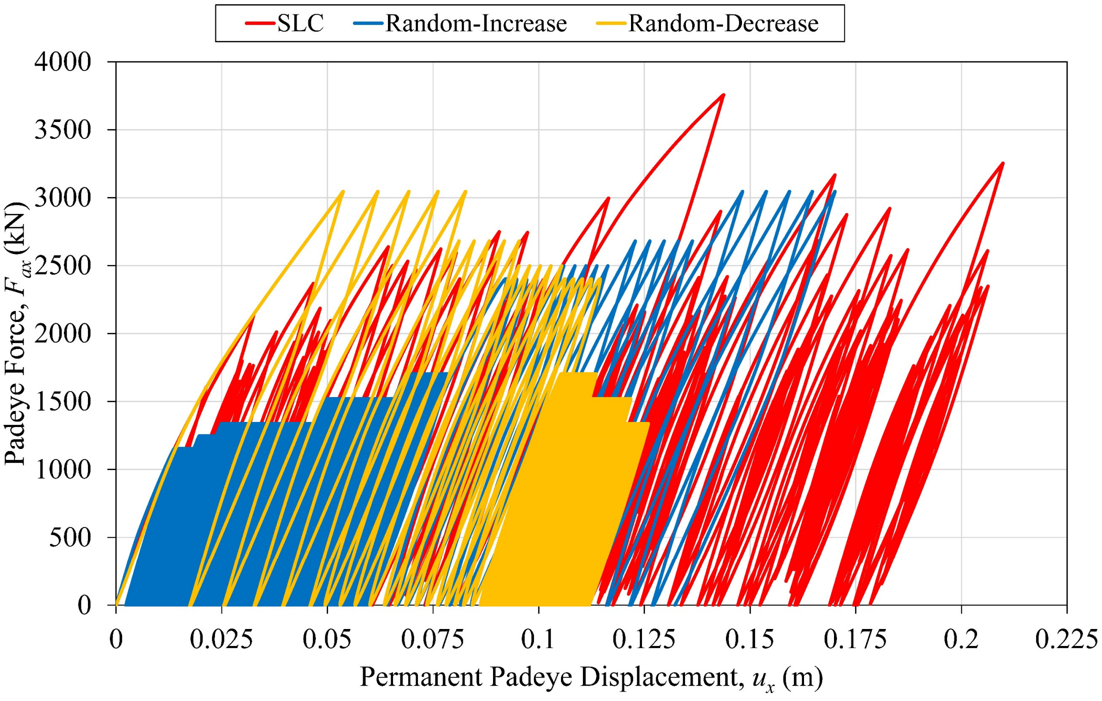

Figure 5.15. Ratcheting behavior in horizontal direction at the padeye with various cyclic amplitudes

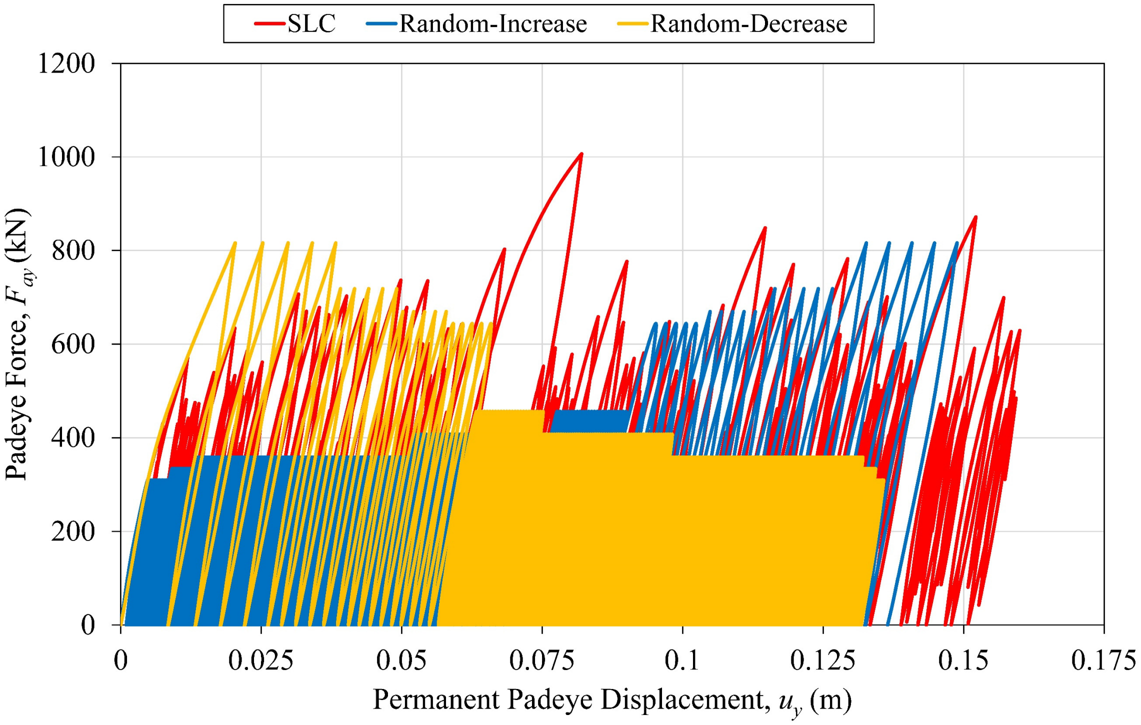

Figure 5.16. Ratcheting behavior in vertical direction at the padeye with various cyclic amplitudes

Also, Figure 5.17 and Figure 5.18 illustrate the displacement at top of caisson for horizontal and vertical directions respectively. For Case 1, a condition of progressively decreasing load amplitude, a large number of small amplitudes less than 60% of maximum amplitude applied after the end of the first 20 cycles produces lower displacements. This is in contrast to Case 2, where small loads are applied at the beginning of the sequence produce lower permanent displacements. After that, the larger amplitudes generate larger cumulative displacements when they are applied lastly in the sequence. The net result of this effect is that applying increasingly greater load amplitudes (Case 2) generates larger cumulative displacements. Thus, application of a more realistic loading history seems to generate higher cumulative displacements.

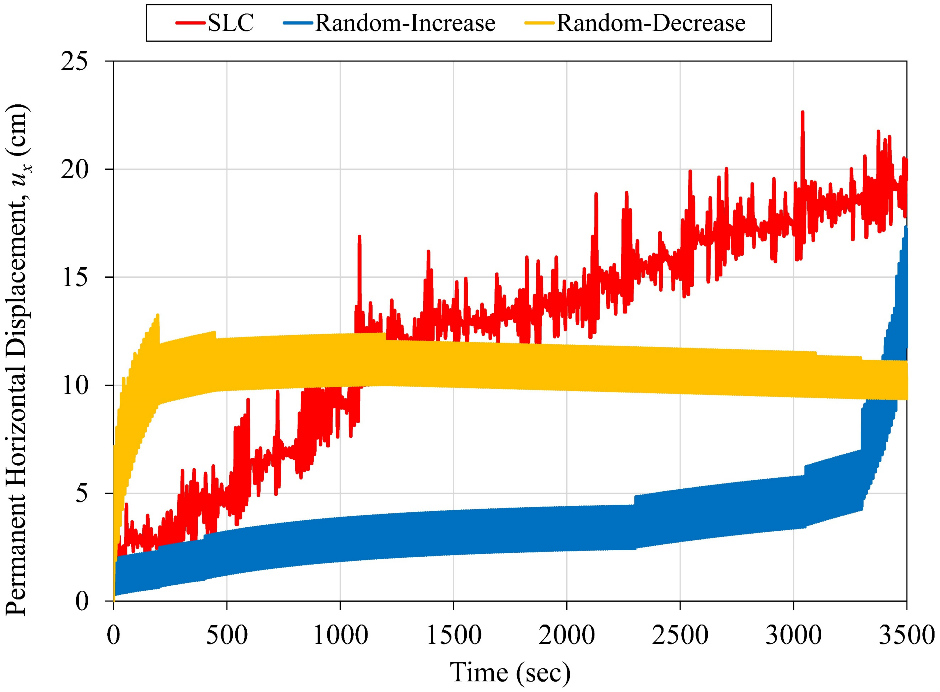

Figure 5.17. Effect of various cyclic amplitudes on horizontal permanent displacement at top of caisson

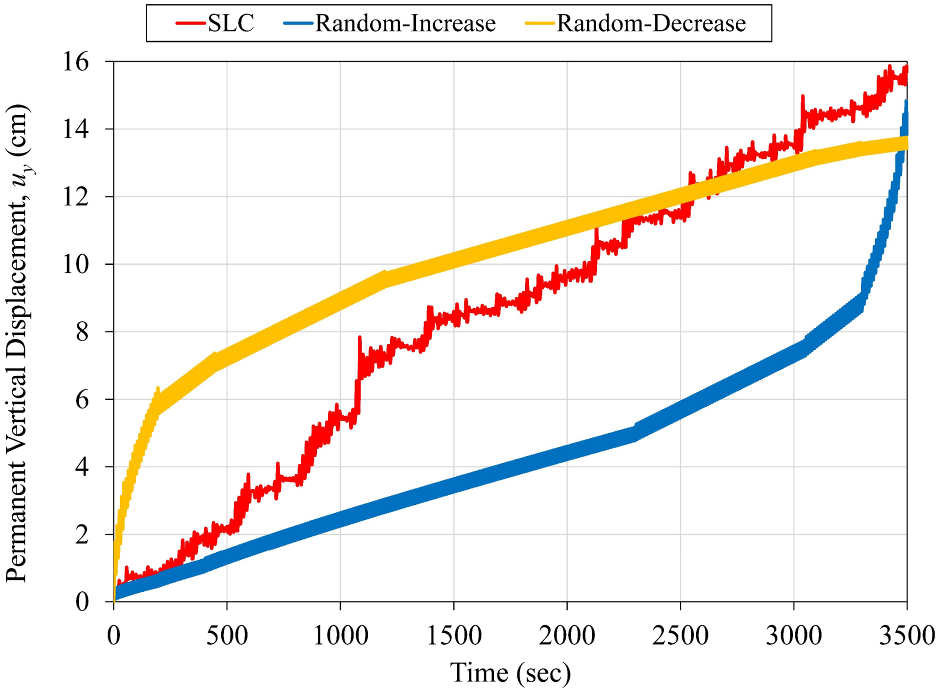

Figure 5.18. Effect of various cyclic amplitudes on vertical permanent displacement at top of caisson

6 SPRING METHODOLOGY

6.1 Soil Constitutive

This model simulates the nonlinear behavior of force and displacement relation between pile and soil corresponding to the concept of bounding surface plasticity (Dafalias, 1986; Dafalias and Herrmann, 1986; Simo and Hughes, 1998). The concept of this model consists of two-surface approaches that decomposed into a yield surface and a bounding surface. The nonlinear kinematic hardening component described the evolution of the size of the bounding surface, while the size of the elastic region (the size of the yield surface) remains constant (i.e. no isotropic hardening component). The components of this model depend on the force and displacement relation (*p*-*y* approach). The elastoplastic modulus (K^{ep}) would depend on two conditions:

If the displacement (y) is in the elastic portion, then:

$$K^{ep} = K^{e} = \frac{p}{y} \tag{11}$$

where,

p = the current force at displacement, y .

K^{e} = the soil modulus of the elastic region.

But if the displacement (y) is in the plastic portion, then:

$$K^{ep} = \frac{p}{y} = \frac{K^{p}K^{e}}{K^{p} + K^{e}} \tag{12}$$

where,

K^{p} = the soil modulus of the plastic region.

Getting displacements for each increment along the pile that imbedded in a soil for simulating a centrifuge test with a displacement control, requiring to define the plastic modulus in accordance with the increments of the displacement control by using an equation (Choi et al., 2015):

$$K^p = C_{bb} \, . K^e \frac{|p_{ult}. sign(y) - p|}{|p - p_{yield}|} \tag{13}$$

where,

C_{bb} = a hardening constant for backbone curve depends on undrained shear strength of soil.

p_{ult} = the size of the limit bounding surface.

p_{yield} = the size of the yield surface.

Also, by using the hyperbolic equation (Kondner, 1963) to express the nonlinear behavior of *p-y* curve:

$$p = \frac{y}{\frac{1}{K^e} + \frac{y}{p_{ult}}} \tag{14}$$

Substituting Eq. 14 in Eq. 13:

$$K^p = C_{bb} \, . K^e \frac{\left| p_{ult}. sign(y) - \frac{y}{\frac{1}{K^e} + \frac{y}{p_{ult}}} \right|}{\left| \frac{y}{\frac{1}{K^e} + \frac{y}{p_{ult}}} - p_{yield} \right|}$$

$$K^p = C_{bb} \, . K^e \left| \frac{p_{ult}. [K^e. sign(y). y - y. K^e + p_{ult}. sign(y)]}{K^e. y. p_{yield} - K^e. y. p_{ult} + p_{yield}. p_{ult}} \right| \tag{15}$$

Now, it could be determining the plastic modulus (K^p) to get the elastoplastic modulus (K^{ep}) from Eq. 12.

6.2 Spring Model Parameters

Required model parameters are as follows:

1. Elastic soil stiffness (K^e) can be estimated from empirical correlations regarding the undrained shear strength (s_u) and it can be determined to match centrifuge test data.
2. The yield force (p_{yield}) can be measured by:

   $$p_{yield} = K^e \, . y_{yield} \tag{16}$$

   where,

   y_{yield} = the yield displacement at which the plastic deformation initiated, and it can be calculated from:

   $$y_{yield} = \frac{2.5 \, D \, \gamma_{yield}}{1 + \mu} \tag{17}$$

   where,

   D = diameter of pile

   γ_{yield} = shear strain of soil

   μ = Poisson's ratio of soil
3. The ultimate force (p_{ult}) can be computed depends on the bearing factor (N_p) that proposed by (Murff and Hamilton, 1993) with the following exponential equation:

   $$N_p = N_1 - N_2 \, e^{-\eta z D} \tag{18}$$

   where,

N_1 = the flow-around zone bearing resistance (11.94 for full adhesion, α = 1).

$N_2 = N_1 - (2 + 0.8\alpha)$

$\eta = 0.25 + 0.05\lambda$ when $\lambda < 6$

$\eta = 0.55$ when $\lambda \geq 6$

$\lambda = s_{u0}/(k \times D)$ where (s_{u0} is soil strength at mudline and k is soil strength gradient).

z = soil depth along the pile.

Thus,

$$p_{ult} = 2 \times (N_1 - N_2\, e^{-\eta z D})\, .\, s_u\, .\, D \leq N_1 . s_u\, .\, D \tag{19}$$

In addition, it can be noted that bearing factor is doubled because there is no gapping between the soil and the pile.

4. The hardening soil constant (C_{bb}) can be estimated empirically depends on the shear strength and can be obtained to match centrifuge test data.

6.3 Spring Numerical Simulation

The analysis of laterally loaded pile in soft clay is conducted based on the general finite element method by proposed beam column elements for the pile and nonlinear elastoplastic spring elements for the surrounding soil that simulated the bounding surface plasticity model. The procedure for analyzing the problem of a laterally loaded pile in a soil can be simulated by using an equivalent one-dimensional spring element in the y-direction as shown in Figure 6.1.

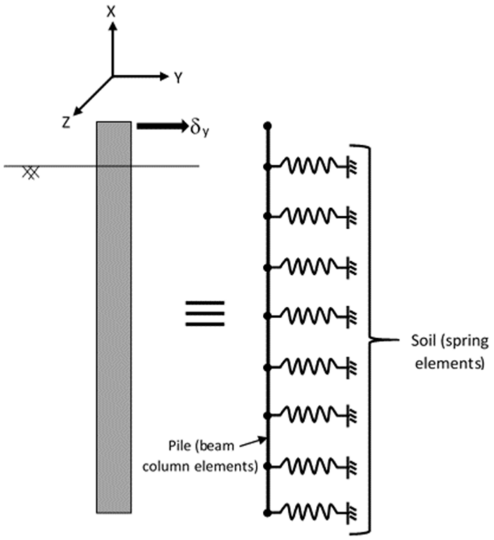

Figure 6.1. Simulation of soil-pile system

The elemental stiffness (k_e) for the beam column element of pile has 6 DOF with the following element matrix equation:

$$[k_e]=\begin{vmatrix}
A_pE_p/\Delta x & 0 & 0 & 0 & 0 & 0 & -A_pE_p/\Delta x & 0 & 0 & 0 & 0 & 0 \\
0 & 12E_pI_p/\Delta x^3 & 0 & 0 & 0 & 6E_pI_p/\Delta x^2 & 0 & -12E_pI_p/\Delta x^3 & 0 & 0 & 0 & 6E_pI_p/\Delta x^2 \\
0 & 0 & 12E_pI_p/\Delta x^3 & 0 & -6E_pI_p/\Delta x^2 & 0 & 0 & 0 & -12E_pI_p/\Delta x^3 & 0 & -6E_pI_p/\Delta x^2 & 0 \\
0 & 0 & 0 & G_pJ_p/\Delta x & 0 & 0 & 0 & 0 & 0 & -G_pJ_p/\Delta x & 0 & 0 \\
0 & 0 & -6E_pI_p/\Delta x^2 & 0 & -4E_pI_p/\Delta x & 0 & 0 & 0 & 6E_pI_p/\Delta x^2 & 0 & 2E_pI_p/\Delta x & 0 \\
0 & 6E_pI_p/\Delta x^2 & 0 & 0 & 0 & -4E_pI_p/\Delta x & 0 & -6E_pI_p/\Delta x^2 & 0 & 0 & 0 & 2E_pI_p/\Delta x \\
-A_pE_p/\Delta x & 0 & 0 & 0 & 0 & 0 & A_pE_p/\Delta x & 0 & 0 & 0 & 0 & 0 \\
0 & -12E_pI_p/\Delta x^3 & 0 & 0 & 0 & -6E_pI_p/\Delta x^2 & 0 & 12E_pI_p/\Delta x^3 & 0 & 0 & 0 & -6E_pI_p/\Delta x^2 \\
0 & 0 & -12E_pI_p/\Delta x^3 & 0 & 6E_pI_p/\Delta x^2 & 0 & 0 & 0 & 12E_pI_p/\Delta x^3 & 0 & 6E_pI_p/\Delta x^2 & 0 \\
0 & 0 & 0 & G_pJ_p/\Delta x & 0 & 0 & 0 & 0 & 0 & G_pJ_p/\Delta x & 0 & 0 \\
0 & 0 & -6E_pI_p/\Delta x^2 & 0 & 2E_pI_p/\Delta x & 0 & 0 & 0 & 6E_pI_p/\Delta x^2 & 0 & 4E_pI_p/\Delta x & 0 \\
0 & 6E_pI_p/\Delta x^2 & 0 & 0 & 0 & 2E_pI_p/\Delta x & 0 & -6E_pI_p/\Delta x^2 & 0 & 0 & 0 & 4E_pI_p/\Delta x
\end{vmatrix} \qquad (20)$$

where,

A_p= the cross-sectional area of pile.

E_p= the elastic modulus of pile.

G_p= the shear modulus of pile.

I_p= the moment of inertia of plie.

J_p= the polar moment of inertia of plie.

Δx= the element size in x-direction.

Thus, the global stiffness matrix (k_g) of pile will be:

$$[k_g] = \sum k_e \tag{21}$$

While k_{spring} will be equal to Eq. 12 at each node for its direction (i.e. its DOF in y-direction):

$$\{k_{spring}\} = K^{ep} \tag{22}$$

Then the global stiffness matrix (k_{gg}) of the system will be:

$$[k_{gg}] = [k_g] + \{k_{spring}\} \tag{23}$$

After that, the nodal unknowns can be determined from the following equation:

$$[k_{gg}]\{q\} = \{Q\} \tag{24}$$

where,

$\{q\}$ = the vector of nodal unknowns

$\{Q\}$ = the vector of applied nodal forces

6.4 Validation and Results of Spring Model

Validation of the proposed spring model would require to calibrate the centrifuge test results (Ilupeju, 2014; Zakeri et al., 2015) to achieve the soil bounding surface plasticity spring model parameters in order to analyze the same soil-pile system that used in the centrifuge test. Thus, the properties of the centrifuge test for the soft clay-pile system was implemented as shown in Table 6.1. While, the soil model parameters for the backbone curve are described in Table 6.2, or they could be determined approximately from the following equations for the elastic soil stiffness and the backbone hardening soil constant, respectively:

$$K^e = 30.053\,(s_u)^{3.6374} \tag{25}$$

and,

$$C_{bb} = 6.96\,e^{-27.72\,s_u/p_a} \tag{26}$$

where,

p_a = atmospheric pressure.

Table 6.1. Soil-pile system properties

Soil properties			Pile properties	
s_{u0}	1.5492 kPa		D	0.9144 m
k	1.0632 kPa/m		L	30.5 m
μ	0.5		E_p	208E+6 kPa
α	1		μ_p	0.3
$\overline{\gamma}$	6.12 kN/m^3		t_p	0.0508 m

Table 6.2. Model parameters for backbone curve

Depth (z), m	Elastic Soil Stiffness (K^e), kPa	Hardening Soil Constant (C_{bb})
0.322883	2.300E+03	1.389028
1.33948	8.500E+03	0.467896
2.356077	1.210E+04	0.604094
3.372673	1.500E+04	0.961988
4.38927	2.500E+04	1.347318
5.405867	4.899E+04	1.2
6.422463	4.900E+04	1.11337
7.43906	4.910E+04	0.801711
8.455657	4.930E+04	0.520061
9.472253	1.418E+05	0.359084
10.48885	2.081E+05	0.268059
11.50545	3.093E+05	0.191472
12.52204	4.235E+05	0.142707
13.53864	5.364E+05	0.112445
14.55524	5.999E+05	0.099882
15.57183	7.760E+05	0.074997
16.58843	1.073E+06	0.050722
17.60503	1.601E+06	0.029757
18.62162	2.144E+06	0.019403
19.63822	2.595E+06	0.014384
20.65482	3.398E+06	0.009176
21.67141	4.522E+06	0.005485
22.68801	6.129E+06	0.003028
23.70461	6.906E+06	0.002365
24.7212	7.426E+06	0.002027
25.7378	7.974E+06	0.001737

The comparison between the results that computed by the proposed soil spring model and that measured from the centrifuge test showed a good agreement for the bending moment along the pile (Figure 6.2) and the lateral deflection of the pile (Figure 6.3), in addition to the cyclic backbone *p-y* curves for different depths along the pile (Figure 6.4).

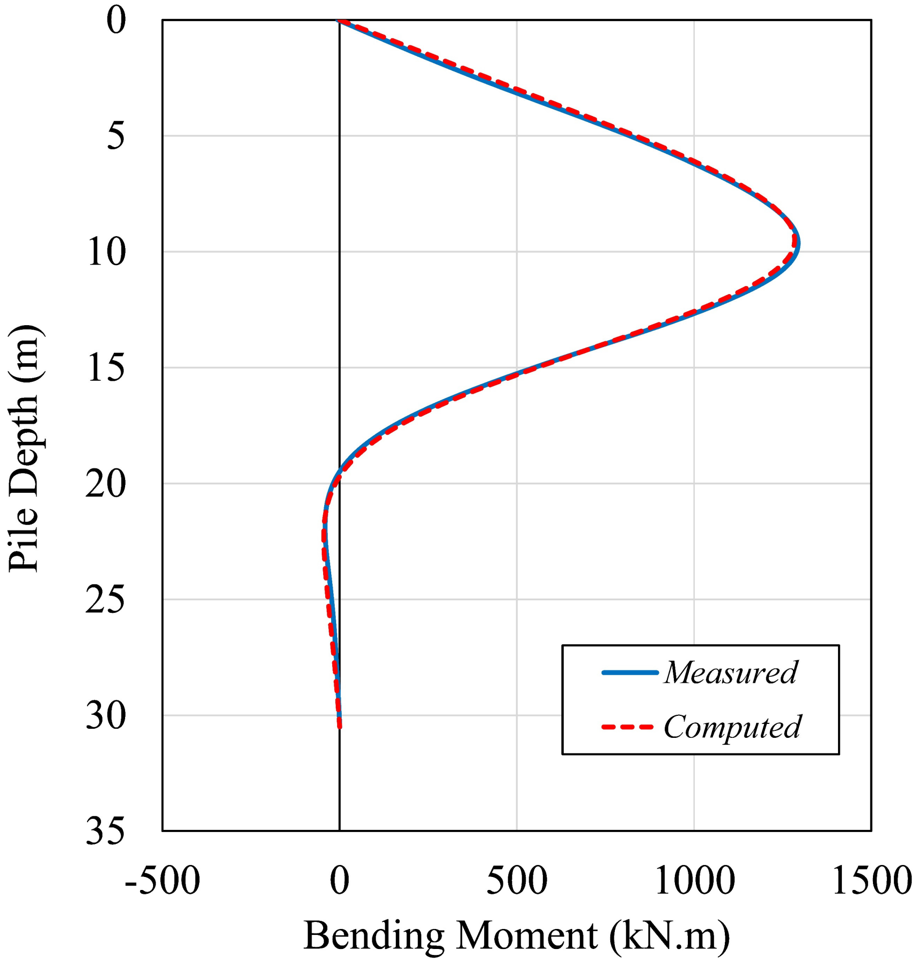

Figure 6.2. Comparison between centrifuge test measurements and proposed model computations for bending moment of pile

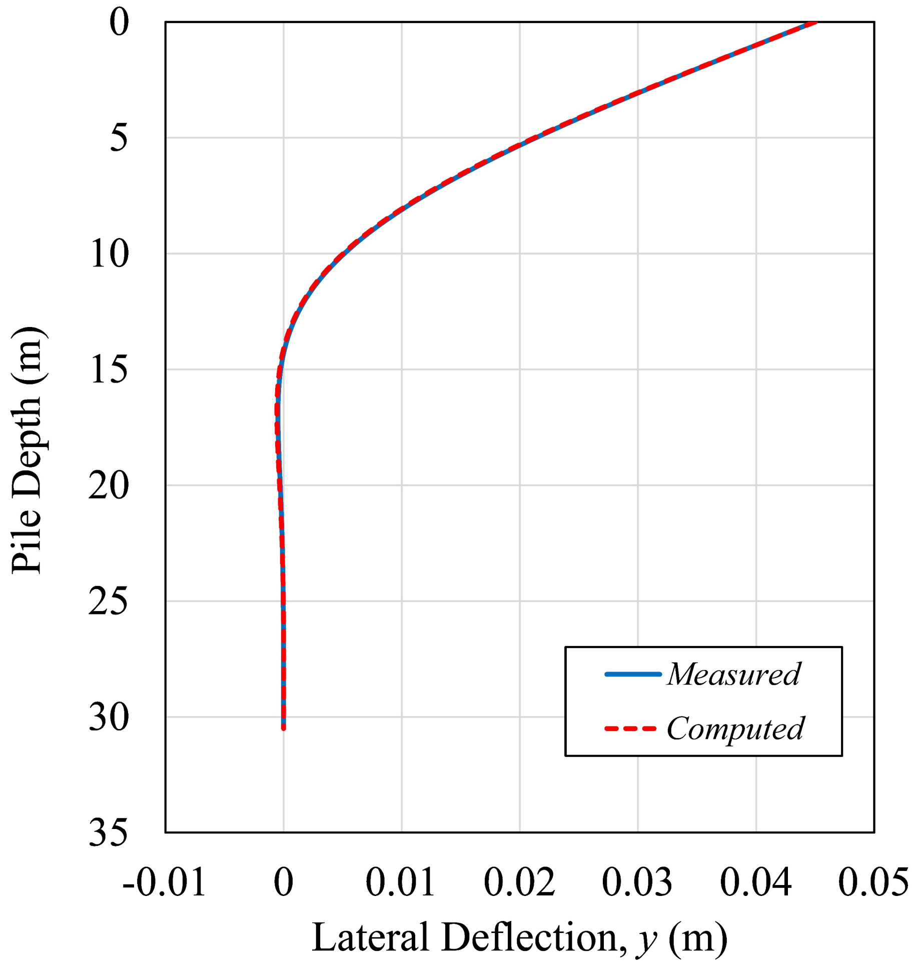

Figure 6.3. Comparison between centrifuge test measurements and proposed model computations for lateral deflection of pile

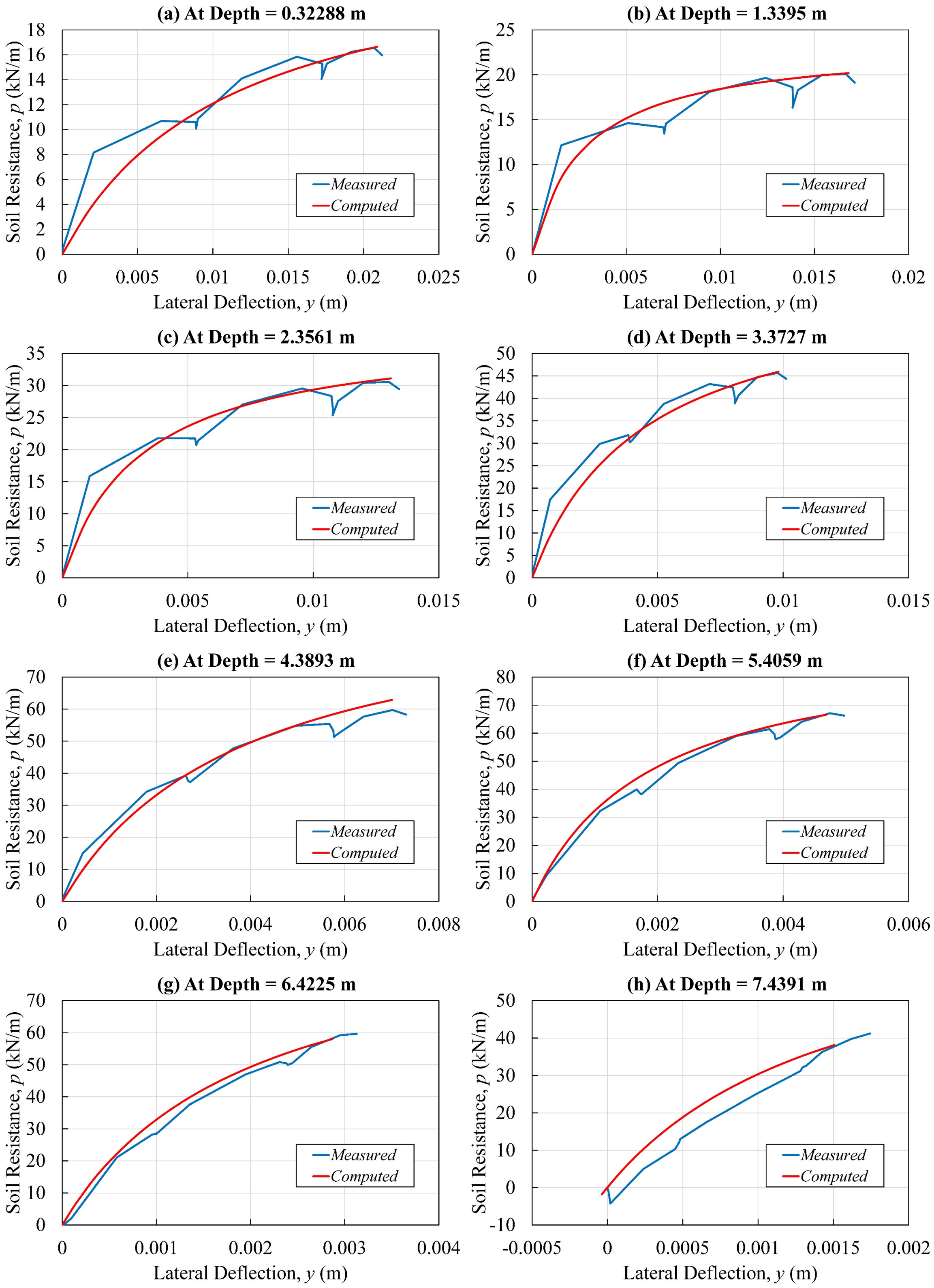

Figure 6.4. Comparison between the *p-y* results of proposed model and centrifuge test

Additionally, implementation of unloading-reloading cases for the laterally loaded pile can be proceeded by using the Equation (15) by changing the backbone hardening constant (C_{bb}) with the unloading hardening constant (C_{un}) for the unloading condition and the reloading hardening constant (C_{re}) for the reloading condition. The values of unloading and reloading constants can be dependent on the depth of soil and the number of loading cycles of the soil-pile system. Thus, the unloading hardening constant (C_{un}) and the reloading hardening constant (C_{re}) for the cyclic loads of the same soil-pile system that mentioned before are tabulated in Table 6.3 and Table 6.4, respectively. The comparison between the results that computed by the proposed soil cyclic spring model and that measured from the centrifuge test showed a good agreement for the bending moment along the pile (Figure 6.5) and the lateral deflection of the pile (Figure 6.6) at the end of the 10th, 20th, 50th, and 140th cycles, in addition to the cyclic *p-y* curves at the end of each cycle, as shown for example at the 10th cycle (Figure 6.7).

Consequently, from comparing the bending moment of the subsequent cycles from utilizing the proposed soil spring model shown in Figure 6.8, it can be noticed that the bending moment decreases gradually with increasing the number of cycles. Thus, the proposed model can catch the soil degradation under the cyclic loading.

Table 6.3. Unloading hardening soil constant (C_{un})

Depth (m)	Number of Cycles															
	1	10	20	30	40	50	60	70	80	90	100	110	120	130	140	150
0.322883	2.100	1.680	1.470	1.365	1.260	1.155	1.050	1.040	1.029	0.987	0.956	0.949	0.924	0.903	0.893	0.882
1.33948	0.800	0.640	0.520	0.520	0.480	0.424	0.400	0.396	0.392	0.388	0.384	0.382	0.376	0.372	0.368	0.364
2.356077	1.100	0.825	0.660	0.660	0.605	0.605	0.528	0.517	0.512	0.495	0.490	0.484	0.468	0.457	0.451	0.446
3.372673	1.850	1.388	1.110	1.110	1.055	0.962	0.925	0.907	0.897	0.870	0.851	0.845	0.823	0.805	0.796	0.786
4.38927	2.700	2.025	1.620	1.566	1.485	1.350	1.296	1.242	1.229	1.215	1.202	1.193	1.180	1.161	1.148	1.134
5.405867	2.450	2.083	1.715	1.715	1.593	1.470	1.421	1.409	1.397	1.384	1.372	1.360	1.348	1.335	1.323	1.311
6.422463	2.300	1.955	1.679	1.610	1.541	1.426	1.380	1.334	1.323	1.311	1.300	1.297	1.295	1.286	1.277	1.265
7.43906	2.200	1.650	1.540	1.540	1.518	1.408	1.364	1.342	1.331	1.320	1.309	1.298	1.296	1.291	1.280	1.276
8.455657	3.000	1.350	1.320	1.200	1.260	1.260	1.230	1.200	1.185	1.170	1.155	1.149	1.146	1.140	1.134	1.125
9.472253	0.214	0.211	0.209	0.207	0.205	0.203	0.201	0.199	0.197	0.195	0.193	0.191	0.189	0.187	0.186	0.184
10.48885	0.191	0.189	0.187	0.185	0.183	0.181	0.180	0.178	0.176	0.174	0.173	0.171	0.169	0.167	0.166	0.164
11.50545	0.167	0.166	0.164	0.162	0.161	0.159	0.158	0.156	0.155	0.153	0.151	0.150	0.148	0.147	0.145	0.144
12.52204	0.149	0.148	0.146	0.145	0.144	0.142	0.141	0.139	0.138	0.137	0.135	0.134	0.132	0.131	0.130	0.129
13.53864	0.136	0.135	0.134	0.132	0.131	0.130	0.128	0.127	0.126	0.124	0.123	0.122	0.121	0.120	0.118	0.117
14.55524	0.130	0.129	0.128	0.126	0.125	0.124	0.123	0.121	0.120	0.119	0.118	0.117	0.115	0.114	0.113	0.112
15.57183	0.116	0.115	0.114	0.113	0.112	0.111	0.110	0.109	0.107	0.106	0.105	0.104	0.103	0.102	0.101	0.100
16.58843	0.100	0.099	0.098	0.097	0.096	0.095	0.094	0.093	0.092	0.091	0.091	0.090	0.089	0.088	0.087	0.086
17.60503	0.081	0.081	0.080	0.079	0.078	0.077	0.077	0.076	0.075	0.074	0.074	0.073	0.072	0.071	0.071	0.070
18.62162	0.069	0.068	0.068	0.067	0.066	0.066	0.065	0.064	0.064	0.063	0.062	0.062	0.061	0.061	0.060	0.059
19.63822	0.061	0.061	0.060	0.060	0.059	0.058	0.058	0.057	0.057	0.056	0.056	0.055	0.054	0.054	0.053	0.053
20.65482	0.052	0.051	0.051	0.050	0.050	0.049	0.049	0.048	0.048	0.047	0.047	0.046	0.046	0.045	0.045	0.044
21.67141	0.042	0.042	0.041	0.041	0.041	0.040	0.040	0.039	0.039	0.039	0.038	0.038	0.038	0.037	0.037	0.036
22.68801	0.034	0.033	0.033	0.033	0.032	0.032	0.032	0.031	0.031	0.031	0.030	0.030	0.030	0.030	0.029	0.029
23.70461	0.031	0.030	0.030	0.030	0.029	0.029	0.029	0.028	0.028	0.028	0.028	0.027	0.027	0.027	0.027	0.026
24.7212	0.029	0.028	0.028	0.028	0.028	0.027	0.027	0.027	0.027	0.026	0.026	0.026	0.026	0.025	0.025	0.025
25.7378	0.027	0.027	0.027	0.026	0.026	0.026	0.026	0.025	0.025	0.025	0.025	0.024	0.024	0.024	0.024	0.023

Table 6.4. Reloading hardening soil constant (C_{re})

Depth (m)	Number of Cycles															
	1	10	20	30	40	50	60	70	80	90	100	110	120	130	140	150
0.322883	2.000	1.500	1.460	1.300	1.200	1.100	1.040	1.030	1.020	0.960	0.950	0.940	0.920	0.900	0.880	0.870
1.33948	0.750	0.563	0.525	0.488	0.450	0.413	0.398	0.394	0.390	0.386	0.383	0.379	0.375	0.371	0.364	0.360
2.356077	1.000	0.700	0.690	0.620	0.590	0.580	0.520	0.515	0.510	0.490	0.485	0.480	0.465	0.455	0.450	0.445
3.372673	1.750	1.138	1.138	1.068	1.015	0.945	0.910	0.901	0.893	0.858	0.849	0.840	0.814	0.796	0.788	0.779
4.38927	2.500	1.625	1.625	1.525	1.400	1.375	1.250	1.238	1.225	1.213	1.200	1.188	1.175	1.150	1.138	1.125
5.405867	2.350	1.763	1.763	1.622	1.504	1.457	1.410	1.398	1.387	1.375	1.363	1.351	1.340	1.328	1.316	1.304
6.422463	2.200	1.760	1.650	1.584	1.474	1.386	1.342	1.331	1.320	1.309	1.298	1.296	1.287	1.276	1.265	1.254
7.43906	2.100	1.575	1.575	1.575	1.470	1.365	1.344	1.334	1.323	1.313	1.302	1.300	1.292	1.281	1.271	1.260
8.455657	2.500	1.400	1.400	1.375	1.325	1.250	1.200	1.188	1.175	1.163	1.150	1.148	1.143	1.138	1.138	1.138
9.472253	0.214	0.211	0.209	0.207	0.205	0.203	0.201	0.199	0.197	0.195	0.193	0.191	0.189	0.187	0.186	0.184
10.48885	0.191	0.189	0.187	0.185	0.183	0.181	0.180	0.178	0.176	0.174	0.173	0.171	0.169	0.167	0.166	0.164
11.50545	0.167	0.166	0.164	0.162	0.161	0.159	0.158	0.156	0.155	0.153	0.151	0.150	0.148	0.147	0.145	0.144
12.52204	0.149	0.148	0.146	0.145	0.144	0.142	0.141	0.139	0.138	0.137	0.135	0.134	0.132	0.131	0.130	0.129
13.53864	0.136	0.135	0.134	0.132	0.131	0.130	0.128	0.127	0.126	0.124	0.123	0.122	0.121	0.120	0.118	0.117
14.55524	0.130	0.129	0.128	0.126	0.125	0.124	0.123	0.121	0.120	0.119	0.118	0.117	0.115	0.114	0.113	0.112
15.57183	0.116	0.115	0.114	0.113	0.112	0.111	0.110	0.109	0.107	0.106	0.105	0.104	0.103	0.102	0.101	0.100
16.58843	0.100	0.099	0.098	0.097	0.096	0.095	0.094	0.093	0.092	0.091	0.091	0.090	0.089	0.088	0.087	0.086
17.60503	0.081	0.081	0.080	0.079	0.078	0.077	0.077	0.076	0.075	0.074	0.074	0.073	0.072	0.071	0.071	0.070
18.62162	0.069	0.068	0.068	0.067	0.066	0.066	0.065	0.064	0.064	0.063	0.062	0.062	0.061	0.061	0.060	0.059
19.63822	0.061	0.061	0.060	0.060	0.059	0.058	0.058	0.057	0.057	0.056	0.056	0.055	0.054	0.054	0.053	0.053
20.65482	0.052	0.051	0.051	0.050	0.050	0.049	0.049	0.048	0.048	0.047	0.047	0.046	0.046	0.045	0.045	0.044
21.67141	0.042	0.042	0.041	0.041	0.041	0.040	0.040	0.039	0.039	0.039	0.038	0.038	0.038	0.037	0.037	0.036
22.68801	0.034	0.033	0.033	0.033	0.032	0.032	0.032	0.031	0.031	0.031	0.030	0.030	0.030	0.030	0.029	0.029
23.70461	0.031	0.030	0.030	0.030	0.029	0.029	0.029	0.028	0.028	0.028	0.028	0.027	0.027	0.027	0.027	0.026
24.7212	0.029	0.028	0.028	0.028	0.028	0.027	0.027	0.027	0.027	0.026	0.026	0.026	0.026	0.025	0.025	0.025
25.7378	0.027	0.027	0.027	0.026	0.026	0.026	0.026	0.025	0.025	0.025	0.025	0.024	0.024	0.024	0.024	0.023

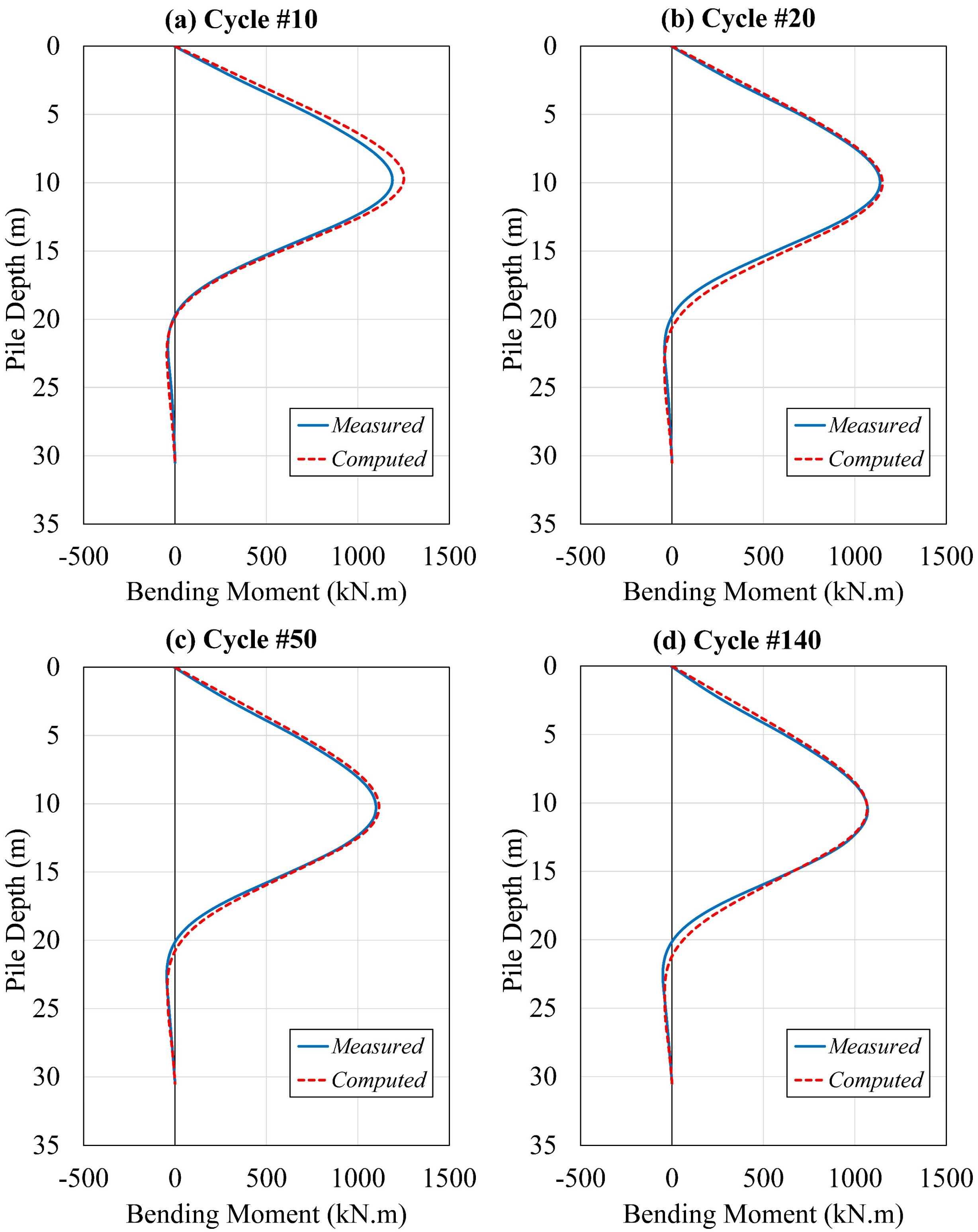

(a) Cycle #10

(b) Cycle #20

(c) Cycle #50

(d) Cycle #140

Figure 6.5. Comparison between centrifuge test measurements and proposed model computations for bending moment of pile at different cycle numbers

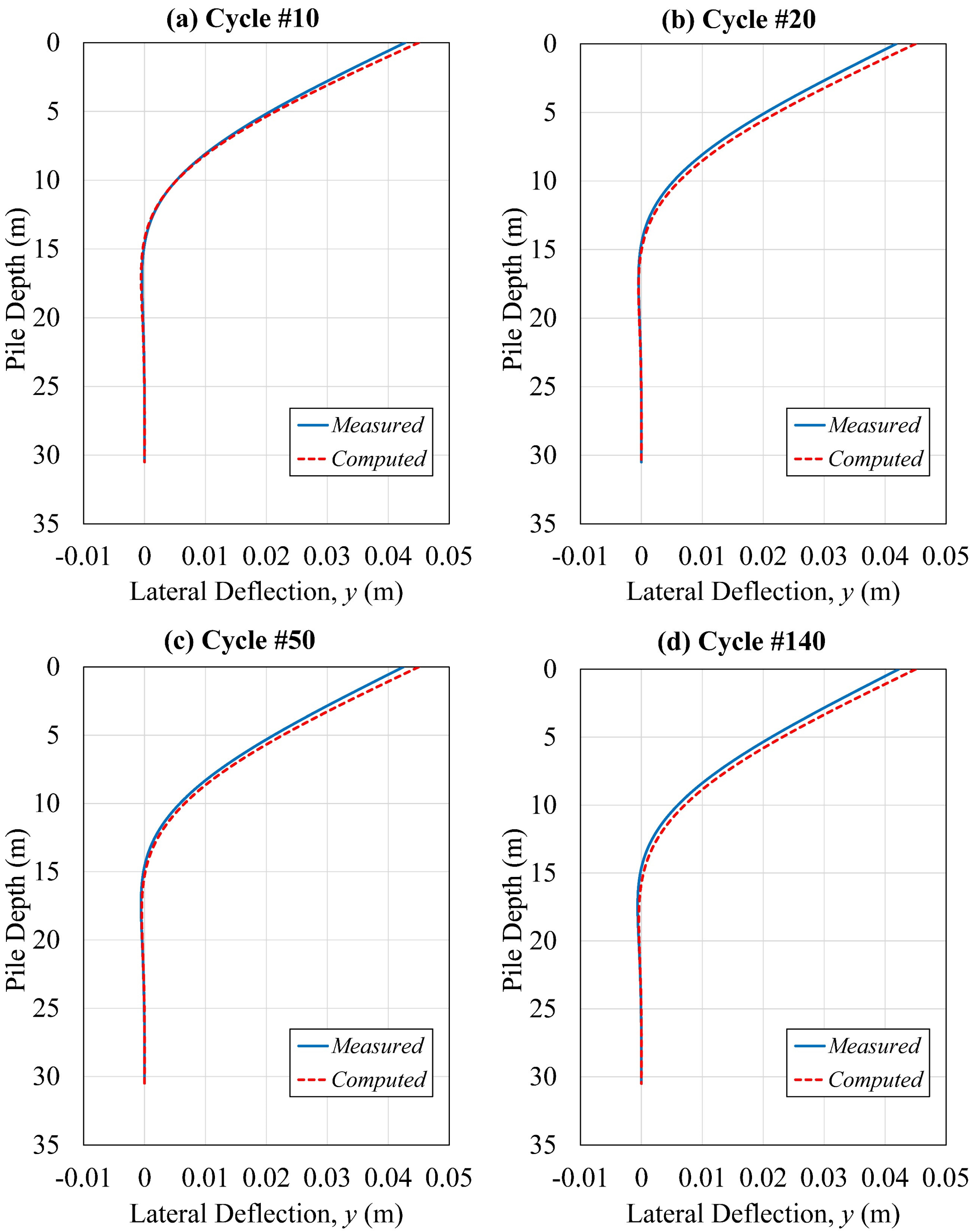

Figure 6.6. Comparison between centrifuge test measurements and proposed model computations for lateral deflection of pile at different cycle numbers

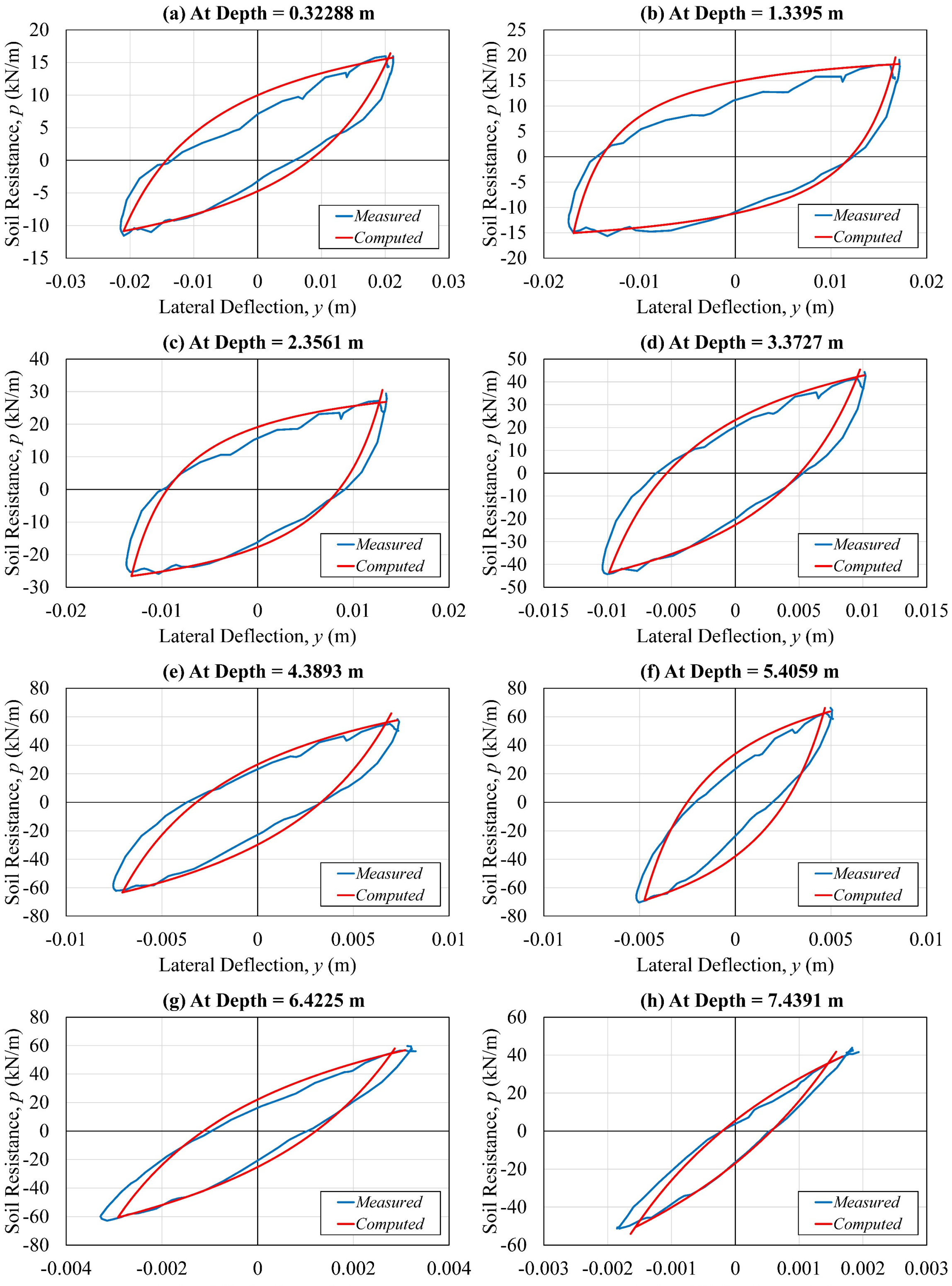

Figure 6.7. Comparison between the *p-y* results of proposed model and centrifuge test at the end of 10th cycle

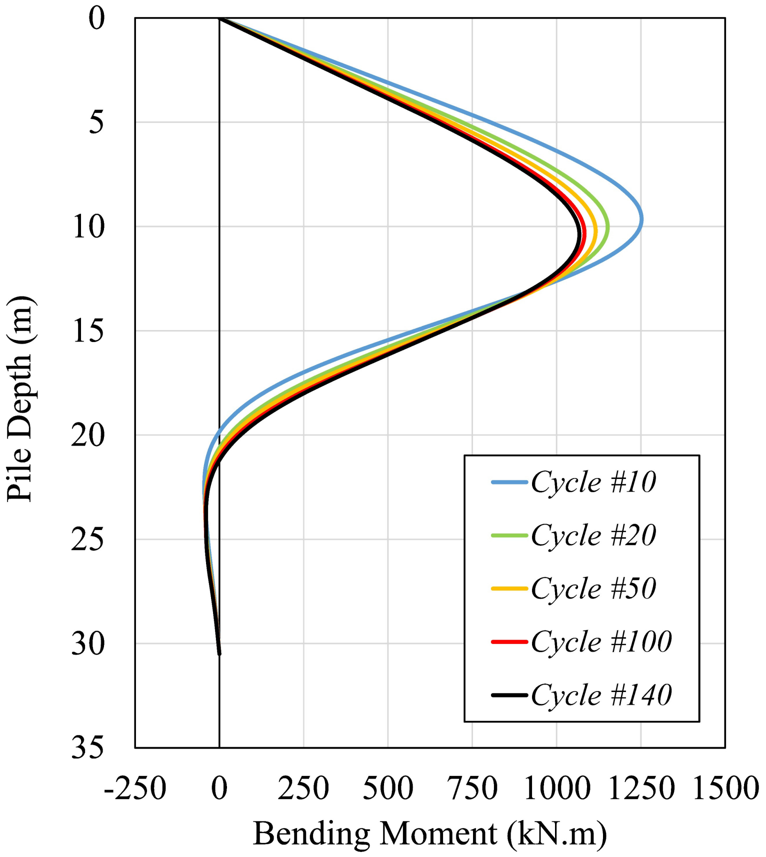

Figure 6.8. Bending moment diagram along the pile depth for different cycle numbers

7 CONCLUSIONS AND RECOMMENDATIONS

7.1 Overview

This dissertation deals with a range of topics relevant to geotechnical modeling of retaining walls and piles/caissons in clay under cyclic loading. Two approaches have been used in this study: the continuum and the spring methodologies. The continuum methodology is based on two-dimensional finite element model and axisymmetric with asymmetric Fourier elements finite element model using the software ABAQUS. The model has been successfully calibrated by using experimental results (Gilbert et al., 2015; Senanayake, 2016) and validated by comparisons to field measurement data from the Union Pacific Railroad (UPRR) project at College Station, Texas.

7.2 Wall Problem

This work has presented a bounding surface plasticity model (i.e. a nonlinear kinematic hardening model) to study the behavior of a soil-wall system under cyclic loading in order to predict the cumulative plastic deformation and the ratcheting behavior of the soil. As this model is included in the ABAQUS library, it is readily accessible to practitioners interested in cyclic response of walls and foundations in clay soils. The proposed model has produced reasonable results. In addition to the numerical validation mentioned previously, the model predictions are in reasonable conformance to the measured response of a retaining wall system subjected to live loads from adjacent railroad operations.

Nonlinear kinematic model approaches might be used to predict well the behavior of soil masses subjected to cyclic loads, such as trains passing near a wall-soil system. Such simulation can assist designers in evaluating the safety of retaining walls that support railroad tracks by accurately predicting the cumulative plastic deformation. Current design methods based on linear elasticity or limit equilibrium methods are not capable of predicting cumulative cyclic displacements; therefore, modifying these methods to achieve less conservative designs is not recommended. The full nonlinear analyses capable of predicting the cumulative plastic deformations proposed in this paper may be applied for this purpose.

Submitting a tabulated result that illustrated the power law relation between the lateral displacement at the top-height of wall and the vertical settlement under the center of train track can be useful to designers for predicting the settlements under the railroad track from the observed lateral wall deflections or vice versa.

After conducting a parametric study of factors potentially affecting wall performance under cyclic live loads, key conclusions can be summed up as follows:

1. Increasing the initial elastic modulus of the soil regarding the undrained soil strength, as E/s_u ratio, between the range of (500-800) with 100% of full train load can lead to decrease the lateral wall deflection by up to 79%. Moreover, the bending moment that computed from the proposed model was less than the allowable bending moment of wall for each E/s_u ratio excepting the one with 500 that had exceeded the allowable moment.
2. Increasing the cycles of loading can affect the lateral displacements, the bending moments, and the lateral soil pressure distributions along the wall, which will increase them as shown in Figure 4.7, Figure 4.8, and Figure 4.9 respectively. Nevertheless,

these results will gradually decrease for the succeeding cycles due to the ratchet strain that gradually decreased between the subsequent cycles with increasing the number of cycles, as depicted in Figure 4.10, Figure 4.11, and Figure 4.12.

3. The model is very sensitive to the σ_0/σ_{max} ratio, such that lateral displacement, bending moment, and soil pressure along the wall can change significantly for differences in this ratio as small as of 0.01. Lateral displacement, bending moment and soil pressure all tend to decrease with increasing σ_0/σ_{max} . For instance, increasing the σ_0/σ_{max} ratio from 0.09 to 0.10 with E/s_u=800 and 100% of full train load can lead to decrease the lateral displacement by up to 63%, as shown in Figure 4.14.
4. Increasing the wall stiffness (EI), where the sheet pile moment of inertia (I) is increased while Young's modulus is held constant, decreases the maximum lateral wall displacement by up to 49% over the range of (PZ22-PZ40) in the case of E/s_u=800 and 100% of full train load, as shown in Figure 4.18. Also, the bending moment (Figure 4.19) and the lateral soil pressure (Figure 4.20) under the base of excavation will increase with increasing the EI of wall. The lateral soil pressure above the base of excavation will be unnoticeable difference as the EI of wall increases.
5. Generally, increasing the wall height (H_E) above the base of excavation will increase the wall displacements. For example, considering increasing H_E over a range of 8-12 ft, with E/s_u=800 and 100% of full train load, increases the deflection of top-height wall by a factor of 1.52, as shown in Figure 4.21. In addition, the maximum wall moment increases with increasing the wall height at the end of 10000 cycles of the case of 100% train load, as depicted in Figure 4.22. In contrast, the maximum lateral

soil pressure under the level of excavation for each case of different wall height can decrease with increasing the H_E of the system, as shown in Figure 4.24.

6. Increasing the distance ($Dist$) between the edge of train track and the top of wall over a range of 6-10 ft, using E/s_u=800 and 100% of the full train load, decreases the maximum lateral displacement at top of the wall by up to 74%, as presented in Figure 4.25. In addition, the maximum wall bending moment (Figure 4.26) will decrease by up to 76% with increasing the distance ($Dist$).

7.3 Caisson Problem

This study presents a numerical study of permanent displacements for caissons and short piles in clay subjected to cyclic loading. Constitutive behavior is defined by a nonlinear kinematic hardening model capable of generating plastic deformations at stress levels less than the soil strength such that ratcheting behavior (Figure 3.2) can be simulated. Solution to the boundary value problem involves a finite element model employing Fourier elements to analyze an axisymmetric pile subjected to asymmetric loading. Comparison of the Fourier analysis to a true 3-dimensional analysis (Figure 3.9) shows good agreement. The constitutive model and Fourier elements are contained in the respective material and element libraries in the standard version of ABAQUS (Simulia, 2014); thus, the methodology presented herein is generally amenable to routine design use. Current design methods for predicting pile displacements, such as *p-y* curves or finite element models employing conventional elastoplastic constitutive laws, are generally not capable of predicting cumulative displacements under cyclic loading. Thus, the approach outlined in this paper addresses a significant gap in state of practice for understanding and predicting pile behavior under cyclic loading.

The material model requires definition of four soil parameters: soil strength in uniaxial compression σ_{max} (or alternatively undrained shear strength s_u), Poisson's ratio μ, Young's modulus E, and the initial yield stress σ_0. The strength profile is established by conventional site investigations, while the Poisson's ratio under undrained loading is established by the incompressibility constraint. Thus, reliable prediction of permanent displacements largely centers around selection of appropriate E and σ_0 values. The approach advocated by the authors (illustrated by Figure 3.16) is to estimate these values through calibrations to model test measurements of cumulative displacements under lateral cyclic loading.

The findings of a parametric study of a typical caisson in a normally consolidated clay can be summarized as follows:

1. Cumulative displacements under cyclic loading are highly sensitive to the soil initial stiffness, with an order of magnitude difference in predicted displacements occurring over the range E/s_u = 200 to 900 that was considered in the study (Figure 4.44). Calibration to the University of Texas data (Gilbert et al., 2015; Senanayake, 2016) showed that E/s_u = 90 provided a good match between prediction and measurement. However, the experimental data from this study was from tests in a remolded kaolinite test bed which could arguably have a low stiffness relative to natural clay deposits.
2. The initial yield stress σ_0/σ_{max} is a second soil property significantly affecting cumulative displacements (Figure 4.49). The recommended range by Anastasopoulos et al. (2011) σ_0/σ_{max} = 0.1 to 0.3 is supported by the analysis in this study showing σ_0/σ_{max} = 0.1 providing a good match to the University of Texas data.

3. At shallow load angles (e.g. ψ = 15 degrees or less) the soil-pile interface adhesion factor has a modest influence on predicted cumulative displacements under cyclic loading, less than 30% (Figure 4.56) when a range α = 0.7 to 1.0 is considered. At higher load angles (ψ = 30 degrees, Figure 4.57) predicted cumulative displacements become significantly more sensitive to adhesion α. In general, load angle ψ strongly influences predicted cumulative displacements, with Figure 4.61 showing an eightfold increase in displacements corresponding to an increase in load angle ψ = 0 to 45 degrees.
4. Load reversals have a somewhat complex effect on predicted horizontal cumulative displacements. Under conditions of full load reversal, ζ = -1, the reversal has the effect of restoring the pile to its original position, such that the cumulative displacement is virtually zero (Figure 4.69). However, partial reversal, ζ = -0.2 to -0.5, can produce cumulative displacements by some 20% over the zero reversal, ζ = 0, condition.
5. When considering load histories of variable amplitude, the sequence of large loading events can have a moderate but noticeable effect on predicted cumulative displacements. Large load amplitudes occurring early in the loading history lead to lower cumulative displacements compared to displacements produced by large amplitude loads occurring at the end of the loading history. The particular case analyzed in Figure 4.75 and Figure 4.76, which show that this effect can be on the order of 25%.

In addition, this study addressed the cyclic and directional response of suction caissons anchors under the single-line and multiline cyclic loadings with various soil types regarding the permanent displacements of soil-caisson system for floating offshore wind turbines. The cumulative displacements of suction caissons for FOWT under cyclic loading can be significantly affected by the anchor type of single-line and multiline mooring systems, as shown in Figure 5.5, Figure 5.7, and Figure 5.10 . It can be indicated that the permanent displacements from adapting the multiline anchor system have achieved a reduction in contrast to the conventional method of a single-line anchor system for floating wind farms. Furthermore, the directions of wind, wave, and current (WWC) have an additional influence in predicting the long-term deformations occurring over the range WWC = 0° to 60° that was considered in the study. The suction caisson anchor can be considered likely to be accommodating to the multiline anchor system under cyclic loadings. However, the suction caissons have a low aspect ratio (length/diameter) less than 6. The key conclusion of this research has shown that the usage of the multiline anchor system in a FOWT would result in a considerable reduction in the permanent displacements of suction caisson anchors.

Moreover, applying random uniform load histories with two sequences of increasing and decreasing the load amplitudes. Thus, the effect of applying the case of increasing load amplitudes generates larger cumulative displacements, as shown in Figure 5.17 and Figure 5.18. But the implementation of a realistic loading history seems to produce higher cumulative displacements than the random uniform histories.

7.4 Lateral Pile (Spring Model)

The proposed model for the cyclic nonlinear *p-y* curve of piles in soft clay during the cyclic loading is shown to provide a better match to centrifuge test results than the widely used API model. Comparison of model predictions to static and cyclic tests indicates that the nonlinear hardening plasticity assumption satisfactorily predicts significant aspects of pile response, such as the accumulation of cyclic displacement and degradation of soil stiffness.

The proposed spring model can overcome the drawback with the API clay model, which underestimates load capacity measured in cyclic centrifuge tests. The proposed model can be implemented with MATLAB and with ABAQUS/Standard by using a UEL subroutine.

The proposed model offers enhanced abilities for the analysis of monotonic and cyclic lateral pile responses. The model can reproduce the plastic behavior of soil-pile system results from the pile response to lateral loading. The theoretical framework of this model is based on a kinematic hardening of bounding surface plasticity mechanism.

This spring model can be useful in simulating the response of piles anchoring platforms experiencing cyclic loads and the response of suction caissons experiencing cyclic mooring loads for which the accumulated lateral displacements are significant to offshore structures in designing anchors subject to cyclic loads and restrictions related to the maximum accumulated displacements.

7.5 Future Work

Future research along the lines of that investigated in this research can include the following:

1. Study the influence of a gap behind the retaining wall and the caisson under the cyclic loads on the behavior of these structures regarding the deformations and soil pressure.
2. Study the effect of the natural frequency of the wind turbine with respect to the velocity of the cyclic loads acting on the soil-pile systems.
3. Investigate soil-structure interaction for walls and piles in sands under cyclic loads by implementing a subroutine in ABAQUS for estimating the stress-dependent soil modulus and ultimate stress.
4. Using different anchors other than the suction caisson for the multiline mooring system.
5. Study the behavior of caisson foundations in regard to the effects of scour and liquefaction issues under the cyclic loading.

REFERENCES

AASHTO (1994). *LRFD specifications for highway bridges*, American Association of State Highway Officials, Washington, D.C.

AASHTO (1996). *Standard specifications for highway bridges*, American Association of State Highway Officials, Washington, D.C.

AASHTO (2014). *AASHTO LRFD bridge design specifications*, American Association of State Highway and Transportation Officials, Washington, DC.

Abdel-Rahman, K., and Achmus, M. (2005). "Finite element modelling of horizontally loaded monopile foundations for offshore wind energy converters in Germany." *Proceedings of the International Symposium on Frontiers in Off-shore Geotechnics (ISFOG)*, S. Gourvenec, and M. Cassidy, eds., Taylor and Francis, Perth, 391-396.

ABS (2013). "Guide for Building and Classing Floating Offshore Wind Turbine Installations. Standardization." American Bureau of Shipping.

Anastasopoulos, I., Gelagoti, F., Kourkoulis, R., and Gazetas, G. (2011). "Simplified constitutive model for simulation of cyclic response of shallow foundations: validation against laboratory tests." *Journal of Geotechnical and Geoenvironmental Engineering*, 137(12), 1154-1168.

Andersen, K. (2015). "Cyclic soil parameters for offshore foundation design." *Frontiers in Offshore Geotechnics III*, 5.

API (2003). *Recommended practice for planning, designing and constructing fixed offshore platforms–working stress design (RP 2A-WSD)*, American Petroleum Institute.

AREMA (2010). "American railway engineering and maintenance-of-way association." 1312.

Aubeny, C. (2017). *Geomechanics of Marine Anchors*, CRC Press.

Aubeny, C., Han, S., and Murff, J. (2003). "Inclined load capacity of suction caissons." *International Journal for Numerical and Analytical Methods in Geomechanics*, 27(14), 1235-1254.

Aubeny, C., Murff, J., and Moon, S. (2001). "Lateral undrained resistance of suction caisson anchors." *International Journal of Offshore and Polar Engineering*, 11(3).

Babu, G. S., and Basha, B. M. (2008). "Optimum design of cantilever sheet pile walls in sandy soils using inverse reliability approach." *Computers and Geotechnics*, 35(2), 134-143.

Bentler, J. G., and Labuz, J. F. (2006). "Performance of a cantilever retaining wall." *Journal of geotechnical and geoenvironmental engineering*, 132(8), 1062-1070.

Bowles, J. E. (1988). *Foundation analysis and design*, McGraw-Hill.

Bowles, J. E. (1996). *Foundation analysis and design*, McGraw-Hill.

Bransby, P., and Milligan, G. (1975). "Soil deformations near cantilever sheet pile walls." *Géotechnique*, 25(2), 175-195.

Briaud, J.-L. (2013). *Geotechnical engineering: unsaturated and saturated soils*, John Wiley & Sons.

California Department of Transportation (2011). *Trenching and Shoring Manual*, Offices of Structure Construction, Department of Transportation, State of California. USA.

Choi, J. I., Kim, M. M., and Brandenberg, S. J. (2015). "Cyclic p-y Plasticity Model Applied to Pile Foundations in Sand." *Journal of Geotechnical and Geoenvironmental Engineering*, 141(5), 04015013.

Clough, G., and Duncan, J. (1991). "Earth pressures." *Foundation engineering handbook*, Springer, 223-235.

Clukey, E. C., and Morrison, M. J. "A centrifuge and analytical study to evaluate suction caissons for TLP applications in the Gulf of Mexico." *Proc., Design and performance of deep foundations: Piles and piers in soil and soft rock*, ASCE, 141-156.

Colliat, J., Boisard, P., Andersen, K., and Schroeder, K. "Caisson foundations as alternative anchors for permanent mooring of a process barge offshore Congo." *Proc., Offshore Technology Conference*, Offshore Technology Conference.

Coulling, A. J., Goupee, A. J., Robertson, A. N., Jonkman, J. M., and Dagher, H. J. (2013). "Validation of a FAST semi-submersible floating wind turbine numerical model with DeepCwind test data." *Journal of Renewable and Sustainable Energy*, 5(2), 023116.

Dafalias, Y. F. (1986). "Bounding surface plasticity. I: Mathematical foundation and hypoplasticity." *Journal of Engineering Mechanics*, 112(9), 966-987.

Dafalias, Y. F., and Herrmann, L. R. (1986). "Bounding surface plasticity. II: Application to isotropic cohesive soils." *Journal of Engineering Mechanics*, 112(12), 1263-1291.

DNV (2014). "Design of Offshore Wind Turbine Structures, DET NORSKE VERITAS AS."

Esmaeili, M., and Fatollahzadeh, A. (2012). "Effect of train live load on railway bridge abutments." *Journal of Bridge Engineering*, 18(6), 576-583.

EWEA (2016). "The European offshore wind industry-key trends and statistics 2015." *I. Pineda (Ed.)*.

Finn, W. L., Wu, G., and Yoshida, N. "Seismic response of sheet pile walls." *Proc., Proceedings, 10 th World Conference on Earthquake Engineering*, 1689-1694.

Fontana, C. M., Hallowell, S. T., Arwade, S. R., DeGroot, D. J., Landon, M. E., Aubeny, C. P., Diaz, B., Myers, A. T., and Ozmutlu, S. (2018). "Multiline anchor force dynamics in floating offshore wind turbines." *Wind Energy*.

Georgiadis, M., and Anagnostopoulos, C. (1998). "Lateral pressure on sheet pile walls due to strip load." *Journal of geotechnical and geoenvironmental engineering*, 124(1), 95-98.

Gerolymos, N., and Gazetas, G. (2006). "Development of Winkler model for static and dynamic response of caisson foundations with soil and interface nonlinearities." *Soil Dynamics and Earthquake Engineering*, 26(5), 363-376.

Gerolymos, N., Gazetas, G., and Tazoh, T. "Static and dynamic response of yielding pile in nonlinear soil." *Proc., Proceedings of the 1st Greece–Japan workshop: seismic design, observation and retrofit of foundations, Athens*, 25-35.

Gilbert, R. B., Wang, S.-T., Senanayake, A., and Rendon, E. (2015). "Design of wind turbine monpiles for lateral loads." Technical report, Bureau of Safety and Environmental Enforcement.

Goodman, L., Lee, C., and Walker, F. (1961). "The feasibility of vacuum anchorage in soil." *Geotechnique*, 1(3), 356-359.

Gopal Madabhushi, S., and Chandrasekaran, V. (2005). "Rotation of cantilever sheet pile walls." *Journal of geotechnical and geoenvironmental engineering*, 131(2), 202-212.

Greco, V. R. (2006). "Lateral earth pressure due to backfill subject to a strip of surcharge." *Geotechnical & Geological Engineering*, 24(3), 615-636.

GTS (2004). "Guidelines for Temporary Shoring." Railway and Union Pacific, 25pp.

Haiderali, A., Nakashima, M., and Madabhushi, S. "Cyclic lateral loading of monopiles for offshore wind turbines." *Proc., 3rd International Symposium on Frontiers in Offshore Geotechnics (ISFOG 2015), Oslo, Norway*.

Hall, M. (2017). "MoorDyn—Users Guide." *Department of Mechanical Engineering, University of Maine: Orono, ME, USA*.

Hall, M., and Goupee, A. (2015). "Validation of a lumped-mass mooring line model with DeepCwind semisubmersible model test data." *Ocean Engineering*, 104, 590-603.

Hong, Y., He, B., Wang, L., Wang, Z., Ng, C. W. W., and Mašín, D. (2017). "Cyclic lateral response and failure mechanisms of semi-rigid pile in soft clay: centrifuge tests and numerical modelling." *Canadian Geotechnical Journal*, 54(6), 806-824.

Huang, C.-C., Menq, F.-Y., and Chou, Y.-C. (1999). "The effect of the bending rigidity of a wall on lateral pressure distribution." *Canadian Geotechnical Journal*, 36(6), 1039-1055.

Ilupeju, O. A. (2014). "Soil-Spring Model for Fatigue Evaluation of Cyclic-Loaded Offshore Conductors."

Ishibashi, I., and Zhang, X. (1993). "Unified dynamic shear moduli and damping ratios of sand and clay." *Soils and Foundations*, 33(1), 182-191.

Jarquio, R. (1981). "Total lateral surcharge pressure due to strip load." *Journal of Geotechnical and Geoenvironmental Engineering*, 107(ASCE 16585 Proceeding).

Jeanjean, P. "Re-assessment of py curves for soft clays from centrifuge testing and finite element modeling." *Proc., Offshore Technology Conference*, Offshore Technology Conference.

Jonkman, B., and Jonkman, J. (2016). "FAST v8. 16.00 a–bjj." *National Renewable Energy Laboratory*.

Jonkman, B., and Kilcher, L. (2012). "TurbSim User's Guide: Version 1.06. 00, Tech. rep." National Renewable Energy Laboratory (NREL) Golden, CO.

Jonkman, J., Butterfield, S., Musial, W., and Scott, G. (2009). "Definition of a 5-MW reference wind turbine for offshore system development." *National Renewable Energy Laboratory, Golden, CO, Technical Report No. NREL/TP-500-38060.*

Jonkman, J., Robertson, A., and Hayman, G. (2015). "HydroDyn user's guide and theory manual." *National Renewable Energy Laboratory*.

Jonkman, J. M., and Buhl Jr, M. L. (2005). "FAST user's guide." *National Renewable Energy Laboratory, Golden, CO, Technical Report No. NREL/EL-500-38230*.

Kim, J. S., and Barker, R. M. (2002). "Effect of live load surcharge on retaining walls and abutments." *Journal of geotechnical and geoenvironmental engineering*, 128(10), 803-813.

King, G. (1995). "Analysis of cantilever sheet-pile walls in cohesionless soil." *Journal of geotechnical engineering*, 121(9), 629-635.

Klinkvort, R. T., and Hededal, O. (2013). "Lateral response of monopile supporting an offshore wind turbine." *Proceedings of the Institution of Civil Engineers-Geotechnical Engineering*, 166(2), 147-158.

Kondner, R. L. (1963). "Hyperbolic stress-strain response: cohesive soils." *J. Geotech. Engrg. Div.*, 89(1), 115-143.

Krabbenhoft, K., and Damkilde, L. (2003). "A general non-linear optimization algorithm for lower bound limit analysis." *International Journal for Numerical Methods in Engineering*, 56(2), 165-184.

Krabbenhoft, K., Damkilde, L., and Krabbenhoft, S. (2005). "Ultimate limit state design of sheet pile walls by finite elements and nonlinear programming." *Computers & structures*, 83(4), 383-393.

Kuo, K., and Hunt, H. (2013). "An efficient model for the dynamic behaviour of a single pile in viscoelastic soil." *Journal of Sound and Vibration*, 332(10), 2549-2561.

Lau, B. H. (2015). "Cyclic behaviour of monopile foundations for offshore wind turbines in clay." University of Cambridge.

Li, D., Hyslip, J., Sussmann, T., and Chrismer, S. (2016). *Railway geotechnics*, CRC Press.

Li, W., Igoe, D., and Gavin, K. (2015). "Field tests to investigate the cyclic response of monopiles in sand." *Proceedings of the Institution of Civil Engineers-Geotechnical Engineering*, 168(5), 407-421.

Lombardi, D., Bhattacharya, S., and Wood, D. M. (2013). "Dynamic soil–structure interaction of monopile supported wind turbines in cohesive soil." *Soil Dynamics and Earthquake Engineering*, 49, 165-180.

Long, J., and Vanneste, G. (1994). "Effects of cyclic lateral loads on piles in sand." *Journal of Geotechnical Engineering*, 120(1), 225-244.

Lyamin, A., and Sloan, S. (2002). "Lower bound limit analysis using non-linear programming." *International Journal for Numerical Methods in Engineering*, 55(5), 573-611.

Matlock, H. (1970). "Correlations for design of laterally loaded piles in soft clay." *Offshore Technology in Civil Engineering's Hall of Fame Papers from the Early Years*, 77-94.

Milligan, G. (1983). "Soil deformations near anchored sheet-pile walls." *Geotechnique*, 33(1), 41-55.

Misra, B. (1980). "Lateral pressures on retaining walls due to loads on surface of granular backfill." *Soils and Foundations*, 20(2), 31-44.

Mohammadrajabi, M. (2016). "Live load effects of railroads on retaining walls and temporary shoring." *(Doctoral dissertation)*Texas A&M University, College Station, Texas.

Motta, E. (1994). "Generalized Coulomb active-earth pressure for distanced surcharge." *Journal of Geotechnical Engineering*, 120(6), 1072-1079.

Murff, J. D., and Hamilton, J. M. (1993). "P-ultimate for undrained analysis of laterally loaded piles." *Journal of Geotechnical Engineering*, 119(1), 91-107.

Pappusetty, D., and Pando, M. A. (2013). "Numerical evaluation of long term monopile head behavior for ocean energy converters under sustained low amplitude lateral loading." *International Journal of Civil and Structural Engineering*, 3(4), 669.

Pettigrew, N. R., Xue, H., Irish, J. D., Perrie, W., Roesler, C. S., Thomas, A. C., and Townsend, D. W. (2008). "The Gulf of Maine Ocean Observing System: generic lessons learned in the first seven years of operation (2001-2008)." *Marine Technology Society Journal*, 42(3), 91-102.

Randolph, M., Cassidy, M., Gourvenec, S., and Erbrich, C. "Challenges of offshore geotechnical engineering." *Proc., Proceedings of the international conference on soil mechanics and geotechnical engineering*, AA Balkema Publishers, 123.

Randolph, M. F., Gaudin, C., Gourvenec, S. M., White, D. J., Boylan, N., and Cassidy, M. J. (2011). "Recent advances in offshore geotechnics for deep water oil and gas developments." *Ocean Engineering*, 38(7), 818-834.

Robertson, A., Jonkman, J., Masciola, M., Song, H., Goupee, A., Coulling, A., and Luan, C. (2014). "Definition of the semisubmersible floating system for phase II of OC4." National Renewable Energy Lab.(NREL), Golden, CO (United States).

Senanayake, A. I. M. J. (2016). "Design of large diameter monopiles for offshore wind turbines in clay." Doctoral dissertation.

Senpere, D., and Auvergne, G. A. "Suction anchor piles-a proven alternative to driving or drilling." *Proc., Offshore Technology Conference*, Offshore Technology Conference.

Simo, J., and Hughes, T. (1998). "Computational Inelasticity. Springer: New York."

Simulia (2014). "ABAQUS Documentation." Dassault Systèmes, Providence, RI, USA.

Smethurst, J., and Powrie, W. (2007). "Monitoring and analysis of the bending behaviour of discrete piles used to stabilise a railway embankment." *Geotechnique*, 57(8), 663-677.

Tatsuoka, F., Tateyama, M., and Koseki, J. (1996). "Performance of soil retaining walls for railway embankments." *Soils and Foundations*, 36(Special), 311-324.

Templeton, J. S. (2009). "Finite element analysis of conductor/seafloor interaction." *Offshore Technology Conference*, Offshore Technology Conference, Houston, Texas, USA.

UIC (2006). *Code 776-1 R, Loads to be considered in railway bridge design*, International Union of Railways, Paris.

UMaine (2013). "University of Maine. Mooring E0130: Central Maine Shelf, Gulf of Maine Moored Buoy Program, Physical Oceanography Group, School of Marine Sciences." <http://gyre.umeoce.maine.edu/buoyhome.php>.

Viselli, A. M., Goupee, A. J., and Dagher, H. J. (2015). "Model test of a 1: 8-scale floating wind turbine offshore in the gulf of maine." *Journal of Offshore Mechanics and Arctic Engineering*, 137(4), 041901.

Viselli, A. M., Goupee, A. J., Dagher, H. J., and Allen, C. K. (2016). "Design and model confirmation of the intermediate scale VolturnUS floating wind turbine subjected to its extreme design conditions offshore Maine." *Wind Energy*, 19(6), 1161-1177.

Viswanadham, B., Madabhushi, S., Babu, K., and Chandrasekaran, V. (2009). "Modelling the failure of a cantilever sheet pile wall." *International Journal of Geotechnical Engineering*, 3(2), 215-231.

Wang, C.-D. (2007a). "Lateral force and centroid location caused by horizontal and vertical surcharge strip loads on a cross-anisotropic backfill." *International Journal for Numerical and Analytical Methods in Geomechanics*, 31(13), 1443-1475.

Wang, C.-D. (2007b). "Lateral force induced by rectangular surcharge loads on a cross-anisotropic backfill." *Journal of Geotechnical and Geoenvironmental Engineering*, 133(10), 1259-1276.

Wiemann, J., Lesny, K., and Richwien, W. (2004). "Evaluation of the pile diameter effects on soil-pile stiffness." *Proceedings of the 7th German Wind Energy Conference (DEWEK), Wilhelmshaven*.

Yu, L.-q., Wang, L.-z., Guo, Z., Bhattacharya, S., Nikitas, G., Li, L.-l., and Xing, Y.-l. (2015). "Long-term dynamic behavior of monopile supported offshore wind turbines in sand." *Theoretical and Applied Mechanics Letters*, 5(2), 80-84.

Zakeri, A., Clukey, E., Kebadze, B., Jeanjean, P., Walker, D., Piercey, G., Templeton, J., Connelly, L., and Aubeny, C. (2015). "Recent advances in soil response modeling for well conductor fatigue analysis and development of new approaches." *Offshore Technology Conference*, Offshore Technology Conference, Houston, Texas, USA.

Ziegler, L., and Muskulus, M. (2016). "Lifetime extension of offshore wind monopiles: Assessment process and relevance of fatigue crack inspection." *Proceedings of the 12th EAWE PhD Seminar on Wind Energy in Europe (DTU Lyngby, Denmark)*, 25-27.

APPENDIX

FINITE ELEMENT SIMULATION WITH ABAQUS

A.1 Cyclic Amplitudes

To simulate the cyclic loads for a problem as shown in Figure A - 1, it needs to write as below in the input file:

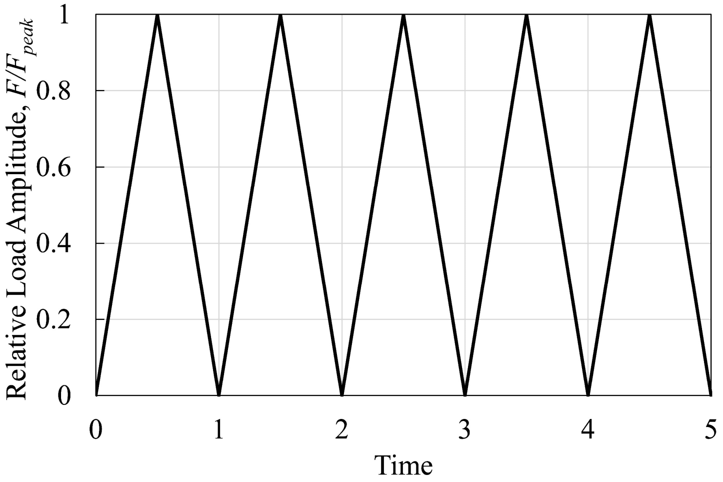

Figure A - 1. Cyclic loading (e.g. 5 cycles)

```
*AMPLITUDE, NAME=CYCLE, DEFINITION=SMOOTH STEP
0, 0
0.5, 1
1, 0
1.5, 1
2, 0
2.5, 1
3, 0
3.5, 1
4, 0
4.5, 1
5, 0
```

After that, use the same name (CYCLE) in the STEP section for the loads in the input file.

A.2 Axisymmetric Simulation

To simulate the Fourier elements with any Fourier mode, it needs to add the OFFSET option with a large number such as 100000 to the element define, as below:

*ELEMENT, TYPE=CAXA44, OFFSET=100000 ⇐ (for soil elements)

*ELEMENT, TYPE=SAXA14, OFFSET=100000 ⇐ (for caisson elements)

Also, to simulate the cyclic loads at the padeye of a caisson with axisymmetric-Fourier elements model, it needs to be aware of the way of applying the loads at the padeye when dealing with multiline systems for caisson. The ordinary method is to apply an opposite direction (-F) for the original force (+F) at the same padeye but this method would be wrong because the opposite direction (-F) will be the reverse force of the original load (+F) and that means the vertical components ($-F_y$) of the negative load will be in the wrong direction of applying the multiline concept, as shown in Figure A - 2.

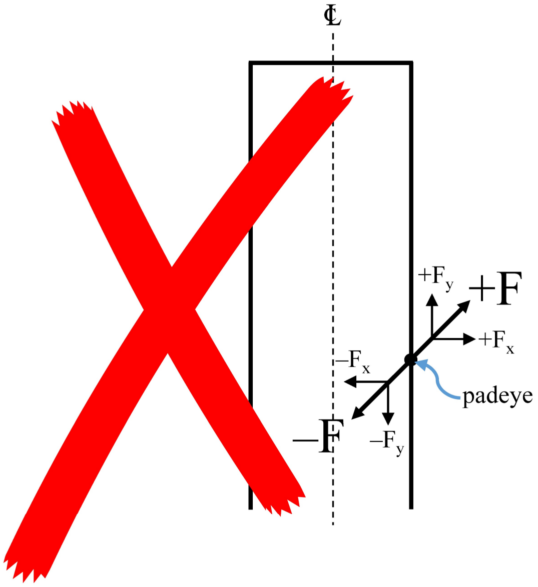

Figure A - 2. Wrong method

To do it right, there are two methods: The first method (Figure A - 3) is to apply the negative load (-F) on another node (padeye 2) at the parallel caisson wall which is the same node number of padeye 1 and adding (100000×Fourier element mode) to get the node number of padeye 2, e.g., if the node number of padeye 1 is 2019, the node number of padeye 2 will be 2019+(100000×4)= 402019 on the other side of the caisson wall. In addition, it needs to define the amplitudes in two parts depends on the load directions in x-axis and y-axis, as:

```
*AMPLITUDE, NAME=CYCLE_X, DEFINITION=SMOOTH STEP
……..
……..

*AMPLITUDE, NAME=CYCLE_Y, DEFINITION=SMOOTH STEP
……..
……..
```

But be sure to define all amplitudes in CYCLE_Y group in positive direction.

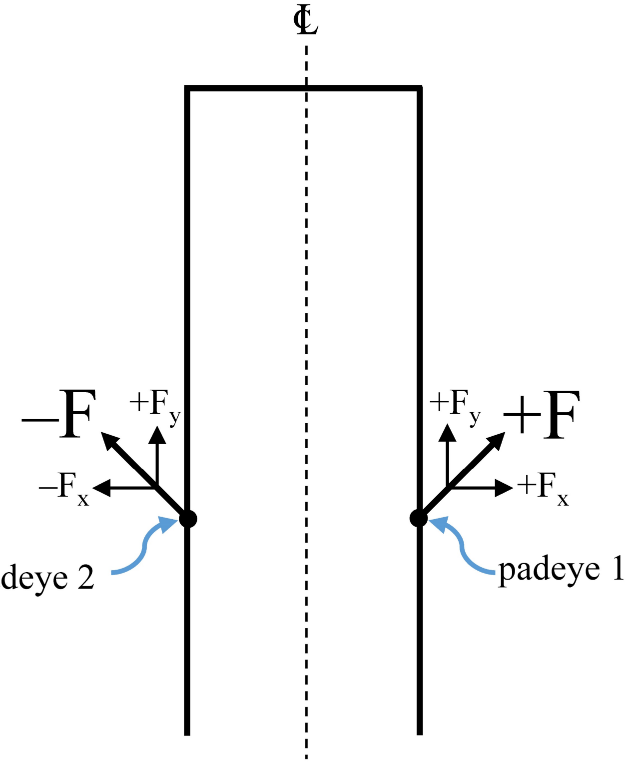

Figure A - 3. First method

The second method (Figure A - 4) is to apply the positive load (+F) and the negative load (-F) on the same node (center-padeye) by defining a new node at the centerline of caisson which is an elongation of the trajectory of the force at the padeye of the caisson wall and these two nodes (padeye and center-padeye) should be connected with a rigid element such as CONN3D2 element. Also, it needs to define the amplitudes in two parts depends on the load directions in x-axis and y-axis for center-padeye node as mentioned before.

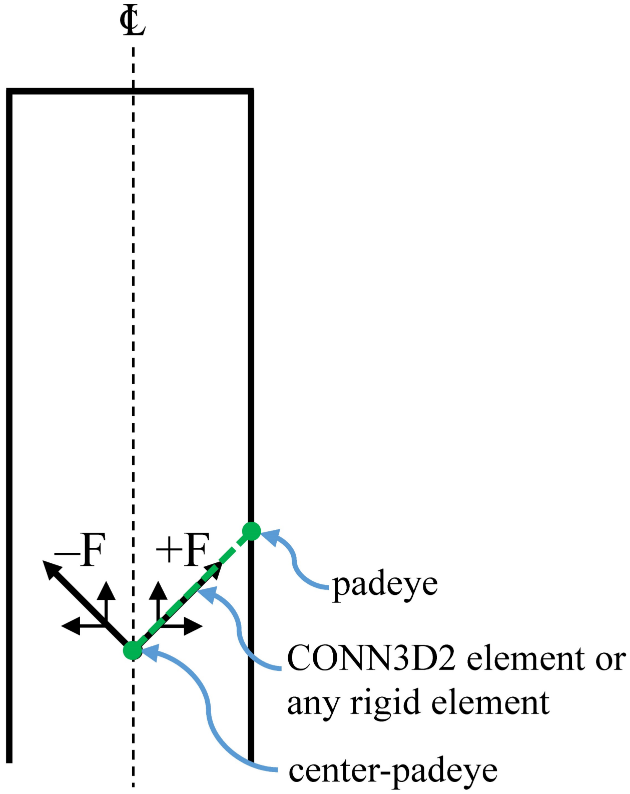

Figure A - 4. Second method

Moreover, the boundary conditions (BC) of the axisymmetric Fourier model need to be defined by generating the nodes on the virtual sides of the Fourier element of the mesh based on the Fourier mode and adding their node numbers to BC groups, for example:

```
*NSET, NSET=BC_SIDES, GENERATE
2213, 2277, 1
102213, 102277, 1
202213, 202277, 1        Node numbers based on Fourier element modes
302213, 302277, 1
402213, 402277, 1
…….
…….

*NSET, NSET=BC_BOTTOM, GENERATE
1, 100, 33
133, 2213, 65
100001, 100100, 33
100133, 102213, 65
200001, 200100, 33
200133, 202213, 65        Node numbers based on Fourier element modes
300001, 300100, 33
300133, 302213, 65
400001, 400100, 33
400133, 402213, 65
…….
…….
```